Electromagnetic radiation and scattering from small canonical structures of double-negative metamaterials

Arslanagic, Samel

Publication date:
2007

Electromagnetic Radiation and Scattering from Small Canonical Structures of Double-Negative Metamaterials

Ph.D. thesis

Samel Arslanagić

March 2007

The present thesis was carried out at the ElectroScience Section, Ørsted•DTU in partial fulfillment of the requirements for the Ph.D. degree from the Technical University of Denmark.

Supervisor: Professor Olav Breinbjerg, Ph.D.

ISBN: 97-8879-11847-72

The thesis was submitted for evaluation in March 2007 and the Ph.D. degree was awarded by the Technical University of Denmark in September 2007. This reprint, in which a few typographical errors have been corrected relative to the thesis on which basis the degree was awarded, was released in October 2007.

Abstract

Electromagnetic Radiation and Scattering from Small Canonical Structures of Double-Negative Metamaterials

Various aspects of double-negative (DNG) and single-negative (SNG) metamaterials (MTMs), with the emphasis on the former, as well as combinations of these with conventional double-positive (DPS) materials, have been investigated. The study was initiated by clarifications of specific theoretical aspects associated with DNG materials, and was subsequently extended to investigations of the radiation and scattering from two- and three-dimensional (2D and 3D) MTM-based canonical problems in electromagnetic theory.

As to the theoretical aspects of DNG materials, the sign, or more generally the branch, of certain derived parameters associated with them, such as wave number, intrinsic impedance, and refractive index is examined. A consistent set of definitions for these parameters, each yielding a specific sign of the parameter in question, is introduced. It is shown that one definition, and thus the sign, may be more convenient than another, but that the correct solution to a given problem can be obtained with all definitions as long as they are used consistently to provide the expected physical behaviour. These findings are confirmed through a canonical example consisting of a DPS/DNG interface upon which an oblique uniform plane wave is incident. This problem is solved under the assumption that the sign of a given parameter can be positive or negative. It is shown that the use of different signs of the derived parameters leads to different functional forms of e.g., the reflection and transmission coefficients, as well as Snell's law of refraction, and moreover, that for all choices of the signs, the physical behaviour of the solution is as expected.

Previous studies on MTM-based 2D and 3D canonical problems have demonstrated the advantages of exploiting specific arrangements of MTMs in rectangular, cylindrical and spherical configurations to design electrically small, resonant structures such as cavities, waveguides, scatterers and radiators. These ideas are extended here to canonical antenna and scattering configurations which consist of electrically small resonant cylindrical and spherical MTM-based structures excited by an arbitrarily located electric line source and an arbitrarily located and oriented electric Hertzian dipole, respectively. Exact analytical solutions, based on eigenfunction series, are derived and then numerically evaluated to study the radiation and scattering from these structures. Specifically, quantities such as the near field, total radiated power, directivity, as well as the total and differential scattering cross sections, are calculated and their variations with respect to various parameters are investigated. It is shown that the electrically small MTM-based structures possess numerous advantages as compared to the corresponding structures based on the DPS materials alone. In particular, it is demonstrated analytically and numerically, that the cylindrical and spherical MTM-based structures can be designed to be resonant even if their electrical size is arbitrarily small. Significant changes of the field radiated by the respective sources, as well as a significant enhancement of the total radiated power and the scattering cross sections are obtained with these cylindrical and spherical MTM-based structures of which the size is of the order of $1/50$ and $1/37$, respectively, of the free-space wavelength. The enhancement of e.g., the total radiated power, as compared to the power radiated by the respective sources alone in free space, is found to be of the order of 55 dB, for cylindrical, and 93 dB, for spherical structures. These resonant effects, not present in the corresponding DPS-based structures, are also found to lead to a possibility of controlling the directivity patterns of specific MTM-based structures, as different resonant modes can be excited depending on the location of the source. The influence of losses and dispersion, present in any realistic MTM, has also been investigated. It is demonstrated that the resonant effects of the electrically small MTM-based structures, and thus the resulting enhancements of e.g., the total radiated power, are diminished as the losses are included, while being confined, but still present, to very narrow bands of frequency upon inclusion of dispersion. In addition to these investigations of electrically small structures, the properties of several structures for which the size is comparable to the free-space wavelength have likewise been examined. The results obtained for these structures clearly show there is no advantage in using MTMs in such structures as compared to DPS materials, this being in sharp contrast to the case of electrically small structures.

Resumé (In Danish)

Elektromagnetisk Udstråling og Spredning Fra Små Kanoniske Strukturer af Dobbelt-Negative Metamaterialer

Forskellige aspekter af dobbelt-negative (DNG) og enkelt-negative (SNG) metamaterialer (MTM), med vægt på førstenævnte, såvel som deres kombinationer med konventionelle dobbelt-positive (DPS) materialer, er blevet undersøgt. Studiet blev påbegyndt med afklaringen af specifikke teoretiske aspekter af DNG materialer, og blev efterfølgende udvidet til undersøgelser af udstråling og spredning fra to- og tre-dimensionelle (2D og 3D) MTM-baserede kanoniske problemer i elektromagnetisk feltteori.

Angående de teoretiske aspekter af DNG materialer undersøges fortegnet, eller mere generelt grenen, for nogle udledte parametre tilknyttet til disse materialer, såsom bølgetal, specifik impedans, og refraktiv index. Der introduceres en konsistent sæt af definitioner for disse parametre, hvor enhver definition giver et bestemt fortegn for parameteren af interesse. Det vises, at en definition, og dermed fortegn, kan være mere bekvem end en anden, men at en korrekt løsning til et givet problem kan opnås med alle definitioner så længe disse benyttes konsekvent til at give den forventede fysiske opførsel. Disse resultater bekræftes via et kanonisk problem bestående af en DPS/DNG grænseflade belyst af en uniform plan bølge under skråt indfald. Problemet løses under antagelsen af, at fortegnet for en given parameter kan være positivt eller negativt. Det vises at brugen af forskellige fortegn for de udledte parametre fører til forskellige funktionelle former af f.eks. reflektions og transmissions koefficienter, såvel som Snell's refraktions lov, og ydermere, at den fysiske opførsel af løsningen er som forventet for alle valg af fortegn.

Tidligere studier af MTM-baserede 2D og 3D kanoniske problemer har demonstreret fordele ved at bruge specifikke ordninger af MTM i rektangulære, cylindriske og sfæriske konfigurationer til at designe elektrisk små resonante strukturer såsom, kaviteter, bølgeledere, spredere og radiatorer. Disse ideer udvides her til kanoniske antenne og sprednings konfigurationer bestående af elektrisk små resonante cylindriske og sfæriske MTM-baserede strukturer exciteret henholdsvis med en vilkårligt placeret elektrisk linie kilde, og en vilkårligt placeret og orienteret elektrisk Hertz dipol. Eksakte analytiske løsninger, baseret på egenfunktions udviklinger, udledes og evalueres numerisk for at studere udstråling og spredning fra disse strukturer. Mere specifikt udregnes størrelser såsom nærfelt, total udstrålet effekt, direktivitet, samt total og differentiel spredningstværsnit, og deres variationer med forskellige parametre undesøges. Det vises, at elektrisk små MTM-baserede strukturer besidder talrige fordele i forhold til de tilsvarende strukturer som alene baseres på DPS materialer. Ydermere demonstreres det analytisk og numerisk, at MTM-baserede cylindriske of sfærsike strukturer kan designes til at være resonante på trods af deres elektrisk små størrelse. Betydelige ændringer af feltet udstrålet fra de respektive kilder, såvel som betydelig forøgelse af den totale udstrålede effekt og spredningstværsnit, opnås med disse cylindriske of sfærsike MTM-baserede strukturer som har en størrelse på henholdsvis $1/100$ og $1/37$ af frit-rums bølgelængden. Førøgelsen af f.eks. den totale udstrålede effekt, sammenlignet med effekten udstrålet fra de respektive kilder i frit rum, er i størrelsesorden 55 dB, for cylindriske, og 93 dB, for sfæriske strukturer. Disse resonante effekter, som ikke er tilstede for de tilsvarende DPS-baserede strukturer, fører ligeledes til en mulighed for at kontrollere udstrålingsdiagrammer for direktivitet for specifikke MTM-baserede strukturer, eftersom forskellige modes kan exciteres afhængig af placeringen af kilden. Indflydelsen af tab og dispersion, som er til stede i ethvert realistisk MTM, er ligeledes blevet undersøgt. Det demonstreres, at resonante effekter i elektrisk små MTM-baserede strukturer, og dermed forøgelsen af f.eks. den totale udstrålede effekt, dæmpes med inklusion af tab, mens de indsnævres i frekvens, men ikke forsvinder, med inklusion af dispersion. Udover disse undersøgelser af elektrisk små strukturer er ligeledes egenskaberne af forskellige strukturer hvis dimensioner er sammenlignelige med frit-rums bølgelængden blevet undersøgt. Resultaterne for disse strukturer viser klart, at der ikke er nogen fordel forbundet med at bruge MTM i forhold til DPS materialer, hvilket er i skarp kontrast til tilfældet med elektrisk små strukturer.

Preface

The present thesis contains the work carried out during my Ph.D. study at the ElectroScience Section, Ørsted•DTU, Technical University of Denmark (DTU). The study was initiated in March 2004 and finalized in March 2007. As a part of this study I have spent five and a half months, starting from August 2005, as a visiting scholar at the Electromagnetics Laboratory, University of Arizona, Tucson, Arizona.

There are several people who encouraged and assisted me in this endeavor, and to them I would like to express my gratitude.

I would like to acknowledge my supervisor, Professor Olav Breinbjerg, who directed my attention to the field of metamaterials and for having encouraged me to pursue this Ph.D. study. I also thank him for his inspiring teaching attitude that initially brought my attention to electromagnetic theory some 7 years ago. His invaluable help and numerous fruitful discussions that we had in the course of my Ph.D. study are highly appreciated, as is his sense for details, from which I benefited greatly.

I would also like to extend my deepest gratitude and appreciation to Professor Richard W. Ziolkowski from the University of Arizona, for accepting my request to work with him as a visiting scholar. His inspiring attitude has certainly pushed me towards new directions and goals, and made my Ph.D. study a very exciting one, and certainly worth all the efforts. His insight into the field of metamaterials, and a will to help, facilitated, as well as contributed, greatly to the accomplishment of many of the topics presented in this thesis. Aside from Professor Ziolkowski's enormous help from the professional point of view, his great hospitality and sincere friendship made the entire stay in Tucson an unforgettable affair. Many thanks goes to Mr. Aycan Erentok, who unselfishly assisted me in finding the appropriate accommodation for my stay in Tucson, and with whom I have shared invaluable discussions of electromagnetic as well as daily-life nature.

My Ph.D. was funded by DTU. However, I was fortunate to receive travel support from the Tranes Foundation, the Otto Mønsteds Foundation, and the TICRA Foundation. Their financial support allowed me to travel abroad and made my stay in Tucson more enjoyable. Therefore I sincerely thank these foundations for their generous, and highly appreciated, support.

Finally, I would like to thank my family for their love, patience, and incredible support during this study. In particular, I am deeply appreciative and grateful to my loving wife Mirela Arslanagić for her unseen patience, supportive attitude, and ever optimistic nature, as well as to my dear uncle Sead, ant Senita, and my precious little sisters Azra and Aida. In particular, I thank them for their continuous reminders on the fact that there is a very beautiful life beyond electromagnetic theory.

I devote the thesis to my beloved grandmother Nazira Arslanagić, for the sacrifice she made so that I could be the person I am today.

Technical University of Denmark, 2007 — Samel Arslanagić

List of publications

***Journal publications*:**

1. **S. Arslanagić**, R.W. Ziolkowski and O. Breinbjerg, "Analytical and numerical investigation of the radiation from concentric metamaterial spheres excited by an electric Hertzian dipole," submitted to *Radio Science, Special Issue on Analytical Scattering and Diffraction*, Ed.: P. L. E. Uslenghi, March 2007.
2. **S. Arslanagić**, R.W. Ziolkowski and O. Breinbjerg, "Analytical and numerical investigation of the radiation and scattering from concentric metamaterial cylinders excited by an electric line source," submitted as an Invited Paper to *Radio Science, Special Issue on Analytical Scattering and Diffraction*, Ed.: P. L. E. Uslenghi, Feb. 2007.
3. **S. Arslanagić**, R.W. Ziolkowski and O. Breinbjerg, "Excitation of an electrically small metamaterial-coated cylinder by an arbitrarily located line source," *Microwave and Optical Technology Letters*, vol. 48 (12), pp. 2598-2605, Dec. 2006.
4. **S. Arslanagić** and O. Breinbjerg, "Electric line source illumination of a circular cylinder of lossless double-negative material: an investigation of near field, directivity, and radiation resistance," *IEEE Antennas and Propagation Magazine*, vol. 48 (3), pp. 38-54, June 2006.

***Conference publications*:**

1. **S. Arslanagić**, R.W. Ziolkowski and O. Breinbjerg, "Radiation properties of concentric metamaterial spheres excited by an electric Hertzian dipole," submitted to *Metamaterials 2007: The First International Congress on Advanced Electromagnetic Materials for Microwaves and Optics*, Rome, Italy, October 22-26, 2007.
2. **S. Arslanagić**, R.W. Ziolkowski and O. Breinbjerg, "Far-field properties of a line source-excited electrically small quadrupolar metamaterial cylindrical shell," *International Workshop on Antenna Technology 2007 (iWAT07) − Small and Smart Antennas, Metamaterials and Applications*, Cambridge, UK, March 21-23, 2007, pp. 376-379.
3. **S. Arslanagić**, R.W. Ziolkowski and O. Breinbjerg, "Near-field distribution, directivity and differential scattering cross section for a line source-excited metamaterial-coated electrically small cylinder," *The First European Conference on Antennas and Propagation (EuCAP)*, Nice, France, Nov. 6-10, 2006.
4. **S. Arslanagić**, R.W. Ziolkowski and O. Breinbjerg, "Hertzian dipole excitation of higher order resonant modes in electrically small nested metamaterial shells: source and scattering results," *Proceedings of the IV International Workshop on Electromagnetic Wave Scattering (EWS)*, Gebze, Turkey, Sept. 18-22, 2006, pp. 8.9-8.14.
5. **S. Arslanagić**, R.W. Ziolkowski and O. Breinbjerg, "Fundamentals of metamaterials and their applications in the design of efficient sub-wavelength radiators and scatterers," *International Student Seminar on Microwave Applications of Novel Physical Phenomena*, Rovaniemi, Finland, Aug. 24-25, 2006, pp. 24-26.
6. **S. Arslanagić**, R.W. Ziolkowski and O. Breinbjerg, "Line source excitation of multilayered metamaterial cylinders: source and scattering results," *IEEE APS Int. Symp./USNC/URSI Nat. Radio Science Meeting.*, Albuquerque, NM, USA, July 9-14, 2006, pp. 676-679.
7. **S. Arslanagić**, R.W. Ziolkowski and O. Breinbjerg, "Radiated power and total scattering cross section of multilayered cylinders excited by an electric line source," *The Third Workshop on Metamaterials and Special Materials for Electromagnetic Applications and TLC*, Rome, Italy, March 30-31, 2006, p. 18.

8. **S. Arslanagić** and O. Breinbjerg, "On sign and branch of certain parameters for simple, lossy double-negative materials," *USNC/URSI National Radio Science Meeting*, Boulder, Colorado, USA, Jan. 4-7, 2006, p. 59.

9. **S. Arslanagić** and O. Breinbjerg, "Clarification of the sign of wave number, intrinsic impedance, and refractive index for simple lossless and lossy double negative materials," *EPFL Latsis Symposium 2005, Negative Refraction: Revisiting electromagnetics from microwaves to optics*, Feb. 28−March 2, 2005, p. 78.

10. **S. Arslanagić** and O. Breinbjerg, "Electric line source illumination of lossless left-handed cylinders - a study of near-field and far-field properties," *Proceedings of the Turkish National URSI Committee Meeting*, Bilkent University, Ankara, Turkey, 2004, pp. 19-25.

***Technical reports*:**

1. **S. Arslanagić** and O. Breinbjerg, *A note on the sign of some important parameters for double-negative materials*, Ørsted•DTU, ElectroScience Section, Technical University of Denmark, Internal Report, IR 781, March 2007.

All publications have mainly been prepared by the author of the present work. In all cases, the present author has produced the first version of the publication, and its final form emerged through several correspondences with the other authors of the publication.

Contents

Part I

Main part

CHAPTER 1

INTRODUCTION

The electromagnetics community has recently experienced a broad and intense interest in exploring the properties of various classes of metamaterials (MTMs) and exploiting combinations of them with conventional double-positive (DPS) materials, see e.g., [1]-[3]. The MTMs are artificially engineered materials with properties not readily available in nature and, as such, they may offer new design opportunities that may lead to interesting devices for use in various segments of the electromagnetic spectrum. The different classes of MTMs include single-negative (SNG) materials, such as epsilon-negative (ENG) and mu-negative (MNG) materials, and double-negative (DNG) materials.

The first systematic study of isotropic DNG materials, which are characterized by a negative real part of both the permittivity and permeability, was performed in [4] back in 1967. In this pioneering work, unusual properties, e.g., the reversal of the familiar Snell's law of refraction at the interface between a conventional DPS and a DNG material, and the resulting phenomenon of negative refraction, were reported, and their potential exploitation in a variety of applications was discussed. However, research on these exotic materials stagnated until recently where the first artificial DNG material designs emerged [5]-[10]. Subsequently, there has been a resurgence in interest in artificial media. A considerable amount of theoretical and practical research has already been performed to understand the properties of DNG and related MTMs. Numerous applications have been proposed, e.g., see [1]-[3] and the extensive list of works referenced therein. A brief review of realizations and applications of DNG materials can be found in Chapter 2 of the present work.

As to the DNG material work of a purely theoretical nature, significant attention has been devoted, among other issues, to the clarification of the sign, or more generally the branch, of various parameters, such as the refractive index, wave number, and intrinsic impedance, that describe wave interactions with DNG materials [11]-[23]. In the majority of these works [11]-[20], as well as in [4], it was argued that the simultaneous negative permittivity and permeability in isotropic and lossless DNG materials lead to a negative refractive index. The notion of a negative refractive index stands in sharp contrast to the assumed positive refractive index in conventional DPS materials. As such, this negative refractive index notion was critically analyzed in [22] and [23], in which it was stipulated that the refractive index in DNG materials may as well be positive. Apart from the sign of the refractive index, some of these works also discussed the sign of other parameters in DNG materials, including the wave number and intrinsic impedance. On the basis of these works, it is therefore clear that different authors use different signs for a given parameter, e.g., the refractive index, in a DNG material, and that some authors furthermore claim that a given parameter can only have a specific sign. As a consequence of these disagreements, there is a need to re-examine these matters in more detail and to clarify the sign of the wave number, intrinsic impedance, and refractive index in DNG materials.

A variety of potential applications of MTMs that include, e.g., lenses [11], [12], [19], [24]-[32], novel cavities, waveguides and scatterers [33]-[52], and antennas [53]-[63], have been proposed. Following the rapid development of the design of DNG materials via specific approaches, a large number of devices have been realized and successfully tested [2], [3]. However, other interesting works have proposed numerous potential applications that would emerge if ideal MTMs could be manufactured, and as such they have stimulated a continued interest in further developments of these materials. These applications are derived from the properties of MTM configurations of various shapes such as those involving rectangular, cylindrical, spherical, and elliptical geometries. Among the rectangular geometries, the lossless DNG slab has attracted much attention due to its intriguing perfect lens property [11], which makes it capable of overcoming the traditional diffraction limit encountered in conventional DPS-based lenses.

Moreover, interesting ideas for compact and sub-wavelength cavity resonators, waveguides, scatterers and antennas that exploit MTMs, as well as their combinations with conventional DPS materials, have been suggested [33]-[42], [56]-[59], [61]-[63]. In particular, it was demonstrated that such systems, although electrically small, may be designed to be resonant and that they lead, e.g., to enhanced radiation and scattering properties. Furthermore, it was shown that this is in distinct contrast to designs based only on DPS materials. Although the initial ideas were based on the study of the plane wave properties of sub-wavelength MTM-based structures, the performance characteristics of MTM-based cylindrical [60] and spherical [56], [57] structures have also been analyzed in the presence of localized sources such as line sources (LSs) (for cylindrical structures) and Hertzian dipoles (HDs) (for spherical structures). In these works, the location of the source was restricted to the centers of the respective MTM-based structures. In particular, the possibility of increasing the power radiated by electrically small antennas by using MTM coatings was demonstrated theoretically in [56]. Large values of the radiated power were reported for an electric HD (EHD) surrounded by an electrically small concentric DNG shell. The overall findings related to these scattering and radiating canonical configurations were successfully used for miniaturization purposes, e.g., of realistic electrically small cavity resonators [34], [35], waveguides [39]-[41], and radiating systems such as electrically small coaxially-fed dipole antennas and monopoles [58], [61], and patch antennas [63].

The purpose of the present work is to investigate the radiation and scattering properties of electrically small DNG-based canonical structures of cylindrical and spherical shapes. As a first step in these investigations, some fundamental issues, related to the noted disagreements on the sign of the various wave parameters in DNG materials, are first re-examined. The primary goal of this re-examination is to show that the differences observed in the literature are based on the implicit use of different definitions for different parameters, and to stress that all definitions are equally correct as long as they are used consistently in a solution to a given problem. Subsequently, the radiation and scattering from two- and three-dimensional (2D and 3D) canonical problems consisting of cylindrical and spherical DNG-based structures excited, respectively, by an electric LS (ELS) and an EHD, are investigated. Contrary to previous efforts, this work focuses on the radiation and scattering from these structures when the sources are arbitrarily located. The near- and far-field properties of these configurations are investigated through examination of quantities such as the near-field distributions, total radiated power, scattering cross section, differential cross section, and directivity. For electrically small designs, the advantageous use of DNG materials to improve the radiation and scattering properties is demonstrated. However, owing to the arbitrary location of the sources, additional features are discovered that are not found in the previously studied configurations for which the sources are centered in the respective structures. In particular, the possibility of exciting resonant modes of a given order which, e.g., lead to a resonant increase in the radiated power and the scattering cross section, and which suggest the feasibility of controlling the directivity for specific electrically small designs, is emphasized. Although the emphasis in these investigations is put on DNG materials, some attention is also devoted to SNG materials in similar electrically small designs. In addition to the investigations of electrically small structures, the properties of several structures having larger electrical sizes are likewise examined.

The present report is divided in three parts. Part I (the present chapter and Chapters 2 to 6) is the main body of this report. Part II (Appendices A, B and C) contains manuscripts I, II, and III, respectively, which form the background of Chapters 4 and 5. These manuscripts are journal publication 2, 4, and 1, respectively, see the list of publications on pages iv and v. Finally, Part III (Appendices D to F) contain detailed derivations of the matters presented in Chapters 4 (Appendix D) and 5 (Appendix E), as well as the fundamental concepts related to the dispersion models (Appendix F) used in the present work.

Specifically, Chapter 2 presents an overview of MTMs, with a particular emphasis on DNG materials. The origins, basic properties, development, realizations and applications of DNG materials are discussed. Particular attention is devoted to those properties and applications of DNG materials that serve as a partial inspiration to Chapters 3 to 5. Each of these chapters contain an introductory survey of the literature relevant to them. Chapter 3 re-examines the sign, or more generally the branch, of wave number, intrinsic impedance, and refractive index, in DNG materials. Canonical problems consisting of uniform plane wave (UPW) propagation in unbounded and lossy DNG materials, and of obliquely incident UPWs on a lossless DPS/DNG interface, are included to support the analysis. In Chapters 4 and 5, respectively, the radiation and scattering from DNG-based cylindrical and spherical structures, excited by arbitrarily

located ELS and EHD, respectively, are studied. First, the respective analytical solutions are derived. Second, their numerical evaluations are performed to illustrate the possibility to design electrically small DNG-based resonant systems which possess advantageous radiation and scattering characteristics. As to the cylindrical structures, lossless, lossy, and dispersive DNG materials are investigated in Chapter 4. Various electrically larger DPS and DNG designs are also considered. Analogous considerations for the electrically small, resonant, spherical structures are treated in Chapter 5, although more expansive discussions on some of these topics are given in Appendix C than in Chapter 5. Chapter 6 presents the summary, conclusion, and future directions of this work.

Throughout the present report, the time factor $\exp(j\omega t)$, with ω being the angular frequency and t being the time, is assumed and suppressed.

CHAPTER 2

METAMATERIALS - AN OVERVIEW

As was noted in Chapter 1, considerable efforts have been made recently to understand the properties of metamaterials (MTMs), and particulary double-negative (DNG) materials. It is the purpose of this chapter to review briefly DNG materials, emphasized in the forthcoming chapters of the present work, in terms of their origins, basic properties, realizations, and potential applications. Such a review inevitably touches upon the issues related to single-negative SNG materials also. In order to place the review in a broader perspective, the chapter is introduced by a brief discussion of materials in general, their most general bianisotropic form and the material classifications in terms of material parameters, as well as the need for artificially synthesized materials. Subsequently, the discussion of DNG materials, their realizations as well as interesting applications, is given.

2.1 Introduction

Naturally occurring materials are composed of inhomogeneities or structural units formed by their constitutive atoms and molecules. Depending on the wavelength, λ, of the electromagnetic wave interacting with it, the material can behave as either an inhomogeneous one, where the scattering- and diffraction-like effects prevail, or as an effectively homogeneous one, where the reflection- and refraction-like phenomena are dominant. Since the sizes of the atoms and molecules of naturally occurring materials are of the order of an Angström, it is clear that electromagnetic waves, e.g., in the radio and microwave frequency part of the electromagnetic spectrum, do not sense the atomic details when they are interacting with them. This is because the size of the atoms, as well as their spacing, is very small in comparison to the wavelength λ. In this case, the strictly-speaking inhomogeneous atomistic material can be replaced with a homogeneous one, and the material can then be characterized macroscopically with the so-called constitutive material parameters.

The study of electromagnetic phenomena that occur during the wave-material interactions is accomplished by the use of the laws of electromagnetics formulated by Maxwell's equations, which have the time-harmonic form [64]

$$\nabla \times \vec{E} = -j\omega\vec{B}\,, \tag{2.1a}$$

$$\nabla \times \vec{H} = j\omega\vec{D} + \vec{J}, \tag{2.1b}$$

where $\vec{E}$ [V/m] is the electric field intensity, $\vec{H}$ [H/m] is the magnetic field intensity, $\vec{D}$ [C/m^2] is the electric flux density, $\vec{B}$ [W/m^2] is the magnetic flux density, and $\vec{J}$ [A/m^2] is the electric current density. The four field vectors in (2.1a) and (2.1b) are interrelated through the constitutive relations. In their most general bianisotropic material form, they are given by the expressions [64]

$$\vec{D} = \bar{\bar{\varepsilon}} \cdot \vec{E} + \bar{\bar{\xi}} \cdot \vec{H}\,, \tag{2.2a}$$

$$\vec{B} = \bar{\bar{\zeta}} \cdot \vec{E} + \bar{\bar{\mu}} \cdot \vec{H}\,, \tag{2.2b}$$

where $\bar{\bar{\varepsilon}}$ and $\bar{\bar{\mu}}$ are the permittivity and permeability tensors, respectively, while $\bar{\bar{\xi}}$ and $\bar{\bar{\zeta}}$ are the magneto-electric tensors responsible for any cross-coupling in the material between the electric and magnetic fields. In general, the entries of these tensors are complex, and hence, the most general description of a material involves 72 parameters. Since these material parameter tensors enter into Maxwell's equations

(2.1a) and (2.1b), via the constitutive relations (2.2a) and (2.2b), they may be regarded as the fundamental parameters by which a material is characterized. Depending on the form of the material parameter tensors, the materials can be classified as [64] (a) inhomogeneous, if the tensors are functions of space coordinates, (b), nonlinear, if they depend on the strength of the electromagnetic field, (c) frequency dispersive, or simply dispersive, if they depend on frequency, (d) spatially dispersive, if they contain spatial derivatives, etc. These material classifications also pertain to subclasses of bianisotropic materials such as bi-isotropic, anisotropic, and isotropic materials. When the material parameter tensors in (2.2a) and (2.2b) are scalars, the material is said to be bi-isotropic, and it is anisotropic if the the magneto-electric tensors $\bar{\bar{\xi}} = \bar{\bar{\zeta}} = \bar{\bar{0}}$ while the permittivity and permeability tensors remain. The simplest case is, however, an isotropic material which is a special case of the anisotropic one when the permittivity and permeability are no longer tensors, but rather scalars denoted by ε and μ, respectively. In this isotropic case the constitutive relations read [64]

$$\vec{D} = \varepsilon \vec{E} \,, \tag{2.3a}$$

$$\vec{B} = \mu \vec{H} \,. \tag{2.3b}$$

In most naturally occurring materials, the real parts of the permittivity, ε, and permeability, μ, denoted by ε' and μ', respectively, are positive. However, recent advances in the research of artificial materials, see Section 2.2, have introduced materials that posses simultaneously negative ε' and μ'. In consequence hereof, it is therefore possible to classify materials according to the sign of ε' and μ' [1], see Figure 2.1(a).

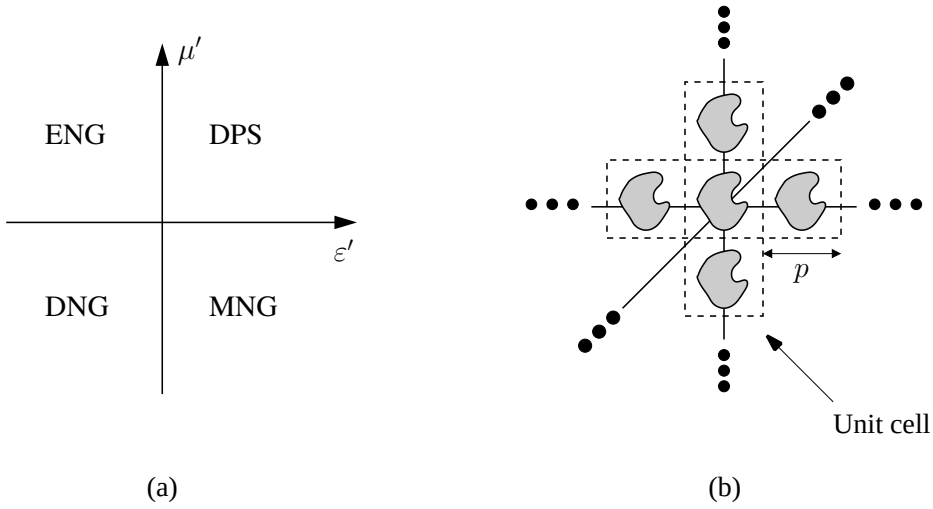

Figure 2.1: *(a) Material classification based on the sign of ε' and μ'. (b) Generic sketch of an artificial material composed of inclusions imbedded in a host material.*

The materials occupying the first quadrant of the $\varepsilon'\mu'$-coordinate system, where $\varepsilon' > 0$ and $\mu' > 0$, are in this work designated double-positive (DPS) materials, the terminology referring to the fact that ε' and μ' are simultaneously positive. Similarly, materials in the second quadrant for which $\varepsilon' < 0$ and $\mu' > 0$ are designated as epsilon-negative (ENG) materials, while those in the fourth quadrant are characterized by $\varepsilon' > 0$ and $\mu' < 0$ and are designated as mu-negative (MNG) materials. With reference to Chapter 1, ENG and MNG materials are classes of SNG materials. The third quadrant in Figure 2.1(a) is occupied with materials for which $\varepsilon' < 0$ and $\mu' < 0$, and may therefore be termed DNG materials[2.1].

DPS, ENG, and MNG materials can be found in nature. Well-known examples of DPS materials are dielectric materials, while, e.g., ENG properties occur at optical frequencies where metals, which essentially behave as plasmas, exhibit a negative permittivity at frequencies below the plasma frequency,

[2.1] In Sections 2.2.1 and 2.2.2 the origin of these designations and alternative terminologies for DNG materials are briefly discussed.

see Section 2.2.3. Moreover, certain classes of ferrimagnetic materials are (anisotropic) MNG materials in the sense that specific entries in their permeability tensors may be negative. Although DPS, ENG, and MNG materials can be found in nature, they often exhibit certain restrictions that render them unusable for specific applications. To exemplify, for applications that require high permittivity, low loss dielectrics, such as for miniaturizing patch antennas, it may be difficult to find good naturally occurring candidates with these desired properties. Moreover, DNG materials, not readily found in nature, were recently shown to offer a wealth of interesting applications. This is turn obviously demands their realization in order to prove their applicability. Clearly, one must therefore resort to the design of artificial materials that could mimic the response of the naturally occurring ones and could, moreover, provide additional tailorable and advantageous features.

The artificial materials are created by distributing inclusions of various shapes into a host medium, see Figure 2.1(b) and [1]-[3], [65], [66], as well as the extensive lists of references included in these works. Figure 2.1(b) shows 6 arbitrarily shaped inclusions, each contained in a unit cell whose average size is p, which must be distributed periodically along the various directions (indicated by the 3 dots) in order to artificially synthesize the material. In order for the concept of permittivity and permeability to be valid for these so-designed materials, i.e., in order for them to be effectively homogeneous, the size and the spacing between the inclusions, which are the structural units of the material, or equivalently the size of the unit cell, must be small compared to the wavelength[2.2]. It is thus understood that the inclusions that form an artificial material perform the same role as atoms and molecules do in naturally occurring materials. Owing to the possibility of changing, e.g., the size, shape, density and locations of these inclusions, one can, in principle, design a material with properties not available in nature and being far superior to those found in naturally occurring materials. The term "*metamaterials*" (*meta* = *beyond* in Greek) is used in the literature as a common term designating these, as well as other common artificial materials. Specific classes include various artificial DPS materials, also known as artificial dielectrics [65], as well as the above introduced ENG, MNG, and DNG materials [1]-[3], but also they include, for examples, the very broad class of materials commonly termed as electromagnetic crystals (ECs) or electromagnetic band-gap (EBG) materials, [66],[67][2.3] as well as high-impedance surfaces (HISs) [68]-[70], which are used in the realizations of artificial magnetic conductors.

2.2 Double negative materials

2.2.1 Veselago's investigations

A very special class of MTMs are the DNG materials. Although the first investigations of these materials occurred long ago [4], their detailed study, realizations and exploitations received significant attention only very recently.

The first systematic study of DNG materials was reported in 1967 by the Russian physicist Viktor Veselago [4]. More specifically, he considered theoretically the propagation of uniform plane waves in isotropic and lossless DNG materials and concluded that the wave vector, $\vec{k}$, (telling the direction of the phase propagation) and the Poynting vector, $\vec{S}$, (telling the direction of the power flow), are oppositely directed in such materials. Indeed, for a uniform plane wave of the form

$$\vec{E} = \vec{E}_0 \, e^{-j\vec{k}\cdot\vec{r}} \,, \tag{2.4a}$$

$$\vec{H} = \vec{H}_0 \, e^{-j\vec{k}\cdot\vec{r}} \,, \tag{2.4b}$$

where $\vec{E}_0$ and $\vec{H}_0$ are constant electric and magnetic field amplitudes independent of the position vector $\vec{r}$, Maxwell equations (2.1a) and (2.1b) for isotropic materials described by (2.3a) and (2.3b) give

[2.2] A so-called effective-homogeneity condition given by $p = \lambda/4$ has been employed in [2]. To ensure that the resulting artificial material is effectively homogeneous it must be made of inclusions with sizes and spacings smaller than the effective-homogeneity limit. Above this limit, the permittivity and permeability concepts become invalid and one must resort to alternative views on such artificial materials, as noted at the end of this section.

[2.3] These materials are formed by periodic arrangements of inclusions, whose sizes are on the order of a wavelength. Therefore, these materials can not be described in terms of effective material parameters and periodic media concepts must be used to describe their properties [66]. No further mention of EBG materials and HISs will be made in this work.

$$\vec{k} \times \vec{E} = \omega\mu\vec{H} \,, \tag{2.5a}$$

$$\vec{k} \times \vec{H} = -\omega\varepsilon\vec{E} \,. \tag{2.5b}$$

The relations (2.5a) and (2.5b) show that the vectors $\vec{E}$, $\vec{H}$, and $\vec{k}$ are related by the right-hand rule in a DPS material ($\varepsilon > 0$, $\mu > 0$), and by a left-hand rule in a DNG material ($\varepsilon < 0$, $\mu < 0$). Owing to these observations, materials in which $\varepsilon < 0$ and $\mu < 0$ were referred to as "left-handed" (LH) materials in [4]. Since the flow of power is still defined by the Poynting vector [4], [12]

$$\vec{S} = \vec{E} \times \vec{H}^* \,, \tag{2.6}$$

where $*$ indicates the complex conjugate, it follows that $\vec{k}$ and $\vec{S}$ are parallel in DPS materials, and antiparallel, i.e., collinear and oppositely directed, in DNG materials. In other words, the phase of an electromagnetic wave in a DNG material propagates backwards, towards its source, in the direction opposite to that of the power, which propagates away from the source. Thus, the propagating waves supported by DNG materials are backward waves. These phenomena were all accounted for in [4] by adopting a negative refractive index in DNG materials, which is in sharp contrast to conventional DPS materials for which the refractive index is assumed to be positive.

In his seminal work [4], Veselago suggested that the backward-wave nature of DNG materials, and hence their negative refractive index, may possibly lead to several interesting phenomena and improvements of various devices, such as, e.g., lenses, see Section 2.2.4. The novel phenomena that Veselago envisaged to occur in DNG materials were the following:

1. Reversal of the Doppler and Vavilov-Čerenkov effects.
2. Reversal of the refraction process at the interface between DPS and DNG materials, which leads to the phenomenon referred to as the negative refraction.
3. The possibility of constructing a lens by using a DNG slab of thickness d and material parameters $\varepsilon_s = -\varepsilon_0$ and $\mu_s = -\mu_0$, which is located in free space. It was argued that such a slab may focus the radiation of a point source located in front of the slab to a point focus behind, as well as inside, the slab.

Apart from these interesting phenomena, Veselago further argued that DNG materials must necessarily exhibit dispersion, since constant, frequency-independent negative material parameters imply negative energy would be stored physically in the electromagnetic fields.

The reversal of the refraction process at the interface between DPS and DNG materials is very important. In essence, this reversal means that the wave undergoes a negative refraction at such an interface, and thus that the power is refracted on the same side of the interface normal from which the wave is incident. In order to describe such a reversed refraction process properly by the Snell's refraction law, Veselago [4] adopted a negative refractive index in the DNG material[2.4].

Some 30 years after the work of Veselago, negative refraction was reconsidered in [11] in regards to the so-called "perfect lens" effect. The work of [11] investigated focusing with a specifically designed DNG slab embedded in free space and showed that it is capable of overcoming the traditional diffraction limit encountered in conventional DPS lenses. This suggestion led to a renewed and increased interest in the theory and applications of DNG materials, see Sections 2.2.3 and 2.2.4. During the initial stages of these investigations of DNG materials, the notion that a negative refractive index, as originally suggested in [4], was one of their main characteristics was accepted as the correct one by parts of the scientific community, see Chapter 3. However, as shown in Chapter 3, the sign of the refractive index and related wave propagation parameters in a DNG material is a matter of choice, as long as they all are treated self-consistently to produce the correct solutions and interpretations of various physical phenomena, including negative refraction.

[2.4] According to [71] the first speculations on the phenomenon of negative refraction and backward waves took place long before the work of Veselago, but as noted in [2, Ch. 1], it was Veselago [4] who performed the first systematic study of materials that exhibit these and other unusual effects, see also [71] for more details.

2.2.2 Terminology

As already mentioned, materials that simultaneously have negative permittivity and permeability are in this work referred to as DNG materials. As was noted above, these materials were termed LH materials in [4]. The term DNG materials was coined in [12] with the aim of emphasizing the fact that both of its material parameters are negative. However, several other terminologies have been suggested for these novel materials. These include negative-refractive index materials [17], backward-wave media [22], Veselago media [72], and negative phase velocity materials [73], to mention a few. An interesting discussion of the advantages and drawbacks of these terminologies can be found in [2, Ch. 1].

In similitude to the term DNG material, and following the path put forth in [1, Ch. 1], the terms ENG and MNG materials are used throughout this work, as noted in Section 2.1, to designate materials with negative (positive) permittivity (permeability) and positive (negative) permittivity (permeability), respectively.

2.2.3 Realizations

Already in his initial work [4], Veselago recognized the lack of isotropic DNG materials in nature due to the absence of isotropic MNG materials. At that time, no realizations of such materials were reported. A significant period of time then elapsed until the first realizations emerged.

Some 30 years after Veselago's theoretical considerations, artificial means to realize ENG and MNG materials on a separate basis were reported in [5]-[7]. More specifically, [5] and [6] showed that an effectively homogeneous material with a negative permittivity in the microwave frequency range can be realized by the wire structure (WS) shown in Figure 2.2(a). This structure consists of an array of thin and infinitely long metallic wires spaced a distance p from each other and each having the radius r. Both p and r are much smaller than the wavelength, thereby ensuring the fulfillment of the effective-homogeneity condition. The relative effective permittivity of the WS was found to be

$$\varepsilon_r(\omega) = 1 - \frac{\omega_{pe}^2}{\omega^2 - j\omega\Gamma_e} \,, \tag{2.7}$$

where ω_{pe} is the electric plasma frequency and Γ_e is the electric damping factor. These parameters depend on p and r, whereas the damping factor Γ_e also is dependent on the conductivity of the metallic wires. From (2.7) it is clear that the real part of $\varepsilon_r(\omega)$ is negative for $\omega < \sqrt{\omega_{pe}^2 - \Gamma_e^2}$, which in the absence of losses means that $\varepsilon_r(\omega) < 0$ for $\omega < \omega_{pe}$. It is also clear that the imaginary part is responsible for the description of the losses.

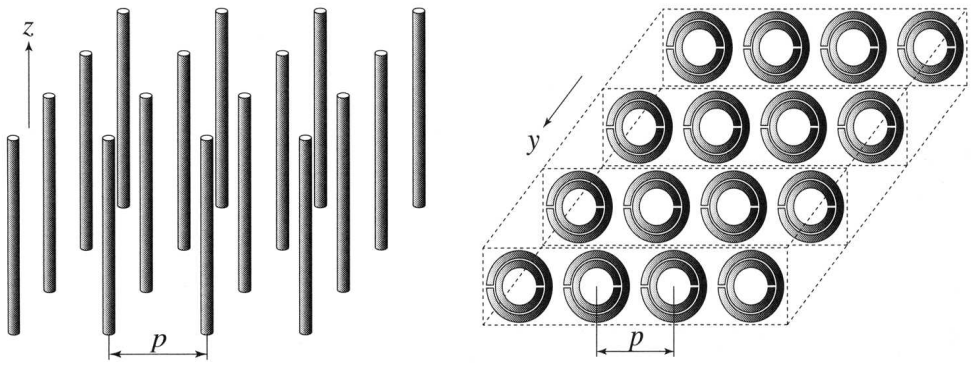

(a) (b)

Figure 2.2: *(a) ENG material realization in terms of a periodic array of wires, and (b) MNG material realization in terms of an array of conducting split ring resonators. See the main text for explanations. The figure is taken from [2].*

Artificial magnetism and the associated strong magnetic response was created at the microwave frequencies in [7] through the use of the structure shown in Figure 2.2(b). This structure is composed of an array

of resonant circular metallic elements, called split ring resonators (SRRs), and has a resonant frequency response for which the relative effective permeability is given by

$$\mu_r(\omega) = 1 - \frac{F\omega^2}{\omega^2 - \omega_{0m}^2 - j\omega\Gamma_m} \ . \tag{2.8}$$

In this expression the quantity F depends of the spacing, p, between the SRRs and the radius of the smaller ring of the SRR. Moreover, ω_{0m} is the magnetic resonance frequency, and Γ_m is the magnetic damping factor, both parameters being dependent on the dimensions of the individual SRRs as well as their spacing. Moreover Γ_m also depends on the properties of the metallic rings. The result in (2.8) is rather interesting since in the lossless case ($\Gamma_m = 0$) it provides negative $\mu_r(\omega)$ in the frequency range $\omega_{0m} < \omega < \omega_{pm}$, with ω_{pm} being the magnetic plasma frequency given by $\omega_{pm} = \omega_{0m}/\sqrt{1-F}$ [2, Ch. 1].

As noted in [5]-[7], the structures depicted in Figure 2.2 are anisotropic, since the permittivity in (2.7) only holds true when the electric field is parallel to the wires, while the permeability in (2.8) is obtained only when the magnetic field is parallel to the axis of SRRs. In this regard, the structures in Figure 2.2 are one-dimensional (1D) ENG and MNG structures[2.5] [2, Ch. 1].

With the demonstrated feasibility to realize ENG and MNG materials in the microwave region on a separate basis, the path to DNG materials was paved. Indeed, soon after the introduction of the WS and SRRs, the two approaches were combined and the first DNG structure was successfully devised for use at microwave frequencies (at around 5 GHz) [8], see Figure 2.3(a) for a photograph of this structure.

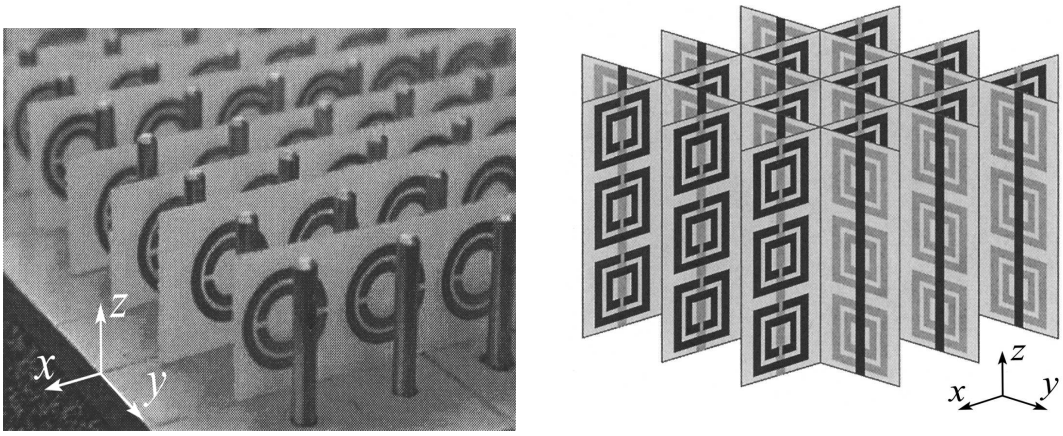

(a) (b)

Figure 2.3: *The first realizations of DNG materials at microwave frequencies. (a) 1D DNG material comprised of the WS and circular SRRs [8], and (b) 2D DNG material comprised of the WS and rectangular SRRs placed in two orthogonal planes [10]. (a) and (b) are taken from [72] and [3], respectively.*

The material in Figure 2.3(a) is an example of 1D DNG material. Similar 1D DNG material was devised in [9] (at around 3.5 GHz) where the circular SRRs were replaced by rectangular ones. However, placing the conducting wires and SRRs in two orthogonal planes, a two-dimensional (2D) DNG material was achieved which reduces the amount of anisotropy relative to the 1D case. It was created for microwave frequencies in [10] (at around 10.5 GHz), see Figure 2.3(b).

[2.5] The history of the WS on the one hand, as the basic element to create electric effects from non-dielectric materials, and the SRR structure, as the basic element to create magnetic effects from non-magnetic materials, on the other, is rather long. According to [2, Ch. 1], [71] and [72], the WS, which is an artificial dielectric material also known as a "rodded" medium or artificial plasma, has been known since the 1960s where it was used in the design of dielectric lenses as well as emulations of plasmas at microwave frequencies, see, e.g., [74], [75]. Indeed the permittivity in (2.7) resembles the plasma permittivity, see, e.g., [64]. Moreover, different versions of SRRs as candidates to create magnetism have been considered in the well-known textbook [76].

The reversal of Snell's law of refraction and the associated negative refraction, noted by Veselago [4] as one of the main signatures of DNG materials, was confirmed experimentally for the structure shown in Figure 2.3(b) for the first time in [15] and subsequently in [16].

Before proceeding further with other interesting realizations of DNG and related materials, it is noted that the permittivity in (2.7) is in fact the familiar Drude dispersion model, while the permeability in (2.8) is very intimately related to the Lorentz dispersion model, see, e.g., [1, Ch. 1], [64], and [77, Ch. 19]. Indeed, both Drude and Lorentz dispersion models, as well as various slight modifications of these, are frequently used in the analytical and numerical studies of DNG and related materials [1, Ch. 1]. An excellent overview of the various forms and modifications of these models, as applied to DNG materials, is found in [78, Ch. 2]. Drude and Lorentz dispersion models are also adopted in the present work, whenever the influence of dispersion, as well as frequency-dependent losses are taken into account, see Chapters 4 and 5. In appendix F, a detailed analytical and numerical study of these dispersion models is presented and the feasibility to produce negative material parameters over a limited band of frequencies is demonstrated.

The first realizations of DNG materials were based on appropriate arrangements of the WS and SRR inclusions. Owing to the resonant nature of these so-designed materials, they may exhibit high losses and narrow bandwidths when the simultaneously negative material parameters are achieved [2, Ch. 1]. This is due mainly to the strong dispersion in the frequency region close to the resonance frequency of the individual SRRs, i.e., the negative values are attained near the resonance frequency where the losses are largest and, hence, this leads to increased losses at those frequencies, see Appendix F, Section F.3, where numerical investigations of the Lorentzian-like permeability in (2.8) have been performed. Indeed, the transmission through the first DNG material [8] was shown to be very low with a loss of approximately 30 dB. In direct consequence hereof, a considerable interest has emerged in the optimization of DNG materials with the overall goal being to achieve designs with lower losses and larger bandwidths over which the DNG behaviour is attained. As a result, numerous versions of the WS and SRRs have been suggested [79]-[85]. In particular, designs which utilize inclusions such as the axially symmetric SRRs [79], [80], the Ω-shaped SRRs [81]-[83], as well as the so-called S-rings [83], [84], were realized, and their low-loss and broad-band behaviours were experimentally confirmed in [1, Ch. 4] and [83]. It is interesting to note that arrays of inclusions of Ω-shaped rings on the one hand and S-rings on the other provide DNG materials without use of the infinite metallic wires used in the initial realizations of these materials, see Figure 2.3.

Although [7] and [8] stipulated that the SRR structure shown in Figure 2.2(b) is anisotropic, it was, however, shown to possess a slight bianisotropy [86], i.e., to obey the constitutive relations (2.2a) and (2.2b). To alleviate the bi-anisotropy, the so-called broad-side coupled SRR design to achieve negative permeability at microwave frequency was suggested in [86] and [87]. One advantage of a DNG material employing the broad-side coupled SRRs is the possibility of a planar design, as compared to the non-planar and bulky DNG material in [8]-[10], which thus renders them useful in, e.g., waveguide applications [87].

The realizations of DNG materials surveyed so far are either 1D or 2D in the sense that the simultaneously negative permittivity and permeability values over a certain frequency band are obtained for specific orientations of the electric and magnetic fields. However, three-dimensional (3D) realizations of MNG [88] and DNG [89]-[91] materials have likewise been suggested.

Apart from the above realizations, which rely heavily on resonant inclusions such SRRs, there exist another means of implementing DNG materials which avoids the use of the resonant inclusions, but rather exploits appropriately loaded transmission lines [92]-[95]. In distinct contrast to the initial, rather bulky DNG material shown in Figure 2.3, the transmission-line based designs are planar and are therefore preferable in microwave integrated circuit applications. Moreover, they exhibit lower losses and larger bandwidths over which their effective material parameters are negative, which is yet another desirable feature. Although the designs in [92]-[95] are either 1D or 2D, 3D DNG materials using the concept of transmission lines have been suggested [96].

The axially symmetric SRR used in [1, Ch. 4] and [84] as an element of DNG materials in the microwave part of the spectrum, has originally been proposed for use at optical (near-IR and visible) frequencies

[79], [80]. A specific design of DNG materials at optical frequencies is described in [97], while [98] includes some very interesting ideas for DNG materials at these frequency ranges. Moreover, the WS and SRRs composite versions of DNG materials have also been created at terahertz frequencies [99]-[101]

2.2.4 Applications

The field of MTMs and their potential applications is growing very rapidly as is, for instance, evidenced by the textbooks [1]-[3], several special issues [102]-[105], and overview works [73], [106]-[109], and the numerous applications that have already been proposed. These proposals are of a rather broad nature and encompass, among others, applications that aim at the development of, e.g., lenses [11], [12], [19], [24]-[32], cavity, waveguide, and scattering structures [33]-[52], as well as antennas [53]-[63].

While some of the applications are potential, i.e., they constitute ideas and give suggestions on what could be done if ideal MTMs could be manufactured, others are of a more practical nature and have already been confirmed experimentally. Obviously, an experimental verification of the potential applications requires the existence of the appropriate MTM. Due to the ease of manufacturing DNG materials in terms of appropriately loaded transmission lines and the resulting planar geometries, various devices for use at microwave frequencies, such such as super-resolving lenses, power dividers, couplers, leaky-wave and electrically small antennas, antenna arrays with reduced beam squinting, to mention a few, all possessing comparable or advantageous properties as compared to the corresponding DPS-based designs, have been proposed, built, and successfully tested, see e.g., [2] and [3]. It is, however, beyond the scope of the present work to go further into these applications.

In this section, however, some attention is devoted to those potential applications that have initiated the strong interest in DNG and related materials, such as the perfect lens [11]. Moreover, the concepts of sub-wavelength cavity resonators [33]-[37], waveguides [36]-[41], scatterers [36], [37], [42], [48], and electrically small MTM-based antennas [56]-[63], which all are closely related to the present work, see Chapters 4 through 6, are also briefly elucidated.

The negative refraction at the interface between DPS and DNG materials was already used in [4] to propose unusual refracting devices. In particular, it was argued that, e.g., lenses which normally defocus electromagnetic waves when made of DPS materials, will focus them, and vice versa, when the DPS materials are replaced by DNG ones. As another direct consequence of negative refraction Veselago furthermore envisaged that a flat DNG slab in free space could function as a lens. More specifically, he noted that a DNG slab of material parameters $\varepsilon_s = -\varepsilon_0$, $\mu_s = -\mu_0$, and a thickness d can focus the radiation from a point source (PS) located in free space at a distance $a < d$ in front of the slab to a point inside the slab, as well as to a point in free space behind the slab. These matters are easily deduced via simple ray tracing considerations which are depicted in Figure 2.4, where an image of the point source is found inside the slab (at a distance a to the right of the first interface) as well as behind the slab (at a distance $d - a$ to the right of the second interface). The formation of the image points I1 and I2 is due to the negative refraction that takes place at the two DNG interfaces of the slab.

These ideas were reconsidered much later in [11], where truly remarkable properties of such a slab configuration were revealed and the concept of the perfect lens was introduced. In particular, [11] discovered that the traditional diffraction limit encountered in conventional lenses could be overcome by the flat DNG slab configuration considered in [4]. Apart from perfectly focusing the propagating waves, the proposed DNG slab also was found to amplify the usually decaying evanescent part of the spectrum of the point source field. It was therefore concluded that, in theory, such a lens may offer focusing with infinite resolution. The concept of the perfect lens suggested by [11] stimulated a great deal of interest into the focusing abilities of flat DNG slabs [12], [19], [26]-[30], and it was soon realized that the dispersion and losses present in realistic DNG materials degrade the perfect focusing effects in the sense introduced in [11]. However, nearly-perfect lenses with sub-wavelength imagining capabilities were reported [26], [27], and even experimental verifications of the sub-wavelength focusing were undertaken in [30] and [31] with structures similar to the composite WS and SRRs, see Figure 2.2, as well as with the transmission-line based implementation of DNG materials [32].

Another, very interesting field of applications of DNG and related materials emerged as it was discovered that such materials may offer miniaturized configurations such as cavity resonators, waveguides,

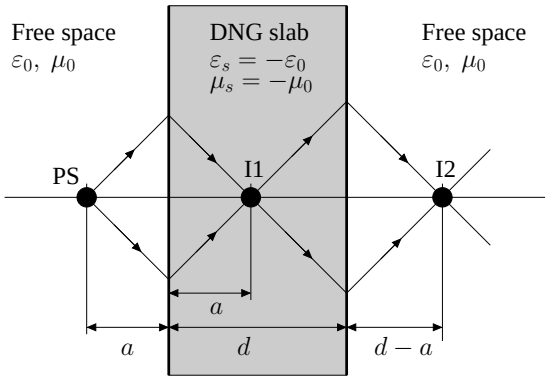

Figure 2.4: *Focusing of the propagating modes of the point source* (PS) *by a DNG slab of thickness* d *and material parameters* $\varepsilon_s = -\varepsilon_0$ *and* $\mu_s = -\mu_0$*. As a consequence of the negative refraction taking place at the two interfaces of the DNG slab, the PS is focused to a point* I1 *inside the slab and to a point* I2 *behind the slab.*

scatterers, and antennas with very desirable properties. In particular, an idea of a sub-wavelength 1D cavity resonator using a pair of DPS and DNG slabs immersed between two perfectly conducting plates, see Figure 2.5 (a), was presented in [33].

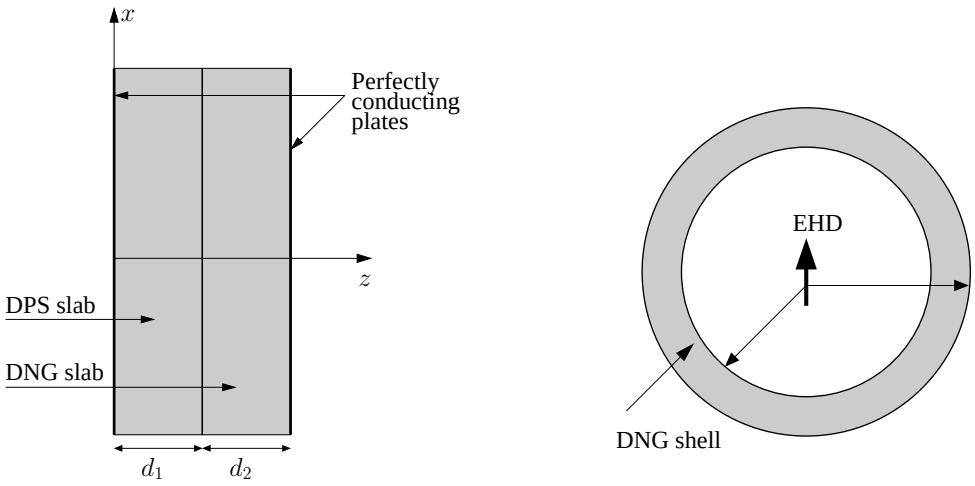

Figure 2.5: (a) *Sub-wavelength compact 1D cavity resonator introduced in [33].* (b) *Antenna configuration consisting of an electrically small electric dipole surrounded by a concentric DNG spherical shell [56]. See the main text for explanations.*

The dispersion relation of the cavity resonator depicted in Figure 2.5(a) was shown to be [33]

$$\frac{\tan(n_{\text{DPS}} k_0 d_1)}{\tan(n_{\text{DNG}} k_0 d_2)} = \frac{n_{\text{DPS}}|\mu_2|}{n_{\text{DNG}}|\mu_1|}\,, \tag{2.9}$$

where k_0 is the free-space wave number, μ_1, n_{DPS} and d_1 are the permeability, refractive index, and thickness, respectively, of the DPS slab, while μ_2, n_{DNG} and d_2 are the corresponding quantities of the DNG slab. From (2.9) there is no constraint on the sum of the thicknesses, d_1 and d_2, of the two slabs as is the case for resonators filled with conventional DPS materials for which resonance occurs if the total thickness of the resonator is at least half of the operating wavelength. Instead, the ratio of d_1 and d_2 multiplied with appropriate propagation constants is constrained. Thus, in principle, this resonator may resonate even for thicknesses that are arbitrarily smaller than the traditional size-limit of half of

the wavelength, and may therefore be conceived as sub-wavelength cavity resonators. This behaviour is, as noted in [33], due to the backward waves in the DNG slab, which introduce a phase advance that compensates and even cancels the phase delay introduced by the DPS slab when the material parameters and thicknesses of the DPS and DNG slabs are carefully selected. The theoretical ideas put forth in [33] were confirmed experimentally in [1, Ch. 4], [34] and [35].

The concept of 1D sub-wavelength cavity resonators based on DPS-DNG layers was also shown to hold when ENG-MNG layers are used instead of DPS-DNG layers [36]. This is also the case for 2D as well as 3D configurations [36],[37]. The same concept, which relies on appropriate pairing of DPS materials with MTMs, or appropriate pairing of certain MTMs, was extended to include the miniaturization of waveguiding structures [36]-[38]. These guiding structures were found to support propagating modes even when their transverse dimensions are much smaller than the operating wavelength, i.e., mode propagation below the cut-off frequencies of the corresponding DPS-based waveguides was demonstrated. Unusual rectangular waveguides with transversal dimensions much smaller than the wavelength which support propagating modes below the cut-off frequency of a hollow waveguide have also been proposed in [39], studied further in [40], and realized experimentally in [41].

The basic ideas presented in [33] and [36]-[38] have moreover been successfully exploited in electrically small MTM-based scatterers, which were found to exhibit significantly reduced or enhanced scattering cross sections [42], [48]. These interesting properties are unattainable with correspondingly small scatterers comprised of DPS materials only.

On the basis of the same miniaturization principles described above for cavity resonators, waveguides, and scatterers, it has been suggested that one could miniaturize antennas and still retain comparable or even obtain more advantageous characteristics as compared to conventional DPS-based antennas [53]-[63]. In particular, the reduction of size of annular ring patch antennas by loading them appropriately with DPS and DNG materials was reported in [62], and the radiation properties of similar sub-wavelength resonant configurations have been thoroughly studied recently in [63]. In addition, interesting proposals for increasing the power radiated by electrically small dipole antennas by use of MTMs were given in [56], [57], which were subsequently extended to efficient electrically small antennas that may possibly overcome the traditional Chu limit (which specifies the smallest attainable quality factor for a given electrical size of the antenna, thereby providing a fundamental relationship between antenna size and its quality factor) [58], [59]. This research was mainly inspired by [56] where large radiated power was reported for a canonical antenna configuration consisting of an electrically small electric dipole (ESED) surrounded by a concentric DNG spherical shell, see Figure 2.5(b). The dramatic increase in the radiated power obtained in [56] was explained in terms of the possibility to design a DNG shell that performs the function of a natural matching element to the highly capacitive ESED in free space.

The feasibility of electrically small MTM-based configurations that posses significantly enhanced scattering characteristics [48] and that modify advantageously the radiation properties of electrically small antennas [56] has served as a partial inspiration for the present work. Similar aspects are further investigated in subsequent chapters for 2D and 3D canonical configurations excited by 2D and 3D sources of electromagnetic radiation, see Chapters 4 and 5.

2.3 Summary

An overview of MTMs was given in this chapter. The overview was initiated by a brief account on bianisotropic materials, and was subsequently extended to isotropic materials. A classification of these materials on the basis of the sign of their fundamental parameters, i.e., the permittivity and permeability, was then performed, and the concept of DPS, DNG, and SNG materials was introduced. Specific emphasis was devoted to DNG materials, in which sense their origins, consequences, as put forth by Veselago [4], terminology, and realizations were discussed. In particular, the first realizations of DNG materials, which employed the WS and SRRs, as introduced in [8]-[10], for use at microwave frequencies, was discussed. Moreover, various applications of MTMs, and particularly DNG materials, e.g., the imaging capabilities of DNG materials and the idea of the perfect lens, were surveyed. In addition, the interesting potential application of MTMs to design electrically small cavities, waveguides, scatterers and radiators, this being in distinct contrast to the corresponding designs which exploit conventional DPS materials, was surveyed.

CHAPTER 3

THE SIGN OF CERTAIN PARAMETERS IN DOUBLE-NEGATIVE MATERIALS

Important points of the study on the sign of wave number, intrinsic impedance, and refractive index, in double-negative (DNG) materials are summarized in this chapter. First, the arguments for the necessity of such a study are presented, and then a proper set of definitions of these parameters is established. The possible signs obtained by these definitions are subsequently discussed, and their validity is confirmed by considering the solution to a canonical example consisting of an obliquely incident uniform plane (UPW) on an interface separating semi-infinite double-positive (DPS) and DNG regions.

The content of the present chapter represents a summary of [21].

3.1 Introduction

The sign of certain parameters such as wave number, intrinsic impedance, and refractive index in DNG materials has been the subject of some recent discussion and disagreements, see e.g., [11]-[23]. In most of these works [11]-[20], including the pioneering work of Veselago [4], the attention was focused on resolving the sign of the refractive index. Moreover, a few of these works discussed one or both of the remaining parameters. As to the sign of the refractive index, both positive as well as negative signs were suggested for a DNG material. A negative refractive index in a simple and lossless DNG material was adopted already in [4], since, as concluded there, the UPW refraction process at a plane interface between DPS and DNG materials is then properly described, i.e., the negative refraction, mentioned briefly in Chapter 2, then occurs for such an interface. The rationale behind Veselago's use of a negative refractive index was mainly based on the fact that by doing so, the Snell's refraction law, which governs the mentioned refraction process, then assumes the standard form, see Section 3.4 for further details. The arguments in favor of a negative refractive index were also presented much later in [11]-[20]. Contrary to these works, [22] and [23] argued that a refractive index in a DNG material can likewise by positive. In particular, [22] showed, by considering UPW propagation in a simple and lossless DNG material, that the refractive index could be assumed positive if the unit propagation vector, defining the direction of phase propagation, is defined to form a left-handed set of vectors with the electric and magnetic fields.

The signs of the two other parameters, i.e., the wave number and intrinsic impedance, were not considered in [4]. However, in a recent work [20], Veselago associated a positive intrinsic impedance with a DNG material, which also was the case in e.g., [11], [12], [14], and [17]. Moreover, [12] showed that a negative refractive index in a DNG material implies a negative wave number.

It is therefore clear that different authors use different signs for a given parameter, e.g., the refractive index, in a DNG material, and that some authors furthermore claim that a given parameter can only have a specific sign.

To clarify these discussions and disagreements, it is useful to re-examine the sign of the wave number, intrinsic impedance and refractive index in DNG materials. The purpose of the examination is to show that the above differences are based on the implicit use of different definitions for different parameters, and to stress that all definitions are equally correct as long as they are used consistently in a solution to a given problem. Therefore, as the introductory part of this examination, a proper set of definitions of the derived parameters must be established.

The basis of the examination is the obvious yet important fact that Maxwell's equations only include

the fundamental parameters, i.e., the permittivity and permeability, of which the sign in, e.g., DPS and DNG materials are fixed and well-known, see Chapter 2, Section 2.1. However, they do not include parameters such as wave number, intrinsic impedance, and refractive index. These are introduced for convenience and may therefore be referred to as derived parameters, and their introduction requires, of course, a consistent and proper choice of definitions. As will be shown, each of the definitions yields a specific sign of these parameters, which thus opens for a possibility of different signs for one and the same parameter. The analysis below shows that one definition may be more convenient, or perhaps even more advantageous, than another, but that the correct solution to a given problem can be obtained with either definition (and thus sign) as long as they are used consistently and provide the expected physical behaviour. The differences in the use of various definitions, and thus signs or branches of the derived parameters are manifested in the different functional forms of the solution to a given problem. Moreover, it is shown that the sign of one derived parameter does not influence the sign of another.

3.2 Definitions of derived parameters

The basis for a proper and consistent set of definitions of the derived parameters such as wave number, k_c, intrinsic impedance, η_c, and refractive index, n_c, is obtained through a consideration of UPW propagation in an unbounded and simple, lossless or lossy material. The electric and magnetic fields associated with the UPW are denoted by $\vec{E}$ and $\vec{H}$, respectively, while its average power flow density is denoted by $\vec{P}_{av}$. As noted in [21], the sign of the derived parameters in a given material is chosen according to some definitions that ensure the fulfilment of necessary physical conditions such as, e.g., the radiation condition. Presently, simple, lossy materials are considered. Such materials are characterized by a permittivity ε_c (or a relative permittivity $\varepsilon_{c,r}$) and a permeability μ_c (or a relative permeability $\mu_{c,r}$), given by

$$\varepsilon_c = \varepsilon' - j\varepsilon'' = \varepsilon_0(\varepsilon'_r - j\varepsilon''_r) = \varepsilon_0\varepsilon_{c,r} \ , \tag{3.1a}$$

$$\mu_c = \mu' - j\mu'' = \mu_0(\mu'_r - j\mu''_r) = \mu_0\mu_{c,r} \ , \tag{3.1b}$$

where $\mathcal{R}e\{\varepsilon_c\} = \varepsilon' = \varepsilon_0\varepsilon'_r$ and $\mathcal{R}e\{\mu_c\} = \mu' = \mu_0\mu'_r$ denote the real part of ε_c and μ_c, respectively, and $\mathcal{I}m\{\varepsilon_c\} = -\varepsilon'' = -\varepsilon_0\varepsilon''_r$ and $\mathcal{I}m\{\mu_c\} = -\mu'' = -\mu_0\mu''_r$, respectively, denote their imaginary part. In addition, ε'_r, ε''_r, μ'_r, and μ''_r denote the corresponding relative quantities, while ε_0 and μ_0 are the free-space permittivity and permeability, respectively.

The below established definitions of the derived parameters, which apply for DPS as well as DNG materials, are difficult to find in the literature, see, e.g., [64], [77], [110]-[115]. However, by a closer inspection of these works, the definitions below are naturally inferred[3.1]:

Wave Number - The following two definitions are naturally introduced:

- ***Definition 1***: The wave number, k_c, is given through the dispersion relation $k_c^2 = \omega^2\epsilon_c\mu_c$, with the requirement that $\mathcal{R}e\{k_c\} > 0$.
- ***Definition 2***: The wave number, k_c, is given through the dispersion relation $k_c^2 = \omega^2\epsilon_c\mu_c$, with the requirement that $\mathcal{R}e\{k_c\} < 0$.

Intrinsic impedance - The following two definitions are naturally introduced:

- ***Definition 1***: The intrinsic impedance, η_c, is the ratio of those components of the $\vec{E}$ and $\vec{H}$ fields of a linearly polarized UPW which form a right-handed set of vectors with the power propagation direction, i.e., with $\vec{P}_{av}$.
- ***Definition 2***: The intrinsic impedance, η_c, is the ratio of those components of the $\vec{E}$ and $\vec{H}$ fields of a linearly polarized UPW which form a right-handed set of vectors with the phase propagation direction.

Refractive index - The following four definitions are naturally introduced:

[3.1] It must be noted that these well-known works on electromagnetic theory consider materials which are in the present context referred to as DPS materials.

- ***Definition 1***: The refractive index, n_c, is the ratio between the speed of an electromagnetic wave in free space, c_0, to that in the material, denoted by v_p.
- ***Definition 2***: The refractive index, n_c, is the ratio between the speed of an electromagnetic wave in free space, c_0 and the component of the phase velocity in the direction of power propagation.
- ***Definition 3***: The refractive index, n_c, is given through the relation $n_c^2 = \epsilon_{c,r}\mu_{c,r}$, with the requirement that $\mathcal{R}e\{n_c\} > 0$.
- ***Definition 4***: The refractive index, n_c, is given through the relation $n_c^2 = \epsilon_{c,r}\mu_{c,r}$, with the requirement that $\mathcal{R}e\{n_c\} < 0$.

3.3 Lossy DNG material

3.3.1 Configuration and analytical solution

To illustrate the use of the various definitions of the derived parameters established in Section 3.2, the propagation of a linearly polarized UPW in an unbounded, simple and lossy, DNG material, henceforth termed the DNG material, characterized by the permittivity (3.1a) and permeability (3.1b), is considered. As noted in Chapter 2 $\varepsilon' < 0$ (or $\varepsilon'_r < 0$), and $\mu' < 0$ (or $\mu'_r < 0$) in a DNG material. Moreover, $\varepsilon'' > 0$ and $\mu'' > 0$ due to the assumed passive nature of the material [1], [65].

The Helmholtz's (HE) equation for the electric field given by

$$\nabla^2\vec{E} + \omega^2\varepsilon_c\mu_c\vec{E} = 0\,, \tag{3.2}$$

is first recalled. With a proper orientation of a rectangular (x, y, z) coordinate system, the solution of interest can then be expressed as

$$\begin{aligned}\vec{E}(z) &= \hat{x}E_x(z) = \hat{x}E_x^+(z) + \hat{x}E_x^-(z) = \hat{x}\left(E_{xo}^+e^{-jk_cz} + E_{xo}^-e^{jk_cz}\right)\\ &= \underbrace{\hat{x}E_{xo}^+e^{-k''z}e^{-jk'z}}_{\text{1st. PS}} + \underbrace{\hat{x}E_{xo}^-e^{k''z}e^{jk'z}}_{\text{2nd. PS}}\,,\end{aligned} \tag{3.3}$$

where E_{xo}^+ and E_{xo}^- are the amplitudes of the electric fields of the first (1st.) and second (2nd.) partial solution (PS) given by $\hat{x}E_x^+(z)$ and $\hat{x}E_x^-(z)$, respectively, while $k_c = k' - jk''$ is the wave number, with $\mathcal{R}e\{k_c\} = k'$ and $\mathcal{I}m\{k_c\} = -k''$, being its real and imaginary parts, respectively. The associated magnetic field is

$$\begin{aligned}\vec{H}(z) &= \frac{1}{-j\omega\mu_c}\hat{y}\frac{\partial}{\partial z}E_x(z) = \hat{y}H_y^+(z) + \hat{y}H_y^-(z)\\ &= \underbrace{\hat{y}\frac{k_c}{\omega\mu_c}E_{xo}^+e^{-k''z}e^{-jk'z}}_{\text{1st. PS}} + \Big[\underbrace{-\hat{y}\frac{k_c}{\omega\mu_c}E_{xo}^-e^{k''z}e^{jk'z}}_{\text{2nd. PS}}\Big]\,,\end{aligned} \tag{3.4}$$

while the complex Poynting vector $\vec{S} = \vec{E}\times\vec{H}^*$ is

$$\vec{S} = \hat{z}\frac{k_c^*}{\omega\mu_c^*}|E_{xo}^+|^2e^{-2k''z} - \hat{z}\frac{k_c^*}{\omega\mu_c^*}|E_{xo}^-|^2e^{2k''z} + \hat{z}\frac{k_c^*}{\omega\mu_c^*}E_{xo}^-E_{xo}^{+*}e^{2jk'z} - \hat{z}\frac{k_c^*}{\omega\mu_c^*}E_{xo}^+E_{xo}^{-*}e^{-2jk'z}\,. \tag{3.5}$$

Thus, the average power flow density, $\vec{P}_{av} = (1/2)\mathcal{R}e\{\vec{S}\}$, is

$$\vec{P}_{av} = \underbrace{\hat{z}\frac{1}{2}\mathcal{R}e\Big\{\frac{k_c^*}{\omega\mu_c^*}\Big\}|E_{xo}^+|^2e^{-2k''z}}_{\text{1th. PS}} + \underbrace{\Big[-\hat{z}\frac{1}{2}\mathcal{R}e\Big\{\frac{k_c^*}{\omega\mu_c^*}\Big\}|E_{xo}^-|^2e^{2k''z}\Big]}_{\text{2nd. PS}}\,, \tag{3.6}$$

with the quantity

$$\frac{k_c^*}{\omega\mu_c^*} = \frac{k'\mu' + k''\mu''}{\omega[(\mu')^2 + (\mu'')^2]} + j\frac{k''\mu' - k'\mu''}{\omega[(\mu')^2 + (\mu'')^2]} \,. \tag{3.7}$$

It is important to emphasize that (3.3), and thereby (3.4) and (3.6), represent a valid solution provided that the dispersion relation

$$k_c^2 = (k' - jk'')^2 = \omega^2\varepsilon_c\mu_c \,, \tag{3.8}$$

which also can be written as

$$k'^2 - k''^2 = \omega^2(\varepsilon'\mu' - \varepsilon''\mu'') \,, \tag{3.9a}$$

$$2k'k'' = \omega^2(\varepsilon''\mu' + \varepsilon'\mu'') \,, \tag{3.9b}$$

is satisfied. As shown in [21] (3.9a) and (3.9b) lead to the following expressions for k' and k''

$$k' = \pm\frac{1}{\sqrt{2}}\omega\sqrt{\varepsilon'\mu' - \varepsilon''\mu'' + |\varepsilon_c||\mu_c|} \,, \tag{3.10a}$$

$$k'' = \pm\frac{1}{\sqrt{2}}\omega\sqrt{\varepsilon''\mu'' - \varepsilon'\mu' + |\varepsilon_c||\mu_c|} \,, \tag{3.10b}$$

where $|\varepsilon_c| = \sqrt{\varepsilon'^2 + \varepsilon''^2}$ and $|\mu_c| = \sqrt{\mu'^2 + \mu''^2}$. In these expressions, as well as throughout the present chapter, the arguments of the square root function $\sqrt{\cdot}$ are real and positive, and the function itself is chosen to be the positive square root function.

The quantities k' and k'' in (3.10a) and (3.10b), respectively, can be positive or negative. However, when specific physical conditions are imposed on solution represented by (3.3),(3.4), and (3.6), it is found that the signs of k' and k'' depend on each other, and furthermore, that this dependence comes in terms of two possible combinations of the signs of k' and k''.

In order to associate meaningful physics with the solutions (3.3), (3.4), and (3.6), the so-called radiation condition that ensures a proper physical behaviour of the solution must be imposed. With the source producing (3.3), (3.4), and (3.6) and assuming it is located at $z \to -\infty$, the radiation condition, which guarantees that the average power flow density $\vec{P}_{av} = (1/2)\mathcal{R}e(\vec{S})$ is in the positive z-direction and, furthermore, that the fields, as well as $\vec{P}_{av}$, are attenuated in this direction, is imposed.

Once the solution and the pertinent radiation condition have been established, it is next of interest to examine the signs of the derived parameters, as obtained by the definitions given in Section 3.2. More specifically, the signs of the derived parameters for a given selected partial solution (PS) to the HE equation are found such that the chosen solution is in compliance with the imposed radiation condition.

3.3.2 Wave number

First, the wave number, $k_c = k' - jk''$ is considered. It is shown that the two definitions of k_c lead to two possible combinations of the signs of k' and k'' which satisfy the imposed radiation condition in DNG materials. These choices depend on the PS to the HE equation that is selected to analyze the wave propagation. The cases of interest are treated below.

1. *Definition 1 of k_c:* From (3.8), this definition gives $k_c = k' - jk''$, with $k' > 0$. Since $k'k'' < 0$, as implied by (3.9b), it follows that $k'' < 0$. Thus, the 2nd. PS must be selected in order to satisfy the imposed radiation condition. That is, we set $E_{xo}^+ = 0$ and thus get

$$\vec{E} = \hat{x}E_x^-(z) = \hat{x}E_{xo}^- e^{k''z}e^{jk'z} \,, \tag{3.11a}$$

$$\vec{H} = \hat{y}H_y^-(z) = -\hat{y}\frac{k_c}{\omega\mu_c}E_{xo}^- e^{k''z}e^{jk'z} \,, \tag{3.11b}$$

$$\vec{P}_{av} = -\hat{z}\frac{1}{2}\frac{k'\mu' + k''\mu''}{\omega[(\mu')^2 + (\mu'')^2]}|E_{xo}^-|^2 e^{2k''z} \,. \tag{3.11c}$$

From (3.10a) and (3.10b) it follows that

$$k' = \frac{1}{\sqrt{2}}\omega\sqrt{\varepsilon'\mu' - \varepsilon''\mu'' + |\varepsilon_c||\mu_c|}\,, \tag{3.12a}$$

$$k'' = -\frac{1}{\sqrt{2}}\omega\sqrt{\varepsilon''\mu'' - \varepsilon'\mu' + |\varepsilon_c||\mu_c|}\,. \tag{3.12b}$$

2. *Definition 2 of k_c:* From (3.8), this definition gives $k_c = k' - jk''$, with $k' < 0$. Since $k'k'' < 0$, as implied by (3.9b), it follows that $k'' > 0$. Thus, the 1st. PS must be selected in order to satisfy the imposed radiation condition. That is, we set $E^-_{xo} = 0$ and thus get

$$\vec{E} = \hat{x}E^+_x(z) = \hat{x}E^+_{xo}e^{-k''z}e^{-jk'z}\,, \tag{3.13a}$$

$$\vec{H} = \hat{y}H^+_y(z) = \hat{y}\frac{k_c}{\omega\mu_c}E^+_{xo}e^{-k''z}e^{-jk'z}\,, \tag{3.13b}$$

$$\vec{P}_{av} = \hat{z}\frac{1}{2}\frac{k'\mu' + k''\mu''}{\omega[(\mu')^2 + (\mu'')^2]}|E^+_{xo}|^2e^{-2k''z}\,. \tag{3.13c}$$

From (3.10a) and (3.10b) it follows that

$$k' = -\frac{1}{\sqrt{2}}\omega\sqrt{\varepsilon'\mu' - \varepsilon''\mu'' + |\varepsilon_c||\mu_c|}\,, \tag{3.14a}$$

$$k'' = \frac{1}{\sqrt{2}}\omega\sqrt{\varepsilon''\mu'' - \varepsilon'\mu' + |\varepsilon_c||\mu_c|}\,. \tag{3.14b}$$

In summary, there exist two possible combinations of the signs of k' and k'' in a DNG material. One can either choose $k' > 0$, $k'' < 0$, in which case the 2nd. PS must be selected, or $k' < 0$, $k'' > 0$, in which case the 1st. PS must be selected. Moreover, for both of these combinations, the directions of the phase- and power propagation are opposite, as expected in a DNG material.

With reference to [21], it is noted that also in the case of corresponding DPS materials, there are two possible combinations of the signs of k' and k''. However, in this case, the product $k'k''$ is positive for both of the possible combinations. By comparing further the results for DNG and DPS materials, it is found that in order to use the same PS solution, i.e., the same functional form of the solution, in DNG and DPS materials, a different sign for k' must be chosen, while the sign of k'' remains unaltered.

3.3.3 Intrinsic impedance

Second, the intrinsic impedance, $\eta_c = \eta' - j\eta''$, with $\mathcal{R}e\{\eta_c\} = \eta'$ and $\mathcal{I}m\{\eta_c\} = -\eta''$, being its real and imaginary parts, respectively, is considered. It is shown that the two definitions of η_c lead to a positive or a negative η', as well as to η'' which solely depends on the ratio of the electric and magnetic loss tangents in the material. These results are shown to hold for both possible combinations of the sign of k' and k'', and thus regardless of the chosen PS to the HE. The cases of interest are treated below.

1. Select the 2nd. PS, in which case $k_c = k' - jk''$, where $k' > 0$ and $k'' < 0$.

   Definition 1 of η_c: This definition gives

$$\eta_c = \frac{E^-_x}{H^-_y} = -\frac{\omega\mu_c}{k_c} = -\omega\frac{\mu'k' + \mu''k''}{k'^2 + k''^2} - j\omega\left(-\frac{\mu''k' - \mu'k''}{k'^2 + k''^2}\right) = \eta' - j\eta''\,, \tag{3.15}$$

   and therefore, with the previously given signs of μ', μ'', k', and k'', it is seen that

$$\eta' > 0 \quad \text{always}\,, \tag{3.16a}$$

$$\eta'' \gtrless 0 \quad \text{if} \quad \frac{\mu''}{\mu'} \gtrless \frac{k''}{k'}\,. \tag{3.16b}$$

Definition 2 of η_c: This definition gives

$$\eta_c = -\frac{E_x^-}{H_y^-} = \frac{\omega\mu_c}{k_c} = \omega\frac{\mu' k' + \mu'' k''}{k'^2 + k''^2} - j\omega\frac{\mu'' k' - \mu' k''}{k'^2 + k''^2} = \eta' - j\eta'' \,, \tag{3.17}$$

and therefore, with the previously given signs of μ', μ'', k', and k'', it is seen that

$$\eta' < 0 \quad \text{always} \,, \tag{3.18a}$$

$$\eta'' \gtrless 0 \quad \text{if} \quad \frac{\mu''}{\mu'} \lessgtr \frac{k''}{k'} \,. \tag{3.18b}$$

2. Select the 1st. PS, in which case $k_c = k' - jk''$, where $k' < 0$ and $k'' > 0$.

Definition 1 of η_c: This definition gives

$$\eta_c = \frac{E_x^+}{H_y^+} = \frac{\omega\mu_c}{k_c} = \omega\frac{\mu' k' + \mu'' k''}{k'^2 + k''^2} - j\omega\frac{\mu'' k' - \mu' k''}{k'^2 + k''^2} = \eta' - j\eta'' \,, \tag{3.19}$$

and therefore, with the previously given signs of μ', μ'', k', and k'', it is seen that

$$\eta' > 0 \quad \text{always} \,, \tag{3.20a}$$

$$\eta'' \gtrless 0 \quad \text{if} \quad \frac{\mu''}{\mu'} \gtrless \frac{k''}{k'} \,. \tag{3.20b}$$

Definition 2 of η_c: This definition gives

$$\eta_c = -\frac{E_x^+}{H_y^+} = -\frac{\omega\mu_c}{k_c} = -\omega\frac{\mu' k' + \mu'' k''}{k'^2 + k''^2} - j\omega\left(-\frac{\mu'' k' - \mu' k''}{k'^2 + k''^2}\right) = \eta' - j\eta'' \,, \tag{3.21}$$

and therefore, with the previously given signs of μ', μ'', k', and k'', it is seen that

$$\eta' < 0 \quad \text{always} \,, \tag{3.22a}$$

$$\eta'' \gtrless 0 \quad \text{if} \quad \frac{\mu''}{\mu'} \lessgtr \frac{k''}{k'} \,. \tag{3.22b}$$

These results clearly show that $\eta' > 0$ by definition 1, while $\eta' < 0$ by definition 2. Once a given definition of η_c is chosen, the sign of η' is known. However, this is not the case with the sign of η'' for which $\eta'' \gtrless 0$ if $\mu''/\mu' \gtrless k''/k'$ by definition 1, and $\eta'' \gtrless 0$ if $\mu''/\mu' \lessgtr k''/k'$ by definition 2. These observations are independent of the choice of the possible combinations of the sign of k' and k'', i.e., they hold true regardless of the chosen PS to the HE.

As shown in [21], the conditions which determine the sign of η'', which are of the form $\mu''/\mu' \gtrless k''/k'$ can be transformed into a simpler form given by

$$\frac{\mu''}{\mu'} \gtrless \frac{\varepsilon''}{\varepsilon'} \,, \tag{3.23}$$

which thus invokes only the fundamental parameters ε_c and μ_c. Since the electric and magnetic loss tangents, $\tan\delta_e$ and $\tan\delta_m$, respectively, are $\tan\delta_e = \varepsilon''/\varepsilon'$ and $\tan\delta_m = \mu''/\mu'$, it is thus concluded that the ratio of the electric and magnetic loss tangents in a DNG material determines the sign of η''.

In summary, in a lossy DNG material, $\eta' > 0$ by definition 1 of η_c, while $\eta' < 0$ by definition 2. Furthermore, definition 1 gives $\eta'' > 0$ ($\eta'' < 0$) if $\mu''/\mu' > \varepsilon''/\varepsilon'$ ($\mu''/\mu' < \varepsilon''/\varepsilon'$), while definition 2 gives $\eta'' > 0$ ($\eta'' < 0$) if $\mu''/\mu' < \varepsilon''/\varepsilon'$ ($\mu''/\mu' > \varepsilon''/\varepsilon'$). As noted previously, these results are unaffected by the choice of the sign of k' and k'', and hence hold regardless of the PS to the HE.

Similar inequalities for the sign of η'' are also obtained for a lossy DPS material [21].

3.3.4 Refractive index

Finally, the refractive index, $n_c = n' - jn''$, with $\mathcal{R}e\{n_c\} = n'$ and $\mathcal{I}m\{n_c\} = -n''$, being its real and imaginary parts, respectively, is discussed. It is shown that the first two definitions of n_c lead to a real, positive or negative, refractive index, while the last two definitions of n_c lead to complex refractive index. In the complex case, it is furthermore shown that there exist two possible combinations of the signs of n' and n''. The results obtained by each of the four definitions of the refractive index given in Section 3.2 are shown to hold regardless of the possible combination of the signs of k' and k'', and thus irrespective of the choice of the PS to the HE.

The presentation of the results obtained by definitions 1 and 2 of n_c is facilitated by first noting the following. The electric field of the two PSs is from (3.3)

$$\vec{E}(z) = \hat{x} E_{xo}^{\pm} e^{\mp k'' z} e^{\mp j k' z} \,, \tag{3.24}$$

where the upper sign applies for $k' < 0$, $k'' > 0$ (1st. PS) and the lower sign applies for $k' > 0$, $k'' < 0$ (2nd. PS). In real notation this becomes

$$\vec{E}(z,t) = \mathcal{R}e\{\vec{E}(z) e^{j\omega t}\} = \hat{x} E_{xo}^{\pm} e^{\mp k''} \cos(\omega t \mp k' z) \,, \tag{3.25}$$

and to maintain a constant phase with increasing time it is thus required that

$$\frac{dz}{dt} = \pm \frac{\omega}{k'}. \tag{3.26}$$

Using $k' = \mp(1/\sqrt{2})\omega \sqrt{\varepsilon'\mu' - \varepsilon''\mu'' + |\varepsilon_c||\mu_c|}$ from (3.10a), the relation (3.26) becomes

$$\frac{dz}{dt} = -\sqrt{2} \, \frac{1}{\sqrt{\varepsilon'\mu' - \varepsilon''\mu'' + |\varepsilon_c||\mu_c|}}, \tag{3.27}$$

which is negative since the argument of the square root in (3.27) is positive, see Section 3.3.1. Thus, the phase velocity, $\vec{v}_p$, is

$$\vec{v}_p = \hat{z} \frac{dz}{dt} = -\hat{z} \frac{\sqrt{2}}{\sqrt{\varepsilon'\mu' - \varepsilon''\mu'' + |\varepsilon_c||\mu_c|}} \,, \tag{3.28}$$

which is true for $k' < 0$, $k'' > 0$ as well as $k' > 0$, $k'' < 0$. It is noted that both PSs lead, of course, to the same phase velocity $\vec{v}_p$ given by (3.28). It is furthermore useful to recall the following important facts:

- The speed of an electromagnetic wave is the magnitude of the phase velocity, $\vec{v}_p$, in (3.28), i.e., it equals $|\vec{v}_p|$. In a DNG material, this is equivalent to the component of $\vec{v}_p$ in the negative z-direction, since this is the direction of the phase propagation.
- In a lossy DNG material, the component of $\vec{v}_p$ in the direction of power propagation, i.e., in the direction of $\vec{P}_{av}$, is the component of $\vec{v}_p$ in the positive z-direction. Thus, in that case, this component of the phase velocity is the negative of the speed of an electromagnetic wave.

With respect to definitions 3 and 4 it is first recalled that the refractive index is given by

$$n_c^2 = (n' - jn'')^2 = \varepsilon_{c,r}\mu_{c,r} \,. \tag{3.29}$$

which can be rewritten as

$$n'^2 - n''^2 = \varepsilon_r'\mu_r' - \varepsilon_r''\mu_r'' \,, \tag{3.30a}$$

$$2n'n'' = \varepsilon_r''\mu_r' + \varepsilon_r'\mu_r'' \,. \tag{3.30b}$$

In similitude to the corresponding equations for k' and k'' given in Section 3.3.1, it is easily deduced that (3.30a) and (3.30b) give

$$n' = \pm\frac{1}{\sqrt{2}}\sqrt{\varepsilon_r'\mu_r' - \varepsilon_r''\mu_r'' + |\varepsilon_{c,r}||\mu_{c,r}|}\,, \tag{3.31a}$$

$$n'' = \pm\frac{1}{\sqrt{2}}\sqrt{\varepsilon_r''\mu_r'' - \varepsilon_r'\mu_r' + |\varepsilon_{c,r}||\mu_{c,r}|}\,, \tag{3.31b}$$

where $|\varepsilon_{c,r}| = \sqrt{\varepsilon_r'^{\,2} + \varepsilon_r''^{\,2}}$ and $|\mu_{c,r}| = \sqrt{\mu_r'^{\,2} + \mu_r''^{\,2}}$, and, as noted previously, the arguments of the square roots in (3.31a) and (3.31b) are real and positive numbers.

With the above observations in mind, the results for n_c, as defined by definitions 1 through 4, are as given below.

1. *Definition 1 of* n_c: This definition gives

$$n_c = n' = \frac{c_0}{|\vec{v}_p|} = \frac{c_0}{\vec{v}_p \cdot (-\hat{z})} = c_0\frac{\sqrt{\varepsilon'\mu' - \varepsilon''\mu'' + |\varepsilon_c||\mu_c|}}{\sqrt{2}}\,. \tag{3.32}$$

2. *Definition 2 of* n_c: This definition gives

$$n_c = n' = \frac{c_0}{\vec{v}_p \cdot \hat{z}} = -c_0\frac{\sqrt{\varepsilon'\mu' - \varepsilon''\mu'' + |\varepsilon_c||\mu_c|}}{\sqrt{2}}\,. \tag{3.33}$$

3. *Definition 3 of* n_c: From (3.29), this definition gives $n_c = n' - jn''$, with $n' > 0$. Since $n'n'' < 0$, as implied by (3.30b), it follows that $n'' < 0$. In this case, relations (3.31a) and (3.31b), respectively, give

$$n' = \frac{1}{\sqrt{2}}\sqrt{\varepsilon_r'\mu_r' - \varepsilon_r''\mu_r'' + |\varepsilon_{c,r}||\mu_{c,r}|}, \tag{3.34a}$$

$$n'' = -\frac{1}{\sqrt{2}}\sqrt{\varepsilon_r''\mu_r'' - \varepsilon_r'\mu_r' + |\varepsilon_{c,r}||\mu_{c,r}|}. \tag{3.34b}$$

4. *Definition 4 of* n_c: From (3.29), this definition gives $n_c = n' - jn''$, with $n' < 0$. Since $n'n'' < 0$, as implied by (3.30b), it follows that $n'' > 0$. In this case, relations (3.31a) and (3.31b), respectively, give

$$n' = -\frac{1}{\sqrt{2}}\sqrt{\varepsilon_r'\mu_r' - \varepsilon_r''\mu_r'' + |\varepsilon_{c,r}||\mu_{c,r}|}, \tag{3.35a}$$

$$n'' = \frac{1}{\sqrt{2}}\sqrt{\varepsilon_r''\mu_r'' - \varepsilon_r'\mu_r' + |\varepsilon_{c,r}||\mu_{c,r}|}. \tag{3.35b}$$

In summary, definitions 1 and 2 always give a real positive and negative refractive index, respectively, while definitions 3 and 4 give a complex refractive index. As to the signs of n' and n'' obtained by definitions 3 and 4, one can either choose $n' > 0$, $n'' < 0$ (definition 3) or $n' < 0$, $n'' > 0$ (definition 4). The results obtained by the four definitions apply regardless of the choice of the possible combinations of signs of k' and k'', and hence irrespective of the choice of the PS to the HE. This follows at once for definitions 1 and 2, while definitions 3 and 4 require further attention. To this end it is recognized that the derivation of (3.31a) and (3.31b) did not exploit the choice of the possible combinations of the signs for k' and k'', and therefore the values of n' and n'' are independent of the signs of k' and k'' [3.2].

[3.2] The fact that definitions 1 and 2 give a real refractive index in a lossy DNG material should cause no concern. The necessary radiation condition remains satisfied provided that the sign of k'' in (3.24) is selected properly. The selection of the sign of k'' only influences the choice of the PS to the HE, and vice versa. It does not influence the fact that definition 1 (2) gives a real positive (negative) refractive index. The consequence of using these two definitions is thus that an additional parameter, which is k'', must be used to obtain a full description of the solution.

In closing the present section, an alternative means of demonstrating that the results obtained by definitions 3 and 4 do not depend on the signs of k' and k'' is next illustrated. The main points are easily deduced from the defining equations of the complex wave number, k_c and the complex refractive index, n_c. From Section 3.2 the defining equation for the wave number reads

$$k_c^2 = \omega^2 \varepsilon_c \mu_c. \tag{3.36}$$

while the refractive index (definitions 3 and 4) is given by

$$n_c^2 = \varepsilon_{c,r} \mu_{c,r}. \tag{3.37}$$

Since $\varepsilon_c = \varepsilon_0 \varepsilon_{c,r}$ and $\mu_c = \mu_0 \mu_{c,r}$, see (3.1a) and (3.1b), a close connection between (3.36) and (3.37) is revealed by the following result

$$k_c^2 = \omega^2 \varepsilon_c \mu_c = \omega^2 \varepsilon_0 \mu_0 \varepsilon_{c,r} \mu_{c,r} = k_0^2 n_c^2, \tag{3.38}$$

where $k_0^2 = \omega^2 \varepsilon_0 \mu_0$ denotes the square of the free-space wave number. Rearranging (3.38) as

$$k'^2 - k''^2 = k_0^2 (n'^2 - n''^2), \tag{3.39a}$$

$$k'k'' = k_0^2 n'n'', \tag{3.39b}$$

immediately reveals that both of the possible choices $n' > 0$, $n'' < 0$ and $n' < 0$, $n'' > 0$ are independent on whether $k' > 0$, $k'' < 0$ or $k' < 0$, $k'' < 0$. This is due to the fact that a negative left-hand side of (3.39b) is always obtained since $k'k'' < 0$ in a DNG material. However, this is in line with the right-hand side of (3.39b), which likewise is negative for the possible combination of signs of n' and n'' ($\omega > 0$, $\varepsilon_0 > 0$, and $\mu_0 > 0$ is assumed).

Similar results are also found for lossy DPS materials, with the exception that the allowed combination of the signs of the respective parameters yields a positive number on both sides of the equality sign in (3.39b), see [21].

3.3.5 Overview

A summary of the results obtained in Sections 3.3.1 to 3.3.4 is given in Figure 3.1.

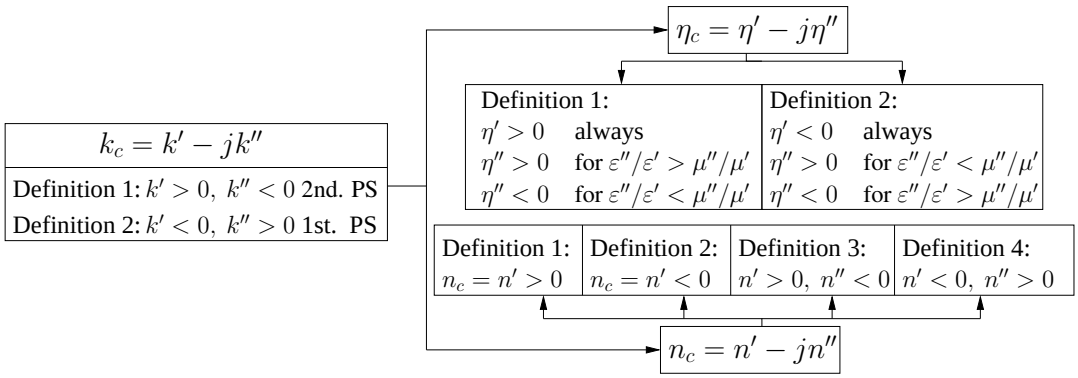

Figure 3.1: *Overview of the sign of the derived parameters in a lossy DNG material.*

It is found that in DNG materials, the two definitions of the wave number, $k_c = k' - jk''$, give two combinations of the signs of k' and k'', and that in both cases, the product $k'k''$ is negative. For both of these definitions, the signs of intrinsic impedance and refractive index may be chosen as indicated in the figure. It is important to realize that the results for η_c and n_c, are independent of the two possible choices of the signs of k' and k'', and thus are true regardless of the chosen PS to the HE.

Moreover, the results in Figure 3.1 also apply when the DNG material is lossless. In this case, the relevant signs and equations are obtained by setting $\varepsilon'' = 0$ and $\mu'' = 0$ in (3.1a) and (3.1b), respectively, which also implies that $k'' = \eta'' = n'' = 0$.

Due to the independence of the results for the various derived parameters from each other, the specific expressions that relate these parameters thus depend on the definitions used to define these parameters in the first place. As an illustration in the lossless case, it is found that, if the wave number $k_c = k'$ is defined by definition 1, i.e., $k' > 0$, and e.g., the refractive index $n_c = n'$ is defined by definition 1, i.e., $n' > 0$, then the relation between these two parameters is necessarily given by

$$k_c = k' = k_0 n_c = k_0 n' \,, \tag{3.40}$$

while it given by

$$k_c = k' = -k_0 n_c = -k_0 n' \,, \tag{3.41}$$

if $k_c = k'$ is defined by definition 1 and $n_c = n'$ is defined by definition 2 (or 4), i.e., if $n_c = n' < 0$.

It is furthermore very interesting to note that the signs of k' and k'' depend on each other, as do the signs of n' and n'' when definitions 3 and 4 of n_c are used. Thus, the sign of e.g., k' or n' also reveals the sign of k'' or n'', respectively, in a lossy material. However, the signs of η' and η'' are independent of each other since the sign of η'' is determined solely by the ratio of the electric and magnetic loss tangents in the material. As a consequence, in order to investigate the influence of a specific choice of sign of these parameters in a solution to a given problem that involves DNG materials, it is sufficient to assume simple and lossless materials.

3.4 Plane wave reflection/refraction at a DPS/DNG interface

Having discussed the various combinations of the signs of the derived parameters in DNG materials, it is next of interest to demonstrate that all possible signs, see Figure 3.1, are equally valid in a solution to a given problem. This is illustrated through a consideration of a simple canonical problem consisting of a UPW incident obliquely on a planar DPS/DNG interface. Owing to the comments made at the end of Section 3.3.5, it is sufficient to assume lossless DPS and DNG materials.

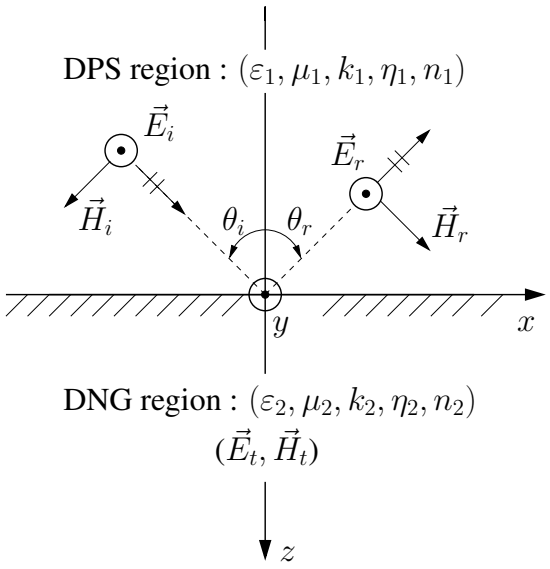

Figure 3.2: *Oblique incidence of a TE UPW at a plane interface separating DPS and DNG regions.*

The configuration of the canonical problem is depicted in Figure 3.2. With no loss of generality, a transverse electric (TE) UPW $(\vec{E}_i, \vec{H}_i)$ is incident obliquely, at an angle of incidence θ_i, at a plane interface at $z = 0$ which separates a DPS region ($-\infty < (x, y) < \infty$, $-\infty < z \leq 0$) from a DNG one ($-\infty < (x, y) < \infty$, $0 \leq z < \infty$). The permittivity and permeability of the DPS region are $\varepsilon_1 = \varepsilon_0 \varepsilon_{1r} > 0$ and $\mu_1 = \mu_0 \mu_{1r} > 0$, respectively, while those of the DNG region are $\varepsilon_2 = \varepsilon_0 \varepsilon_{2r} < 0$ and $\mu_2 = \mu_0 \mu_{2r} < 0$. In addition, the wave number, intrinsic impedance, and refractive index are chosen as $k_1 = \omega\sqrt{\varepsilon_1 \mu_1} > 0$, $\eta_1 = \omega\mu_1/k_1 > 0$, and $n_1 = \sqrt{\varepsilon_{1r}\mu_{1r}} > 0$ (and thus $k_1 = k_0 n_1$), respectively,

in the DPS region, while different combinations of the signs of wave number, k_2, intrinsic impedance, η_2, and refractive index, n_2, are considered in the DNG region.

As the incident field $(\vec{E}_i, \vec{H}_i)$ hits the interface at $z = 0$, part of it is reflected back into the DPS region at an angle of reflection, $\theta_r > 0$, in the form of a reflected field $(\vec{E}_r, \vec{H}_r)$, while the rest is refracted into the DNG region in the form of a refracted field $(\vec{E}_t, \vec{H}_t)$. The field is refracted into the DNG region at an angle of refraction, θ_t, of which the sign is determined below. Mathematically, the incident fields are given by

$$\vec{E}_i(x,z) = \hat{y}E_{iy}(x,z) = \hat{y}E_{io}e^{-jk_1(x\sin\theta_i + z\cos\theta_i)} \,, \tag{3.42a}$$

$$\vec{H}_i(x,z) = \hat{x}H_{ix}(x,z) + \hat{z}H_{iz}(x,z) = E_{io}\frac{k_1}{\omega\mu_1}\left[-\hat{x}\cos\theta_i + \hat{z}\sin\theta_i\right] e^{-jk_1(x\sin\theta_i + z\cos\theta_i)} \,, \tag{3.42b}$$

while the reflected fields are

$$\vec{E}_r(x,z) = \hat{y}E_{ry}(x,z) = \hat{y}E_{ro}e^{-jk_1(x\sin\theta_r - z\cos\theta_r)} \,, \tag{3.43a}$$

$$\vec{H}_r(x,z) = \hat{x}H_{rx}(x,z) + \hat{z}H_{rz}(x,z) = E_{ro}\frac{k_1}{\omega\mu_1}\left[\hat{x}\cos\theta_r + \hat{z}\sin\theta_r\right] e^{-jk_1(x\sin\theta_r - z\cos\theta_r)} \,. \tag{3.43b}$$

where E_{io} and E_{ro} are the magnitudes of the incident and reflected fields, respectively. The refracted fields, which apply for a positive as well as a negative wave number k_2, are given by

$$\vec{E}_t(x,z) = \hat{y}E_{ty}(x,z) = \hat{y}E_{to}e^{j|k_2|(x\sin\theta_t + z\cos\theta_t)} \,, \tag{3.44a}$$

$$\vec{H}_t(x,z) = \hat{x}H_{tx}(x,z) + \hat{z}H_{tz}(x,z) = -E_{to}\frac{|k_2|}{\omega\mu_2}\left[-\hat{x}\cos\theta_t + \hat{z}\sin\theta_t\right] e^{j|k_2|(x\sin\theta_t + z\cos\theta_t)} \,, \tag{3.44b}$$

where E_{to} denotes the magnitude of the refracted electric field. The angle of refraction, θ_t, is defined such that it has the value of -90^o at the negative x-axis, and the value of 0^o along the positive z-axis, and all the intermediate values in the quadrant spanned by these axes, see Figure 3.2.

The quantities θ_r, θ_t, E_{ro}, and E_{to}, are unknown and must be determined. This is done in the following where it is also shown that correct solutions are possible with any choice of signs of the derived parameters. First, the case in which $k_2 > 0$ (Case A) is considered, and second the case in which $k_2 < 0$ (Case B) is considered. In both cases, the influence of a positive as well as a negative η_2 and n_2 on the resulting solutions is discussed.

3.4.1 Case A

The positive wave number k_2 in the DNG region is obtained by the first definition of the wave number, see Section 3.3.2. Thus, $k_2 = \omega\sqrt{\varepsilon_2\mu_2}$, i.e., $|k_2| = k_2$ is substituted in (3.44a) and (3.44b), which thus is the explicit form of the PS representing the refracted electric and magnetic fields[3.3]. Applying the electromagnetic boundary conditions, which require the continuity of the tangential components of the total electric and magnetic fields at the interface $z = 0$, one obtains

$$\left(E_{io}\, e^{-jk_1 x\sin\theta_i} \;+\; E_{ro}\, e^{-jk_1 x\sin\theta_r}\right) = E_{to}\, e^{jk_2 x\sin\theta_t} \,, \tag{3.45}$$

$$\frac{k_1}{\omega\mu_1}\left(-E_{io}\cos\theta_i\, e^{-jk_1\cos\theta_i} \;+\; E_{ro}\cos\theta_r\, e^{-jk_1\cos\theta_r}\right) = \frac{k_2}{\omega\mu_2}\, E_{to}\cos\theta_t\, e^{-jk_1 x\sin\theta_t} \,. \tag{3.46}$$

Since (3.45) and (3.46) must be satisfied for all x, the phase matching gives

$$-k_1 x\sin\theta_i = -k_1 x\sin\theta_r = k_2\sin\theta_t \,. \tag{3.47}$$

[3.3] This PS is the proper one for $k_2 > 0$ since it implies that the power propagation is away from the interface while the phase propagation is towards the interface, as expected in a DNG material. More specifically, it is the z-dependent part of the phase of the refracted field, i.e., the one given by the term $\exp(jk_2 z\cos\theta_t)$ that is propagated toward the interface. Due to the angle of incidence, the x-dependent part of the phase of the refracted field, i.e., the one determined by the term $\exp(jk_2 x\sin\theta_t)$, is necessarily always propagated along the positive x-axis. The sign of θ_t, which is still unknown, will then reveal whether the field is refracted in the xz-plane for which $x > 0$ or $x < 0$, see Figure 3.2.

As a consequence, the angles of incidence and reflection are identical, i.e.,

$$\theta_i = \theta_r \ , \tag{3.48}$$

which is the familiar Snell's reflection law, and furthermore

$$\frac{k_1}{k_2} = -\frac{\sin\theta_t}{\sin\theta_i} \ , \tag{3.49}$$

which is the Snell's refraction law (SRL). The expression in (3.49) is rather interesting as it implies that $\theta_t < 0$ since $k_1 > 0$, $k_2 > 0$ and $\theta_i > 0$. Physically, this means that as the incident wave enters into the DNG region it is refracted under a negative angle θ_t, i.e., it bends at the same side of the normal to the interface from which it is incident. This is the phenomenon of negative refraction mentioned briefly in Chapter 2 as one of the major signatures of DNG materials. The form of the SRL in (3.49) is also referred to as the anomalous form [23] due to the presence of the "$-$" sign on its right-hand side. Thus, when a positive wave number k_2 is assumed for the DNG material, the refraction process is properly described by the anomalous form of the SRL given by (3.49).

It is customary to express the SRL in terms of the refractive indices of the two media. While $n_1 > 0$ is assumed, the expressions for n_2 as obtained by the four definitions established in Section 3.2 are given in Table 3.1. The connection between k_2 and n_2 for the various definitions of n_2, as well as the resulting form of the SRL, is likewise shown in the table.

Definition of n_2	$k_2(n_2)$	SRL
1: $n_2 = \ \sqrt{\varepsilon_{2r}\mu_{2r}}$	$k_2 = \ \omega k_0 n_2$	$N = -\Theta$
2: $n_2 = -\sqrt{\varepsilon_{2r}\mu_{2r}}$	$k_2 = -\omega k_0 n_2$	$N = \ \Theta$
3: $n_2 = \ \sqrt{\varepsilon_{2r}\mu_{2r}}$	$k_2 = \ \omega k_0 n_2$	$N = -\Theta$
4: $n_2 = -\sqrt{\varepsilon_{2r}\mu_{2r}}$	$k_2 = -\omega k_0 n_2$	$N = \ \Theta$

Table 3.1: *The refractive index n_2 in terms of the four definitions, its connection to the wave number k_2 of the DNG region, and the resulting form of the SRL terms of the refractive indices, n_1 and n_2. Note that $N = n_1/n_2$ and $\Theta = \sin\theta_t/\sin\theta_i$.*

These results show that for a positive wave number k_2 of the DNG material, both positive (definitions 1 and 3) as well as negative (definitions 2 and 4) n_2 can be used. The choice of the sign of n_2 merely has an implication on the form of the SRL. With a positive n_2, the SRL takes on the anomalous form, while the standard form, i.e., the one which lacks the "$-$" sign in front of the term Θ [23], is used when n_2 is negative. The fact that the SRL assumes the standard form, which also occurs for the corresponding problem involving two DPS regions, is the only reason for choosing a negative n_2 in the DNG material, as was done in, e.g., the work of Veselago [4], see also [23]. However, as the present results show, this is only a choice since a positive n_2 can be assumed as well, provided that the anomalous SRL is subsequently used.

Having clarified the details related to the SRL, it is next of interest to determine the unknown magnitudes E_{ro} and E_{to}, and thus determine the reflection and transmission coefficients, $\Gamma = E_{ro}/E_{io}$ and $\tau = E_{to}/E_{io}$, respectively, at the interface $z = 0$, also known as the Fresnel equations. As noted before, the intrinsic impedance of the DPS region, η_1, is assumed positive, while both a positive, as well as a negative intrinsic impedance of DNG region, η_2, are investigated. In mathematical terms,

$$\eta_1 = \frac{\omega\mu_1}{k_1} \tag{3.50}$$

while

$$\eta_2 = -\frac{\omega\mu_2}{k_2} > 0 \ , \tag{3.51a}$$

by definition 1 of η_2, and

$$\eta_2 = \frac{\omega\mu_2}{k_2} < 0 \,, \tag{3.51b}$$

by definition 2 of η_2, see Section 3.3.3. Thus, (3.45) and (3.46) read

$$(E_{io} \, + \, E_{ro} \,) = E_{to} \,, \tag{3.52}$$

$$\frac{1}{\eta_1} \, (-E_{io} \, + \, E_{ro}) \cos\theta_i = \mp \frac{1}{\eta_2} \, E_{to} \cos\theta_t \,. \tag{3.53}$$

where the upper (lower) sign on the right-hand side of (3.53) applies for $\eta_2 > 0$ ($\eta_2 < 0$). Combining (3.52) and (3.53), one finds that

$$\Gamma = \frac{\eta_2 \cos\theta_i \mp \eta_1 \cos\theta_t}{\eta_2 \cos\theta_i \pm \eta_1 \cos\theta_t} \,, \tag{3.54a}$$

$$\tau = \frac{2\eta_2 \cos\theta_i}{\eta_2 \cos\theta_i \pm \eta_1 \cos\theta_t} \,. \tag{3.54b}$$

Thus, for a positive wave number k_2 in the DNG material, both positive (definition 1) as well as negative (definition 2) η_2 can be used. The choice of the sign of η_2 merely has an implication on the functional form of the expressions for the reflection and transmission coefficients. With a positive η_2, these coefficients take on the same functional form as obtained for the corresponding problem which includes two DPS regions, see, e.g., [64, Ch. 3]. However, when a negative η_2 is used, a slightly different functional form of these coefficients is obtained as evidenced by (3.54a) and (3.54b).

It is interesting to note that, since $\eta_2 = -|\eta_2|$ when $\eta_2 < 0$, (3.54a) and (3.54b) can be written as

$$\Gamma = \frac{|\eta_2| \cos\theta_i - \eta_1 \cos\theta_t}{|\eta_2| \cos\theta_i + \eta_1 \cos\theta_t} \,, \tag{3.55a}$$

$$\tau = \frac{2|\eta_2| \cos\theta_i}{|\eta_2| \cos\theta_i + \eta_1 \cos\theta_t} \,, \tag{3.55b}$$

which thus apply for $\eta_2 > 0$ as well as for $\eta_2 < 0$. When $\theta_i = 0$, making $\theta_r = \theta_t = 0$, (3.55a) and (3.55b) reduce to those obtained for normal incidence, i.e.,

$$\Gamma = \frac{|\eta_2| - \eta_1}{|\eta_2| + \eta_1} \,, \tag{3.56a}$$

$$\tau = \frac{2|\eta_2|}{|\eta_2| + \eta_1} \,. \tag{3.56b}$$

In the particular case where $\varepsilon_2 = -\varepsilon_1$ and $\mu_2 = -\mu_1$, the intrinsic impedance η_2 is $\eta_2 = \eta_1$ (when $\eta_2 > 0$) and $\eta_2 = -\eta_1$ (when $\eta_2 < 0$), or alternatively, $|\eta_2| = \eta_1$. It then clearly follows from (3.56a) and (3.56b) that $\Gamma = 0$ and $\tau = 1$, respectively, such that the well-known relation $1 + \Gamma = \tau$, see e.g., [64, Ch. 3], is satisfied for both $\eta_2 = \eta_1 > 0$ and $\eta_2 = -\eta_1 < 0$.

3.4.2 Case B

When the second definition of k_2 is used, the results in Section 3.3.2 show that $k_2 = -\omega\sqrt{\varepsilon_2\mu_2}$. In this case, one therefore substitutes $|k_2| = -k_2$ in (3.44a) and (3.44b), and obtains the explicit form of the PS for the refracted electric and magnetic fields. Using the same procedure as in Section 3.4.1, one finds that the Snell's reflection law is as given by (3.48), while the SRL now takes on the following form

$$\frac{k_1}{k_2} = \frac{\sin\theta_t}{\sin\theta_i} \,. \tag{3.57}$$

This expression likewise implies that θ_t is negative since $k_1 > 0$, $k_2 < 0$ and $\theta_i > 0$. Thus, as expected, the previously mentioned phenomenon of negative refraction, also takes place in the present case. The form of the SRL in (3.57) is the standard form. Thus, contrary to the case of a positive k_2, where the anomalous form of the SRL applies, the refraction process is now properly described by the standard form of the SRL given by (3.57).

As demonstrated in Section 3.3.4, the sign of the refractive index obtained by the four definitions is unaffected by the sign of the wave number, i.e., unaffected by the choice of the PS. Consequently, the SRL, as expressed in terms of n_1 and n_2, is the same for $k_2 < 0$ as for $k_2 > 0$, which is found for the four definitions of n_2 in Table 3.1. Thus, when the wave number k_2 of the DNG region is negative, the anomalous form of the SRL is found when n_2 is chosen positive (definitions 1 and 3), while the standard from applies when n_2 is chosen negative (definitions 2 and 4).

As to the Fresnel equations, it is first useful to recall from Section 3.3.3 that the two definitions of the intrinsic impedance give results that likewise are unaffected by the choice of the sign of the wave number and, hence, unaffected by the choice of the PS. Therefore, the respective expressions for the reflection and transmission coefficients in the present case are identical to those given by (3.54a) through (3.56b) obtained for $k_2 > 0$, this being true for $\eta_2 > 0$ as well as $\eta_2 < 0$. In the present case, however, $\eta_2 = \omega\mu_2/k_2 > 0$ by definition 1, and $\eta_2 = -\omega\mu_2/k_2 < 0$ by definition 2, since $k_2 < 0$.

3.5 Summary

This chapter summarized the results of the study on the sign of wave number, $k_c = k' - jk''$, intrinsic impedance, $\eta_c = \eta' - j\eta''$, and refractive index, $n_c = n' - jn''$, in DNG materials. The background for such a study emerged from the obvious disagreements in the literature on the sign of these derived parameters. In order to clarify them, several definitions of the derived parameters were established by considering UPW propagation in simple, lossy DNG materials. More specifically, two definitions were introduced for k_c on the one hand, and η_c on the other hand, while four definitions were introduced for n_c. Each of these definitions gives a specific sign of the parameter in question, thus opening for a possibility of having different signs for one and the same parameter.

In particular, it was found that in a lossy DNG material, the first definition of k_c gives $k' > 0$ and $k'' < 0$, while the second one gives $k' < 0$ and $k'' > 0$. Moreover, for both of these two possibilities for k_c, the first definition of η_c gives $\eta' > 0$, and the second one gives $\eta' < 0$, while the sign of η'' is, by means of both definitions, dependent solely on the ratio of the electric and magnetic loss tangents in the material. As to the sign of n_c, it was found that definitions 1 and 2 give a real refractive index, while definitions 3 and 4 give a complex refractive index. More specifically, the first (second) definition of n_c gives $n' > 0$ ($n' < 0$), while according to the third (fourth) definition, $n' > 0$, $n'' < 0$ ($n' < 0$, $n'' > 0$). These results were also found to hold for both possible combinations of the signs of k' and k''.

It was thus shown that the observed disagreements in the literature are based on the implicit use of different definitions for one and the same parameter. Moreover, it was demonstrated, through a detailed investigation of UPW reflection/refraction at a DPS/DNG interface, that all definitions, and thus signs of these parameters are equally correct as long as they are used consistently in the solution procedure. The difference in the use of various definitions, and thus signs of the derived parameters, is shown to be manifested merely in the different functional forms of the solution to the problem of interest, i.e., in the different forms of e.g., refracted fields, Fresnel equations and SRL.

CHAPTER 4

2D METAMATERIAL-BASED CANONICAL CONFIGURATIONS

In this chapter, the radiation and scattering properties of two-dimensional (2D) metamaterial (MTM)-based canonical structures, such as concentric cylinders and single cylinders, excited by an arbitrarily located electric line source (ELS), are investigated. First, the analytical solution to the problem of concentric cylinders is derived, and second, their near- and far-field properties are analysed through an investigation of such parameters as the total radiated power, directivity, and total scattering cross section. Subsequently, the same solution is used to study the near-field properties of single cylinders. In general, the results obtained for the MTM-based structures are compared to those for the corresponding structures made of conventional double-positive (DPS) materials. In the examination of concentric cylinders, both electrically small structures as well as those of a larger size are considered, while only the latter sizes are emphasized for single cylinders. Lossless, lossy, as well as dispersive MTM-based configurations are investigated.

The present chapter represents mainly a summary of Manuscript I (MI) found in Appendix A, and Manuscript II (MII), found in Appendix B. Moreover, the analytical details not contained in these manuscripts nor in the present chapter are given in Appendix D.

4.1 Introduction

Numerous properties and potential applications of cylindrically shaped MTMs, as well as their combinations with conventional DPS materials, have been studied [24], [36], [37], [42]-[50], [53], [60]. The concept of the perfect lens consisting of a planar slab of a specific double-negative (DNG) material [11], see also Chapter 2, has been extended to perfect cylindrical lenses [24]. Moreover, the plane wave scattering properties and other features of MTM cylinders, have been investigated, see e.g., [36], [37], [42]-[50], [53], and [60]. In particular, it has been demonstrated [36], [37], [48] that electrically small, i.e., sub-wavelength, cylindrical MTM structures, formed by single cylinders or cylindrical shells, can be designed to be resonant and to possess advantageous radiation and scattering characteristics in contrast to the corresponding structures made of conventional DPS materials. More specifically, it was shown that such MTM structures lead to significant enhancements of the total radiated power as well as the total and differential scattering cross sections [36], [37], [48]. Apart from the field of sub-wavelength cylindrical MTM-based cavities, waveguide, and scatterers, other features, such as the focusing effects of DNG cylinders [44], their surfaces polaritons and extinction properties [45], have likewise been studied. In addition, some attention has been devoted to the scattering properties of a collection of several MTM cylinders [49] illuminated by a plane wave, as well as to scattering [50] and radiation [53] characteristics of perfectly electric cylinders coated with DNG materials.

4.2 Configuration and analytical solution

A cross section of the 2D configuration of interest is depicted in Figure 4.1. A circularly cylindrical core of radius ρ_1 (region 1), covered with a concentric cylindrical shell of outer radius ρ_2 (region 2), is imbedded in an infinite ambient medium (region 3). The structure is illuminated by an infinite ELS of

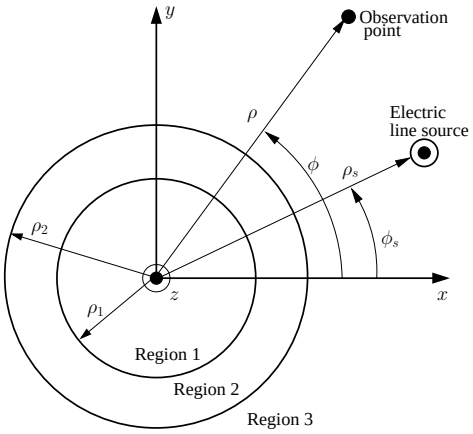

Figure 4.1: *The configuration of the ELS-excited concentric pair of cylinders.*

a constant electric current I_e[4.1]. The axes of the cylinders and the ELS are parallel, and the ELS can be located in any of the three regions. Region i, with $i = 1$ and 2 is characterized by a permittivity and a permeability, denoted by $\varepsilon_i = \varepsilon_i' - j\varepsilon_i''$ and $\mu_i = \mu_i' - j\mu_i''$, respectively, and a wave number $k_i = \omega\sqrt{\varepsilon_i \mu_i}$, where the branch of the square root is chosen so that $\mathcal{I}m\{k_i\} \leq 0$. Each of these regions can be composed of simple DPS materials and/or MTMs[4.2]. The exterior region, region 3, is free space with the permittivity ε_0 and permeability μ_0, and thus the wave number $k_0 = \omega\sqrt{\varepsilon_0 \mu_0}$ and intrinsic impedance $\eta_0 = \sqrt{\mu_0/\varepsilon_0}$. A cylindrical coordinate system (ρ, ϕ, z) and the associated Cartesian coordinate system (x, y, z) are introduced such that the z-axis coincides with the axis of the cylinders. The coordinates of the observation point are (ρ, ϕ), while the coordinates of the ELS are (ρ_s, ϕ_s).

While the ELS and the concentric cylinders can be considered as a radiating system when the ELS is located in regions 1 and 2, and in region 3 at moderate distances from the cylinders, this combination usually is considered as a scattering system when the ELS is moved infinitely far away from the cylinders. The solution to these radiating and scattering problems is straightforward, and proceeds as follows. Using the cylindrical wave functions with origins at $\rho = 0$, the electric field generated by the ELS in an infinite medium characterized by ε_{ELS}, μ_{ELS}, and k_{ELS} is given by the well-known expression [117, Ch. 11]

$$\vec{E}_{\text{ELS}}(\rho, \phi) = -\hat{z} I_e \frac{\omega \mu_{\text{ELS}}}{4} \sum_{n=0}^{N_{max}} \tau_n \, U_n(\rho) \, \cos[n(\phi - \phi_s)] \,, \tag{4.1}$$

where $U_n(\rho) = J_n(k_{\text{ELS}}\rho) H_n^{(2)}(k_{\text{ELS}}\rho_s)$ for $\rho \leq \rho_s$ and $U_n(\rho) = J_n(k_{\text{ELS}}\rho_s) H_n^{(2)}(k_{\text{ELS}}\rho)$ for $\rho \geq \rho_s$. The function $J_n(\cdot)$ is the Bessel function of order n and is chosen to represent the field for $\rho \leq \rho_s$ due to its non-singular behaviour at the origin, while $H_n^{(2)}(\cdot)$ is the Hankel function of second kind and order n, and is chosen for $\rho \geq \rho_s$ because it represents an outward propagating wave that complies with the radiation condition. The symbol τ_n is the Neumann number; thus $\tau_n = 1$ for $n = 0$, and $\tau_n = 2$ otherwise. Furthermore, N_{max} is the truncation limit in the numerical implementation of the infinite summation in the exact solution, chosen to ensure the convergence of the expansion. Moreover, the subscript ELS $= 1$ or 2 when the ELS is located in region 1 or 2, respectively, while the subscript ELS $= 0$ when the ELS is located in region 3.

The unknown scattered field in the region containing the ELS and the unknown total fields in the other regions are also expanded in terms of cylindrical wave functions in a manner similar to the ELS field given by (4.1) and, thus, are given by

[4.1] This type of illumination corresponds to TM polarization. The results for TE polarization, which results for a magnetic line source illumination, follow readily from the duality theorem, and they are thus not included inhere.

[4.2] The choice of the branch of the square root in the expression for k_i such that $\mathcal{I}m\{k_i\} \leq 0$ corresponds to defining the wave number by its second definition, according to which $\mathcal{R}e\{k_i\} < 0$ in a DNG material, and $\mathcal{R}e\{k_i\} > 0$ in a DPS material, see Chapter 3 and [21]. Since the so-obtained signs of $\mathcal{R}e\{k_i\}$ are different in DPS and DNG materials, then the same functional form of the solution applies in these cases. Similar observations hold true for the 3D canonical configurations investigated in Chapter 5.

$$\vec{E}_{ps}(\rho,\phi) = -\hat{z} I_e \frac{\omega\mu_p}{4} \sum_{n=0}^{N_{max}} \tau_n V_{p,n}(\rho)\, \cos[n(\phi-\phi_s)] \,, \tag{4.2}$$

where $p = 1$ for region 1, in which case $\mu_p = \mu_1$ and $V_{1,n}(\rho) = C_{1n} J_n(k_1\rho)$, while $p = 2$ for region 2, in which case $\mu_p = \mu_2$ and $V_{2,n}(\rho) = C_{2n} J_n(k_2\rho) + C_{3n} Y_n(k_2\rho)$, with $Y_n(\cdot)$ being the Neumann function of order n, and finally, $p = 3$ for region 3, in which case $\mu_p = \mu_0$ and $V_{3,n}(\rho) = C_{4n} H_n^{(2)}(k_0\rho)$. Thus, these fields involve the expansion coefficients C_{in}, with $i = 1,\ldots,4$, which are unknown and must be determined. The expressions in (4.1) and (4.2) represent multipole expansions of the fields, i.e., the terms $n = 0, 1, 2, \ldots$ are the monopolar, dipolar, quadrupolar, etc., modes, respectively.

Enforcing the boundary conditions, requiring the continuity of the tangential components of the total electric and magnetic fields at the interfaces $\rho = \rho_1$ and $\rho = \rho_2$, it follows that the unknown expansion coefficients C_{in}, with $i = 1,\ldots,4$, are found as the solution of the following matrix equation

$$\vec{C}_n = \left[\bar{\bar{M}}_n\right]^{-1} \vec{\Lambda}_n \,, \quad n = 0, 1, 2, \ldots N_{max} \tag{4.3}$$

where $\vec{C}_n = [C_{1n}, C_{2n}, C_{3n}, C_{4n}]$ is the vector containing the four expansion coefficients, $\vec{\Lambda}_n = [\Lambda_{1n}, \Lambda_{2n}, \Lambda_{3n}, \Lambda_{4n}]$ is the so-called excitation vector, which depends on the location of the ELS, and the matrix $\bar{\bar{M}}_n$ is a four-by-four matrix that depends on the values of the cylindrical waves at the two interfaces. The explicit form of the excitation vector $\vec{\Lambda}_n$ for the ELS locations in regions 1, 2, and 3, as well as the matrix $\bar{\bar{M}}_n$ are given in MI.

The figures of merit employed in the numerical investigations are the total radiated power (henceforth termed the total power), the directivity, and the total scattering cross section (henceforth termed the total cross section), where the latter is evaluated when the ELS is moved infinitely far away from the concentric cylinders (attention has also been devoted to the differential cross section, see MI for further details). Since the configuration is infinite in the z-direction, all of the quantities are determined on a *per unit length* basis.

As to the total power, specific attention is devoted to the so-called power ratio (PR), which is the ratio of the total power radiated by the ELS in the presence of the concentric cylinders to the power radiated by the ELS in free space[4.3]. With reference to MI, the PR can be expressed as

$$\text{PR} = \frac{1}{2} \sum_{n=0}^{N_{max}} \tau_n^2 (3-\tau_n) |\alpha_n|^2 \,. \tag{4.4}$$

while the directivity, D, defined as the ratio of the radiation intensity to the total average power per unit angle, can be expressed as

$$D(\phi) = \frac{2 \left| \sum_{n=0}^{N_{max}} \tau_n j^n \alpha_n \cos[n(\phi-\phi_s)] \right|^2}{\sum_{n=0}^{N_{max}} \tau_n^2 (3-\tau_n) |\alpha_n|^2} \,. \tag{4.5}$$

The quantity $\alpha_n = C_{4n}$ when the ELS is in region 1 or 2, and $\alpha_n = J_n(k_0\rho_s) + C_{4n}$ when the ELS is in region 3.

The total cross section, σ_t, defined as the ratio of the power contained in the scattered far field to the incident power density at the origin, evaluated when the ELS is moved infinitely far away from the cylinders (i.e., for $\rho_s \to \infty$) along an arbitrary direction ϕ_s, is given by[4.4]

$$\sigma_t = \frac{2}{k_0} \sum_{n=0}^{N_{max}} \tau_n^2 (3-\tau_n) |C'_{4n}|^2 \,, \tag{4.6}$$

[4.3] With reference to MII, it is found that the PR related to the system consisting of the ELS-excited concentric cylinders is equivalent to the radiation resistance (per unit length), inhere denoted by $R_{t,2D}$, of that system normalized by the radiation resistance (per unit length), inhere denoted by $R_{i,2D}$, of the ELS alone in free space. If the total power radiated by the ELS in the presence of a given structure is P_t, and the power radiated by the ELS alone in free space is P_i, then obviously PR $= P_t/P_i$. Since $P_t = I_e^2 R_{t,2D}/2$ and $P_i = I_e^2 R_{i,2D}/2$, see e.g., [113, p. 82], it is easily deduced that PR $= R_{t,2D}/R_{i,2D}$.

[4.4] When the ELS is moved infinitely far away from the concentric cylinders, the incident field generated by the ELS constitutes locally a plane wave. Thus, the the total cross section in (4.6) recovers the usual plane wave cross section, see Appendix D, Section D.2.

with the coefficient $C_{4n}^{'} = C_{4n}/H_n^{(2)}(k_0\rho_s)$, where C_{4n} has been defined previously. Thus, $C_{4n}^{'}$ is obtained as a solution of (4.3), i.e., the same equation which yields C_{4n}, except for the fact that the term $H_n^{(2)}(\cdot)$, which is contained in the excitation vector $\vec{\Lambda}_n$ for the ELS in region 3, i.e., see Table 1 in MI, has been canceled out.

4.3 Electrically small designs

The advantageous use of DNG materials in electrically small designs, as compared to those made of DPS materials only, is next demonstrated through a numerical analysis of the derived figures of merit. A given structure is referred to by its properties in region 1 and 2, i.e., a DPS-MTM structure indicates that region 1 is made of a DPS material while region 2 is the specified MTM material.

4.3.1 Resonance condition

The aim of the present analysis is to demonstrate the possibility of enhancing the PR and the total cross section using the electrically small DNG-based structures. To achieve this goal, it is useful to first find the conditions for which such enhancements may occur. Since both the PR in (4.4) and σ_t in (4.6), are proportional to the magnitude of C_{4n}, large values of these quantities will result if $|C_{4n}|$ is large. As explained in MI, such large values are related to the presence of the so-called natural modes, and the corresponding peaks in the expansion coefficients are referred to as the natural resonances (NRs) of the structure. These resonances can occur in DPS-based structures only if their size is at least of the order of the operating wavelength [1], [37], [48], [57]. These wavelength sized NRs will be discussed briefly in Section 4.4. However, by making the structure from well-selected arrangements of DPS and DNG materials, the expansion coefficients may exhibit NRs even if the size of the structures is significantly smaller than the operating wavelength [1], [37], [48]. These resonances are referred to as sub-wavelength sized NRs (also termed interface resonances in [1], [37] and [48]). These statements are general and are therefore applicable for the 3D canonical configurations considered in Chapter 5.

With reference to MI and relation (4.3), it is noted that $|C_{4n}|$ become large, and a resonance occurs, when the magnitude of the determinant of $\bar{\bar{M}}_n$, $\det\{\bar{\bar{M}}_n\}$, attains a minimum. Since the structures are electrically small, the small argument expansions of the functions contained in $\det\{\bar{\bar{M}}_n\}$ are used to derive an approximate analytical expression for the resonance condition. With the assumption of lossless materials in regions 1 and 2, and the constraints that the products $|k_1|\rho_1$, $|k_2|\rho_1$, $|k_2|\rho_2$, and $k_0\rho_2$ are much smaller than unity, it can be shown that the $|C_{4n}|$ exhibit a resonance when the approximate condition

$$\frac{\rho_1}{\rho_2} \simeq \sqrt[2n]{\frac{(\mu_2+\mu_1)(\mu_2+\mu_0)}{(\mu_2-\mu_1)(\mu_2-\mu_0)}}, \quad n \geq 1 \tag{4.7}$$

is met[4.5]. The resonance condition in (4.7) depends on the mode number, n, and the permeabilities of the three regions. Moreover, it involves only the ratio of ρ_1 and ρ_2 and, thus, does not depend on how small or large either of these radii are individually. In order to define a given resonant structure on the basis of (4.7) one can start by selecting its material parameters and either its inner or outer radius. Then, (4.7) is used to determine the outer or inner radius for a given n, which, as a result, will be the dominant mode excited in this structure[4.6]. It is important to note that the resonance condition in (4.7) holds for $n \geq 1$ since the monopolar mode does not exhibit a resonant behaviour for the range of parameters investigated inhere. Furthermore, this resonance condition is independent of the frequency. Thus, it provides an accurate estimate of the ratio of ρ_1 and ρ_2 at the resonance, but it does not reveal the frequency at which the resonance occurs. As shown in Section 4.3.2.1, this frequency can be selected almost arbitrarily in the sense that a resonance is expected for all frequencies which make the structure electrically small for the selected geometrical and material parameters. As furthermore shown in Section 4.3.2.4, the

[4.5] The complete derivation of (4.7) is found in Appendix D, Section D.4.2.

[4.6] Though certain small terms have been neglected in the derivation of (4.7), see Appendix D, Section D.4.2, it is a very accurate approximation for the radii ratio at resonance, as will be demonstrated later in this chapter. Thus, the resonance condition in (4.7) serves as a guideline to estimate the resonant configuration.

range of frequencies for which a resonance occurs is rather broadband when non-dispersive materials are considered, while it narrows significantly when dispersion is taken into account.

The condition in (4.7) is identical to that obtained in [37] and [48] for plane wave scattering from similar cylindrical structures. It requires that at least one of the parameters μ_1 or μ_2 be negative, i.e., a mu-negative (MNG)- or a DNG-based structure is required. In order to fulfill the condition in (4.7), the negative values of μ_1 and/or μ_2 can not be selected arbitrarily, see MI for the constraints on the these parameters. Below, only the DNG-based structures are considered. Comments on the MNG-based structures, for which the TM polarization offers the same resonance features as the DNG-based ones, are given in MI.

An interesting observation for the configurations in which the ELS is located in region 1 along the axis of the cylinders, i.e., for $\rho_s = 0$, is next made. From Table 1 in MI one notes that the non-zero elements of the excitation vector $\vec{\Lambda}_n$ for the ELS in region 1 are $\Lambda_{3n} = \mu_1 J_n(k_1\rho_s)H_n^{(2)}(k_1\rho_1)$ and $\Lambda_{4n} = k_1 J_n(k_1\rho_s)H_n^{(2)\prime}(k_1\rho_1)$, which are both proportional to $J_n(k_1\rho_s)$. Since $J_n(0) = 0$ for $n > 0$, only $C_{i0} \neq 0$, and thus only the monopolar mode radiates when the ELS is located on the axis of the cylinders. Since there is no electrically small monopolar resonant structure for the range of parameters to be investigated here, it follows that the resonances associated with the excitation of higher-order modes ($n = 1, 2, 3, \ldots$) occur only if the ELS is located off the cylinder axis, i.e., for $\rho_s > 0$. As will be shown in Chapter 5, this is not the case with the resonant 3D canonical spherical configurations, which naturally allow the source to be located at center of the concentric spheres. The present findings for the $\rho_s = 0$ cylindrical case are in agreement with [60] where it was noted that such 2D configurations do not affect the field distribution as well as the power radiated by the ELS. However, in sharp contrast to the $\rho_s = 0$ case, the 2D configurations with $\rho_s > 0$ show the resonant behaviour. The presence of this resonant behaviour in several DNG-based structures and its absence in the corresponding DPS-based cases will be demonstrated below.

4.3.2 Dipolar structures

Numerical results for the so-called dipolar structures, i.e., the structures in which the dipolar mode is excited as the dominant one, are next discussed.

Region 1 is assumed to be free space, while region 2 is composed of a DNG material with $\varepsilon_2 = -\varepsilon_0$ and $\mu_2 = -4\mu_0$. Region 3 is, as noted before, free space. The inner radius of region 2 is set to $\rho_1 = 6$ mm. Assuming that $n = 1$, $\rho_1 = 6$ mm, the resonance condition (4.7) then yields $\rho_2 = 10$ mm for the selected material parameters of the three regions. This outer radius value is the one at which the resonance and, thus, the enhancement of the total power, as well as the total cross section, is expected.

In order first to illustrate the observations made in Section 4.3.1 about the independence of the resonance condition (4.7) on the frequency, three distinct frequencies, f_1, f_2, and f_3, for which the above defined dipolar structure is electrically small, are first selected. These are given in Table 4.1. The respective electrical sizes of the largest dimension of the structure defined above, which is $2\rho_2 = 20$ mm, are also included there. Since the largest dimension involved in the structure is of the order of λ_0/x, $x = 37.5,\ 50$ and 75, it follows that electrically small designs are utilized for all three frequencies.

$f_1 = 200$ MHz ; $\lambda_0 = 1.5$ m	$f_2 = 300$ MHz ; $\lambda_0 = 1$ m	$f_3 = 400$ MHz ; $\lambda_0 = 0.75$ m
$2\rho_2 = 20$ mm $= \lambda_0/75$	$2\rho_2 = 20$ mm $= \lambda_0/50$	$2\rho_2 = 20$ mm $= \lambda_0/37.5$
$k_2\rho_2 = 0.084$	$k_2\rho_2 = 0.126$	$k_2\rho_2 = 0.168$

Table 4.1: *Three frequencies f_1, f_2 and f_3 which are used to illustrate the frequency independence of the resonance condition in (4.7). The electrical size of the dipolar DPS-DNG structure in the three cases is also included.*

The dipolar DPS-DNG structure is compared to the DPS-DPS structures having the same material and geometrical parameters as the dipolar DPS-DNG structure, with the exception that $\varepsilon_2 = \varepsilon_0$ and $\mu_2 = 4\mu_0$. Consequently, the structures under examination are a DNG or a DPS cylindrical shell in the presence of an ELS that can be located in any of the three regions.

4.3.2.1 Total power - power ratio

Figure 4.2 shows the PR as a function of the outer shell radius ρ_2 for the dipolar DPS-DNG structure for the three frequencies: $f_1 = 200$ MHz, $f_2 = 300$ MHz, and $f_3 = 400$ MHz. The ELS is in region 1 at $\rho_s = 5.99$ mm for all three cases.

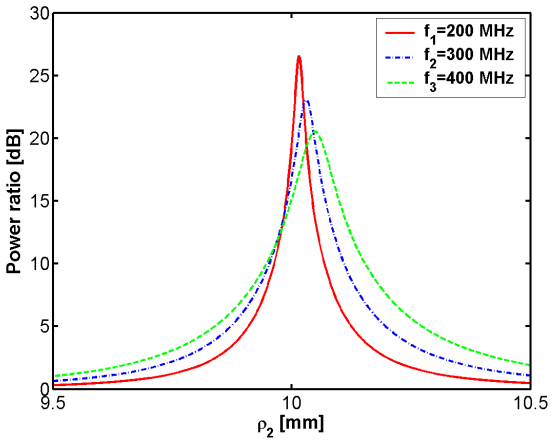

Figure 4.2: *Power ratio as a function of the outer shell radius ρ_2 for the frequencies $f_1 = 200$ MHz, $f_2 = 300$ MHz, and $f_3 = 400$ MHz. The ELS is in region 1 at $\rho_s = 5.99$ mm*

Regardless of the frequency, resonance peaks, although somewhat displaced from each other, are found. More specifically, for $f_1 = 200$ MHz, which is the electrically smallest case, the resonance is attained at $\rho_2 = 10.015$ mm, which is very close to the approximate result of 10 mm predicted by the resonance condition. Moreover, the $f_2 = 300$ MHz and $f_3 = 400$ MHz cases lead to a resonance at $\rho_2 = 10.03$ mm and $\rho_2 = 10.049$ mm, respectively, which also are close to the approximate value of 10 mm. The fact that the value of ρ_2 in the electrically smallest case is closest to the approximative value of 10 mm is expected since the approximation used in the derivation of the resonance condition becomes increasingly more accurate as the size becomes smaller. This is also the reason for the larger values of the PR at resonance in the electrically smaller cases. These observations are in line with the statements made is Section 4.3.1 concerning the frequency independence of the resonance condition. As stated there, and as confirmed in Figure 4.2, the resonant behaviour is expected for those frequencies which guarantee an electrical small size of the structure.

With these results in mind, the properties of the DPS-DNG, as well as the DPS-DPS structures are next investigated for a specific frequency. To this end, the frequency $f_2 \equiv f_0 = 300$ MHz is selected and the results throughout this chapter are recorded for this value.

The PR as a function of the outer shell radius ρ_2 is depicted in Figure 4.3(a) for the dipolar DPS-DNG and DPS-DPS structures when the ELS is in region 1 at $\rho_s = 5.99$ mm . While, as noted previously, a resonance peak (of value PR $\simeq$ 23 dB or PR $\simeq$ 200) is found at $\rho_2 = 10.03$ mm for the DPS-DNG structure, no resonances are observed for the DPS-DPS structure and the PR is close to unity. As noted in MI, similar results hold true when the ELS is in regions 2 and 3. This clearly shows the advantage of the electrically small dipolar DPS-DNG structure over the corresponding DPS-DPS structure.

In order to assess the influence of the ELS location on the resonant enhancement of the total power, Figures 4.3(b) and (c) show the PR as a function of the ELS location ρ_s, when the ELS is in region 1 and 2, respectively, for the dipolar DPS-DNG and DPS-DPS structures having the fixed radii values: $\rho_1 = 6$ mm and $\rho_2 = 10.03$ mm. In both cases and irrespective of the ELS location, the DPS-DPS structure offers no enhancement. On the other hand, the corresponding DPS-DNG structures produce very large PRs, this being particularly the case when the ELS is close to the surface of the DNG shell.

When the ELS is in region 1, the PR increases from approximately zero to approximately 23 dB when the ρ_s values are increased in this region. The fact that there is no enhancement for the near-the-origin ELS locations agrees well with the previous observation that the ELS must be offset from the axis of

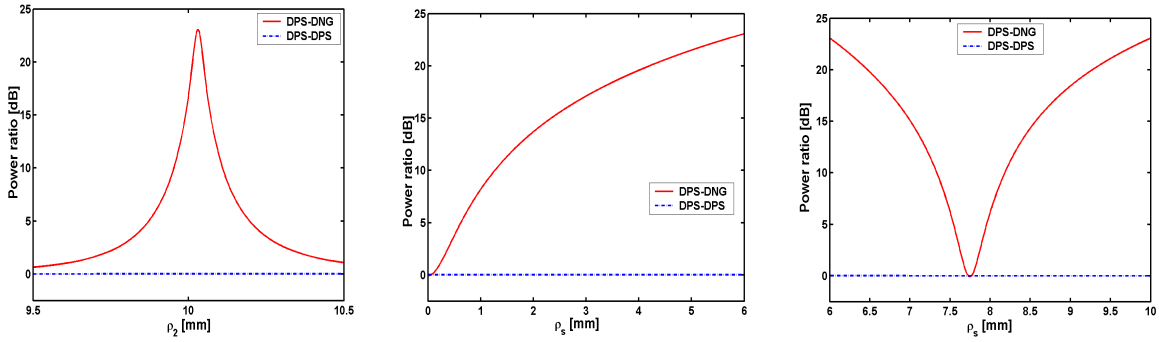

(a) (b) (c)

Figure 4.3: *(a): Power ratio as a function of the outer shell radius ρ_2 when the ELS is in region 1 at $\rho_s = 5.99$ mm (a) and as a function of the ELS location ρ_s when the ELS is in region 1 (b) and 2 (c) for the dipolar DPS-DNG and DPS-DPS structures.*

the cylinders to excite, in this case, the resonant dipolar mode. As the near-field investigations discussed below will confirm, the monopolar mode is dominant for small values of ρ_s. When the ELS is in region 2, the largest PR values are obtained when the ELS is close to the interfaces at ρ_1 and ρ_2. However, the PR curve in this region is particularly interesting because it exhibits a minimum for $\rho_s = 7.746$ mm, where the total power radiated by the ELS in the presence of the DNG shell is actually slightly lower than the power radiated by the ELS alone. Thus, as the ELS is moved through the DNG region, its ability to excite the resonant dipolar mode changes, although the structure was from the outset designed to excite the resonant dipolar mode. As confirmed by the near-field results given below, the ELS can only couple to the monopolar mode at the specific location $\rho_s = 7.746$ mm, and therefore it can not cause a resonant enhancement of the total radiated power for this location.

When the ELS is in region 3, similar phenomena have been observed as above for the locations of the ELS near to the DNG shell, while the PR is slowly decreasing for increasing ρ_s values, see MI.

4.3.2.2 Near field

The near-field results throughout this section are illustrated by showing the quantity $20\log_{10}|\vec{E}(\rho,\phi)|$, where $\vec{E}(\rho,\phi)$ denotes the total electric near field normalized by 1 V/m, in a circular region of radius $3\rho_2$ centered at the cylinder axis (z-axis). For specific ELS locations, the electric near-field results are augmented by the magnetic near-field results, in which case the ϕ-component of the total magnetic field, H_ϕ, or more specifically the quantity $20\log_{10}|H_\phi(\rho,\phi)/1\ [\text{V/m}]|$ is shown in the same circular region.

Figure 4.4(a) shows the electric near field of the ELS when it is located in free space, while Figure 4.4(b) shows the electric near field of the DPS-DPS structure excited by the ELS. In both cases the ELS is located at $\rho_s = 0.001$ mm.

As can be observed in Figure 4.4(a), the field radiated by the ELS in free space has, of course, the monopolar form, while the near field in Figure 4.4(b) is very similar to that in Figure 4.4(a). Thus, the DPS-DPS structure practically does not influence the radiation from the ELS. As a consequence, the DPS-DPS structure is not expected to produce any enhancement of the desired quantities, this being in line with the behaviour of the DPS-DPS structure observed in Figure 4.3. Similar near-field results, not included here, for the DPS-DPS structure, have been obtained for other locations of the ELS in regions 1, 2, and 3.

The electric near field for the dipolar DPS-DNG structure with $\rho_2 = 10.03$ mm is shown in Figures 4.5(a)-(c) for various locations of the ELS in region 1, while the ϕ-component of the magnetic field is shown in 4.5(d).

For $\rho_s = 0.001$ mm, a monopolar form of the electric near field is observed in Figure 4.5(a).This confirms that for locations of the ELS close to the origin, the monopolar mode is the dominant one, and hence, that no enhancement of the total radiated power is expected for such ELS locations. This is in agreement with the previous statements regarding the necessity of exciting the higher order modes in order to obtain the enhancement. However, as the ELS is moved just slightly away from the origin to, e.g.,

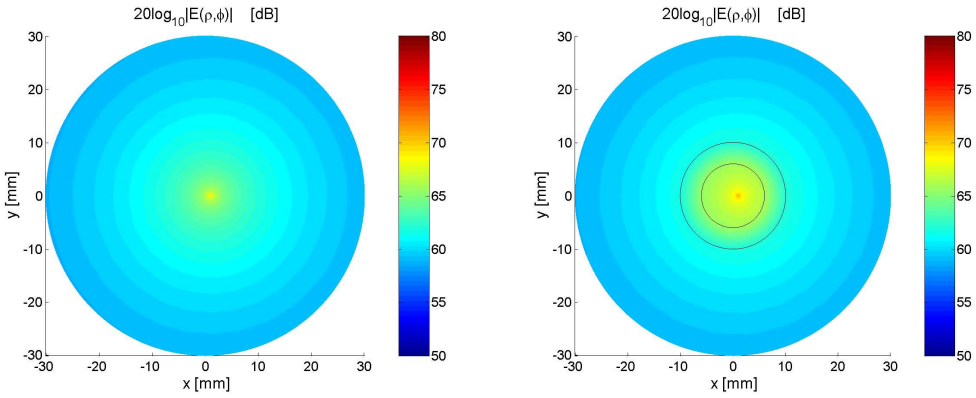

Figure 4.4: *Electric near field of the ELS in free space (a), and in the presence of the DPS-DPS structure (b). In both cases the ELS is located at* $\rho_s = 0.001$ *mm. The curves representing the cylindrical surfaces of the DPS-DPS structure are also shown in (b).*

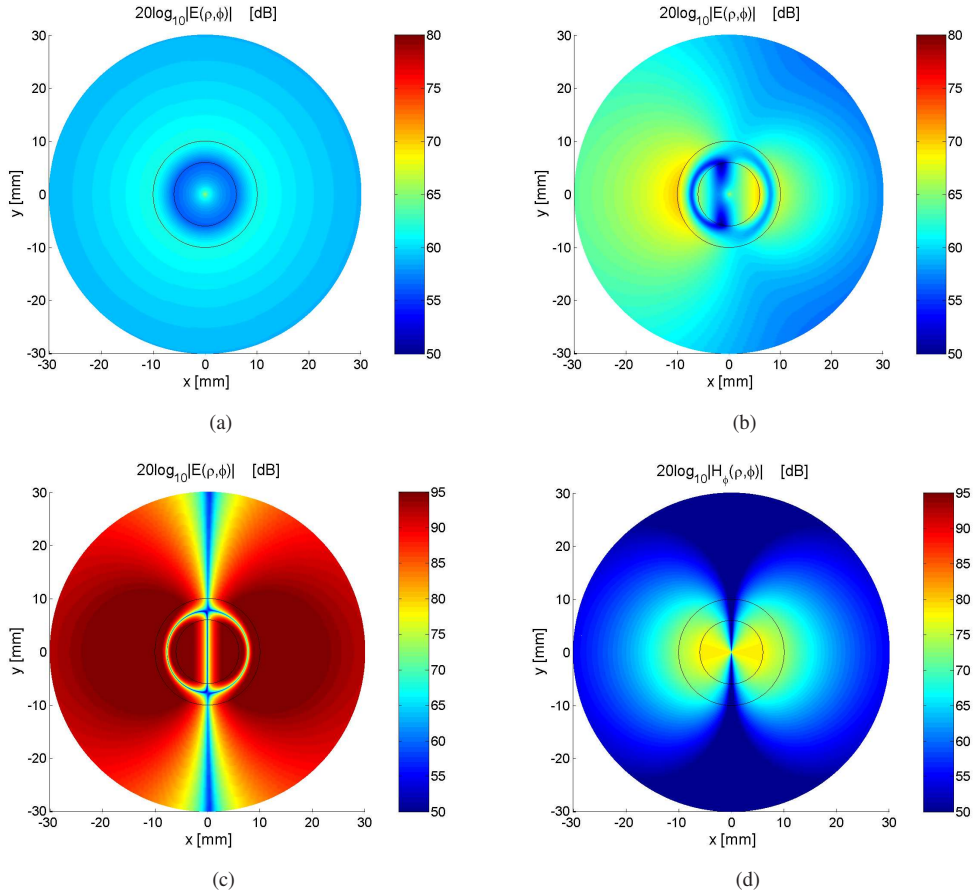

Figure 4.5: *Electric near field of the dipolar DPS-DNG structure when the ELS is located at* $\rho_s = 0.001$ *mm (a),* $\rho_s = 0.125$ *mm (b), and* $\rho_s = 5.99$ *mm (c), and the* ϕ*-component of the magnetic near field of the same structure when the ELS is located at* $\rho_s = 5.99$ *(d). Note that the dynamic range in (c) is larger than in (a)-(b). The curves representing the cylindrical surfaces of the DPS-DNG structure are also shown in the figure.*

$\rho_s = 0.125$ mm, the monopolar mode is mixed with the dipolar mode, as confirmed by Figure 4.5(b). Moving the ELS further from the origin, e.g., to $\rho_s = 5.99$ mm, leads to the electric near field shown

in Figure 4.5(c) that has a clear dipolar form. This is also the case for the ϕ-component of the magnetic near field depicted in Figure 4.5(d) for the same ELS location. At this ELS location, an enhancement of about 23 dB of the total radiated power is found in Figure 4.3(b). This result clearly shows that an ELS radiating in the presence of the dipolar DPS-DNG structure resonantly excites the dipolar mode, which thus causes the enhancement of the total power[4.7]. Although both exhibit a dipolar form, the electric and magnetic near fields in Figures 4.5(c) and (d), do show some notable differences worth mentioning. In particular, when the ELS locations are close to the origin, as well as for certain ELS locations inside region 2 (i.e., in a small annular region containing this ELS location), the magnitude of the electric field is small. A cut of these near fields for $\phi = 0^o$ is shown in Figure 4.6(a) and (b), respectively. It is found that the electric field is diminished as the ELS approaches the origin, and furthermore that it exhibits a minimum at $\rho_s \simeq 7.755$ mm inside region 2. None of these phenomena are observed for the magnetic near field. Use will be made of these observations at the end of the near-field examinations.

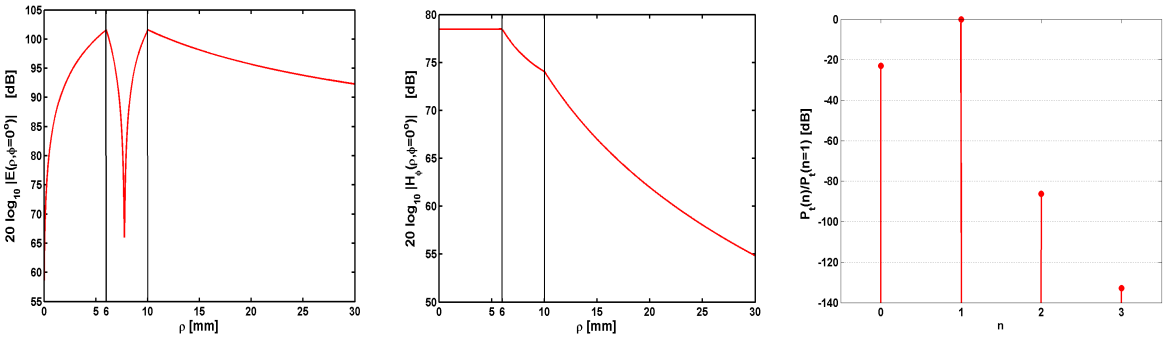

(a) (b) (c)

Figure 4.6: *The $\phi = 0^o$-cut of the electric (a) and magnetic (b) near field. (c) The total power of the dipolar DPS-DNG structure contained in the n'th mode, $n = 0, 1, 2$ and 3, normalized by the power in the dipolar mode.*

To provide an additional insight into the obvious connection between the excitation of the dipolar mode and the associated resonant enhancement of the total power, the total power spectrum in the n'th mode for the dipolar DPS-DNG structure with $\rho_s = 5.99$ mm is shown in Figure 4.6(c). More specifically, the total power in the $n = 0, 1, 2,$ and 3 modes, normalized by the the total power in the dipolar mode is depicted. As observed, the major part of the power is contained in the dipolar mode, while only a very small amount is contained in the three other modes (no power is contained in the $n > 3$ modes). With the vast majority of the total power being contained in the dipolar mode it is therefore clear that this mode is indeed the dominant one, and that its resonant excitation leads to the reported enhanced properties of the DPS-DNG structure.

As to the ELS locations in region 2, the interesting behaviour of the PR values for the dipolar DPS-DNG structure in Figure 4.3(c), reveal that no enhancement is found for $\rho_s = 7.746$ mm and in a very close vicinity of this location. The near field for this particular location is depicted in Figure 4.7 where a monopolar form is observed at distances away from the DNG shell.

This monopolar behaviour is rather interesting since the DPS-DNG structure was designed specifically to excite the resonant dipolar mode. The strong presence of the monopolar mode at $\rho_s = 7.746$ mm results in no enhancement of the total power, as observed in Figure 4.3(c). It also suggests that for the ELS locations close to this critical value, the near field is a mixture of the dipolar and the stronger monopolar mode. Thus, gradual transformations of the field pattern as the ELS traverses region 2, e.g., from the dipolar form (near ρ_1) to the monopolar form (near and at $\rho_s = 7.746$ mm) and back again to the dipolar form (near ρ_2), are in evidence. The result of these transformations is the reduced PR

[4.7] With the ELS in region 2, the near field has a dipolar form for the ELS locations near the DNG shell surfaces, and thus the maximum PR shown in Figure 4.3(c) is a result of the excitation of the resonant dipolar mode. With the ELS in region 3 being moved away from the DNG shell, the strength of the excitation of the dipolar mode gradually decreases and then the monopolar mode begins to dominate. This accounts for the behaviour of the PR noted at the end of Section 4.3.2.1 and further explained in MI.

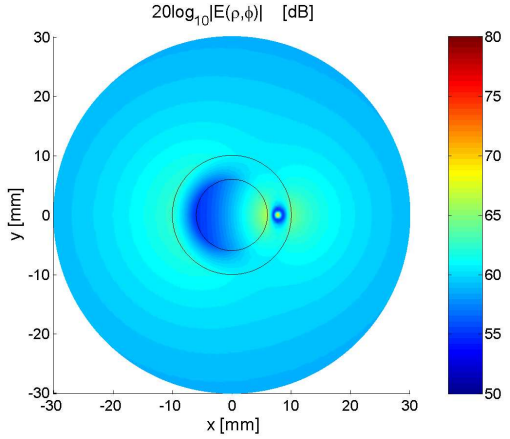

Figure 4.7: *Electric near field of the resonant dipolar DPS-DNG structure. The ELS is in region 2 at* $\rho_s = 7.746$ *mm.*

values for ELS locations around the critical value of $\rho_s = 7.746$ mm. Similar gradual transformations of the near field have been observed in Figures 4.5(a) and (b) for ELS locations close to the origin. These gradual transformations of the pattern with changing ELS location will be analysed further in Section 4.3.2.3.

In summary, the above results show that the enhancement of the total power is obtained whenever the resonant dipolar mode is excited, while this is not the case when the monopolar mode is dominant. This is in agreement with the predictions of the resonance condition (4.7). It is therefore important to understand why the monopolar mode dominates for certain ELS locations as mentioned above, even when the dipolar DPS-DNG structure was designed to excite the dominant dipolar mode.

With reference to the footnote on page 39 and Figure 4.5(c), where the electric near field of the dipolar DPS-DNG structure is shown for the particular ELS location $\rho_s = 5.99$ mm, as well as MI, it is found that once the resonant dipolar mode is excited, the near fields are in general unaffected by the precise location of the ELS. It is only the details such as e.g., the amount of asymmetry in the pattern, see MI (Appendix A), and the precise ELS location for which minimum electric near field is found in region 2, see Figures 4.5(c) and 4.6(a), which are slightly influenced by the ELS location (although not included inhere, it was verified that e.g., a change in the ELS location from $\rho_s = 5.99$ mm in Figure 4.5(c) to $\rho_s = 1$ mm leads to a shift in the location for minimum electric near field for region 2 from $\rho_s \simeq 7.755$ mm in Figure 4.6(a) to $\rho_s \simeq 7.801$ mm). Therefore, the electric- and magnetic near-field results for the resonant dipolar mode shown in Figure 4.5(c) and (d) constitute the natural dipolar mode of the structure. Therefore, in order to excite such a mode, the ELS must be placed at locations where the field is large, which is why it is excited most strongly when the ELS is near the surfaces of the DNG shell. On the other hand, if the ELS is placed at locations for which the electric field of the dipolar mode is minimum, the dipolar mode is very weakly excited, or not excited at all. Among others, these locations are found near the origin, as well as inside region 2, where a narrow annular region in which the field is low has been identified. This explains why the monopolar mode is dominant, and hence no enhancement of the total power is found for such ELS locations. Taking into account the thickness of region 2, i.e., the DNG shell, which is $\rho_2 - \rho_1 = 4.02$ mm, the ELS location, $\rho_s = 7.755$ mm, where the electric near field in region 2 is a minimum, see Figure 4.6(a), is practically the same as the location, $\rho_s = 7.746$ mm, for which no enhancement of the total power was found in Figure 4.3(c).

4.3.2.3 Directivity

Having demonstrated, both analytically and numerically, the possibility of designing electrically small resonant dipolar DNG-based structures, it is next of interest to examine the radiation patterns of such structures.

Figure 4.8(a) shows the directivity patterns for a number of ELS locations for the DPS-DNG and

DPS-DPS structures.

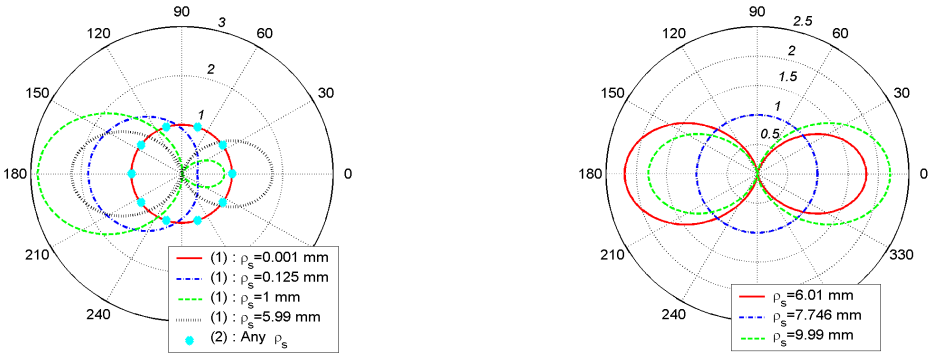

(a) (b)

Figure 4.8: *Directivity for various ELS locations in region 1 for both DPS-DPS (labeled by (2)) and DPS-DNG structures (labeled by (1)) (a), and in region 2 for only DPS-DNG structures.*

In general, the directivity results are in clear agreement with the near-field results discussed above. As to the DPS-DNG structure, the following is noted. For $\rho_s = 0.001$ mm, the structure acts as an omnidirectional radiator and the directivity pattern is monopolar. However, for $\rho_s = 0.125$ mm, the directivity has a form, which is a mixture of more modes, and the maximum directivity, D_{max}, attained in the $\phi = 180^o$-direction, is $D_{max} = 1.86$. For $\rho_s = 1$ and 5.99 mm, the directivity takes on the dipolar form, although it is not symmetric, and the maximum directivities, likewise attained in the $\phi = 180^o$- direction, are $D_{max} = 2.86$ and $D_{max} = 2.15$, respectively. The asymmetry in the pattern is reduced, accompanied with the reduction in the maximum directivity, as the location of the ELS is moved toward the surface of the DNG shell. In comparison, the directivity of the corresponding DPS-DPS structure has a monopolar form regardless of the ELS location. Thus, in addition to enhanced PR values, an electrically small dipolar DPS-DNG structure provides the possibility of reshaping the pattern from the monopolar form to the dipolar one by changing the location of the ELS.

When the ELS is in region 2, a dipolar pattern is found for the DPS-DNG structures for the ELS locations close to the surfaces of the DNG shell, with $D_{max} = 2.19$, while a perfectly monopolar pattern is found for $\rho_s = 7.746$ mm. This is illustrated in Figure 4.8(b) and is in agreement with the PR and near-field results. It is linked to the previously mentioned gradual transformation from the dipolar to the monopolar and back to the dipolar mode of radiation.

As shown in MI, the directivity pattern attains a dipolar form also when the ELS is in region 3 provided that moderate distances between the ELS and the DNG shell are considered.

4.3.2.4 Total cross section

With reference to Section 4.2, the ELS in region 3 is, with no loss of generality, moved infinitely far from the DPS-DNG and DPS-DPS structures along the $\phi_s = 0^o$ - direction. This corresponds in practice to a TM polarized uniform plane wave being incident on the structure from the $\phi_s = 0^o$- direction. Figure 4.9 shows σ_t, or more specifically the quantity $10\log_{10}(\sigma_t/1\text{ [m]})$, as a function of the outer shell radius ρ_2 for the dipolar DPS-DNG and DPS-DPS structures. While σ_t of the DPS-DPS structure is very low, it is considerably enhanced by the presence of the DNG shell, in particular for the case when $\rho_2 = 10.03$ mm, where a resonance peak of magnitude close to 1 dB is observed although the structure is electrically small. The resonances in the PR and σ_t for the dipolar DPS-DNG structure occur for the same geometrical parameters, and in the terminology introduced in [57] for the corresponding spherical case, the present radiating and scattering systems are reciprocal.

It is interesting to note that the present DPS-DPS structure must increase its outer radius ρ_2 by approximately 20 times in order to yield σ_t of the same order of magnitude as the dipolar DPS-DNG structure does. Thus, the electrically small dipolar DPS-DNG structure does exhibit characteristics generally attributed to larger scatterers.

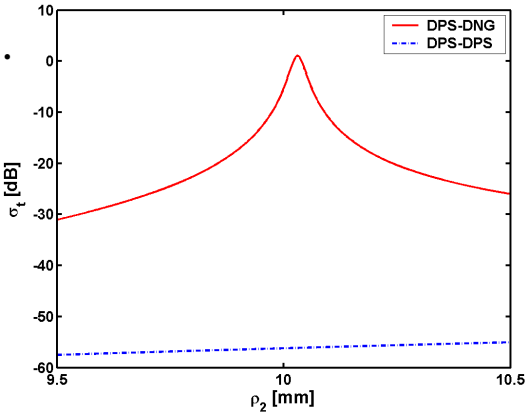

Figure 4.9: *The total cross section σ_t as a function of the outer shell radius ρ_2 for the dipolar DPS-DNG and DPS-DPS structures.*

4.3.3 Effects of loss and dispersion

This section investigates the influence of dispersion and loss on the resonant behaviour of the electrically small DPS-DNG structures. From Chapter 2 it is recalled that dispersion in DNG materials is oftentimes accounted for by the familiar Drude and Lorentz dispersion models, and this is also the case here. Thus, region 2 of the DPS-DNG structure, i.e., the DNG shell, is assigned permittivity $\varepsilon_2(\omega)$ and permeability $\mu_2(\omega)$ values which obey the Drude and Lorentz dispersion models mentioned in Chapter 2. These models are given by

$$\varepsilon_2(\omega) = \varepsilon_0 \left[1 - \frac{\omega_{pe}^2}{\omega(\omega - j\Gamma_e)}\right] \quad \text{and} \quad \mu_2(\omega) = \mu_0 \left[1 - \frac{\omega_{pm}^2}{\omega(\omega - j\Gamma_m)}\right], \tag{4.8a}$$

when the lossy Drude model is employed, while the lossy Lorentz model of the permittivity and permeability, respectively, reads

$$\varepsilon_2(\omega) = \varepsilon_0 \left[1 - \frac{\omega_{pe}^2}{\omega^2 - j\Gamma_e\omega - \omega_{er}^2}\right] \quad \text{and} \quad \mu_2(\omega) = \mu_0 \left[1 - \frac{\omega_{pm}^2}{\omega^2 - j\Gamma_m\omega - \omega_{mr}^2}\right], \tag{4.8b}$$

where ω_{pe} and ω_{pm} are the electric and magnetic plasma frequencies, while Γ_e and Γ_m are the electric and magnetic damping factors (also known as the electric and magnetic collision frequencies, respectively), see also Chapter 2. In the Lorentz models, ω_{er} and ω_{mr} are the resonance frequencies of the permittivity and permeability, respectively. While Γ_e and Γ_m are selected arbitrarily, the values of ω_{pe} and ω_{pm} must be determined for both models such that these properly recover, at the angular frequency of operation $\omega_0 = 2\pi f_0$, with $f_0 = 300$ MHz, the lossless values of $\varepsilon_2 = -\varepsilon_0$ and $\mu_2 = -4\mu_0$, which were used for the non-dispersive DPS-DNG structures in Section 4.3.2. Thus, as explained in Appendix F, Section F.3, which includes further details related to these models, ω_{pe}^2 and ω_{pm}^2 for the Drude model are determined from the real part of $\varepsilon_2(\omega)$ and $\mu_2(\omega)$, respectively, evaluated at ω_0 to recover the desired material parameter values. For the Lorentz models, with the assumption that the losses are small, the frequency of operation f_0 must lie above the resonance frequency of the material parameters to obtain the required negative values of $\varepsilon_2(\omega)$ and $\mu_2(\omega)$. Since the angular frequencies of the permittivity and permeability at resonance are given by $\omega_{er} = 2\pi f_{er}$ and $\omega_{mr} = 2\pi f_{mr}$, we set $f_{er} = f_{mr} = f_r = 290$ MHz and then determine the values of ω_{pe}^2 and ω_{pm}^2 for the Lorentz models from the desired values of the real parts of $\varepsilon_2(\omega)$ and $\mu_2(\omega)$.

For both models, moderate losses are considered with $\Gamma_e = \Gamma_m = 10^{-3}\omega_0$. This implies that a DNG shell is considered that is dispersive and contains a small, but not negligible loss. The effects of dispersion and losses on the performance of the electrically small resonant dipolar DPS-DNG structure examined in Section 4.3.2 are shown in Figure 4.10.

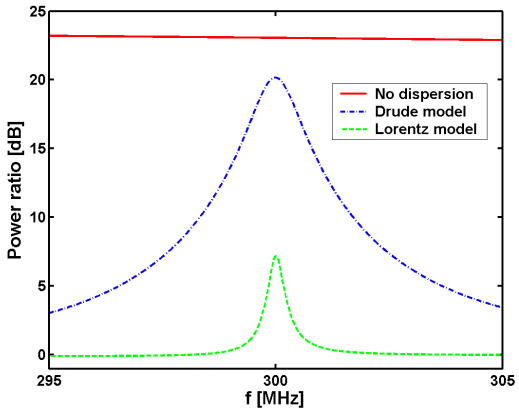

Figure 4.10: *Power ratio as a function of frequency for the dipolar DPS-DNG structure in which the DNG shell is described by a non-dispersive model, and by Drude and Lorentz dispersion models. The ELS is in region 1 at* $\rho_s = 5.99$ *mm.*

In general, the PR is almost constant in the depicted frequency range when the DNG shell is non-dispersive, and, thus, these structures are rather broadband. This broadband behaviour is expected since the electrical size of the dipolar DPS-DNG structure is small for the range of frequencies considered in Figure 4.10[4.8], and thus, the resonance condition in (4.7) is independent of the frequency. On the other hand, the results clearly show that dispersion in the DNG shell narrows considerably the bandwidth of the resonance, which is, nonetheless, still attained at $f_0 = 300$ MHz. The Lorentz model implies a much narrower bandwidth than the Drude model. This narrower bandwidth in the Lorentz model case is obtained since this model is resonant, and thus its material parameters exhibit rapid variations near $f_0 = 300$ MHz. Moreover, the maximum PR obtained with either lossy dispersion model is lower than in the non-dispersive case, with the decrease in the amplitude of the PR being most profound for the Lorentz model (the PR values evaluated at 300 MHz are PR $\simeq$ 23 dB for the non-dispersive case, PR $\simeq$ 20 dB for the Drude model, and PR $=$ 7 dB for the Lorentz model). This behaviour is expected since the loss is more severe in the Lorentz model (even though the same collision frequencies were used as in the Drude model) because the frequency of operation is near the resonance frequency of the material parameters. At 300 MHz $\varepsilon_2 = \varepsilon_0(-1-j0.002)$, $\mu_2 = \mu_0(-4-j0.005)$ (Drude model), while $\varepsilon_2 = \varepsilon_0(-1-j0.03)$, $\mu_2 = \mu_0(-4-j0.07)$ (Lorentz model). Thus, the electric and magnetic loss tangents, $\tan\delta_e = \varepsilon_2''/|\varepsilon_2'|$ and $\tan\delta_m = \mu_2''/|\mu_2'|$ are, respectively, $\tan\delta_e = 0.002$ and $\tan\delta_m = 0.00125$ for Drude model, and $\tan\delta_e = 0.03$ and $\tan\delta_m = 0.0175$ for Lorentz model. If the collision frequencies were $\Gamma_e = \Gamma_m = 0$ for both dispersion models, the maximum value of the PR at 300 MHz attained with both models is the same as the value for the lossless and non-dispersive case. This is because no loss is then present in the dispersion models, see MI, which also includes additional investigations of the effects of loss in the DNG material.

Similar results, not included here, have been obtained for the dipolar DPS-DNG structures for which the ELS is located in regions 2 and 3.

4.4 Designs of larger size

The present section considers designs of larger electrical size. The discussion is initiated with the case of concentric cylinders, for which the analytical solution is found in Section 4.2, and is subsequently continued to the case of a single DNG or DPS cylinder.

[4.8]The particular frequency range $f \in [295 - 300]$ MHz was selected in order to contrast more clearly the non-dispersive case from the two dispersive cases around the frequency of operation $f_0 = 300$ MHz, at which the resonance of interest to this chapter is expected.

4.4.1 Concentric cylinders

In the course of the brief discussion of the wavelength and sub-wavelength sized NRs in Section 4.3, it was noted that sufficiently large DPS-based structures can lead to the NRs if the size of the object is comparable to multiples of the wavelength [37], [48]. To illustrate this point, it is sufficient to investigate DPS-DPS structures having the same material parameters as in Section 4.3.2, and compare them with the corresponding DPS-DNG structure, likewise having the material parameters as given in Section 4.3.2. The frequency of operation is $f_0 = 300$ MHz, and the ELS is located at the origin, i.e., $\rho_s = 0$. It is recalled that in the electrically small cases treated in Section 4.3, this particular ELS location does not yield a resonant behaviour since only the monopolar mode can be excited. The inner radius of region 2 is fixed at $\rho_1 = 10$ mm, and the outer one varies in the interval $\rho_2 \in [10, 300]$ mm. Figure 4.11 shows the behaviour of the PR as a function of the outer shell radius ρ_2.

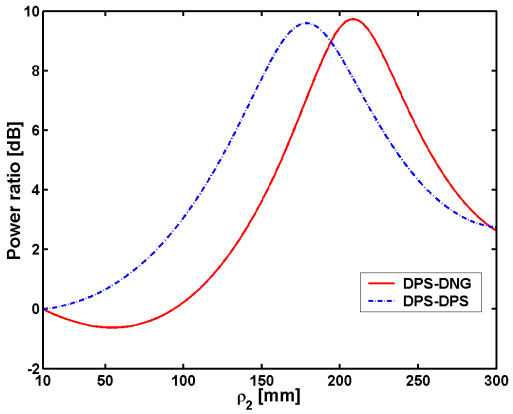

Figure 4.11: *Power ratio as a function of the outer shell radius ρ_2 for the DPS-DNG and DPS-DPS cylindrical structures for large values of ρ_2 allowing wavelength sized NRs.*

For the DPS-DPS structure the resonance is attained at $\rho_2 = 178.49$ mm and for the DPS-DNG structure at $\rho_2 = 208.36$ mm. The maximum value is PR $= 9.59$ dB for the DPS-DPS structure, and for the DPS-DNG structure it is PR $= 9.72$ dB. Thus, when the size of the cylinders is in the wavelength sized NR regime, the DPS-DNG structure does not offer any advantage over the corresponding DPS-DPS structure. This conclusion is in line with the results given in [46] and [47]. This behaviour holds in fact for all locations of the ELS, and is in sharp contrast to the electrically small DPS-DNG structures treated in Section 4.3, where the sub-wavelength sized NRs, caused by pairing of ordinary DPS materials with DNG materials, led to very large PR values.

The wavelength sized NR phenomenon is familiar from, e.g., wave guide and cavity theory. The natural mode of a cylindrical wave guide or a cavity will occur if the structure has certain dimensions [117]. In particular, for TM polarization in an open circular dielectric resonator of radius a and a wave number k inside the dielectric, the first resonance occurs at $ka = 1.84$ [117, p. 472]. In the present case, the resonances occur at $k_2\rho_2 = 2.24$ for the DPS-DPS structure, and for the DPS-DNG structure at $k_2\rho_2 = 2.62$.

4.4.2 Single cylinder

The configuration of a single DNG or a DPS cylinder having its dimensions comparable to the wavelength is next considered. This configuration follows at once from that of the concentric cylinders depicted in Figure 4.1 by e.g., replacing region 2 with the free space. In the notation of Section 4.2, the cylinder under examination is thus a core cylinder of radius ρ_1 imbedded in free space, see Figure 4.1. To conform with the notation of MII, where the complete analytical as well as numerical treatment of the present problem is performed, the cylinder radius is $\rho_1 \equiv a$ and the ELS is assumed to be external to the cylinder and located at a distance b from the cylinder. The permittivity and permeability of the cylinder are real scalars denoted, respectively, by $\varepsilon_c = \varepsilon_r\varepsilon_0$ and $\mu_c = \mu_r\mu_0$, with ε_r and μ_r being, respectively, its relative permittivity and permeability. Moreover, the wave number inside the cylinder is denoted by $k_c = \omega\sqrt{\varepsilon_c\mu_c}$, and is chosen to be positive in a DPS material, and negative in a DNG material.

The solution to the present problem is obtained by specializing the solution to the concentric cylinder case found in Section 4.2, and the necessary steps of this specialization, as well as the final results, are found in MII and Appendix D. Therefore, only the numerical results which elucidate the properties of the near field are included below. With reference to MII, it is found that the near-field properties are also good representatives of the far-field behaviours of the investigated cylinder configurations, of which a detailed account is found in MII. Moreover, the near field is described here since it reveal some interesting focusing effects of the ELS field for the DNG cylinder configurations, although none of these configurations are found to be suitable in, e.g., potential antenna designs. This is in contrast to the DPS cylinder configurations which, as found below, in many instances provide a directive pattern with a distinct main lobe.

In the numerical calculations, which are performed for different geometrical and material parameters, the coordinate system is aligned such that the ELS is placed along the positive x-axis at a distance b from the cylinder. Moreover, for easy reference, a cylinder having the material parameters $(\varepsilon_c, \mu_c) = (\varepsilon_r\varepsilon_0, \mu_r\mu_0)$ is referred to as a "$\varepsilon_r\varepsilon_0\mu_r\mu_0$" DPS cylinder for $\varepsilon_r > 0$, $\mu_r > 0$, and as a "$|\varepsilon_r|\varepsilon_0|\mu_r|\mu_0$" DNG cylinder for $\varepsilon_r < 0$, $\mu_r < 0$ (that is, a "$2\varepsilon_0 1\mu_0$" DPS cylinder is a cylinder for which $\varepsilon_r = 2$ and $\mu_r = 1$, while a "$2\varepsilon_0 1\mu_0$" DNG cylinder is a cylinder for which $\varepsilon_r = -2$ and $\mu_r = -1$). As in the case of concentric cylinders, the near-field investigations are performed by calculating the quantity $20\log_{10}|\vec{E}(\rho,\phi)/1\ \text{[V/m]}|$ where $\vec{E}$ is the total field, inside as well as outside the cylinder. This quantity is shown in a circular region of radius $3(a+b)$ centered at the cylinder axis (z-axis). In order to facilitate the comparison of the results, the dynamic range is kept constant throughout the forthcoming figures.

The effect of the DNG material is particularly notable in the case of a "$1\varepsilon_0 1\mu_0$" cylinder. A few examples of such results are shown in Figures 4.12 and 4.13, which depict the near field for the cylinders having radii $2\lambda_0$ and $4\lambda_0$, as well as $8\lambda_0$, respectively. In all cases, the ELS is located at a fixed distance $b = 1\lambda_0$ from the cylinder.

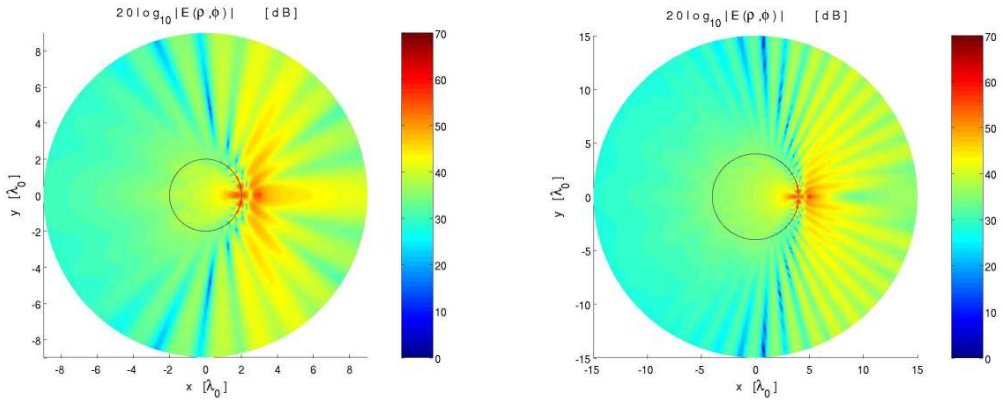

(a) (b)

Figure 4.12: *Electric near field of the "$1\varepsilon_0 1\mu_0$" DNG cylinders having radii $a = 2\lambda_0$* (a) *and $a = 4\lambda_0$* (b). *The ELS is at a distance $b = 1\lambda_0$ from the cylinder.*

While the "$1\varepsilon_0 1\mu_0$" DPS cylinder, not shown inhere, is clearly equivalent to the free-space case without any scattering of the ELS field which is thus omnidirectional, the "$1\varepsilon_0 1\mu_0$" DNG cylinder has a significant effect on the field of the ELS by creating a field pattern with several lobes and a shadow region (the field attains much lower values for $\phi \in [125^o - 225^o]$ than for $\phi \in [0^o - 125^o] \bigcup [225^o - 360^o]$). The variation of the field pattern is more pronounced for the cylinders having larger radius. In all cases, there appears to be a formation of a point inside the cylinders at which the field assumes very high values. A similar effect was observed in [44] for the case of plane wave incidence. This formation, though less clear for the cylinder of radius $2\lambda_0$ than for the cylinders of larger radius, suggests that some focusing of the ELS field takes place inside the cylinders. Contrary to the well-known case of the lossless DNG slab configuration with the same material parameters, see, e.g., [4] and [11], no high field values are observed in the region to the left of the cylinders along the negative x-axis. Moreover, the point inside the cylinders at which the field attains a high value does not represent an exact image of the ELS since

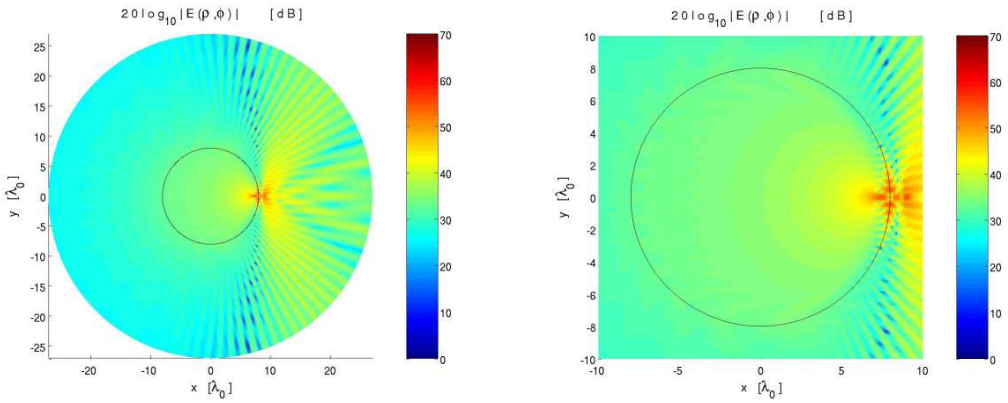

(a) (b)

Figure 4.13: (a) *Electric near field of the "*$1\epsilon_0 1\mu_0$*" DNG cylinder having radius* $a = 8\lambda_0$ *and the ELS at a distance* $b = 1\lambda_0$ *from the cylinder.* (b) *Selected region of* (a) *showing a closer look of the high field value formation.*

the cylinder surface is curved and its aperture is finite. In addition to the high field value formation inside the cylinders, the field also attains rather high values along the part of the cylinder surface which is close to the ELS, see, e.g., Figure 4.13(b).

In order to assess the influence of the material parameters on the near-field behaviour of DNG, as well as DPS cylinders, Figure 4.14 shows the near field for "$2\varepsilon_0 1\mu_0$" DPS and DNG cylinders having the radius $a = 2\lambda_0$ and the ELS being located at $b = 1\lambda_0$.

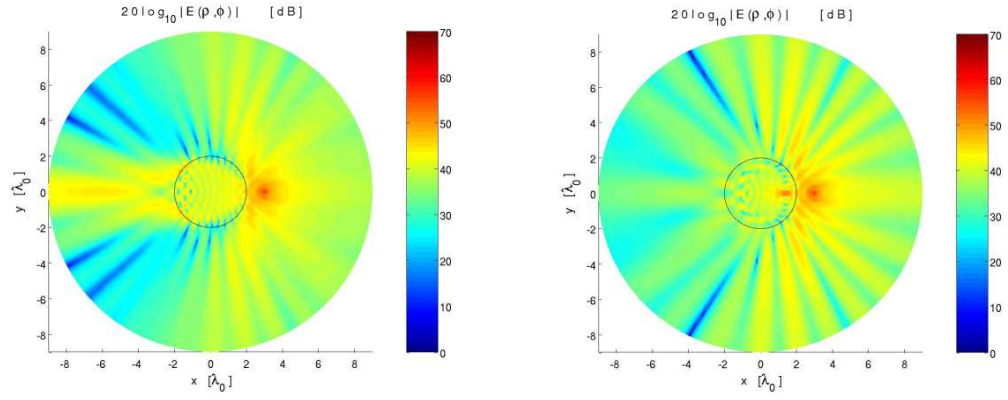

(a) (b)

Figure 4.14: *Electric near field of the "*$2\varepsilon_0 1\mu_0$*" DPS* (a) *and DNG* (b) *cylinders having radius* $a = 2\lambda_0$*. The ELS is at a distance* $b = 1\lambda_0$ *from the cylinder.*

For the DPS cylinder a clear beam formation along the negative x-axis is observed, i.e., the DPS cylinder configuration may be suitable in, e.g., the potential design of a lens-like antenna (as noted in MII, this beam is broadened by increasing the cylinder radius). Some field variation is observed in the half-space in which the ELS is located, and no shadow region is formed. For the DNG cylinder configuration, the field pattern exhibits rather large azimuthal variation, (as noted in MII, these variations are more pronounced for the cylinders of larger radius), and no distinct main lobe, as for the corresponding DPS cylinder, exists[4.9]. The field outside the DNG cylinders is mainly confined to the half-space in which the ELS is located. Furthermore, the field variation is more pronounced for the DNG than for the DPS cylinder in the sense that much deeper nulls are observed in the pattern. Regarding the field transmitted into the

[4.9] Although the directivity properties of single DNG cylinders investigated in this work, see MII, are rather poor, these cylinders may lead to improvements of directivity when used as coatings for perfectly electrically conducting cylinders [53].

DNG cylinders, a clear formation of a high field value is observed. This region of high field values is more pronounced than with the previously shown results for the "$1\varepsilon_0 1\mu_0$" DNG cylinders, suggesting that some focusing of the ELS field is taking place.

The field variation increases notably when the distance between the ELS and the cylinder is increased to, e.g., $b = 2\lambda_0$. For the case of the DNG cylinders, the formation of a high field value inside the cylinders is not well defined as with the $1\lambda_0$ distance considered here, see MII for further details.

It is interesting to note that the numerical results based on the eigenfunction solution technique presented inhere can be interpreted by means of a geometrical optics (GO) ray-tracing technique. Below, only the main points related to the use of this technique are emphasized, while the complete treatment and explanation of the procedure is found in Appendix D, Section D.3.2.

A number of incident rays launched from the ELS and forming angles $\alpha = \pm\,[0,\ 10,\ 20,\ 30,\ 35]^o$ with the x-axis are traced to their intersection points on the surface of the cylinder. At these points, Snell's law of refraction, see e.g., Chapter 3, is then used to determine the directions of the corresponding refracted rays into the cylinder.

To clarify these descriptions, the GO ray-tracing has been performed for the configuration whose near fields were shown in Figure 4.14, and the result is shown in Figure 4.15.

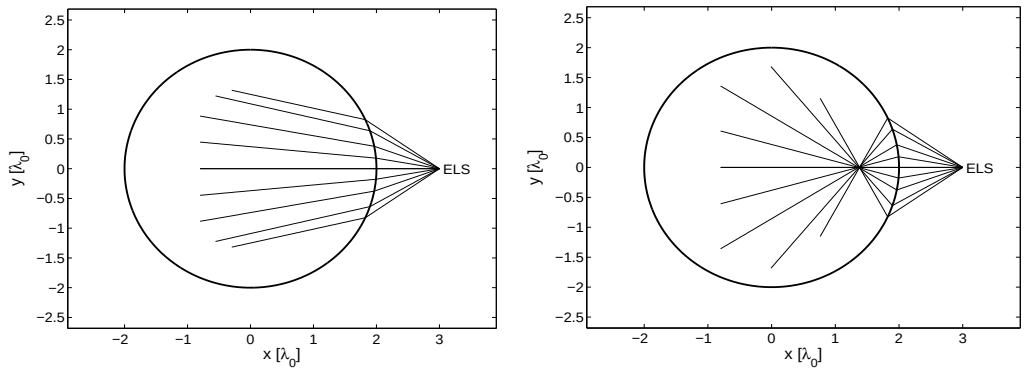

(a) (b)

Figure 4.15: *GO ray-tracing results for "$2\epsilon_0 1\mu_0$" DPS* (a) *and DNG* (b) *cylinders having radius $a = 2\lambda_0$. The ELS is at a distance $b = 1\lambda_0$ from the cylinder. The corresponding eigenfunction solution is shown in Figure 4.14.*

Comparing the results shown in Figures 4.14 and 4.15, it is found that the GO ray-tracing results support the numerical results very well. In particular, the presence of a localized high field value for the DNG cylinder is reproduced.

The GO ray-tracing analysis was likewise performed for other configurations of which the near-fields are depicted in MII . Although these are not included here, it was shown that for all cases, the GO ray-tracing results supported the numerical results very well. The plane wave incidence case [44] has reported a similar GO investigation.

In closing this section it is important to note that DPS and DNG cylinders with various other material parameters have been investigated. Some of these results are found in MII while others have not been included in this work, since they all give rise to observations similar to those made in this section.

4.5 Summary

A canonical configuration consisting of a pair of concentric MTM cylinders excited by an arbitrarily located ELS was investigated in this chapter. The emphasis was put on the use of DNG materials in these canonical configurations, of which the performance was compared to the conventional DPS-based configurations. Their near- and far-field properties were analysed through an investigation of the spatial distribution of the near field, the total radiated power, directivity, and total scattering cross section. The solution derived for the case of concentric cylinders was furthermore applied in the investigation of single

DPS and DNG cylinders. Structures of electrically small as well as large sizes were examined, as was the influence of loss and dispersion present in any MTM.

It was shown that electrically small MTM-based structures can be designed to possess resonances in their radiation and scattering characteristics, whereas this is not the case for the corresponding DPS-based structures. The total radiated power of the ELS excited dipolar DNG-based structures comprised of a DNG shell, i.e., a shell in which the dipolar mode is the dominant mode, was found to be of the order of 200 times larger than the power radiated by the ELS in free space. Moreover, its total scattering cross section was significantly enlarged in comparison to that of the corresponding DPS-based structure comprised of a DPS shell, and the dipolar DNG-based structure was found to exhibit characteristics generally attributed to larger scatterers. The significant enhancements of e.g., the total radiated power, which are associated with the sub-wavelength natural resonances, require off-axis ELS locations and are found to be largest when the ELS is located near the interfaces of the DNG layers.

The feasibility of controlling the directivity of the electrically small dipolar DNG-based structures, as the location of the ELS varies, was demonstrated. This was explained through the interesting fact that, although the dipolar DNG-based structure was designed to be excited in the dominant dipolar mode, other modes, in this case, the monopolar mode, could dominate the interaction process when the ELS is located at specific locations.

As to the dispersion present in the DNG material, it was clearly demonstrated that it narrows the resonances significantly, while the losses decreases the peak values of those resonances.

Moreover, when the size of the DNG-based structure is large enough for the wavelength-sized natural resonances to occur, it was shown that both the DPS-based and DNG-based structures possess resonances in the total radiated power, although they are smaller in amplitude than those obtained for electrically small dipolar DNG-based structures.

Further investigations of electrically large structures such as single DPS and DNG cylinders revealed interesting focusing effects of the ELS field in those cases where the ELS is located near-by the surface of the DNG cylinder. However, none of the investigated single DNG cylinder configurations were found to provide a directive pattern, this being in distinct contrast to the corresponding DPS cylinders, for which a main lobe could clearly be identified.

Although not included in this chapter, the so-called electrically small quadrupolar structures, as well as numerous other configurations of larger sizes, have been investigated in this work, see MI and MII.

CHAPTER 5

3D METAMATERIAL-BASED CANONICAL CONFIGURATIONS

The present chapter investigates the radiation from three-dimensional (3D) metamaterial (MTM)-based canonical structures consisting of concentric spheres excited by an arbitrarily located and oriented electric Hertizan dipole (EHD). The analytical solution is first derived, and then the numerical investigation of the various near- and far-field quantities is performed. The results obtained for the MTM-based structures are compared to those for the corresponding structures which consist of conventional double-positive (DPS) materials. In contrast to the two-dimensional (2D) concentric cylinder cases investigated in Chapter 4, only electrically small 3D concentric spherical structures made of lossless materials are investigated numerically in this chapter. This is due to the fact that the influence of loss and dispersion, as well as the increased electrical size of the structures, basically has the same effects as for the corresponding 2D structures.

This chapter is mainly a summary of the results presented in Manuscript III (MIII), which is found in Appendix C, although some of the results presented in the following are not found in MIII. In MIII, the influence of loss, dispersion, and the electrical size of the concentric spheres is also discussed. The analytical details not contained in either the present chapter or MIII are given in Appendix E.

5.1 Introduction

As with the cylindrical structures studied in Chapter 4, structures of spherical shape formed completely or partly by MTMs have been extensively studied [25], [36], [48], [51], [52]. The concept of the perfect planar [11] and cylindrical [24] lenses has been continued to also include perfect spherical lenses [25]. Moreover, plane wave scattering properties of MTM spheres and spherical shells were studied in [36], [48], where it was demonstrated that, similarly to the cylindrical geometry, such electrically small spherical MTM-based structures can be resonant and e.g., lead to significantly increased scattering cross sections. These sub-wavelength resonance features of such structures were also discussed in [51], while [52] performed an interesting analysis of the extinction properties of double-negative (DNG) spheres. In addition, antenna systems capable of increasing the total radiated power [56], [57], as well as those which offer the possibility of efficient electrically small realistic designs [58], [61], were examined. In particular, the resonant nature of sub-wavelength MTM-based spherical structures demonstrated in [36], [48] for the plane wave incidence case, was exploited in [56] to increase the total radiated power for a canonical antenna configuration consisting of an electrically small electric dipole surrounded by a concentric DNG spherical shell, see also Chapter 2.

5.2 Configuration and analytical solution

The configuration of interest is depicted in Figure 5.1. A sphere (region 1) of radius r_1 is covered concentrically with a spherical shell of radius r_2 (region 2). The concentric spheres are illuminated by an EHD possessing dipole moment $\vec{p}_s = \hat{p}_s\, p_s$ with the orientation $\hat{p}_s$ and complex magnitude p_s. The EHD constitutes a model of an electrically short electric dipole with p_s being the product of the current and length of that dipole. The EHD can be located in any of the three regions and can possess an arbitrary orientation and strength of the dipole moment.

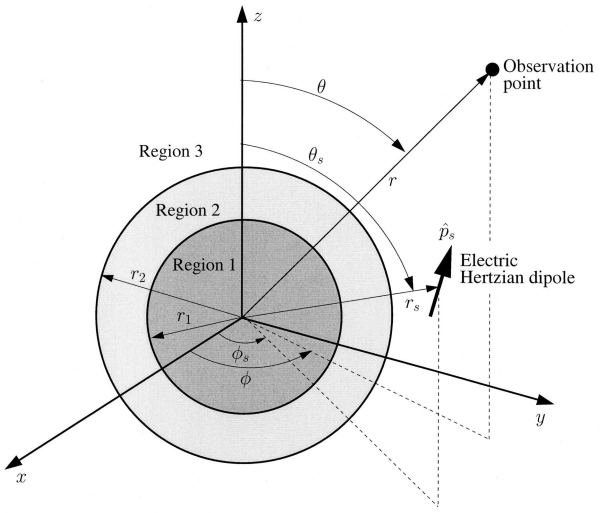

Figure 5.1: *The configuration of the EHD-excited concentric pair of spheres.*

Region i, with $i = 1$ and 2, is characterized by a permittivity and a permeability, denoted by $\varepsilon_i = \varepsilon_i' - j\varepsilon_i''$ and $\mu_i = \mu_i' - j\mu_i''$, respectively, and a wave number $k_i = \omega\sqrt{\varepsilon_i \mu_i}$, where the branch of the square root is chosen such that $\mathcal{I}m\{k_i\} \leq 0$. Each of these regions can be composed of simple DPS materials and/or MTMs. The exterior region (region 3) is assumed to be free space with the permittivity ε_0 and permeability μ_0 and, thus, the wave number $k_0 = \omega\sqrt{\varepsilon_0 \mu_0}$ and intrinsic impedance $\eta_0 = \sqrt{\mu_0/\varepsilon_0}$. A spherical coordinate system (r, θ, ϕ) and the associated Cartesian coordinate system (x, y, z) are introduced such that the origins of both coincide with the common center of the spheres. The coordinates of the observation point and the EHD are (r, θ, ϕ) and (r_s, θ_s, ϕ_s), respectively.

Following the approach of [118, Ch. 8], the electric field generated by the EHD in an infinite medium characterized by ε_{EHD}, μ_{EHD}, and k_{EHD}, can be expressed as an expansion of spherical transverse magnetic (TM) and transverse electric (TE) waves

$$\vec{E}_{\text{EHD}} = \sum_{n=1}^{N_{max}} \sum_{m=-n}^{m=+n} \left[\frac{1}{j\omega\varepsilon_{\text{EHD}}\mu_{\text{EHD}}} \, a_{nm}^{(c)} \, \vec{N}_{nm}^{(\text{TM}),(c)} - \frac{1}{\varepsilon_{\text{EHD}}} \, b_{nm}^{(c)} \, \vec{M}_{nm}^{(\text{TE}),(c)} \right] , \tag{5.1}$$

where the familiar spherical vector wave functions (SVWFs) are

$$\vec{M}_{nm}^{(\text{TE}),(c)}(r, \theta, \phi) = \varepsilon_{\text{EHD}} \, w_n^{(c)}(k_{\text{EHD}} r) \, e^{jm\phi} \left[\frac{jm}{\sin\theta} \, P_n^{|m|}(\cos\theta) \, \hat{\theta} - \frac{d}{d\theta} P_n^{|m|}(\cos\theta) \, \hat{\phi} \right] , \tag{5.2}$$

$$\begin{aligned} \vec{N}_{nm}^{(\text{TM}),(c)}(r, \theta, \phi) = {} & \mu_{\text{EHD}} \, \frac{n(n+1)}{r} w_n^{(c)}(k_{\text{EHD}} r) \, P_n^{|m|}(\cos\theta) \, e^{jm\phi} \, \hat{r} \\ & + \mu_{\text{EHD}} \, \frac{1}{r} \, \frac{d}{dr} \left\{ r w_n^{(c)}(k_{\text{EHD}} r) \right\} \, \frac{d}{d\theta} P_n^{|m|}(\cos\theta) \, e^{jm\phi} \, \hat{\theta} \\ & + \mu_{\text{EHD}} \, \frac{1}{r} \, \frac{d}{dr} \left\{ r w_n^{(c)}(k_{\text{EHD}} r) \right\} \, \frac{jm}{\sin\theta} \, P_n^{|m|}(\cos\theta) \, e^{jm\phi} \, \hat{\phi} \, . \end{aligned} \tag{5.3}$$

The quantities $a_{nm}^{(c)}$ and $b_{nm}^{(c)}$ are the TM and TE expansion coefficients, respectively, of the EHD field,

and they can be expressed as[5.1]

$$a_{nm}^{(c)} = -jk_{\text{EHD}}\frac{p_s}{4\pi}\frac{1}{\mu_{\text{EHD}}}\frac{2n+1}{n(n+1)}\frac{(n-|m|)!}{(n+|m|)!}\left[\hat{p}_s \cdot \vec{N}_{n,-m}^{(\text{TM}),(5-c)}(r_s,\theta_s,\phi_s)\right] , \tag{5.4a}$$

$$b_{nm}^{(c)} = \frac{k_{\text{EHD}}^3}{\omega}\frac{p_s}{4\pi}\frac{1}{\varepsilon_{\text{EHD}}^2}\frac{2n+1}{n(n+1)}\frac{(n-|m|)!}{(n+|m|)!}\left[\hat{p}_s \cdot \vec{M}_{n,-m}^{(\text{TE}),(5-c)}(r_s,\theta_s,\phi_s)\right] . \tag{5.4b}$$

For $r < r_s$ c is equal to 1, and for $r > r_s$ c is equal to 4. The function $w_n^{(1)}(\cdot) = j_n(\cdot)$, where $j_n(\cdot)$ is the spherical Bessel function of order n, is chosen to represent the field for $r < r_s$ due to its non-singular behaviour at the origin, while the function $w_n^{(4)}(\cdot) = h_n^{(2)}(\cdot)$, where $h_n^{(2)}(\cdot)$ is the spherical Hankel function of second kind and order n, is chosen for $r > r_s$ because it represents an outward propagating wave complying with the radiation condition. Furthermore, $P_n^{|m|}(\cdot)$ is the associated Legendre function of the first kind of degree n and order $|m|$. The symbol N_{max} is the truncation limit in a practical numerical implementation of the infinite summation in the exact solution and is chosen in a manner that ensures convergence. Moreover, the subscript EHD $= 1$ or 2 when the EHD is in region 1 or 2, respectively, while EHD $= 0$ when the EHD is in region 3.

The unknown fields in each of the regions, i.e., the scattered field in the region containing the EHD and the total fields in the other regions, are likewise expanded in terms of the SVWFs. The resulting expansions read

$$\vec{E}_{ps} = \sum_{n=1}^{N_{max}}\sum_{m=-n}^{m=+n}\left[\frac{1}{j\omega\varepsilon_p\mu_p}\vec{X}_{p,nm} - \frac{1}{\varepsilon_p}\vec{Y}_{p,nm}\right] , \tag{5.5}$$

where $p = 1$ for region 1, in which case $\varepsilon_p = \varepsilon_1$, $\mu_p = \mu_1$, $\vec{X}_{1,nm} = A_{1,nm}\vec{N}_{nm}^{(\text{TM}),(1)}$ and $\vec{Y}_{1,nm} = B_{1,nm}\vec{M}_{nm}^{(\text{TE}),(1)}$, while $p = 2$ for region 2, in which case $\varepsilon_p = \varepsilon_2$, $\mu_p = \mu_2$, $\vec{X}_{2,nm} = A_{2,nm}\vec{N}_{nm}^{(\text{TM}),(1)} + A_{3,nm}\vec{N}_{nm}^{(\text{TM}),(2)}$ and $\vec{Y}_{2,nm} = B_{2,nm}\vec{M}_{nm}^{(\text{TE}),(1)} + B_{3,nm}\vec{M}_{nm}^{(\text{TE}),(2)}$, and finally, $p = 3$ for region 3, in which case $\varepsilon_p = \varepsilon_0$, $\mu_p = \mu_0$, $\vec{X}_{3,nm} = A_{4,nm}\vec{N}_{nm}^{(\text{TM}),(4)}$ and $\vec{Y}_{3,nm} = B_{4,nm}\vec{M}_{nm}^{(\text{TE}),(4)}$. In these expressions $A_{i,nm}$ and $B_{i,nm}$, with $i = 1,\ldots 4$, respectively, are the unknown expansion coefficients associated with the TM and TE parts of the unknown fields. The expression in (5.5) for region 2 contains the function $w_n^{(2)}(\cdot) = y_n(\cdot)$, where $y_n(\cdot)$ is the spherical Neumann function of order n. The expressions (5.1) and (5.5) represent multipole expansions of the fields, i.e., the $n = 1$ term (for which $m = -1, 0, 1$) is the dipolar mode, the $n = 2$ term (for which $m = -2, -1, 0, 1, 2$) is the quadrupolar mode, and similarly for other terms.

Enforcing the electromagnetic boundary conditions, i.e., requiring the continuity of the tangential components of the total electric and magnetic field (the latter being readily obtained from the Faraday's law, see also Appendix E) at the interfaces $r = r_1$ and $r = r_2$, it can be shown that the unknown expansion coefficients can be determined as

$$\vec{D}_{nm} = \left[\bar{\bar{S}}_n\right]^{-1}\vec{\Omega}_{nm} , \quad n = 1, 2, \ldots N_{max}, \quad \text{and} \quad m = -n, \ldots n \tag{5.6}$$

where $\vec{D}_{nm} = [A_{1,nm}, \ldots, A_{4,nm}, B_{1,nm}, \ldots, B_{4,nm}]$ is the vector containing the eight unknown expansion coefficients and $\vec{\Omega}_{nm} = [\Omega_{1,nm}, \ldots \Omega_{8,nm}]$ is the so-called excitation vector, which depends on the location of the EHD, and the matrix $\bar{\bar{S}}_n$ is an eight-by-eight matrix that depends on the values of the spherical waves at the two interfaces. The explicit form of $\bar{\bar{S}}_n$ and the excitation vector $\vec{\Omega}_{nm}$ for the EHD locations in the regions 1, 2, and 3, is given in MIII.

As explained in MIII, the first four elements of $\vec{\Omega}_{nm}$, i.e., $\Omega_{i,nm}$ with $i = 1,\ldots 4$, are, due to the form of the matrix $\bar{\bar{S}}_n$, only used in the determination of the TM coefficients $A_{i,nm}$, while the last four elements of $\vec{\Omega}_{nm}$, i.e., $\Omega_{i,nm}$ with $i = 5,\ldots 8$, are used only in the determination of the TE coefficients $B_{i,nm}$. This means that the two sets of coefficients are uncoupled. As a consequence, the system of equations in (5.6) can be divided for numerical convenience into two relations, each involving a four-by-four matrix. One is used to determine the $A_{i,nm}$ coefficients, and the other is used to determine the

[5.1] A complete derivation of $a_{nm}^{(c)}$ and $b_{nm}^{(c)}$ is given in Appendix E, Section E.1.3.

$B_{i,nm}$ coefficients, see Appendix E for more details. This fact will also be exploited later in Section 5.3, where the resonance conditions for these coefficients are obtained.

Aside from the spatial near-field distributions, the total radiated power (henceforth termed as the total power) and the directivity, are examined in the numerical investigations. As with the cylindrical geometry treated in Chapter 4, it is of interest to examine the ratio of the total power radiated by the EHD in the presence of the concentric spheres, P_t, to the power radiated by the EHD in free space, P_i. With reference to MIII, the PR is defined by[5.2].

$$\text{PR} = \frac{P_t}{P_i} \,, \tag{5.7}$$

where

$$P_t = \frac{2\pi}{\omega k_0} \sum_{n=1}^{N_{max}} \sum_{m=-n}^{n} \frac{n(n+1)}{2n+1} \frac{(n+|m|)!}{(n-|m|)!} \left[\frac{|\alpha_{nm}|^2}{\varepsilon_0} + \frac{|\beta_{nm}|^2}{\mu_0} \right] \,, \tag{5.8}$$

and

$$P_i = \frac{\eta_0 \pi}{3} \left| \frac{p_s k_0}{2\pi} \right|^2 \,. \tag{5.9}$$

In (5.8), the quantity $\alpha_{nm} = A_{4,nm}$, $\beta_{nm} = B_{4,nm}$ if the EHD is in region 1 or 2, while $\alpha_{nm} = a_{nm}^{(4)} + A_{4,nm}$, $\beta_{nm} = b_{nm}^{(4)} + B_{4,nm}$ if the EHD is in region 3.

The directivity, $D(\theta, \phi)$, given by the ratio of the radiation intensity and the total average power per unit solid angle, can be expressed as

$$D(\phi) = \frac{2\pi}{\eta_0} \frac{|F_{t,\theta}(\theta,\phi)|^2 + |F_{t,\phi}(\theta,\phi)|^2}{P_t} \,, \tag{5.10}$$

where P_t is the total power given by (5.8), while $F_{t,\theta}(\theta,\phi)$ and $F_{t,\phi}(\theta,\phi)$ are the θ- and ϕ- components of the total radiation vector $\vec{F}_t(\theta,\phi)$, which is related to the total electric far field $\vec{E}_t^f$ as $\vec{E}_t^f(r,\theta,\phi) = \vec{F}_t(\theta,\phi)\ \exp(-jk_0)/r$, see Appendix E.

5.3 Resonance condition

As with the electrically small cylindrical structures considered in Chapter 4, it is of interest to investigate the potential of electrically small spherical structures to produce large PR values. Since the PR in (5.7) is proportional to the magnitudes of the expansion coefficients $A_{4,nm}$ and $B_{4,nm}$, large values of the PR are thus expected when $|A_{4,nm}|$ or $|B_{4,nm}|$ become large. With reference to Chapter 4, the peaks in these coefficients, i.e., the resonances, are due to the excitation of the natural modes. As noted there, these resonances can occur in objects made of DPS materials provided that their size is of the order of the operating wavelength. However, when the structure is made of e.g., certain arrangements of DPS and DNG materials, resonances may occur even for electrically small structures.

The method of determining the conditions for which $|A_{4,nm}|$ and $|B_{4,nm}|$ become large is identical to the one used for the 2D configurations in Chapter 4. Each of the coefficients $A_{4,nm}$ and $B_{4,nm}$ are inversely proportional to a given determinant, see MIII and Appendix E, and as shown there, they exhibit maxima when the magnitude of these determinants attain minima. With the assumption of lossless materials in regions 1 and 2, as well as with the assumption that the products $|k_1|r_1$, $|k_2|r_1$, $|k_2|r_2$, and $k_0 r_2$ are much smaller than unity, it can be shown that the TM coefficients $A_{4,nm}$ become resonant when the approximate condition

$$\frac{r_1}{r_2} \simeq \sqrt[2n+1]{\frac{[(n+1)\varepsilon_0 + n\varepsilon_2][(n+1)\varepsilon_2 + n\varepsilon_1]}{n(n+1)(\varepsilon_2 - \varepsilon_0)(\varepsilon_2 - \varepsilon_1)}} \,, \tag{5.11a}$$

[5.2] As for the cylindrical structures treated in Chapter 4, it is understood that the PR figure, inhere related to the system consisting of EHD-excited concentric spheres is equivalent to the radiation resistance, $R_{t,3\text{D}}$, of that system normalized by the radiation resistance, $R_{i,3\text{D}}$, of the EHD alone in free space. Since $P_t = I_e^2 R_{t,3\text{D}}/2$ and $P_i = I_e^2 R_{i,3\text{D}}/2$, see e.g., [113, p. 82], it is easily deduced that $\text{PR} = R_{t,3\text{D}}/R_{i,3\text{D}}$.

is met, while the TE coefficients $B_{i,nm}$ become resonant when the approximate condition

$$\frac{r_1}{r_2} \simeq \sqrt[2n+1]{\frac{[(n+1)\mu_0 + n\mu_2][(n+1)\mu_2 + n\mu_1]}{n(n+1)(\mu_2 - \mu_0)(\mu_2 - \mu_1)}}\,, \tag{5.11b}$$

is met[5.3]. The conditions (5.11a) and (5.11b) are used to determine, for a given set of material parameters and the mode number n, the approximate ratio of r_1 and r_2 that will yield a resonant, concentric pair of electrically small lossless spheres. As was the case with the resonance condition in the cylindrical case, the conditions (5.11a) and (5.11b) do not depend on how small either of the radii r_1 and r_2 are individually. In general, the same features characterize the conditions (5.11a) and (5.11b) as the resonance condition for the corresponding cylindrical structures. They are used to define approximately a given resonance structure, they are independent of the frequency as long as the chosen frequencies implies electrically small sizes, and they can be satisfied if at least one of the parameters, ε_1 or ε_2 for (5.11a), and μ_1 or μ_2 for (5.11b), is negative, see, e.g., [1] and [48] (in [116] it has also been pointed out that for (5.11a) with $n = 1$, the permittivity of regions 1 and 2 must be of opposite sign to fulfill the so-obtained condition). This also means, as mentioned in the beginning of this section, that large values of the PR may result if either $A_{4,nm}$ or $B_{4,nm}$, and not necessarily both, exhibit a resonance. In that case, an epsilon-negative (ENG) or a mu-negative (MNG) material, respectively, is needed in at least one of the regions 1 or 2. On the other hand, the simultaneous fulfillment of (5.11a) and (5.11b) requires either that at least one of the regions, 1 or 2, is a DNG material, or that an ENG-MNG or MNG-ENG structure is used. A resonance for the n'th mode in both the $A_{4,nm}$ and $B_{4,nm}$ coefficients requires the permittivities and permeabilities of regions 1 and 2 to be selected to ensure the same radii ratio for the same mode number n.

5.4 Numerical results

The numerical results for certain electrically small DNG-based structures are discussed and related to those obtained for the corresponding DPS-based structures.

5.4.1 Resonant configurations - definition

Two different structures, namely the dipolar and quadrupolar structures, to be defined below, are chosen to illustrate the results of interest, and their electrical and geometrical parameters are summarized in Table 5.1. Throughout the following discussion, the frequency of operation is $f_0 = 300$ MHz, and thus the free-space wavelength is $\lambda_0 = 1$ m.

Structure	ε_1	μ_1	ε_2	μ_2	r_1 [mm]	r_2 [mm]
Dipolar	ε_0	μ_0	$\pm 3\varepsilon_0$	$\pm 3\mu_0$	10	18.57
Quadrupolar	ε_0	μ_0	$\pm 3\varepsilon_0$	$\pm 3\mu_0$	10	13.55

Table 5.1: *Material and approximate geometrical parameters for the electrically small resonant dipolar and quadrupolar configurations. Positive values of the material parameters indicate a DPS material while negative values indicate a DNG material.*

Region 1 is assumed to be free space, while region 2 is taken to be a DNG or a DPS material. Region 3 is, as noted before, free space. The inner radius of region 2 is set to $r_1 = 10$ mm, and the conditions (5.11a) and (5.11b) are used for this inner radius and the chosen material parameters to yield $r_2 = 18.57$ mm for $n = 1$ and $r_2 = 13.55$ mm for $n = 2$, which are the outer radii at which a resonance and, thus, an enhancement of the total power is expected[5.4]. The structures in which the $n = 1$ mode is excited as

[5.3] The complete derivation of (5.11a) and (5.11b) is given in Appendix E, Section E.4.

[5.4] As for the results predicted by the resonance condition for cylindrical structures, see Chapter 4, the values of r_2 given in Table 5.1 are approximate. However, the exact solution is used in the following to determine the exact value of this radius, which is subsequently used in the numerical analysis of various figures of merit. In this sense, the approximate value of r_2 basically serves as a guide for the numerical determination of the exact value.

the dominant one are referred to as the dipolar structures, while those that excite the dominant $n = 2$ mode are referred to as the quadrupolar structures. It is interesting to observe from (5.11a) and (5.11b) as well as from Table 5.1, that a considerably thinner structure is needed to excite the quadrupolar mode than the dipolar one for fixed material parameters. Since the largest dimension involved in the structure corresponds to $2r_2 \simeq 37$ mm $\simeq \lambda_0/27$ for the dipolar structure, and $2r_2 \simeq 27$ mm $\simeq \lambda_0/37$ for the quadrupolar structure, the designs are indeed electrically small for this choice of the frequency of operation.

The EHD is taken to be z-oriented, i.e., $\hat{p}_s = \hat{z}$, and to be located on the positive x- axis, i.e., with the coordinates $(r_s,\ \theta_s = 90^o,\ \phi_s = 0^o)$. The magnitude of the dipole moment is $p_s = 0.01$ Am. Thus, the structures under examination are a DNG or a DPS spherical shell in the presence of a z-oriented EHD that is located at an arbitrary distance on the positive x-axis.

5.4.2 Dipolar structures

5.4.2.1 Total power - power ratio

Figure 5.2(a) shows the PR as a function of the outer shell radius r_2 for the dipolar DPS-DNG and DPS-DPS structures when the EHD is in region 1 at $r_s = 5$ mm. As can be seen in the figure, a resonance peak of value PR $\simeq 63$ dB, or PR $\simeq 1.99 \times 10^6$, occurs for the DPS-DNG structure at $r_2 = 18.69$ mm, which is very close to the approximate value of 18.57 mm obtained from (5.11a) and (5.11b). In contrast, no resonance is found for the corresponding DPS-DPS structure where the PR is somewhat below 0 dB for the considered values of r_2. These results clearly show the advantage of the electrically small dipolar DPS-DNG structure over the corresponding DPS-DPS one. Similar results, not included here, have been obtained for the same structures when the EHD is located in regions 2 and 3. The peak at $r_2 = 18.69$ mm for the DPS-DNG structure is rather broad for this lossless and non-dispersive case. Large PRs are obtained for a range of r_2 values, e.g., PR > 30 dB for $r_2 \in [18, 19.5]$ mm. Moreover, the peak value of the PR as well as the value of r_2 for which the peak PR is attained for the dipolar DPS-DNG structure agree very well with the corresponding peak value of the PR for the same radius reported in [56], [57], but for the EHD located at the center of the spheres[5.5].

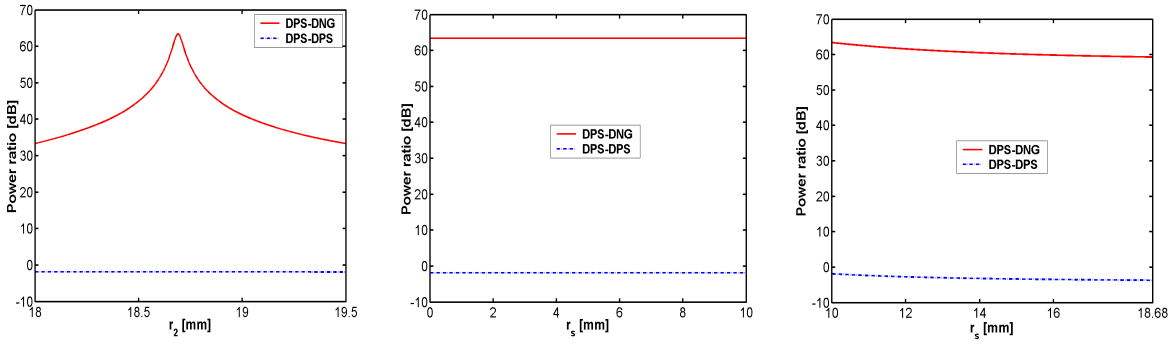

Figure 5.2: *Power ratio as a function of the outer shell radius r_2 when the EHD is in region 1 at $r_s = 5$ mm (a), and as a function of the EHD location r_s when the EHD is in region 1 (b) and 2 (c) for the dipolar DPS-DNG and DPS-DPS structures.*

To investigate the effect of the EHD location on the enhancement of the total power, Figures 5.2(b) and (c), respectively show the PR as a function of the EHD location, r_s, when the EHD is located in regions 1 and 2 for the dipolar DPS-DNG and DPS-DPS structures with $r_1 = 10$ mm and $r_2 = 18.69$ mm. In both

[5.5]The works of [56], [57] showed that the present dipolar DPS-DNG structure having the EHD at the center of the spheres leads to a resonance in both the PR as well as the total scattering cross section of the structure for the same value of r_2. In the terminology introduced in these works, these so-called radiating and scattering configurations were found to be reciprocal. Since the present findings with the arbitrarily located EHD are identical to those where the EHD is at the center of the spheres, it is thus expected that the present configurations also yield resonances in the PR as well as the total cross section for the same value of r_2. Therefore, quantities such as the total and differential scattering cross sections for the present structures are not considered in this work.

cases, the DPS-DPS structure gives no enhancement, while the corresponding DPS-DNG structure gives very large values of the PR. As the EHD moves through region 1, the PR is nearly constant and equal to PR $\simeq$ 63 dB. As the EHD traverses region 2, a very small decrease of the PR values is observed. Thus, the largest values of the PR for the dipolar DPS-DNG structure are found for the EHD locations near the origin, while they are slowly decreasing as the EHD is moved away from the origin. In other words, the values of the PR are not significantly affected as the location of the EHD is changed, this being in sharp contrast to the results for the corresponding cylindrical dipolar structures treated in Chapter 4.

As explained in Manuscript I (Appendix A) and MIII, the different behaviours of the spherical and cylindrical structures are caused by the fact that the latter allows the monopolar mode to dominate for certain ELS locations and, hence, no resonances can occur. In the spherical case, however, there is no monopolar mode regardless of the EHD location. The dipolar mode dominates the radiating process when it is excited and the corresponding enhancement is of the same order of magnitude for all of the considered EHD locations.

When the EHD is in region 3 similar phenomena as above occur for moderate distances between the DNG shell and the EHD. However, the PR slowly diminishes as the EHD is moved further away since the coupling to the dipolar mode diminishes, see MIII.

5.4.2.2 Near field

Next, the above PR enhancement results are confirmed with near-field investigations. For the near-field plots throughout this chapter, the quantity given by $20\log_{10}|E_{t,\theta}|$, where $E_{t,\theta}$ is the θ- component of the total electric field normalized by 1 V/m, is shown. The plane of observation is the xz-plane, and the field is shown in a circular region of radius 30 mm.

Figure 5.3(a) shows the near field of the EHD in free space, while Figure 5.3(b) shows the near field of the DPS-DPS structure (the curves representing the spherical surfaces of the DPS-DPS structure are also shown in Figure 5.3(b)). In both cases the EHD is located at $r_s = 5$ mm.

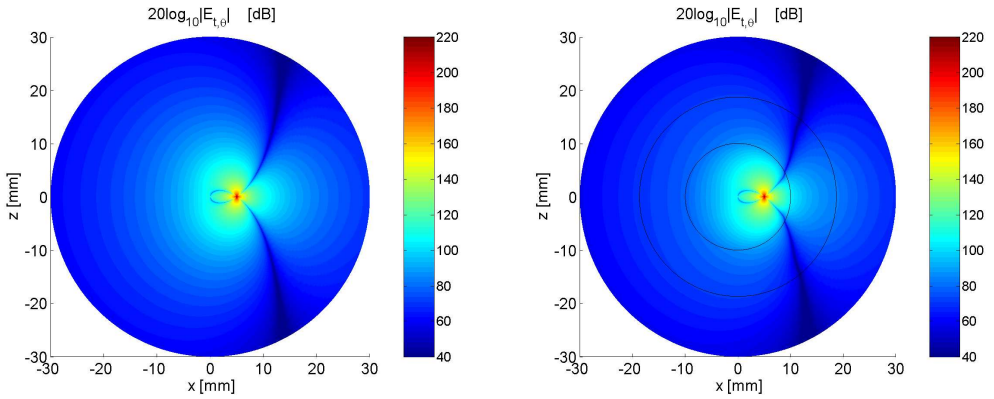

(a) (b)

Figure 5.3: *Electric near field of the EHD in free space (a), and of the DPS-DPS structure (b). In both cases the EHD is located at* $r_s = 5$ *mm.*

The near field of the EHD in free space would, of course, be of the dipolar form in a coordinate system centered at the EHD. However, as is seen in Figure 5.3(a), the near field is asymmetric due to the displacement of the EHD from the origin. The near field in Figure 5.3(b) is very similar to that in Figure 5.3(a), implying that the DPS-DPS structure does not affect the field of the EHD. Therefore, such a structure is not expected to lead to any enhancement of the total power, this being in line with the results given in Figure 5.2. Similar results, not included here, have been obtained for DPS-DPS structures with the EHD in any of the three regions.

The near field of the resonant dipolar DPS-DNG structure with $r_2 = 18.69$ mm is depicted in Figure 5.4(a). It is clear from Figures 5.3 and 5.4(a) that the DNG structure has significantly affected the near field of the EHD. More specifically, the near field in Figure 5.4(a) has a dipolar form. This result indicates that an EHD in the presence of the dipolar DPS-DNG structure resonantly excites a dominant dipolar mode, this being in line with the results predicted by the approximate resonance conditions (5.11a) and

(5.11b). The excitation of the resonant dipolar mode in this structure is responsible for the enhancement of the total power observed in Figure 5.2.

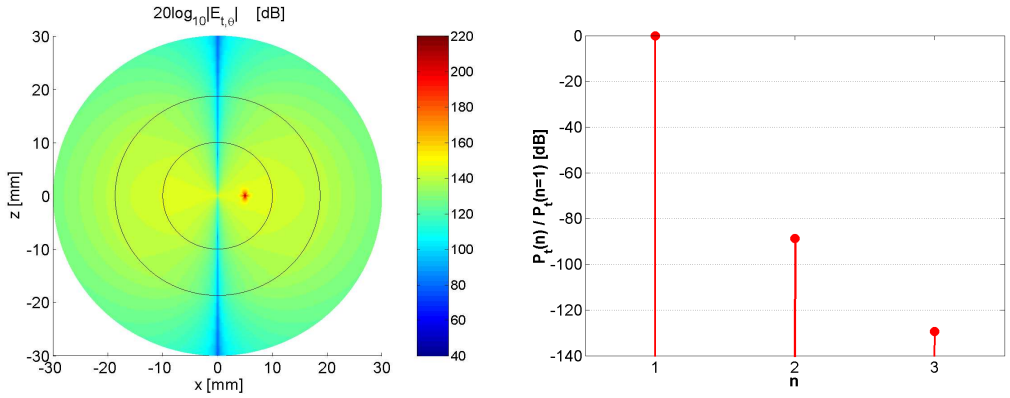

(a) (b)

Figure 5.4: *Electric near field of the dipolar DPS-DNG structure when the EHD is located at* $r_s = 5$ *mm (a), and the total power of the DPS-DNG structure contained in the* n*'th mode,* $n = 1, 2,$ *and* 3*, normalized by the total power in the dipolar mode (b). In (a), the plane of observation is the* xz*-plane, and the field is shown in a circular region of radius* 30 *mm.*

An additional insight into the resonance phenomenon can be obtained from Figure 5.4(b), where the total power spectrum of the n'th mode for this DPS-DNG structure is found. Specifically, the total power in the n'th mode, $n = 1, 2,$ and 3, normalized by the total power in the dipolar mode is depicted. As observed, the vast majority of the total power is contained in the dipolar mode, while only a negligible amount is contained in the next two higher order modes. In particular, $P_t(n = 2)$ and $P_t(n = 3)$ are more than 80 dB below the total power in the dipolar mode, and essentially no power is contained in the $n > 3$ modes.

To parallel the present discussion with that of the corresponding cylindrical dipolar DPS-DNG structures treated in Chapter 4, it is useful to note the following. Although not included here, it was verified that the near field of the electrically small resonant dipolar DPS-DNG structure for other locations of the EHD in regions 1, 2, and 3 (provided that moderate distances between the EHD and the structure are considered when the EHD is in region 3) is very similar to the near field shown in Figure 5.4(a). This means that the excited resonant dipolar mode is the natural dipolar mode of this structure. Consequently, the strongest (weakest) excitation of this mode is obtained by placing the EHD at locations where the field is a maximum (minimum). These findings are general and, therefore, also apply for the quadrupolar (and even higher order) structures considered later in this chapter. Moreover, they are identical to the findings related to cylindrical dipolar DPS-DNG structures treated in Chapter 4. However, the near-field for the dipolar mode in the present spherical case is notably different from that in the cylindrical case, see Chapter 4. In particular, the electric near field in Figure 5.4(a) only attains very low values along the z-axis, while no distinct minima or very low values are found for other observation points, such as near the origin or inside region 2, as was the case for cylindrical dipolar DPS-DNG structures, see in Chapter 4. As a consequence, the EHD can be located almost arbitrarily in the spherical cases and still excite the dipolar mode as the dominant one. In particular, the strength of the near field in Figure 5.4(a) is rather constant for those locations of the EHD used in the examination of the PR, see Figure 5.2, i.e., along the positive x-axis throughout the different regions. Therefore, it is clear that the enhancements observed in Figure 5.2 are comparable in amplitude.

5.4.2.3 Directivity

It is next of interest to briefly examine the radiation properties of the dipolar DPS-DNG and DPS-DPS structures.

Figure 5.5 shows the directivity patterns for the dipolar DPS-DNG and DPS-DPS structures as a function of θ for $\phi = 0^o$ (Figure 5.5(a)), and as a function of ϕ for $\theta = 90^o$ (Figure 5.5(b)). It has

been verified that very much the same directivity patterns are obtained for any r_s in region 1 for both structures.

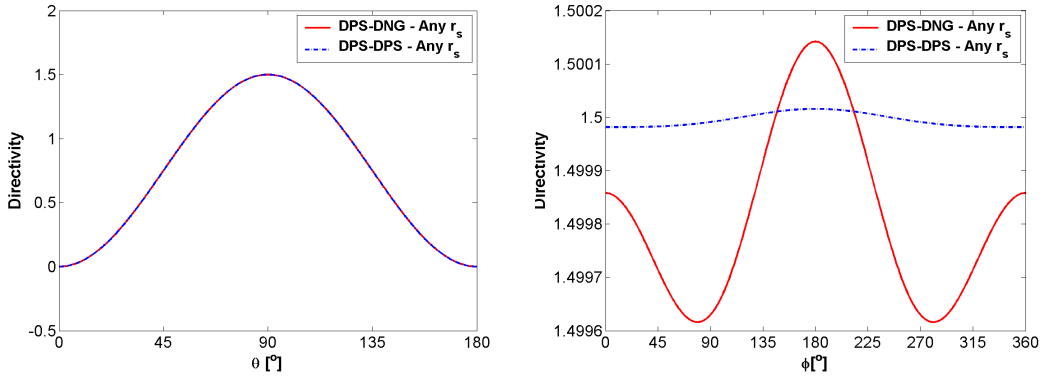

(a) (b)

Figure 5.5: *Directivity for the dipolar DPS-DNG and DPS-DPS structures as a function of θ for $\phi = 0^o$ (a), and as a function of ϕ for $\theta = 90^o$. The EHD is located at any r_s in region 1.*

In general, the directivity results in Figure 5.5(a) agree with the near-field results discussed in Section 5.4.2.2. For both structures a clear dipolar pattern is found with the maximum directivity, D_{max}, attained in the $\theta = 90^o$- direction with the value $D_{max} \simeq 1.5$. It is moreover found from Figure 5.5(b) that the variation of the directivity with ϕ for $\theta = 90^o$ is negligible and that for all ϕ $D_{max} \simeq 1.5$. This omnidirectional pattern in the shown cut, along with the results in Figure 5.5(a), clearly demonstrate that the radiation patterns for the two investigated structures are indeed of the dipolar form identical to that of an EHD, see e.g., [120]. The results for the dipolar DPS-DNG structure are further illustrated in Figure 5.6, which shows the directivity for this structure as a function of θ and ϕ. In this figure a clear dipolar directivity pattern, which is identical to that of an EHD, is observed.

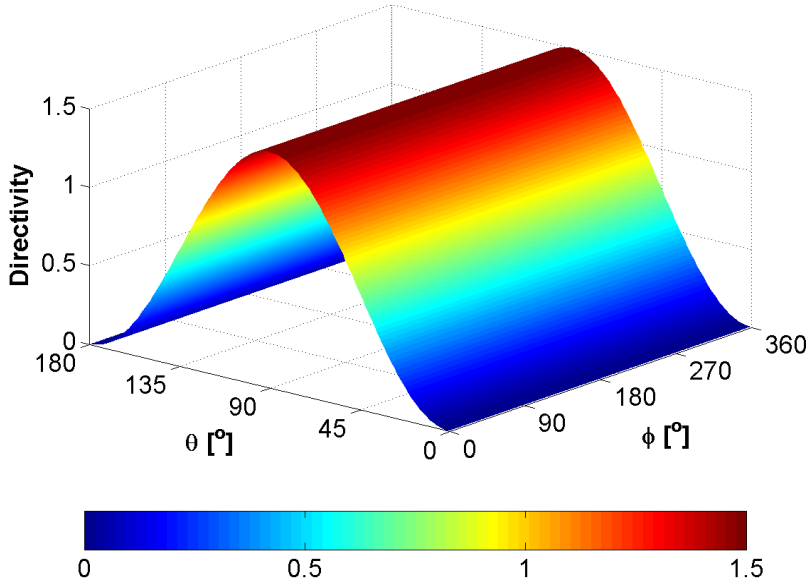

Figure 5.6: *Directivity for the dipolar DPS-DNG structure as a function of θ and ϕ. The EHD is located at any r_s in region 1.*

It is useful to note that since the DPS-DPS structure is electrically small, the dipolar pattern with $D_{max} \simeq$

1.5 in the direction broadside to the structure is expected. However, the same reasoning also explains the result reported for the dipolar DPS-DNG structure. The dominant mode of radiation for this structure is, as explained earlier, the dipolar mode, which is why a directivity pattern of the dipolar form, with $D_{max} \simeq 1.5$, is observed. While this structure leads to the enhancement of the total power, it does not lead to directivity values above the well-known maximum value of $D_{max} = 1.5$ obtained for the EHD alone, see e.g., [120].

Similar results for the dipolar DPS-DNG structures have been obtained for the locations of the EHD in region 2, as well as those in region 3, provided that moderate distances between the EHD and the DNG shell are considered.

5.4.3 Quadrupolar structures

5.4.3.1 Total power - power ratio and near field

Figure 5.7 shows the PR as a function of the outer shell radius r_2 for the quadrupolar DPS-DNG and DPS-DPS structures having $r_1 = 10$ mm and for the EHD being located in region 1 at $r_s = 5$ mm.

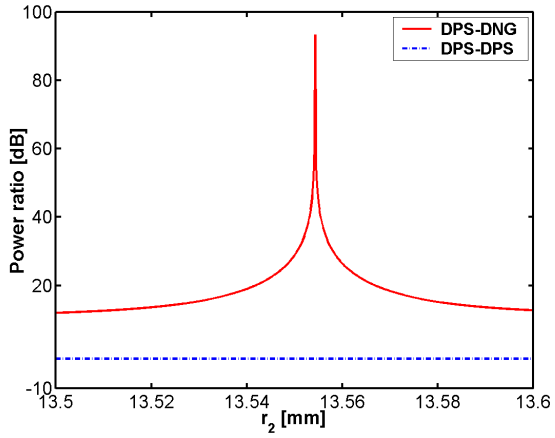

Figure 5.7: *Power ratio as a function of the outer shell radius r_2 for the quadrupolar DPS-DNG and DPS-DPS structures when the EHD is in region 1 at $r_s = 5$ mm.*

As with the dipolar mode, the present DPS-DPS structure does not give any enhancements of the total power. On the other hand, a resonance peak and, thus, a significant enhancement of the total power is observed in Figure 5.7 for the DPS-DNG structure. The maximum PR of the DPS-DNG structure is PR $\simeq$ 93 dB at $r_2 = 13.55$ mm which agrees with the value in Table 5.1 predicted by the resonance conditions (5.11a) and (5.11b). It is also found that the resonant enhancements reported in Figure 5.7 are larger, but extremely narrower than those occurring in the corresponding dipolar DPS-DNG structure.

To verify that these results are due to the resonant excitation of the quadrupolar mode, the near-field and the total power spectra of the n'th mode are again considered. The electric near field for the quadrupolar DPS-DNG structure for which $r_2 = 13.55$ mm is depicted in Figure 5.8(a) for the case where the EHD is located at $r_s = 5$ mm (curves representing the spherical surfaces of the DPS-DNG structure are also shown).

Since the near field has a quadrupolar form, it follows that the EHD in the presence of this DPS-DNG structure excites the quadrupolar mode, and the enhancements of the total power result from this dominant mode. These findings are confirmed with the results given in Figure 5.8(b), where the total power spectrum of the n'th mode, $n = 1, 2$, and 3, normalized by the total power in the quadrupolar mode, is shown. The largest part of the total power is contained in the quadrupolar mode, while only an extremely small amount is contained in the other modes. Again, essentially no total power is contained in the $n > 3$ modes. Results similar to those reported in Figure 5.8 are obtained for the quadrupolar DPS-DNG structure when the EHD is located in regions 2 and 3. One also notes from Figure 5.8(a) that this near field, evaluated at a given distance and direction, is larger (as the dynamic range is larger) than the near field of the corresponding dipolar structure depicted in Figure 5.4(a). These differences in the near-field values

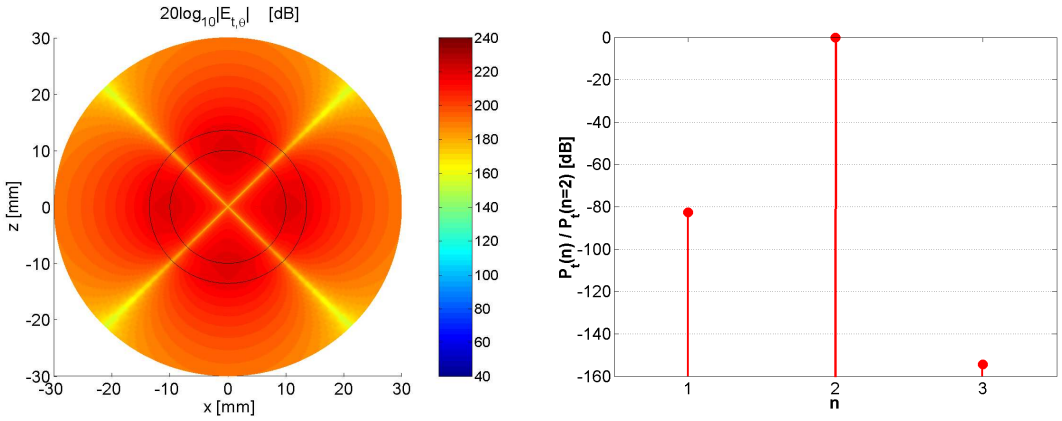

(a) (b)

Figure 5.8: *Quadrupolar DPS-DNG structure: (a) the electric near field when the EHD is in region 1 at* $r_s = 5$ *mm, and (b) the total power in the* n*'th mode,* $n = 1, 2,$ *and 3, normalized by the total power in the quadrupolar mode. In (a), the plane of observation is the* xz*-plane, and the field is shown in a circular region of radius* 30 *mm.*

for the dipolar and quadrupolar structures explain why the PR values are higher for the quadrupolar cases.

Additional near-field results for the quadrupolar DPS-DNG structure are shown in Figures 5.9(a) and (b) for the EHD located at $r_s = 1$ mm and $r_s = 9$ mm, respectively.

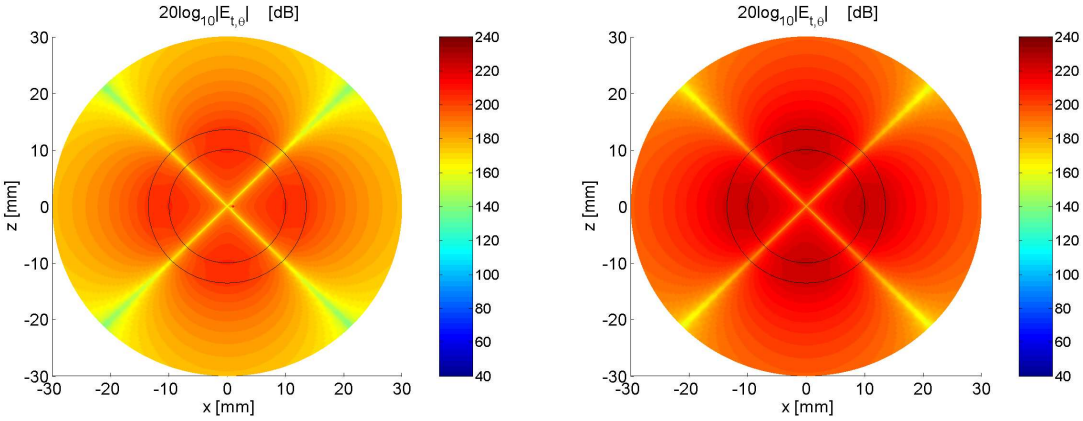

(a) (b)

Figure 5.9: *Electric near field of the quadrupolar DPS-DNG structure when the EHD is in region 1 at* $r_s = 1$ *mm (a) and* $r_s = 9$ *mm (b).*

From these results and the one shown in Figure 5.8(a), it is clear that once the resonant quadrupolar mode is excited, its form is, apart from the field strength, rather unaffected of the location of the EHD. Thus, similar to the previously considered dipolar mode, the excited quadrupolar mode is a natural mode of the structure. As a consequence, placing the EHD at locations where the field is very small (large) leads to a weak (strong) excitation of this mode. With reference to Figures 5.8(a) and 5.9, the small field locations are, amongst others, near the origin. The locations of the largest fields are near the interfaces of the DNG shell along the x- and z-axes. Thus, the excitation of the resonant quadrupolar mode is very weak when the EHD is near the origin, while it is very strong when it is close to the interfaces of the DNG shell along the x-and z-axes.

With the aim of addressing the influence of the location of the EHD on the PR results, Figures 5.10(a), and 5.10(b) show, respectively, the PR as a function of the EHD location, r_s, in regions 1 and 2 for the

quadrupolar DPS-DNG and DPS-DPS structures having the fixed radii: $r_1 = 10$ mm and $r_2 = 13.55$ mm.

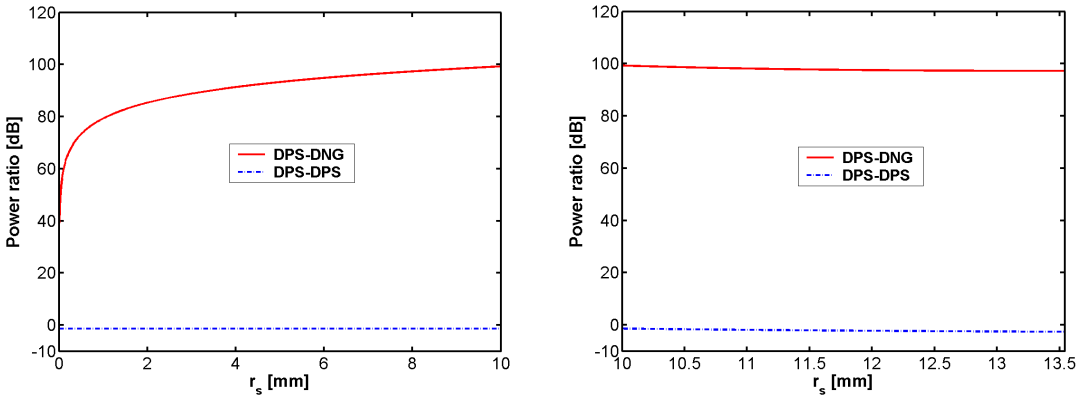

(a) (b)

Figure 5.10: *Power ratio as a function of the EHD location r_s for the quadrupolar DPS-DNG and DPS-DPS structures when the EHD is located in region 1 (a) and region 2 (b).*

While no enhancements are in evidence for the DPS-DPS structure, the quadrupolar DPS-DNG structure produces very large values of the PR for most of the considered EHD locations. Aside from the fact that the enhancements of the total power in the quadrupolar case are larger than those for the dipolar case for the majority of the EHD locations, the overall behaviour of the results given in Figure 5.10 resembles that of the corresponding dipolar DPS-DNG structures. Nonetheless, there are some differences between the PR results in Figures 5.10(a) and 5.2(b). In the former, the PR is increasing in the interval PR $\in [39.3 - 99.3]$ dB for increasing r_s values in region 1. This is in contrast to the dipolar DPS-DNG structure results given in Figure 5.2(a), where the PR is nearly constant in this region. This behaviour of the quadrupolar DPS-DNG structure is not surprising. One recalls that the resonant structure has been designed so that the EHD will dominantly excite the quadrupolar mode. Moreover, with reference to the above discussion on the near-field behaviour and the characterization of the excited quadrupolar mode as the natural mode, it is recalled that this mode is excited most strongly (weakly) when the EHD is located near to the interfaces (origin) of the DNG shell. In particular, it is well known that only the dipolar mode exists at the origin, see, e.g., [56], [64, Ch. 5], [118]. Thus, the enhancements of the total power are diminished significantly as the EHD location is moved near the origin, and they are completely absent when the EHD is located at the common center of the structure, since the structure has *a priori* been designed to excite the quadrupolar, and not the dipolar, mode as the dominant mode. On the other hand, the enhancements are significantly increased as the EHD approaches the surface of the DNG shell.

5.4.3.2 Directivity

Figure 5.11 shows the directivity patterns for the quadrupolar DPS-DNG (labeled by (1)) and DPS-DPS structures (labeled by (2)) as a function of θ for $\phi = 0^o$ (Figure 5.11(a)), and as a function of ϕ for $\theta = 90^o$ (Figure 5.11(b)). It has been verified that very much the same directivity patterns are obtained for any r_s in region 1 for the DPS-DPS structure.

The directivity results in Figure 5.11(a) are in agreement with the near-field results discussed in Section 5.4.3.1. In particular, close to the origin, i.e., for $r_s = 0.000001$ mm, the directivity pattern of the quadrupolar DPS-DNG structure is clearly dipolar, and is thus identical to the directivity of the corresponding DPS-DPS structure. Thus, for such small r_s values, the resonant quadrupolar mode can not be excited, and the dipolar mode becomes dominant, which, as mentioned previously, is the reason for no enhancement of the total power for these EHD locations. However, by moving the EHD slightly away from this distance to e.g., $r_s = 0.001$, see Figure 5.11(a), the directivity of the DPS-DNG structure takes on the quadrupolar form, although not symmetric in this particular cut. The maximum directivity $D_{max} \simeq 2.2$ is attained along the $\theta = 0^o$- and $\theta = 180^o$- directions. This value is slightly larger than the value obtained for the EHD alone and the previously considered dipolar DPS-DNG structure. By

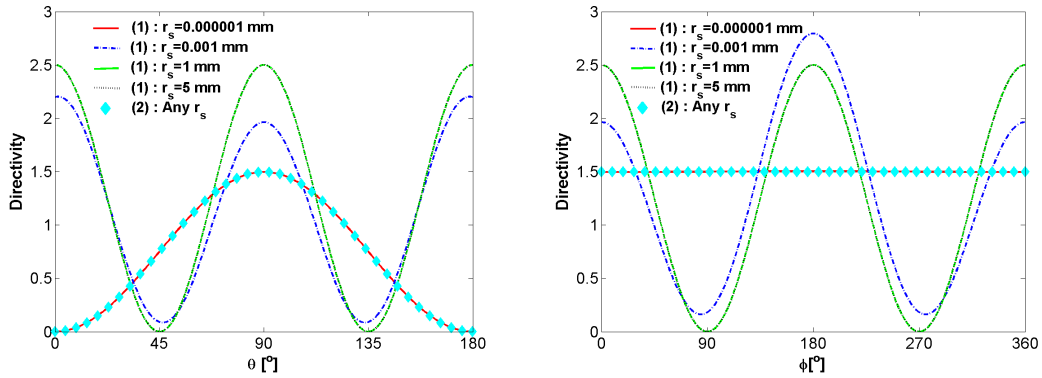

(a) (b)

Figure 5.11: *Directivity for various EHD locations in region 1 for the quadrupolar DPS-DNG (labeled by (1)) and DPS-DPS (labeled by (2)) structures as a function of θ for $\phi = 0^o$ (a), and as a function of ϕ for $\theta = 90^o$ (b).*

moving the EHD further away, e.g., to $r_s = 1$ and 5 mm, the directivity of the quadrupolar DPS-DNG structure attains a symmetric quadrupolar pattern with $D_{max} \simeq 2.5$ attained along the $\theta = 0^o$-, $\theta = 90^o$- and $\theta = 180^o$- directions. As is observed, the same directivity patterns are obtained for $r_s = 1$ mm and $r_s = 5$ mm, this clearly demonstrating that once the resonant quadrupolar mode is excited, the pattern is influenced minimally, or not influenced at all, by the location of the EHD.

It is moreover interesting to note from Figure 5.11(b) that once the resonant quadrupolar mode is excited in the DPS-DNG structure, the directivity patterns exhibit notable variations with ϕ for $\theta = 90^o$. This behaviour is expected for the quadrupolar mode of radiation, and is further illustrated in Figure 5.12, which shows the directivity for this structure as a function of θ and ϕ for the EHD located in region 1 at $r_s = 5$ mm. In this figure, the variations of the directivity pattern with θ and ϕ are clearly illustrated, as is the existence of the quadrupolar pattern.

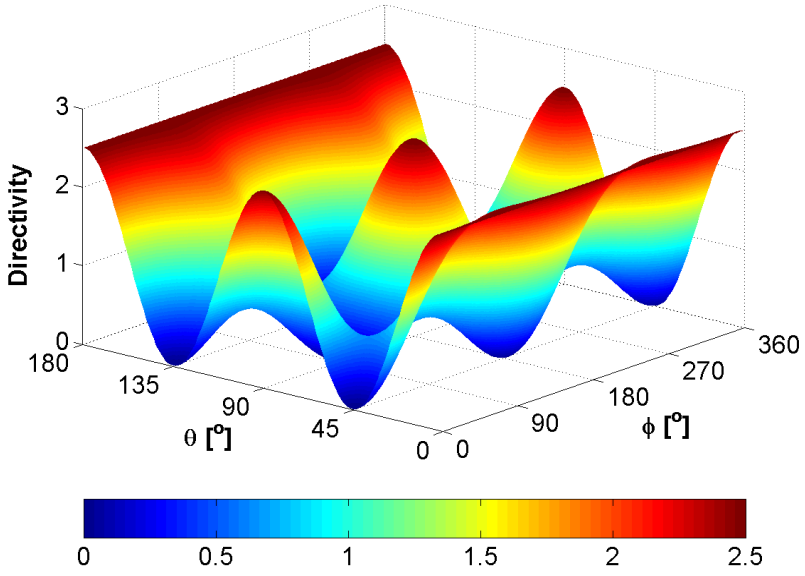

Figure 5.12: *Directivity for the quadrupolar DPS-DNG and DPS-DPS structures as a function of θ and ϕ. The EHD is located at $r_s = 5$ mm in region 1.*

Similar results for the quadrupolar DPS-DNG structures have been obtained for the locations of the EHD in region 2, as well as those in region 3, provided that moderate distances between the EHD and the DNG shell are considered.

5.5 Summary

This chapter summarized specific properties of the canonical configuration consisting of an arbitrarily oriented and located EHD radiating in the presence of a pair of concentric MTM-based spheres. The use of DNG materials in these canonical configurations, of which the performance was compared to the conventional DPS-based configurations, was investigated. An analytical solution in terms of SVWFs was first derived, and this was subsequently employed in a numerical investigation of electrically small dipolar and quadrupolar DNG- and DPS-based structures, comprised of DNG and DPS shells. In the numerical investigations, the near-field spatial distribution, the total radiated power, and the directivity of these structures were examined.

It was found that the electrically small DNG-based structures can be designed to be resonant and thereby lead to significant changes of the field radiated by the EHD as well as significant enhancements of the total radiated power. These enhancements, which are of the order of 63 dB, for the dipolar structures, and 93 dB for the quadrupolar ones, as compared to the power radiated by the EHD in free space, were found to be due to the so-called sub-wavelength sized natural resonances of the DNG-based structures. Their existence was predicted analytically, and it was demonstrated that they do not exist for the corresponding DPS-based structures. It was also shown that changing the location of the EHD within the DNG-based structure had little impact on the total radiated power. This is in distinct contrast to the analogous cylindrical configurations treated in Chapter 4 for which, as an example, the total radiated power of the corresponding dipolar DNG-based structure exhibits large variations with the source location. Nonetheless, the spherical electrically small resonant quadrupolar DNG-based structure was found to exhibit some variation of the total radiated power with the EHD location. In particular, this is the case when the EHD is located near the center of the concentric spheres because the dipolar mode then dominates the interaction process. Thus, although such a resonant DNG-based structure was designed to excite the quadrupolar mode as the dominant one, it was found that other modes, such as the dipolar mode, could be excited for specific source locations and could, thereby, lead to pattern reshaping with the changing source location. Moreover, it was found that the enhancements of the total radiated power, although significantly narrower and more sensitive to variations of the material and geometrical parameters, are considerably larger for the quadrupolar structures than for the dipolar ones. The directivity of the electrically small resonant dipolar DPS-DNG structures was found to be identical to that of the EHD, as well as of the corresponding DPS-DPS structure, with the maximum attainable directivity of 1.5 along the direction broadside to the structure. In the case of the quadrupolar DPS-DNG structure, clear quadrupolar directivity patterns, with the maximum directivity of 2.5 were obtained for the majority of the investigated EHD locations.

Although not included in this chapter, the influence of loss and dispersion present in DNG materials, as well as the increase in the electrical size of the structures and the use of SNG materials, have likewise been investigated in this work, and the pertaining results are found in MIII.

CHAPTER 6

SUMMARY AND CONCLUSIONS

In this study, various aspects of double-negative (DNG) and single-negative (SNG) metamaterials (MTMs), and combinations of these with conventional double-positive (DPS) materials, were investigated. The work has concentrated on the investigation of the radiation and scattering from two- and three-dimensional (2D and 3D) MTM-based structures. Although these investigations emphasized the use of DNG materials in electrically small structures, several designs utilizing larger electrical sizes were also investigated.

Chapter 2 provided an overview of MTMs, particularly DNG materials. Their origins, basic properties, realizations and applications were discussed. The importance of Veselago's work [4] from 1967, in which the first systematic investigation of the properties and applications of lossless, isotropic DNG materials was performed, was recognized. Among the important properties of DNG materials revealed by that work included the fact that the directions of the phase and the power of uniform plane waves are opposite in DNG materials, which is a property characteristic of backward waves, and the fact that Snell's law of refraction is reversed at a DPS/DNG interface, which leads to the phenomenon of negative refraction. The very recent, first realizations of DNG materials as introduced in [8]-[10] employed inclusions in the form of specific wire structures and split-ring resonators. As was discussed, those realizations provide negative permittivity and permeability, respectively, at microwave frequencies. The strong recent research activities into the development of other DNG material realizations were also recognized. In particular, several other designs appropriate for use not only at microwave, but also at optical and terahertz, frequencies were mentioned. These DNG realizations were identified as belonging to two groups. The first group contains realizations that rely on resonant inclusions of various shapes, such as SRRs, while in the second group they are based on the appropriately loaded transmission lines. The overview also revealed numerous applications of MTMs, particularly those of DNG materials. While some of these applications have been realized, others require ideal MTMs that are not yet available. Examples include the imaging capabilities of DNG materials and the idea of perfect lenses first introduced in [11]. Moreover, the potential applicability of MTMs to significantly reduce the size, e.g., of cavities, waveguides, scatterers and radiators, a property unattainable with conventional DPS materials, was discussed. In particular, the ability of specifically designed MTM-based configurations to increase the power radiated by electrically small antennas, discussed in [56]-[58] was mentioned.

Chapter 3 provided the first steps into the investigation of radiation and scattering from MTM-based structures. These included some fundamental issues related to the sign, or more generally the branch, of derived electromagnetic parameters in DNG materials including the wave number, $k_c = k' - jk''$, intrinsic impedance, $\eta_c = \eta' - j\eta''$, and refractive index, $n_c = n' - jn''$. The need for such a study emerged from obvious disagreements in the literature on the sign of these parameters. In order to clarify the issues involved in these disagreements, a consistent set of definitions for those parameters was first established. Each was shown to yield a specific sign of the parameter in question and, thereby, to introduce the possibility of having different signs for one and the same parameter. More specifically, two definitions for k_c were introduced on the one hand and for η_c on the other. At the same time four definitions were introduced for n_c. It was demonstrated that the disagreements in the literature are based on the implicit use of different definitions for one and the same parameter. Specifically, it was shown that for a lossy DNG material, one definition of k_c yields $k' > 0$ and $k'' < 0$, while the other gives $k' < 0$ and $k'' > 0$. Moreover, it was found that regardless of the signs of k' and k'', one definition of η_c gives $\eta' > 0$, while the second one gives $\eta' < 0$, while the sign of η'' always depends solely on the ratio of the electric and magnetic loss tangents in the material. As to the sign of n_c, it was found that

two definitions give a real refractive index, while the other two give a complex refractive index. In the real cases, a positive refractive index is obtained with one definition, while a negative refractive index is obtained with the other. Moreover, the other two definitions of n_c give $n' > 0$ and $n'' < 0$, and $n' < 0$ and $n'' > 0$. These properties also hold true for both possible combinations of the signs of k' and k''. The applicability of the various definitions and, thus, the signs of the derived parameters, was demonstrated through an investigation of the reflection/refraction of a uniform plane wave at a DPS/DNG interface. It was shown that all definitions and, thus, the signs of these parameters are equally correct as long as they are used consistently in the solution procedure. The difference in the use of the various definitions and the associated signs of the derived parameters was shown to lead to different functional forms of the solution to the problem of interest, e.g., to different forms of the refracted fields, Fresnel equations and Snell's law of refraction. Nonetheless, it was demonstrated that in all cases, the correct physical behavior of the solution was obtained.

Chapter 4 investigated the radiation and scattering from 2D concentric cylinders excited by an arbitrarily located electric line source (ELS). The analytical solution was derived and subsequently implemented for the particular cases of either a DPS or a DNG shell. Their near- and far-field properties were analysed through an investigation of the spatial distribution of the resulting near fields, total radiated power, directivity, and total, as well as differential, scattering cross sections. Designs of electrically small as well as electrically large sizes were examined. For DNG-based structures, the influence of loss and dispersion were also investigated. Moreover, the analytical solution of the concentric cylinder problem was applied to the study of the properties of single DPS and DNG cylinders.

Particular emphasis was devoted to electrically small dipolar DNG-based structures, i.e., to DNG structures that excite the dominant dipolar mode. Such DNG-based structures were shown to be resonant, i.e., to exhibit resonances, and to lead, for example, to large values of the total radiated power and cross sections, whereas the corresponding DPS-based structures showed none of these characteristics. These resonances, which were termed sub-wavelength natural resonances, were attributed to the excitation of the resonant dipolar mode of such a structure. In the case of lossless DNG-based systems, consisting of an ELS-excited DNG shell, the total radiated power was found to be of the order of 23 dB greater than the power radiated by the ELS in free space even though its size was $1/50$ of the free-space wavelength, λ_0. The total scattering cross section of this structure was also found to be significantly larger than the value produced by the corresponding DPS-based structure. These enhancements were found to depend on the ELS location, and were found to be largest when the ELS was placed near the interfaces of the DNG-based structure. Although not included in the main part of this work, it was shown in Manuscript I (Appendix A) that even larger enhancements of these quantities can be obtained with even smaller (on the order of $\lambda_0/100$) quadrupolar DNG-based structures. It was shown that the enhancements of the quantities of interest require the excitation of the higher order resonant modes, and that they are not found when the monopolar mode is excited. The excitation of higher order modes in turn required off-axis ELS locations.

Apart from providing enhanced radiation and scattering characteristics, the DNG-based cylindrical structures also were found to offer interesting directivity properties. In particular, their directivities could be reshaped by changing the ELS location, thereby leading to the possibility that directive electrically small radiating structures can be designed. This possible control of the directivity is due to the fact that different ELS locations will excite only certain modes or certain combinations of the modes of the electrically small resonant DNG-based structures. For instance, precise locations of the ELS in relation to the investigated DNG-based structures were identified for which the monopolar mode dominated the interaction process and no enhancements occurred even though slightly different locations produced resonant dipolar or quadrupolar mode enhancements.

Attention was also directed to more realistic DNG-based structures, i.e., those including loss and dispersion. It was demonstrated that dispersion significantly reduces the frequency bandwidth of the resonances, while the losses decrease the peak values generated by those resonances. Moreover, it was shown that when the sizes of the structures are large enough for the wavelength-sized natural resonances to occur, the DNG-based structures offer no significant advantage over the corresponding DPS-based ones. They both lead to resonances, e.g., in the total radiated power, although the resulting values of the total radiated power are smaller than those obtained from the electrically small DNG-based structures. Further investigations of the electrically large structures, including single DPS or DNG cylinders, revealed interesting focusing effects of the ELS field when the ELS is located near to the surface of a

DNG cylinder. These focusing effects, initially observed through investigations of the exact spatial near-field distributions, were confirmed by the approximate geometrical optics ray-tracing results. It must be noted that none of the investigated single DNG cylinder configurations were found to provide a directive pattern, this being in contrast to the corresponding DPS cylinders for which a main lobe could clearly be identified. Consequently, these results render such single DNG cylinders as bad candidates, for example, in potential antenna designs.

Chapter 5 considered the properties of a 3D canonical configuration that consists of a pair of concentric spheres excited by an arbitrarily located and oriented electric Hertzian dipole (EHD). This problem was solved analytically and implemented numerically for the particular case of either a DPS or a DNG shell. Their near- and far-field properties were analysed through an investigation of the spatial distribution of the near field, total radiated power and directivity. In the electrically small cases, both dipolar and quadrupolar structures, of which the dimension is of the order of $\lambda_0/27$ and $\lambda_0/37$, respectively, were considered. It was found that these structures can also be designed to be resonant, and thereby exhibit similar phenomena as the corresponding cylindrical structures treated in Chapter 4. Moreover, the effects of loss and dispersion in the spherical cases, as well as the use of larger spherical structures, also were found to be very similar to those found for the cylindrical cases. In particular, the enhancements of the total radiated power were found to be of the order of 63 dB, for the dipolar structures, and 93 dB for the quadrupolar ones. Despite the many similarities, some differences in the behaviours of the cylindrical and spherical DNG-based structures were noticed. For instance, it was shown that changing the EHD location had very little impact on the total radiated power of the spherical dipolar DNG-based structure. This was in complete contrast to the behaviour obtained in Chapter 4 for its cylindrical counterpart. This result was attributed to the obvious lack of a monopolar mode, regardless the EHD location, in the spherical case. The lowest order mode of radiation in the sphere case is the dipolar mode. Nonetheless, it was shown that there are some variations between the results obtained for different higher order resonant modes, e.g., in the total radiated power. For instance, when the electrically small DNG-based structure was designed to excite the resonant quadrupolar mode, the dipolar mode was dominant when the EHD was located near the origin. Thus, pattern reshaping with the changing EHD location was also demonstrated for the spherical electrically small DNG-based structures. In regards to the directivity of the electrically small dipolar DNG-based structures, it was found to be identical irrespective of the EHD location. Like the corresponding DPS-based structures, the maximum attainable directivity is 1.5 along the direction broadside to the direction of orientation of the EHD. In the case of the resonant quadrupolar DNG structure, the quadrupolar directivity patterns exhibited a maximum directivity of 2.5 for the majority of the investigated EHD locations.

The work presented in this thesis can be extended in several ways which can be divided in two categories. The first category regards future investigations of the 2D and 3D MTM-based canonical structures examined in this work, while the second category regards investigations of more realistic antenna MTM-based systems which can be inferred from the investigated canonical structures.

The investigated 2D and 3D MTM-based structures contained at most two material layers excited by an infinitely long ELS and an infinitesimal EHD, respectively, and immersed in free space. It would be of interest to undertake investigations similar to those in Chapters 4 and 5 for structures comprised of several material layers. Moreover, with the aim of possible applications of the MTM-based canonical structures investigated inhere, and provided the required MTMs can be realized, it is anticipated that exact reproduction of sharp boundaries between adjacent layers would be very hard to obtain. In this regard it would be of interest to investigate the influence of imperfections or variations in the layer boundaries on the resonant phenomena in electrically small MTM-based structures. As noted in Chapters 4 and 5, the power ratio figure of a given MTM-based structure excited by the source of relevance, is equivalent to the radiation resistance of that system normalized by the radiation resistance of the source alone. To gain further insight into the behaviour of the investigated electrically small MTM-based structures, the complete Poynting vector should be calculated, thereby providing the knowledge about the reactance of the investigated structures.

Furthermore it would be interesting to examine the properties of a number of realistic antennas that assume ideal MTMs. These antennas could range from those inspired by the above canonical designs but now with more realistic sources of excitation, such as e.g., small dipole antennas and monopoles, as well as more complex structures which e.g., could employ truncated cylinders as well as hemispherical MTM-

based structures backed by a ground plane. In particular, the feasibility of electrically small MTM-based structures in the potential design of efficient electrically small antennas, should be investigated. For the case of e.g. a small center-fed electric dipole surrounded concentrically by a specific MTM shell, very effective electrically small antenna designs were obtained in [58] with no degradation of the radiation pattern. It will therefore be interesting to examine the antenna configurations treated in [58] as the respective excitation becomes displaced from the center of the structures, thereby allowing the excitation of specific higher order resonant modes. In particular, one should examine if the efficient electrically small antennas in [58] can be designed to possess the directive radiation patterns known to exist for the corresponding MTM-based canonical structures treated in Chapters 4 and 6, when the excitations are not located at the center of the employed structures.

Part II

Manuscripts

APPENDIX A

MANUSCRIPT I

Analytical and numerical investigation of the radiation and scattering from concentric metamaterial cylinders excited by an electric line source[1]

Samel Arslanagić[(1)], Richard W. Ziolkowski[(2)], and Olav Breinbjerg[(1)]

[(1)] Ørsted•DTU, ElectroScience Systems, Technical University of Denmark,
Building 348, Ørsteds Plads, DK-2800 Kgs. Lyngby, Denmark,
Tel: +45 4588 1444, Fax: +45 4593 1634,
E-mail: sar@oersted.dtu.dk, ob@oersted.dtu.dk

[(2)] Department of Electrical and Computer Engineering, University of Arizona
1230 E. Speedway Blvd., Tucson, AZ, 85721-0104
Tel: (520) 621-6173, Fax: (520) 621-8076;
E-mail: ziolkowski@arizona.ece.edu

Key terms: *metamaterials*, *radiation*, *scattering*, *sub-wavelength resonances*, *radiation pattern shaping*.

Abstract

An antenna configuration consisting of an arbitrarily located electric line source radiating in the presence of a pair of concentric metamaterial cylinders is investigated analytically and numerically. The near- and far-field properties of these structures are analysed through an investigation of such parameters as the total radiated power, directivity, and total as well as differential scattering cross sections. The results obtained for these metamaterial structures are compared to those for the corresponding structures made of conventional materials. It is shown that electrically small concentric metamaterial structures can be designed to be resonant and to possess advantageous radiation and scattering characteristics in contrast

[1] This manuscript is journal publication no. 2, see the list of publications on pages iv and v.

to the corresponding structures made of conventional materials. More specifically, it is shown that metamaterial structures lead to significant enhancements of the total radiated power as well as the total and differential scattering cross sections. Moreover, the feasibility of controlling the directivity pattern of the electrically small metamaterial structures through appropriate locations of the electric line source is demonstrated. The effects of the dispersion and loss present in the metamaterials are taken into account to study the bandwidth properties of these resonant configurations.

1 Introduction

The electromagnetics community has recently experienced a broad and intense interest in exploring and exploiting the electromagnetic characteristics and properties of various classes of metamaterials (MTMs) and combinations of these with the conventional double-positive (DPS) materials, characterized by a positive real part of both the permittivity and permeability. The different MTMs include double-negative (DNG) materials, characterized by a negative real part of both the permittivity and permeability, considered by Veselago in [1], and single-negative (SNG) materials, characterized by a negative real part of either the permittivity (so-called epsilon-negative (ENG) materials) or the permeability (so-called mu-negative (MNG) materials). A considerable amount of analysis to understand the properties of both DNG and SNG materials have already been performed, see [2]-[4] and the works referenced therein.

The increasing interest in MTMs is due to their unusual electromagnetic properties and the potential to exploit these for a variety of applications [1]-[4]. Different MTM configurations have been considered, particularly canonical rectangular, cylindrical, and spherical shapes. Among the rectangular geometries, the lossless DNG slab has attracted much attention due to its so-called perfect lens property [5]. Moreover, resonance, tunnelling, and transparency properties of DNG and SNG mono- and bi-layers have been investigated see [2]-[4] and [6]. The plane wave scattering properties of MTM cylinders and spheres, as well as their radiation properties when illuminated by more realistic sources of radiation, such as Hertizan dipoles and line sources, have been investigated in detail in [2]-[4] and [7]-[28]. In particular, it has been demonstrated that electrically small MTM cylindrical or spherical shells can be designed to produce resonant configurations [2]-[4], [10], [11], [18]-[27] which lead to significant enhancements of the total radiated power, as well as the total scattering cross section.

The purpose of the present work is to summarize investigations of electrically small resonant concentric MTM cylinders illuminated by an arbitrarily located electric line source (ELS)[2]. More specifically, it is shown that the use of MTMs in such electrically small structures leads to significant enhancement of the total radiated power, as compared to the power radiated by the source into free space. Moreover, it is shown that in the case of the ELS being infinitely far from the cylinders, the total and differential scattering cross section are likewise significantly enhanced when MTMs are used, as compared to the results obtained for the corresponding cylinders composed of only DPS materials. Furthermore, the feasibility of controlling the directivity of the electrically small MTM structures by appropriate alternation of the ELS location is demonstrated; and its use in the design of directive electrically small antennas is discussed.

The present manuscript is organized as follows. In Section 2, the analytical solution to the problem of an arbitrarily located ELS radiating in the presence of a concentric pair of MTM cylinders is derived, and the quantities used to illustrate the subsequent numerical results are defined. In Section 3, the condition for resonance is derived and discussed. Furthermore, some important differences between electrically small two-dimensional (2D) and three-dimensional (3D) structures are emphasized. Moreover, the present results regarding the possibility of achieving enhanced radiation characteristics with resonant MTM cylindrical structures are related to those in [28], where similar configurations have been examined. In Section 4, the numerical results, including the near field, directivity, total and differential cross sections, are shown for some specifically designed electrically small structures. In particular, the so-called dipolar and quadrupolar structures, to be defined in Section 4, will be investigated. In order to study the bandwidth properties of the resonant configurations identified in Section 4, the effects of dispersion are taken into account in Section 5, which moreover includes the analysis of the effects of losses in MTMs. Furthermore, the fundamental distinctions between the resonant electrically small structures

[2]The ELS type of illumination corresponds to TM polarization. The results for the magnetic line source illumination, which correspond to TE polarization, are readily obtained by duality and these are thus not included here.

and those for which the resonant behaviour is related to the overall size of the structure are pointed out in Section 6. Finally, in Section 7, the use of SNG media in the design of electrically small resonant structures is briefly discussed. Throughout this manuscript, the time factor $\exp(j\omega t)$, with ω being the angular frequency and t being the time, is assumed and suppressed.

2 Analytical Solution

A cross section of the 2D configuration of interest is depicted in Figure 1.

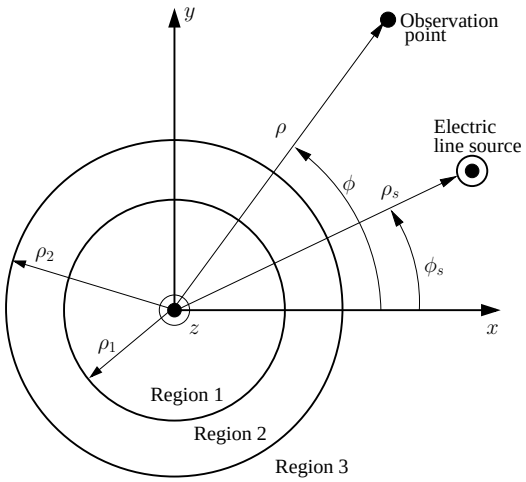

Figure 1: *Configuration of the ELS-excited concentric pair of MTM cylinders.*

A circular cylindrical core of radius ρ_1 (region 1) is covered with a concentric cylindrical shell of outer radius ρ_2 (region 2) and imbedded in an infinite ambient medium (region 3). The structure is illuminated by an infinite ELS of a constant electric current I_e. The axes of the cylinders and the ELS are parallel, and the ELS can be located in any of the three regions. Region i, with $i = 1$ and 2, is characterized by a permittivity and a permeability, denoted by $\varepsilon_i = \varepsilon_i' - j\varepsilon_i''$ and $\mu_i = \mu_i' - j\mu_i''$, respectively, and a wave number $k_i = \omega\sqrt{\varepsilon_i\mu_i}$, where the branch of the square root is chosen so that $\mathcal{I}m\{k_i\} \leq 0$. Each of these regions can be composed of simple DPS, DNG, or SNG materials. The exterior region, region 3, is free space with the permittivity and permeability , and thus the wave number $k_0 = \sqrt{\varepsilon_0\mu_0}$ and intrinsic impedance $\eta_0 = \sqrt{\mu_0/\varepsilon_0}$. A cylindrical coordinate system (ρ, ϕ, z) and the associated Cartesian coordinate system (x, y, z) are introduced such that the z-axis coincides with the axis of the cylinders. The coordinates of the observation point are (ρ, ϕ), while the coordinates of the ELS are (ρ_s, ϕ_s).

Using the cylindrical wave functions with origins at $\rho = 0$, the electric field generated by the ELS in an infinite medium characterized by ε_{ELS}, μ_{ELS}, and k_{ELS} is given by the well-known expression [29, Ch. 11]

$$\vec{E}_{\text{ELS}}(\rho,\phi) = -\hat{z} I_e \frac{\omega\mu_{\text{ELS}}}{4} \begin{cases} \sum_{n=0}^{N_{max}} \tau_n \, J_n(k_{\text{ELS}}\rho) H_n^{(2)}(k_{\text{ELS}}\rho_s) \cos[n(\phi-\phi_s)] & \text{for } \rho \leq \rho_s, \\ \sum_{n=0}^{N_{max}} \tau_n \, J_n(k_{\text{ELS}}\rho_s) H_n^{(2)}(k_{\text{ELS}}\rho) \cos[n(\phi-\phi_s)] & \text{for } \rho \geq \rho_s. \end{cases} \tag{1}$$

where $J_n(\cdot)$ is the Bessel function of order n and is chosen to represent the field for $\rho \leq \rho_s$ due to its non-singular behavior at the origin, while $H_n^{(2)}(\cdot)$ is the Hankel function of second kind and order n, and is chosen for $\rho \geq 0$ because it represents an outward propagating wave that complies with the radiation condition. The symbol τ_n is the Neumann number; i.e., $\tau_n = 1$ for $n = 0$, and $\tau_n = 2$ otherwise. Furthermore, N_{max} is the truncation limit in the numerical implementation of the infinite summation in the exact solution, chosen to ensure the convergence of this expansion. It is noted that $\varepsilon_{\text{ELS}} = \varepsilon_i$, $\mu_{\text{ELS}} = \mu_i$, and $k_{\text{ELS}} = k_i$, $i = 1$ and 2, respectively, when the ELS is in region 1 and 2, while $\varepsilon_{\text{ELS}} = \varepsilon_0$, $\mu_{\text{ELS}} = \mu_0$, and $k_{\text{ELS}} = k_0$ when the ELS is in region 3. The field $\vec{E}_{\text{ELS}}$ in (1) constitutes the known incident field for the scattering problem shown in Figure 1.

The unknown fields in each of the regions (i.e., the scattered field in the region containing the ELS and the total fields in the other regions) are likewise expanded in terms of cylindrical wave functions, and these can thus be expressed as

$$\vec{E}_{1s}(\rho,\phi) = -\hat{z} I_e \frac{\omega\mu_1}{4} \sum_{n=0}^{N_{max}} \tau_n \, C_{1n} J_n(k_1\rho)\cos[n(\phi-\phi_s)], \text{ for } \rho \le \rho_1, \tag{2a}$$

$$\vec{E}_{2s}(\rho,\phi) = -\hat{z} I_e \frac{\omega\mu_2}{4} \sum_{n=0}^{N_{max}} \tau_n \, [C_{2n} J_n(k_2\rho) + C_{3n} Y_n(k_2\rho)]\cos[n(\phi-\phi_s)], \text{ for } \rho_1 \le \rho \le \rho_2, \tag{2b}$$

$$\vec{E}_{3s}(\rho,\phi) = -\hat{z} I_e \frac{\omega\mu_0}{4} \sum_{n=0}^{N_{max}} \tau_n \, C_{4n} H_n^{(2)}(k_0\rho_1)\cos[n(\phi-\phi_s)], \text{ for } \rho \ge \rho_2, \tag{2c}$$

where C_{in}, with $i = 1,\ldots,4$ and $n = 0,1,2,\ldots,N_{max}$, are the unknown expansion coefficients and $Y_n(\cdot)$ is the Neumann function of order n. The expressions (1) and (2) represent multipole expansions of the fields, e.g., the $n = 0$ term corresponds to the monopolar mode, the $n = 1$ term corresponds to the dipolar mode, the $n = 2$ term corresponds to the quadrupolar mode, etc. The corresponding magnetic fields, which are required for the determination of the unknown expansion coefficients, are readily obtained from Faraday's law. Enforcing the electromagnetic field boundary conditions, i.e., requiring the tangential components of the electric and magnetic fields to be continuous at the interfaces at $\rho = \rho_1$ and $\rho = \rho_2$, it follows that the unknown expansion coefficients can be found from the following matrix equation,

$$\vec{C}_n = \left[\bar{\bar{M}}_n\right]^{-1} \vec{\Lambda}_n, \quad n = 0,1,2,\ldots,N_{max} \tag{3}$$

where $\vec{C}_n = [C_{1n}, C_{2n}, C_{3n}, C_{4n}]$ is the vector containing the four unknown expansion coefficients for the n'th term, and $\vec{\Lambda}_n = [\Lambda_{1n}, \Lambda_{2n}, \Lambda_{3n}, \Lambda_{4n}]$ is the excitation vector which depends on the location of the ELS. The elements of this excitation vector are shown in Table 1.

Λ_{in}	ELS in region 1	ELS in region 2	ELS in region 3
Λ_{1n}	$\mu_1 J_n(k_1\rho_s) H_n^{(2)}(k_1\rho_1)$	$-\mu_2 J_n(k_2\rho_1) H_n^{(2)}(k_2\rho_s)$	0
Λ_{2n}	$k_1 J_n(k_1\rho_s) H_n^{(2)\prime}(k_1\rho_1)$	$-k_2 J_n'(k_2\rho_1) H_n^{(2)}(k_2\rho_s)$	0
Λ_{3n}	0	$-\mu_2 J_n(k_2\rho_s) H_n^{(2)}(k_2\rho_2)$	$\mu_0 J_n(k_0\rho_2) H_n^{(2)}(k_0\rho_s)$
Λ_{4n}	0	$-k_2 J_n(k_2\rho_s) H_n^{(2)\prime}(k_2\rho_2)$	$k_0 J_n'(k_0\rho_2)\ H_n^{(2)}(k_0\rho_s)$

Table 1: *The elements Λ_{in}, $i = 1,2,3$ and 4, of the excitation vector $\vec{\Lambda}_n$ when the ELS is located in regions 1, 2, or 3.*

The matrix $\bar{\bar{M}}_n$ is a four-by-four matrix that depends on the values of the cylindrical waves at the two interfaces, and it is given by

$$\bar{\bar{M}}_n = \begin{bmatrix} -\mu_1 J_n(k_1\rho_1) & \mu_2 J_n(k_2\rho_1) & \mu_2 Y_n(k_2\rho_1) & 0 \\ -k_1 J_n'(k_1\rho_1) & k_2 J_n'(k_2\rho_1) & k_2 Y_n'(k_2\rho_1) & 0 \\ 0 & \mu_2\ J_n(k_2\rho_2) & \mu_2\ Y_n(k_2\rho_2) & -\mu_0\ H_n^{(2)}(k_0\rho_2) \\ 0 & k_2\ J_n'(k_2\rho_2) & k_2\ Y_n'(k_2\rho_2) & -k_0\ H_n^{(2)\prime}(k_0\rho_2) \end{bmatrix}. \tag{4}$$

In the above expressions, the prime denotes the derivative with respect to the entire argument.

The figures of merit to be employed in the numerical investigation are the total radiated power, the two-dimensional directivity, and the total as well as the differential scattering cross section, where the latter two parameters are evaluated in the case where the ELS is moved infinitely far away from the concentric

cylinders. Henceforth, these quantities are referred to as simply the total power, the directivity, and the total and differential cross sections, respectively. Since the configuration is infinite in the z-direction, all of the quantities are determined on a *per unit length* basis.

The total power, denoted by P_t, is given by the expression

$$P_t = \lim_{\rho\to\infty} \frac{1}{2\eta_0} \int_{\phi=0}^{2\pi} |\vec{E}_t(\rho,\phi)|^2 \rho d\phi, \tag{5}$$

where $\vec{E}_t$ denotes the total field in region 3. This equals either the sum of the field in (1) for $\rho \geq \rho_s$ and the field (2c) for region 3 when the ELS is in region 3, or it equals the field (2c) for region 3 when the ELS is located in either region 1 or 2. The relevant expression for the total field in (5) is easily obtained by introducing the large argument approximation of the Hankel function [30, Ch. 10]. The resulting expression for the total power becomes

$$P_t = \left(\frac{1}{4}\eta_0 I_e^2\right) \left[\frac{k_0}{4} \sum_{n=0}^{N_{max}} \tau_n^2 (3-\tau_n) |\alpha_n|^2\right], \tag{6}$$

where $\alpha_n = J_n(k_0\rho_s) + C_{4n}$ when the ELS is located in region 3, and $\alpha_n = C_{4n}$ when the ELS is located in either region 1 or 2. The power radiated by the ELS alone in free space, denoted P_i, is given by (5) with $\vec{E}_t$ replaced by $\vec{E}_{\text{ELS}}$ for $\rho \geq \rho_s$. In this case, N_{max} can be set to infinity and it is found that

$$P_i = \left(\frac{1}{4}\eta_0 I_e^2\right) \left[\frac{k_0}{4} \sum_{n=0}^{N_{max}} \tau_n^2 (3-\tau_n) |J_n(k_0\rho_s)|^2\right]_{N_{max}=\infty} = \left(\frac{1}{4}\eta_0 I_e^2\right) \left[\frac{k_0}{2}\right], \tag{7}$$

where the sum has been evaluated using the well-known result in [30, Ch. 10]. Of particular interest to the current investigation is the comparison of the total power in the presence of the concentric MTM cylinders to that radiated by the ELS alone. To this end, the so-called power ratio (PR) is introduced and this is given by

$$\text{PR} = \frac{P_t}{P_i} = \frac{1}{2} \sum_{n=0}^{N_{max}} \tau_n^2 (3-\tau_n) |\alpha_n|^2. \tag{8}$$

The directivity, D, is given by

$$D(\phi) = \lim_{\rho\to\infty} \frac{2\pi\rho |\vec{E}_t(\rho,\phi)|^2}{\int_{\phi=0}^{2\pi} |\vec{E}_t(\rho,\phi)|^2 \rho d\phi} = \frac{2\left|\sum_{n=0}^{N_{max}} \tau_n j^n \alpha_n \cos[n(\phi-\phi_s)]\right|^2}{\sum_{n=0}^{N_{max}} \tau_n^2 (3-\tau_n) |\alpha_n|^2}. \tag{9}$$

In the case where the ELS location is moved infinitely far away in region 3, i.e., for $\rho_s \to \infty$, it is moreover of interest to investigate the behavior of the differential and total cross section of the cylinders. The differential cross section, defined by the square of the ratio of the magnitude of the scattered far field (in region 3) to the magnitude of the incident field at the origin, evaluated when the ELS is moved infinitely far away from the cylinders along an arbitrary direction ϕ_s, is given by

$$\sigma_d = \lim_{\rho\to\infty} \lim_{\rho_s\to\infty\ ;\ \phi_s} \left[2\pi\rho \frac{|\vec{E}_{3s}(\rho,\phi)|^2}{|\vec{E}_{\text{ELS}}(\rho=0)|^2}\right] = \frac{4}{k_0} \left|\sum_{n=0}^{N_{max}} \tau_n C'_{4n} (-1)^n \cos[n(\phi-\phi_s)]\right|^2, \tag{10}$$

with the coefficient $C'_{4n} = C_{4n}/H_n^{(2)}(k_0\rho_s)$, where C_{4n} has been defined previously. Thus the coefficient C'_{4n} is obtained as a solution of (3), i.e., the same equation which yields C_{4n}, except from the fact that the term $H_n^{(2)}(k_0\rho_s)$, which is contained in the excitation vector when the ELS is in region 3, see Table 1, has now been canceled out.

The total scattering cross section, σ_t, defined by the ratio of the power, P_s, contained in the scattered far field to the incident power density, S_i, at the origin, again evaluated when the ELS is moved infinitely far away from the cylinders (i.e., for $\rho_s \to \infty$) along an arbitrary direction ϕ_s, is given by

$$\sigma_t = \lim_{\rho_s\to\rho_s\ ;\ \phi_s} \frac{P_s}{S_i} = \lim_{\rho\to\infty} \lim_{\rho_s\to\rho_s\ ;\ \phi_s} \frac{\int_{\phi=0}^{2\pi} |\vec{E}_{3s}(\rho,\phi)|^2 \rho d\phi}{|\vec{E}_{\text{ELS}}(\rho=0)|^2} = \frac{2}{k_0} \sum_{n=0}^{N_{max}} \tau_n^2 (3-\tau_n) |C'_{4n}|^2. \tag{11}$$

When the ELS is moved infinitely far away from the concentric cylinders, the incident field generated by the ELS constitutes locally a plane wave. Thus, the cross sections in (10) and (11) recover the usual plane wave cross sections.

Numerical results for the above figures of merit are presented and discussed in the following section. It is understood that while the ELS and concentric MTM cylinders can be considered as a radiating system when the ELS is located in regions 1 and 2, as well as when it is located in region 3 at moderate distances from the structure, it can be considered as a scattering system when the ELS is moved infinitely far away from the cylinder. Thus, both the radiating and scattering properties of the structures will be investigated. Throughout the following investigations, a structure is referred to by its properties in region 1 and 2. For instance, a DPS-MTM structure, where the MTM can be either a DNG, ENG, or MNG material, indicates that region 1 consists of a DPS material while region 2 consists of the selected MTM. However, in the majority of the following cases, DPS and DNG materials are employed.

3 Resonance condition - derivation and discussion

In order to provide more insight into the physics associated with the electrically small resonant cylindrical structures, it is useful to first find the conditions for which the enhancements of the total power, total and differential cross sections will occur. Since both the total power (6) and the cross sections (10) and (11) are proportional to $|C_{4n}|^2$, large values of these quantities will result if the amplitude of the expansion coefficient C_{4n} is large. Such large values of the expansion coefficients are related to the presence of the so-called natural modes, and the corresponding peaks in the expansion coefficients are referred to as natural resonances, see e.g., [4], [10]-[12] and the works referenced therein. When the structure of interest is composed of DPS materials, the natural resonances occur only if the size of the structures is on the order of, or larger than, the wavelength inside the material [4], [10]-[12]. These wavelength-sized natural resonances will be discussed briefly in Section 6. However, when the structure is composed of combinations of DPS, DNG, and/or SNG materials, the scattering coefficients may exhibit peaks, and thus resonances, even if the structures are significantly smaller than the wavelength, and such resonances are attributed to the clever pairing of DPS, DNG, and/or SNG materials [4], [10]-[12]. In [4], [10] and [11] these resonances are referred to as interface resonances, but here they are designated as subwavelength-sized natural resonances.

To find the condition for which the amplitudes of the expansion coefficient C_{4n} become large, one first notes that, according to (3), these are proportional to the product of the inverse of the matrix $\bar{\bar{M}}_n$ and the excitation vector $\vec{\Lambda}_n$. Thus, C_{4n} is inversely proportional to the determinant of $\bar{\bar{M}}_n$. When the magnitude of this determinant attains a minimum, the amplitude of C_{4n} becomes large, and a resonance occurs, thus leading to enhancements of the total power and the total and differential cross sections. Since the structures are electrically small, the small argument expansions of the functions contained in $\bar{\bar{M}}_n$, which hold when the products $|k_1|\rho_1$, $|k_2|\rho_1$, $|k_2|\rho_2$, and $|k_0|\rho_2$ are much smaller than unity, are used to derive an approximate analytical expression for the resonance condition. It must be stressed that such a derivation is greatly facilitated by assuming the materials in the three regions to be lossless. For the range of parameters to be investigated here, and with the assumption of lossless materials in regions 1 and 2, it can be shown that C_{4n} exhibits a resonance for when the approximate condition

$$\frac{\rho_1}{\rho_2} \approx \sqrt[2n]{\frac{(\mu_2+\mu_1)(\mu_2+\mu_0)}{(\mu_2-\mu_1)(\mu_2-\mu_0)}}, \tag{12}$$

is met. This condition is used here to determine, for a given set of material parameters, the approximate ratio of ρ_1 and ρ_2 which yields a resonant concentric pair of lossless MTM cylinders[3]. The resonance condition given by (12) depends on the mode number, n, a careful choice of material parameters, and only on the ratio of the inner and outer radii of region 2, and thus not on how small either of these radii are individually. Moreover, it is independent of the frequency in the sense that a resonance can be attained for all frequencies for which a given set of material and geometrical parameters make the structure electrically small. In order to define a given resonant structure on the basis of (12) one can

[3]The adjective *lossless* is omitted in the following discussion. The influence of losses is taken into account in Section 5.

start by selecting its material parameters, and its inner (outer) radius. Then, the condition in (12) is used to determine the outer (inner) radius for a given mode number n. Consequently, this mode will be the dominant mode excited in this structure. It is worth emphasizing that (12) holds for $n \geq 1$, and that for the range of parameters to be investigated here, the monopolar mode does not show a resonant behavior. This implies that there is no electrically small monopolar structure that will have a resonance. The relation (12) is identical to the one obtained in [10], [11] for plane wave scattering from similar cylindrical structures. Though certain small terms have been neglected in the derivation of (12), this condition constitutes a very accurate approximation for the radii ratio at resonance, as will be demonstrated numerically below. Therefore, the expression (12) serves as a guideline to estimate the resonant configuration, i.e., as a starting point for the numerical analysis.

The resonance condition in (12), which for the TM polarization investigated here is independent of the permittivities of the different regions, requires that at least one of the parameters μ_1 or μ_2 is negative. In particular, it can be shown that (12) can be satisfied for

- $\mu_1 > 0$ and $\mu_2 < 0$ if $|\mu_2| < -\min(|\mu_1|, \mu_0)$ or $|\mu_2| > -\max(|\mu_1|, \mu_0)$,
- $\mu_1 < 0$ and $\mu_2 > 0$ if $\mu_2 > |\mu_1| > \mu_0$ or $\mu_2 < |\mu_1| < \mu_0$,
- $\mu_1 < 0$ and $\mu_2 < 0$ if $|\mu_2| > \mu_0 > |\mu_1|$ or $|\mu_2| < \mu_0 < |\mu_1|$.

The DPS-DNG structures are emphasized in the following discussions, while a brief account on the use of SNG materials will be made in Section 7.

An interesting observation for the configurations in which the ELS is located in region 1 along the axis of the cylinders, i.e., in which $\rho_s = 0$, can now be made. From Table 1 it is understood that the non-zero elements of the excitation vector $\vec{\Lambda}_n$ for the ELS in region 1 are proportional to $J_n(k_1\rho_s)$. Since $J_n(0) = 0$ for $n > 0$, only $C_{i0} \neq 0$ and, thus, only the monopolar mode radiates when the ELS is located on the axis of the cylinders. In particular, according to the discussion following (12), there is no electrically small monopolar resonant structure for the range of parameters to be investigated here. Consequently, one concludes that the resonances associated with excitation of higher-order modes ($n = 1, 2, 3, \ldots$) in the electrically small concentric MTM cylinders occur only if the ELS is located off the cylinder axis, i.e., for $\rho_s > 0$. These observations highlight one of the most important differences between the electrically small 2D and 3D structures since the latter lead to resonances when the source is located at the origin [12], [20]-[21]. Moreover, the present findings for the $\rho_s = 0$ case are in agreement with [28], where it was noted that such 2D configurations do not affect the field distribution or the power radiated by the ELS. However, as demonstrated below, the 2D DPS-DNG configurations with $\rho_s > 0$ lead to a resonant behavior and, thus, an enhancement of, e.g., the total power radiated by the ELS when situated close to (or surrounded by) the structure. This behavior if obviously in sharp contrast to the $\rho_s = 0$ case. The presence of resonances in several DPS-DNG structures and their absence in the corresponding DPS-DPS cases will be demonstrated below. Furthermore, as reported in [9] and [15], and demonstrated additionally in Section 6, the larger cylindrical structures exhibit resonances for both the DPS-DPS and DPS-DNG cases when the ELS is located at the center of the cylinders.

4 Numerical results

4.1 Resonant configurations - definition

The material and geometrical parameters selected to illustrate the results for the electrically small resonant structures are summarized in Table 2. Regions 1 and 3 are chosen to be free space, while region 2 is taken to be a DNG material. For these fixed material parameters, the condition in (12) was used to define the approximate geometrical parameters that produce the resonant dipolar and quadrupolar modes. The associated structures are referred to as the resonant dipolar and quadrupolar structures, respectively. The positive material parameters in region 2 of the corresponding DPS-DPS structures are also indicated in Table 2. Thus, the structures under examination are either a DNG or a DPS cylindrical shell in the presence of an ELS, which can be located in any of the three regions. Throughout these investigations the frequency of operation is $f_0 = 300$ MHz, implying that the free-space wavelength is $\lambda_0 = 1$ m. Note that the numerical code was used to determine the precise radii at which the resonance is achieved.

Structure	ε_2	μ_2	ρ_1 [mm]	ρ_2 [mm]
Dipolar	$\pm\varepsilon_0$	$\pm 4\mu_0$	6 mm	10 mm
Quadrupolar	$\pm\varepsilon_0$	$\pm 4\mu_0$	3.8729 mm	5 mm

Table 2: *Material and approximate geometrical parameters for Region 2 of the electrically small resonant dipolar and quadrupolar configurations. Positive values of the material parameters indicate a DPS material while negative values indicate a DNG material.*

From both relation (12) and Table (2) it follows that for fixed material parameters a considerably thinner structure is needed to excite the quadrupolar mode than the dipolar mode. One also notes that the diameter of the resonant dipolar structure is 20 mm , or $\lambda_0/50$ (which corresponds to $k_0\rho_2 = 0.063$), while that of the quadrupolar structure is 10 mm, or $\lambda_0/100$ (which corresponds to $k_0\rho_2 = 0.032$).

4.2 Electrically small dipolar structures

The electrically small resonant dipolar DPS-DNG structure defined in Section 4.1 is examined with respect to its radiation and scattering properties. Furthermore, it is compared to the corresponding DPS-DPS structure.

4.2.1 Total power

Figure 2 shows the PR for the dipolar DPS-DNG and DPS-DPS structures as a function of the outer radius ρ_2, when the inner radius is fixed at $\rho_1 = 6$ mm. The ELS is located in region 1 at $\rho_s = 5.99$ mm. The ELS location is chosen near the interface of the DPS and DNG layers because it produces the largest peak value of the PR.

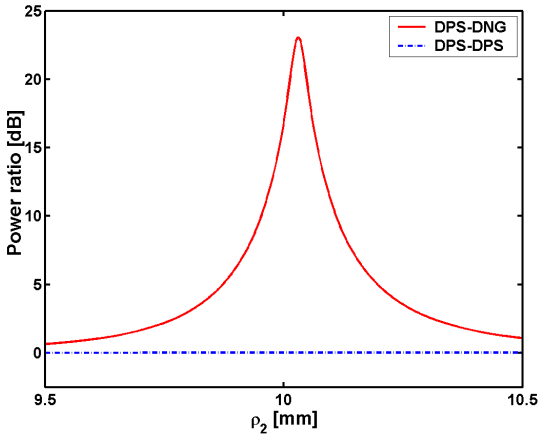

Figure 2: *Power ratio as a function of the outer shell radius ρ_2 for the DPS-DNG and DPS-DPS dipolar structures with $\rho_1 = 6$ mm when the ELS is located in region 1 at $\rho_s = 5.99$ mm.*

For the DPS-DNG structure, a resonance peak (of value or PR $\approx$ 23 dB or PR $\approx$ 200) is found for $\rho_2 = 10.03$ mm, which is very close to the approximate value of 10 mm obtained from (12). The PR values for the corresponding DPS-DPS structure are also given in Figure 2. In contrast to the DPS-DNG structure, no resonances are observed for this DPS-DPS structure, where the PR is very close to unity. Similar results, not included here, have been obtained for DPS-DNG and DPS-DPS dipolar structures when the ELS is located in region 2 or 3.

To demonstrate the influence of the ELS location on the resonant enhancements of the total power, Figures 3(a), 3(b), and 3(c) show the PR as a function of the ELS position, ρ_s, with the ELS in regions 1, 2, and 3, respectively, for the DPS-DNG and DPS-DPS structures having the fixed radii: $\rho_1 = 6$ mm

and $\rho_2 = 10.03$ mm. In particular, the ELS location varies in the interval $\rho_s \in [1 - 5.99]$ mm in Figure 3(a), in $\rho_s \in [6.01 - 9.99]$ mm for Figure 3(b), and in $\rho_s \in [10.01 - 25]$ mm for Figure 3(c).

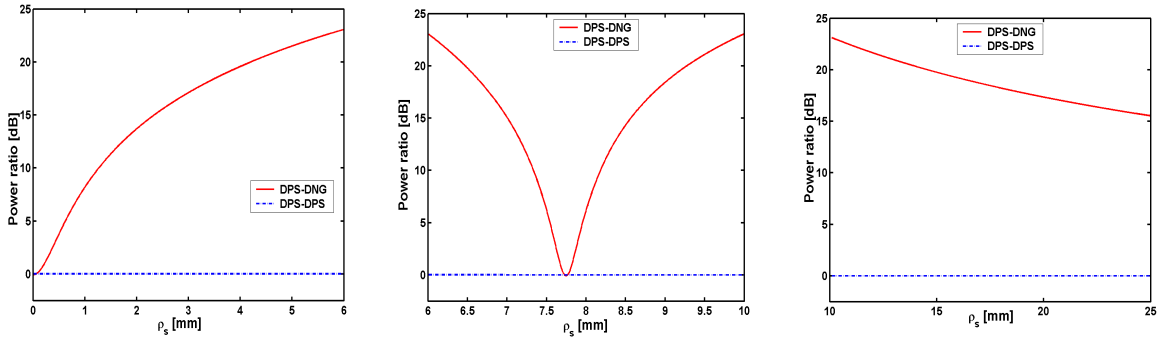

(a) (b) (c)

Figure 3: *Power ratio as a function of the ELS location ρ_s for the dipolar DPS-DNG and DPS-DPS structures when the ELS is located in region 1 (a), region 2 (b), and region 3 (c).*

In all cases and regardless of the location of the ELS, the DPS-DPS structures offer no enhancement, i.e., the PR value is close to unity. In contrast, the corresponding DPS-DNG structures offer very large PR values, this being particularly true when the ELS is close to the surface of the DNG shell.

For increasing ρ_s values in region 1, the PR increases from approximately zero to approximately 23 dB. The fact that there is no enhancement when the ELS is near the origin confirms the previous observation that the ELS must be offset from the axis to excite, in this case, the resonant dipolar mode. As the near-field investigations discussed below will confirm, the monopolar mode is dominant for small values of ρ_s.

For the ELS in region 2, the largest PR values are obtained when the ELS is close to the interfaces at ρ_1 and ρ_2. However, the behavior of the PR is particularly interesting because it exhibits a minimum for a specific ELS position. This minimum occurs at $\rho_s = 7.746$ mm where the total power radiated by the ELS in the presence of the DNG shell is actually slightly lower than the power radiated by the ELS alone. As the ELS is moved in the DNG region, it is found that its ability to excite the resonant dipolar mode changes. In particular, for the minimum PR location value, it is found that the ELS couples only to the monopolar mode, a fact that will likewise be confirmed via the near-field results given below. Since the ELS can not couple to the dipolar mode, it can not cause a resonant enhancement of the total power. In addition to these findings, it is interesting to note that the PR is considerably less sensitive with respect to the position of the ELS than it is to the outer radius of the MTM layer.

For the ELS being located in region 3, the PR is slowly decreasing for increasing ρ_s values.

4.2.2 Near field

Next, the above findings are elucidated with the near-field investigations. For all of the following near-field plots, the total electric near field, denoted by $\vec{E}(\rho, \phi)$, or more specifically, the quantity $20 \log_{10} |\vec{E}(\rho, \phi)|$, where $|\vec{E}(\rho, \phi)|$ has been normalized by 1 V/m, is shown in a circular region of radius $3\rho_2$ centered at the cylinder axis (z-axis).

Figure 4(a) shows the near field of the ELS located in free space, while Figure 4(b) shows the near field of the DPS-DPS structure. In both cases the ELS is located at $\rho_s = 0.001$ mm. As can be observed, the field radiated by the ELS in free space is, of course, of the monopolar form. The near field in Figure 4(b) is very similar to the one depicted in Figure 4(a). This implies that the DPS-DPS structure practically does not influence the radiation from the ELS. Consequently, the electrically small DPS-DPS structure is not expected to lead to any enhancement of the desired quantities, e.g., the total power, this being in line with the behavior of the DPS-DPS structure observed in Figures 2 and 3. Similar near-field results, not included here, for the DPS-DPS structure are obtained for other locations of the ELS in regions 1, 2, and 3.

The near fields for the resonant dipolar DPS-DNG structure are depicted in Figures 5 and 6. When the ELS is located at $\rho_s = 0.001$ mm, the near field has the monopolar form observed in Figure 5(a). This

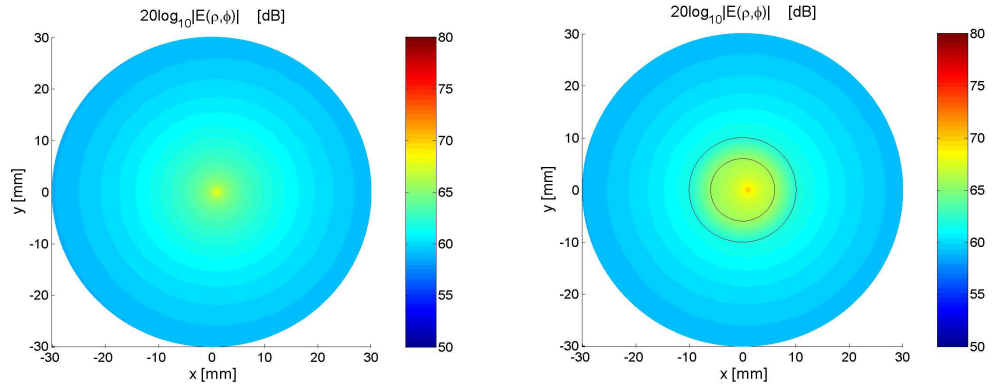

(a) (b)

Figure 4: *Electric near field of the ELS in free space (a), and of the DPS-DPS structure (b). In both cases, the ELS is located at* $\rho_s = 0.001$ *mm. Curves representing the cylindrical surfaces of the DPS-DPS structure are also shown in (b).*

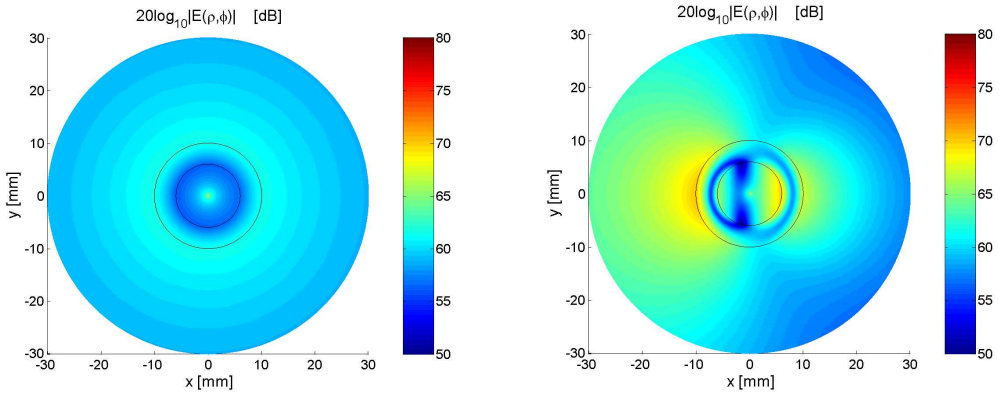

(a) (b)

Figure 5: *Electric near field of the dipolar DPS-DNG structure when the ELS is located at* $\rho_s = 0.001$ *mm (a), and* $\rho_s = 0.125$ *mm (b). Curves representing the cylindrical surfaces of the structure are also shown.*

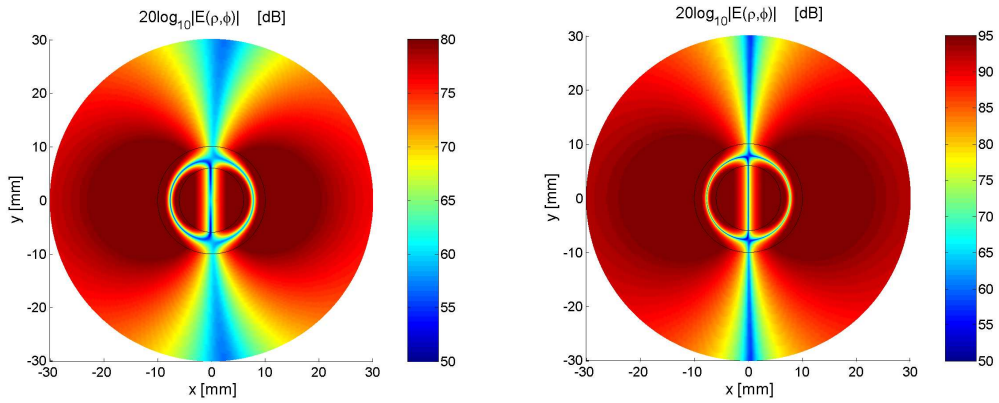

(a) (b)

Figure 6: *Electric near field of the dipolar DPS-DNG structure when the ELS is located at* $\rho_s = 1$ *mm (a), and* $\rho_s = 5.99$ *mm (b). Note that the dynamic range in (b) is larger than the one in (a). Curves representing the cylindrical surfaces of the structure are also shown.*

confirms that for locations of the ELS close to the origin, the monopolar mode is indeed the dominant one, and thus, that no enhancement of the total power is expected for such ELS locations. This is in agreement with the previous statements regarding the necessity of exciting the higher order modes in order to obtain an enhancement. This also means that for these ELS locations, the field radiated by the ELS is not significantly affected by the presence of the DPS-DNG structure. However, as the ELS is moved just slightly away from the origin to $\rho_s = 0.125$ mm, the monopolar mode is mixed with the dipolar mode, as confirmed by Figure 5(b). Moving the ELS even further from the origin, e.g., to $\rho_s = 1$ mm, leads to the near field shown in Figure 6(a) that has a form, which is clearly dominated by the dipolar mode. At this ELS location, an enhancement of about 8 dB of the total power is in evidence in Figure 3(a). As is apparent in Figure 6, these dipolar mode enhancements become even more pronounced as the ELS is moved closer to the DNG shell, e.g., to $\rho_s = 5.99$ mm, where the dipolar mode is excited most strongly. This stronger excitation of the dipolar mode as the ELS is moved closer to the DNG shell is also responsible for the increased symmetry in the total field, which, for example, is present in Figure 6(b).

If the ELS is located in regions 2 or 3, the near fields have a dipolar form when the ELS is located near the surfaces of the DNG shell. This indicates that the maximum PR shown in Figure 3 is a result of the ELS exciting a resonant dipolar mode. When the ELS is in region 3 and is moved further away from the DNG shell, its ability to couple strongly to the dipolar mode is gradually suppressed. This explains the behavior shown in Figure 3(c).

As revealed by Figure 3 (b), the PR of the resonant DPS-DNG structure is altered significantly as the ELS is moved through region 2. In particular, no enhancement is found for $\rho_s = 7.746$ mm. The near field for this particular location is depicted in Figure 7 where a monopolar form is observed at large distances.

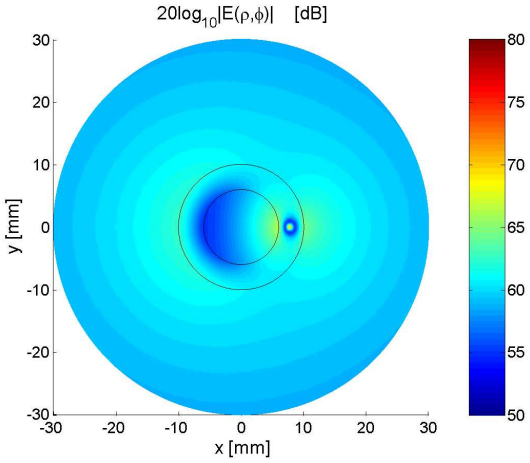

Figure 7: *Electric near field of the resonant dipolar DPS-DNG structure. The ELS is located in region 2 at* $\rho_s = 7.746$ *mm.*

Thus, as noted earlier in connection with the PR results, the ability of the ELS to excite the dipolar mode in this resonant DPS-DNG structure changes significantly as it is moved though the DNG shell, and is, in fact, lost when the ELS is located at $\rho_s = 7.746$ mm. The observation of the monopolar mode for that particular ELS location is rather interesting since the present DPS-DNG structure was designed specifically to excite the dipolar mode as the dominant one. This suggests that when the ELS location is close to this critical value, the near field is a mixture of the dipolar and the stronger monopolar mode. The strong presence of the monopolar mode results in the reduced enhancement of the radiated power observed in Figure 3(b). Similar gradual transformations of the near field have been observed in Figures 5(a) and 5(b) for the ELS locations close to the origin. These gradual transformations of the pattern as the position of the ELS is changed in the different regions will be analyzed further in Section 4.2.2.

Before closing this section, the following observations are in order. The results in Figure 6 show that the near fields for $\rho_s = 1$ mm and $\rho_s = 5.99$ mm are very similar to each other. This means that once the

resonant dipolar mode is excited, its form is almost unaffected by the location of the ELS, and therefore it constitutes the natural dipolar mode of the structure. Therefore, in order to have such a mode dominate the behavior, the ELS must be placed at locations where the field is maximum, which is why it is excited most strongly when the ELS is near the surfaces of the DNG shell. On the other hand, it is very weakly excited, or not excited at all, if the ELS is placed at locations for which the field of the dipolar mode is minimum and, hence, the coupling to that mode is minimized. Among others, these low dipolar field locations are found near the origin, as well as inside region 2. More specifically, the minimum for region 2, e.g., in Figure 6(a), is attained at $\rho = 7.801$ mm, while that in Figure 6(b) is attained at $\rho = 7.755$ mm. These values are very close to $\rho_s = 7.746$ mm at which the minimum PR was found for the ELS locations inside region 2. This confirms that the excitation of the dipolar mode is very weak for such ELS locations. This behavior also explains why the monopolar mode is dominant, and hence no enhancement of the total power is found, when the ELS is located at positions where the near field of the dipolar mode is very low. These observations are general and therefore also apply for the quadrupolar (and even higher order) structures considered later in this manuscript.

4.2.3 Directivity

Having demonstrated, both analytically and numerically, the possibility of designing electrically small resonant MTM-based structures, where the resonant effects in such structures were explained in terms of the excitation of a given resonant mode as the dominant one, it is next of interest to examine the radiation patterns of such structures.

Figure 8(a) shows the directivity patterns for a number of ELS locations for the DPS-DNG and DPS-DPS structures.

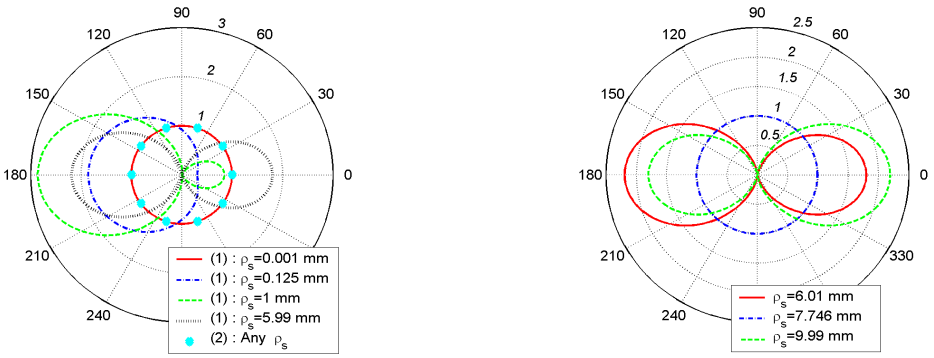

(a) (b)

Figure 8: *Directivity for various ELS locations in region 1 for both DPS-DPS (labeled by (2)) and DPS-DNG structures (labeled by (1)) (a), and in region 2 for only DPS-DNG structures (b).*

For the DPS-DNG structure, these directivity results are in agreement with the near-field results presented above. In particular, close to the origin, i.e., for $\rho_s = 0.001$ mm, the structure acts as an omnidirectional radiator and the directivity pattern is monopolar. However, for $\rho_s = 0.125$ mm, the directivity has a form, which is a mixture of more modes, and the maximum directivity, denoted by D_{max}, which is attained in the $\phi = 180^o$- direction, equals $D_{max} = 1.86$. For $\rho_s = 1$ mm and 5.99 mm, the directivity takes on the dipolar form, although it is not symmetric, and the maximum directivities, likewise attained in the $\phi = 180^o$- direction, are $D_{max} = 2.86$ and $D_{max} = 2.15$, respectively. It is observed that the asymmetry in the pattern is reduced and is accompanied with the reduction of the maximum directivity, as the location of the ELS is moved towards the DNG shell. In comparison, the directivity of the corresponding DPS-DPS structure has a monopolar form, regardless of the ELS location. Thus, apart from enhanced PR values, an electrically small resonant dipolar DPS-DNG structure provides one with the possibility of reshaping the pattern from the monopolar form to the dipolar one by changing the location of the ELS.

When the ELS is in region 2, a dipolar pattern is found for the DPS-DNG structures when the ELS is located near either of the surfaces of the DNG shell, with $D_{max} = 2.19$, while the directivity has

a perfectly monopolar form for $\rho_s = 7.746$ mm. This behavior is illustrated in Figure 8(b) and is in agreement with the PR and near-field results. It is linked to the previously mentioned gradual transition from the dipolar to the monopolar and back to the dipolar mode of radiation. This behavior is further illustrated in Figure 9(a), where the directivity is given for various ELS locations slightly to the left and right of $\rho_s = 7.746$ mm, for $\phi_s = 0^o$. For $\rho_s = 7.5$ mm, the directivity takes on an asymmetric dipolar form for which the main lobe is in the $\phi_s = 180^o$- direction with $D_{max} \approx 3$, while for $\rho_s = 7.7$ mm, it is a mixture of more modes with $D_{max} \approx 2$ attained along the same direction. This is also the case for $\rho_s = 7.8$ mm. On the other hand, for $\rho_s = 8$ mm, the directivity again has a dipolar form with $D_{max} \approx 3$ but now with the main lobe in the direction $\phi = 0^o$. Thus, the main lobe of the directivity pattern is found to be in the same direction as the displacement of the ELS from $\rho_s = 7.746$ mm. In regards to these observations of asymmetry, one also notes from Figures 8(b) and 9(a), that with the ELS location being displaced along the x-axis, the patterns found on both sides of $\rho_s = 7.746$ mm are mirror images of each other with respect to the y-axis. The results of Figures 8 and 9(b) clearly illustrate how the directivity is reshaped from the dipolar to monopolar, and back to the dipolar form, this being in agreement with Figure 3(b).

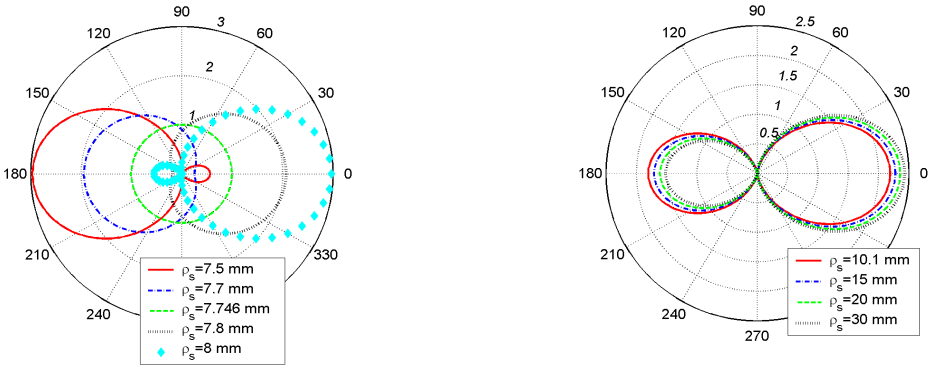

(a) (b)

Figure 9: *Directivity for dipolar DPS-DNG structures for various ELS locations around the critical value of $\rho_s = 7.746$ mm in region 2 (a), and in region 3 (b).*

When the ELS is in region 3 at $\rho_s = 10.1,\ 15,\ 20$ and 30 mm, respectively, the directivity takes on the dipolar forms shown in Figure 9(b). Within the range of ρ_s values investigated here, more power is radiated in the $\phi = 0^o$- direction and the pattern becomes increasingly asymmetric as the ELS moves further away from the DNG shell.

4.2.4 Total and differential cross sections

When the ELS is located in region 3 and is moved infinitely far away from the cylinders, it is of interest to investigate the behavior of the total and differential cross sections, σ_t and σ_d, respectively, given by (10) and (11) in Section 2. This corresponds in practice to the situation where a TM polarized uniform plane wave is incident on the structure from the direction ϕ_s. Without loss of generality, it is assumed that the ELS is moved to infinity along the $\phi_s = 0^o$- direction.

Figure 10 shows σ_t as a function of the outer shell radius ρ_2 when the inner radius is at $\rho_1 = 6$ mm. Results for both the dipolar DPS-DNG and DPS-DPS structures are shown.
While the total cross section of the DPS-DPS structure is very low, it is considerably enhanced by the presence of the DNG shell, in particular for the case with $\rho_s = 10.03$ mm where a resonance peak of magnitude close to 1 dB is observed even though the structure is electrically small. Furthermore, the resonance peaks observed in the PR and total cross section figures occur for the same geometrical parameters for the DPS-DNG structure. With the terminology introduced in [12] for the corresponding sphere case, the present radiating and scattering systems are said to be reciprocal.

The differential cross section is depicted in Figure 11 for the DPS-DNG and DPS-DPS structures. Both patterns have a "pure" dipolar form since the differential cross section is determined only by the

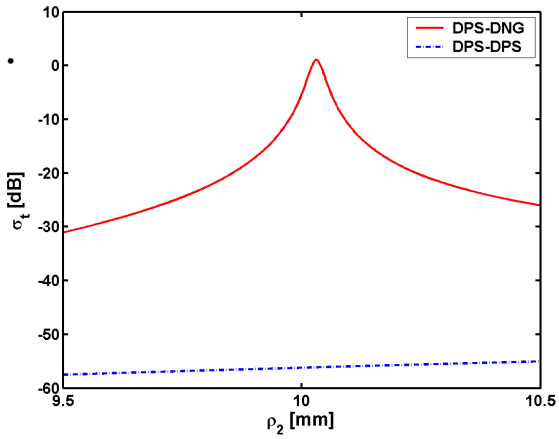

Figure 10: *The total cross section σ_t as a function of the outer shell radius ρ_2 for the dipolar DPS-DNG and DPS-DPS structures.*

scattered field terms. However, the differential cross section of the resonant DPS-DNG structure is found to be considerably larger (the maximum σ_d is $\sigma_{d,max} = 2.54$) than that of the corresponding DPS-DPS structure (where $\sigma_d = 4.88 \times 10^{-6}$).

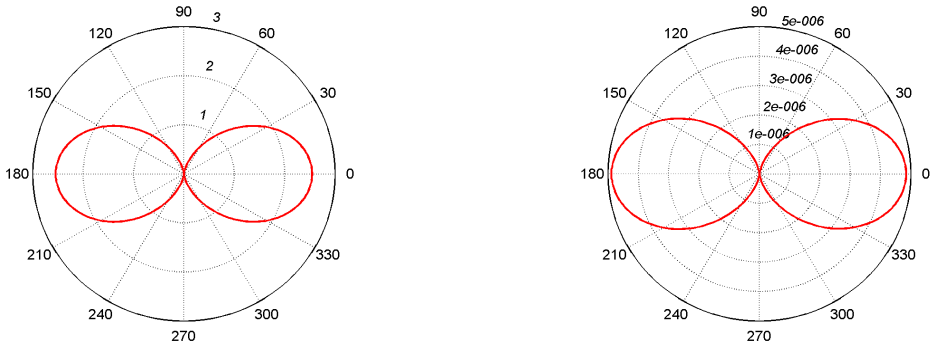

(a) (b)

Figure 11: *The differential cross section σ_d for various ELS locations for the dipolar DPS-DNG (a) and DPS-DPS (b) structures. Note that the scale in Figure 11(b) has a very small dynamic range.*

In concluding this section, it is interesting to note that if the same order of magnitude of σ_t and σ_d produced by the electrically small resonant dipolar DPS-DNG structure considered above is to be obtained by a DPS-DPS structure having the same material parameters and inner radius, its outer radius ρ_2 would have to be increased by approximately 20 times. This implies that the electrically small resonant dipolar DPS-DNG structure exhibits characteristics generally attributed to larger scatterers.

4.3 Electrically small quadrupolar structures

In this section, the radiation and scattering properties of the electrically small resonant quadrupolar DPS-DNG structure defined in Section 4.1 are examined and compared to the corresponding DPS-DPS structure.

Figure 12(a) shows the PR as a function of the outer radius ρ_2 for the quadrupolar DPS-DNG and DPS-DPS structures. The ELS is located in region 1 at $\rho_s = 3.8$ mm. As for the dipolar mode, the location of the ELS near the DPS-DNG interface is chosen because it produces the largest PR.

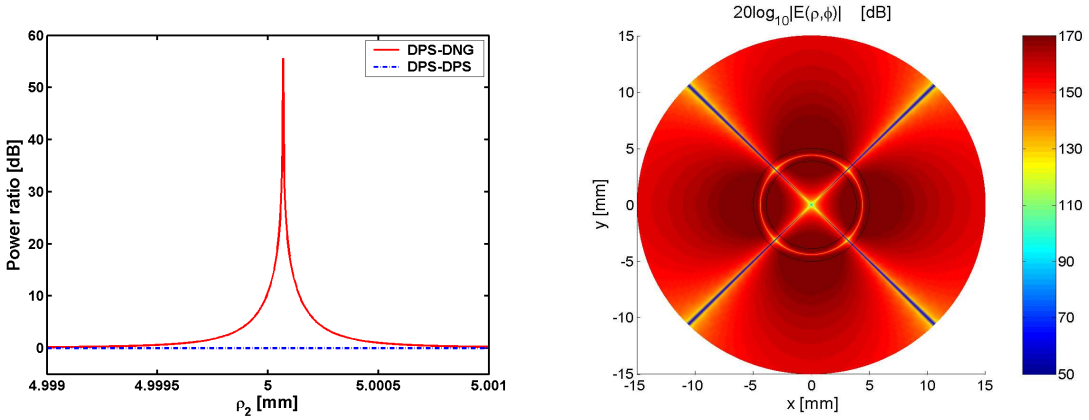

(a) (b)

Figure 12: *(a) Power ratio as a function of the outer shell radius ρ_2 for the quadrupolar DPS-DNG and DPS-DPS structure. (b) Electric near field of the resonant quadrupolar DPS-DNG structure. In both (a) and (b), the ELS is located in region 1 at $\rho_s = 3.8$ mm.*

Resonance, and thus the enhancement of the total power, is indeed observed in Figure 12(a) for the DPS-DNG structure with $\rho_s = 5.000068$ mm. This value is very close to the approximate value of 5 mm listed in Table 2. For this resonant structure, the maximum obtainable PR is approximately 55 dB. In comparison to the dipolar case, the enhancements for the quadrupolar case are significantly larger, but the resonance is also extremely narrow and very sensitive to even very slight changes in the material and the geometrical parameters. Figure 12(a) also shows that no enhancements of the total power are obtained for the corresponding DPS-DPS structure.

In order to confirm that these enhancements of the total power are indeed due to the resonant excitation of the quadrupolar mode in the DPS-DNG structure with $\rho_s = 5.000068$ mm, the electric near field for this DPS-DNG structure when the ELS is located at $\rho_s = 3.8$ mm is illustrated in Figure 12(b). Indeed the near field in this case has the quadrupolar form, thus demonstrating that this mode is indeed the dominant one. Moreover, the near-field values of the field in a given direction in Figure 12(b) are notably larger than the corresponding near-field values for the dipolar DPS-DNG structure, see Figure 6(b). This also explains why the PR values are higher for the quadrupolar than for the dipolar DPS-DNG structure. Results similar to those reported in Figure 12 are obtained for the same quadrupolar DPS-DNG and DPS-DPS structures when the ELS is located in regions 2 and 3

As with the resonant dipolar structures discussed in Section 4.1, it is of interest to examine the influence of the ELS location on the PR obtained by the quadrupolar structures. To this end, Figures 13(a), 13(b) and 13(c) show, respectively, the PR as a function of the ELS position, ρ_s, in regions 1, 2, and 3 for the DPS-DNG and DPS-DPS quadrupolar structures having the fixed radii: $\rho_1 = 3.8729$ mm and $\rho_2 = 5.000068$ mm. In particular, the ELS location varies in the interval $\rho_s \in [1 - 3.8]$ mm for Figure 13(a), in $\rho_s \in [3.9 - 4.99]$ mm for Figure 13(b), and in $\rho_s \in [5.1 - 15]$ mm for Figure 13(c).

It is found that the DPS-DPS quadrupolar structures offer no enhancement, while the corresponding DPS-DNG structures offer very large values of the PR, this being particularly true when the ELS is located near the surfaces of the DNG shell. Moreover, it is clear that as the ELS location changes in the three regions, the behavior of the PR for the DPS-DNG quadrupolar structures is similar to that found in Figure 3 for the corresponding dipolar structures. Therefore, only the main distinctions between the dipolar and quadrupolar cases will be made in the following. In particular, it is found that the enhancements of the total power reported in Figure 13, reaching peak values as high as PR ≈ 55 dB for the ELS locations near the interfaces between the regions, are considerably higher than the PR ≈ 23 dB obtained for the dipolar structures. The existence of a sharp minimum in the quadrupolar DPS-DNG structure also exists, as Figure 13(b) confirms, in similitude with the dipolar DPS-DNG structure. Furthermore, the ability of the ELS to excite the dominant resonant mode changes significantly as its location is moved through the DNG shell. As for the resonant dipolar DPS-DNG structure, the change in the ELS location has a direct impact on the PR values as well as the shape of the near-fields and the directivity. Specifi-

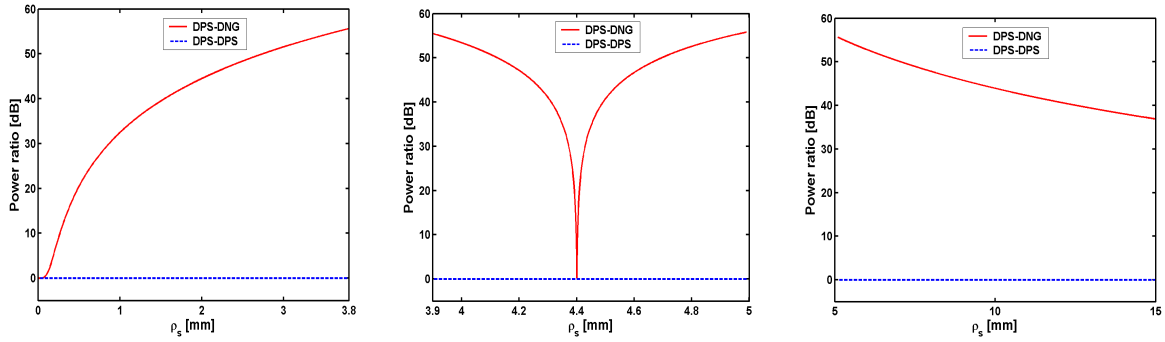

(a) (b) (c)

Figure 13: *Power ratio as a function of the ELS location ρ_s for the quadrupolar DPS-DNG and DPS-DPS structures when the ELS is located in region 1 (a), region 2 (b), and region 3 (c).*

cally, no enhancement of the total power is found for $\rho_s = 4.400486$ mm. This is due to the fact that for this location of the ELS, the the monopolar mode is dominant [4]. This is confirmed by the results given in Figure 14 which shows the directivity for a number of ELS locations in region 2 for the DPS-DNG structure.

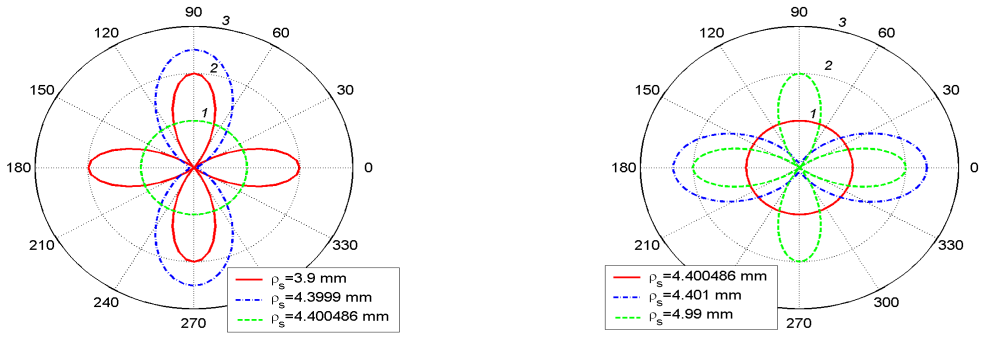

(a) (b)

Figure 14: *Directivity for various ELS locations in region 2 for the quadrupolar DPS-DNG structure.*

While the directivity has a symmetric quadrupolar form (with $D_{max} \approx 2$) when the ELS is close to the DNG surfaces, it has a symmetric, and rather directive, dipolar form (with $D_{max} \approx 2.5$) with the main lobes along the y- and x- axes, respectively, when the ELS is just to the left (e.g., at $\rho_s = 4.3999$ mm) and right (e.g., at $\rho_s = 4.401$ mm) of $\rho_s = 4.400486$ mm. Moreover, when the ELS is located at $\rho_s = 4.400486$ mm, a clear monopolar pattern is produced. This explains the null in the PR results shown in Figure 13(b). These pattern results demonstrate that it is possible to achieve a gradual transformation of the directivity from the quadrupolar to the dipolar to the monopolar form, and back again, as the ELS is moved through the DNG shell. The details of this transformation are illustrated in Figure 15, where the directivity is shown for ELS locations near $\rho_s = 4.3999$ mm, $\rho_s = 4.400486$ mm, and $\rho_s = 4.401$ mm, respectively, in Figures 15(a), 15(b), and 15(c). It is interesting to observe that rather directive beams of $D_{max} \approx 2.9$ are found in Figures 15(a) and 15(c). The pattern variations shown in Figure 15 are in agreement with the PR values reported in Figure 13(b). They serve as a confirmation

[4]With reference to the remarks at the end of Section 4.2.2, the excited quadrupolar mode is likewise a natural mode of the structure in the sense that its form basically is unaffected by the ELS locations. Thus, placing the ELS at locations where the field is very low will not excite this mode. With reference to Figure 12(a), these low field locations are, amongst others, near the origin as well as inside region 2 in a very narrow annular region centered on the radius $\rho = 4.4$ mm.

that a particular resonant mode must be excited to achieve enhancements of the total radiated power. It is important to emphasize that not only can one control the modal form of the directivity pattern with the DPS-DNG quadrupolar structure, but one can also control the direction of the enhancement. The change between the vertical and horizontal dipolar patterns as the ELS is located at specific positions confirms this behavior. The gradual transformations from the monopolar to the dipolar to the quadrupolar mode of radiation are also found when the ELS location moves in region 1 from the origin toward the DNG shell. Thus, the quadrupolar structure, as compared to the dipolar one, offers an additional mode of radiation and, thus, an additional degree of freedom in controlling the pattern through the movement of the ELS location.

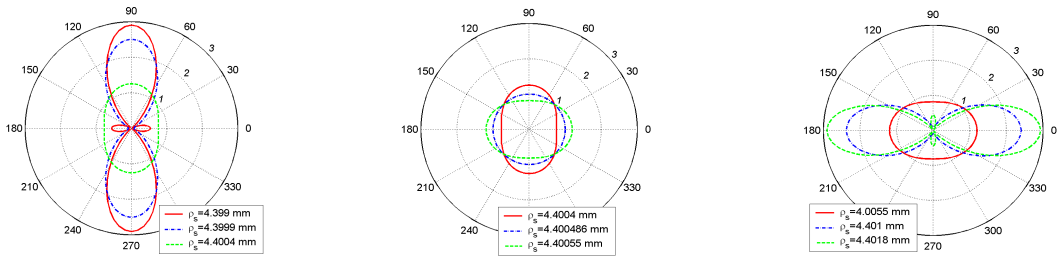

(a) (b) (c)

Figure 15: *The changes in the directivity as the ELS location is varied in region 2 of the DPS-DNG structure. (a) to the left of the critical radius, (b) near and at the critical radius, and (c) to the right of the critical radius.*

In the case of the ELS being moved infinitely far away from the structure along the direction $\phi_s = 0$, the total cross section reported in Figure 16 is obtained for the DPS-DNG and DPS-DPS structure. As shown, a resonant enhancement is observed at $\rho_2 = 5.000068$ mm (which is indeed the same ρ_2 at which the resonance was observed in the PR values), while no enhancement is found for the corresponding DPS-DPS structure. In addition, at the radius for which the resonance is achieved for the quadrupolar DPS-DNG structure, the difference between σ_t for DPS-DNG and DPS-DPS structures is larger for the quadrupolar structures than for the dipolar ones. Although not included inhere, significant enhancements of the differential cross section, were obtained for the quadrupolar DPS-DNG structure relative to the correspondingly sized DPS-DPS structure.

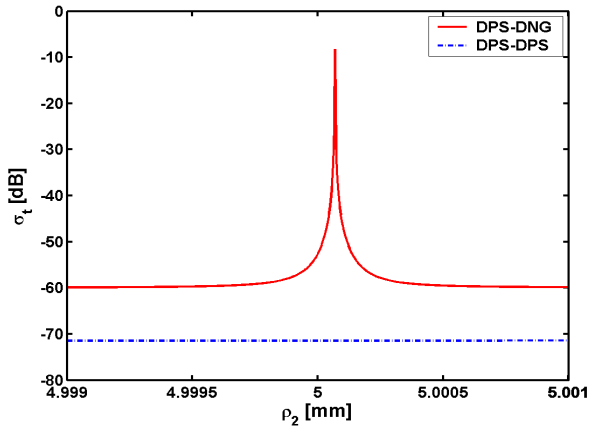

Figure 16: *The total cross section σ_t as a function of the outer shell radius ρ_2 for the electrically small resonant quadrupolar DPS-DNG and DPS-DPS structures.*

Effects of dispersion and losses

To assess the effects of dispersion and losses on the resonant behavior of the DPS-DNG structures, the well-known Drude and Lorentz models of both the permittivity and permeability were used. The lossy Drude models of the permittivity and permeability are given, respectively, by the expressions

$$\varepsilon_2(\omega) = \varepsilon_0 \left(1 - \frac{\omega_{pe}^2}{\omega(\omega - j\Gamma_e)}\right), \tag{13a}$$

$$\mu_2(\omega) = \mu_0 \left(1 - \frac{\omega_{pm}^2}{\omega(\omega - j\Gamma_m)}\right), \tag{13b}$$

while the lossy Lorentz models of the permittivity and permeability are given, respectively, by the expressions

$$\varepsilon_2(\omega) = \varepsilon_0 \left(1 - \frac{\omega_{pe}^2}{\omega^2 - j\Gamma_e\omega - \omega_{er}^2}\right), \tag{14a}$$

$$\mu_2(\omega) = \mu_0 \left(1 - \frac{\omega_{pm}^2}{\omega^2 - j\Gamma_m\omega - \omega_{mr}^2}\right), \tag{14b}$$

In the above relations ω_{pe} and ω_{pm} are the electric and magnetic plasma frequencies, while Γ_e and Γ_m are the electric and magnetic collision frequencies. In the Lorentz models, ω_{er} and ω_{mr} are the resonance frequencies of the permittivity and permeability, respectively. These models were designed to recover at the angular frequency of operation, $\omega_0 = 2\pi f_0$, where $f_0 = 300$ MHz, the values of the lossless permittivity and permeability given in Table 2. For the Drude models, ω_{pe}^2 and ω_{pm}^2 are determined from the real part of (13a) and (13b), respectively, evaluated at ω_0 to recover the desired material parameter values. For the Lorentz models, with the assumption that the losses are small, the frequency of operation f_0 must lie above the resonance frequency to obtain the required negative values of the material parameters. Since the angular frequencies of the Lorentz model permittivity and permeability are given by $\omega_{er} = 2\pi f_{er}$ and $\omega_{mr} = 2\pi f_{mr}$, we set $f_{er} = f_{mr} = f_r = 290$ MHz and then determine the values of ω_{pe}^2 and ω_{pm}^2 from the desired values of the real parts of (14a) and (14b).

For both models, the following two cases are considered. In the first case, the collision frequencies are set to zero, i.e., $\Gamma_e = \Gamma_m = 0$. This means the DNG shell is lossless but dispersive. In the second case, the collision frequencies are set to $\Gamma_e = \Gamma_m = 10^{-3}\omega_0$. This means the DNG shell is dispersive and contains a small, but non-negligible loss. The effects of dispersion and losses on the performance of the electrically small resonant dipolar DPS-DNG structures examined in Section 4.2 are shown in Figure 17.

The general characteristics of these results are that the PR is almost constant in the depicted frequency range when the DNG shell is non-dispersive, and thus these structures are rather broadband. This broadband behavior is expected since the electrical size of the dipolar DPS-DNG structure is small for the range of frequencies considered in Figure 17(a), and thus, the resonance condition in (12) holds for all of these frequencies. On the other hand, the results clearly show that when dispersion is introduced into the DNG shell, the bandwidth of the resonance attained at $f_0 = 300$ MHz is narrowed considerably. The Lorentz model results have a much narrower bandwidth, than those obtained with the Drude model, this being particularly the case when the two dispersion models are lossless, see Figure 17(a). The narrower bandwidth in the Lorentz model case is explained by the fact that this model is resonant, and thus its material parameters exhibit rapid variations near $f_0 = 300$ MHz. Furthermore, it is interesting to note that the maximum of the PR obtained with either lossless dispersion model occurs at $f_0 = 300$ MHz and is the same value obtained in the non-dispersive case. The inclusion of loss in the two dispersion models has basically two effects. First, as Figure 17(b) shows, the resonances in the PR still occur at $f_0 = 300$ MHz, but they are somewhat broadened relative to the two lossless dispersive cases considered in Figure 17(a). Second the maximum of PR obtained with either lossy dispersion model is lower that in the non-dispersive case. In particular, the PR values at $f_0 = 300$ MHz are PR $\approx$ 23 dB for the non-dispersive case, PR $\approx$ 20 dB for the Drude model, and PR $\approx$ 7 dB for the Lorentz model. Thus,

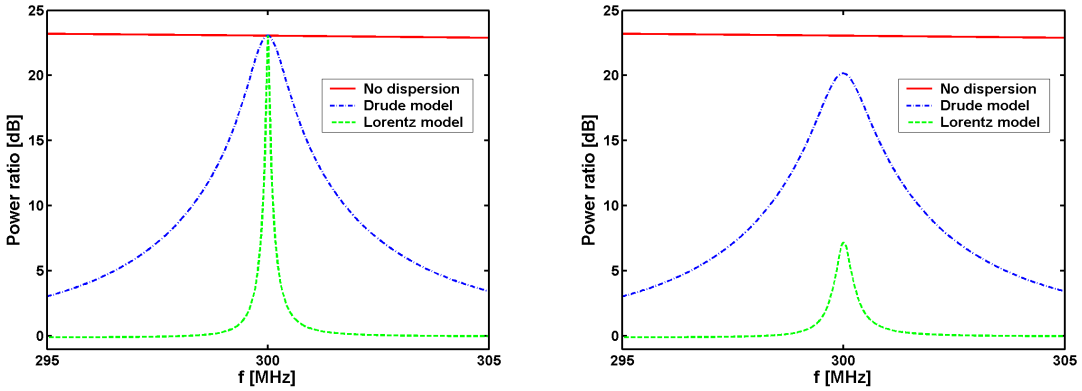

(a) (b)

Figure 17: *Power ratio as a function of the frequency for the DPS-DNG cases in which the DNG shell is described by a non-dispersive model, and by the Drude and Lorentz dispersion models with (a)* $\Gamma_e = \Gamma_m = 0$ *and (b)* $\Gamma_e = \Gamma_m = 10^{-3}\omega_0$. *The ELS is located in region 1 at* $\rho_s = 5.99$ *mm.*

the decrease in the amplitude of PR is most profound for the lossy Lorentz dispersion model. This behavior is expected since the loss is more severe in the Lorentz model (even though the same collision frequencies were used as in the Drude model) because there is a resonance and the frequency of operation is near the resonance frequency. In particular, for the indicated model parameters, one finds at $f_0 = 300$ MHz that $\varepsilon_2 = \varepsilon_0(-1 - j0.002)$, $\mu_2 = \mu_0(-4 - j0.005)$ for the Drude model, and that $\varepsilon_2 = \varepsilon_0(-1 - j0.03)$, $\mu_2 = \mu_0(-4 - j0.07)$ for the Lorentz model. Thus, the electric and magnetic loss tangents: $\tan\delta_e = \varepsilon_2''/|\varepsilon_2'|$ and $\tan\delta_m = \mu_2''/|\mu_2'|$, are, respectively, $\tan\delta_e = 0.002$, $\tan\delta_m = 0.00125$ (Drude model) and $\tan\delta_e = 0.03$, $\tan\delta_m = 0.0175$ (Lorentz model). Similar results, not included here, have been obtained for the dipolar DPS-DNG structures for which the ELS is located in regions 2 and 3.

The effects of losses on the performance of the DPS-DNG structures are further investigated by assuming that the DNG shell is lossy but dispersionless. To this end, five lossy cases, for which the permeabilities and magnetic loss tangents are evaluated at $f_0 = 300$ MHz, are summarized in Table 3. Only the magnetic loss is included since, as shown in Section 4, it is the permeability, and not the permittivity, of the DNG shell that determines the overall behavior for this TM case[5].

Parameter	Case 1	Case 2	Case 3	Case 4	Case 5
μ_2/μ_0	$-4 - j0.0004$	$-4 - j0.004$	$-4 - j0.04$	$-4 - j0.4$	$-4 - j4$
$\tan\delta_m$	0.0001	0.001	0.01	0.1	1

Table 3: *Five lossy cases for the additional investigation on the effects of loss.*

In Figure 18(a), the PR is shown for the five lossy cases as a function of the ELS location when it is in region 2. The lossless case, treated in Section 3, is likewise included for reference purposes. As observed in Figure 18(a), the PR curve is broadened and the total power enhancements are diminished as the losses are increased. While a small amount of loss (Cases 1 and 2) has little impact on the PR values, a moderate amount of loss (Case 3) significantly influences the enhancement of the total power. In Case 3 the maximum PR is half of the lossless case value. However, it is only after the inclusion of very large losses (Cases 4 and 5) that very small or practically no enhancements occur. The decrease in the PR values as the losses increase is due to the fact that the inclusion of losses gradually suppresses the excitation of the resonant higher order modes and, hence, favors the monopolar mode. This is confirmed by the

[5]Note that very large electric loss will have a strong impact on the results reported here. However, as long as the electric loss is comparable to the magnetic loss considered here, it can be neglected.

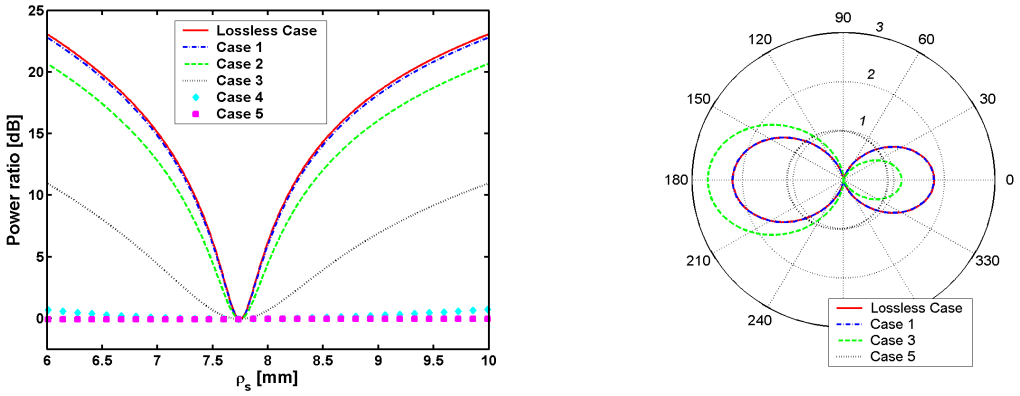

(a) (b)

Figure 18: *Influence of the losses on the dipolar DPS-DNG structure: (a) PR as a function of the ELS location ρ_s in region 2, and (b) the directivity when the ELS is located at $\rho_s = 6.01$ mm. The lossless dipolar DPS-DNG structure is included for reference purposes.*

directivity results given in Figure 18(b). One finds that while Case 1 has essentially the same directivity as the lossless case and Case 3 still retains a dipolar form of the directivity, Case 5 actually produces a directivity pattern that is dominated by the monopolar mode. Additional investigations, not included here, have revealed that the inclusion of even larger magnetic losses produces a perfect monopolar pattern.

Note that only the results for the resonant dipolar DPS-DNG structures have been presented. It must be stressed that similar effects occur when the resonant quadrupolar and higher-order DPS-DNG structures are considered. Although not included in this manuscript, it has been shown that these structures have significantly narrower bandwidths and are even more sensitive to the inclusion of dispersion and small losses.

6 Wavelength-sized natural resonances

It was noted above that very electrically small concentric MTM cylinders with the ELS located exactly at the origin can not lead to total power enhancements because the ELS is only able to excite the monopolar mode and none of the higher-order modes that are required for these enhancements. Nonetheless, it is important to mention that with sufficiently large DPS- and DNG-based structures, the wavelength-sized natural resonances of those structures can be excited. They occur when the size of the object is comparable to multiples of the wavelength [10], [11]. To illustrate this point, it is sufficient to investigate DPS-DPS and DPS-DNG structures having the same material parameters given in Table 2 but with larger radii. As above, the frequency of operation is $f_0 = 300$ MHz ; and the ELS is located at the origin, i.e., $\rho_s = 0$. The inner radius of region 2 is fixed at $\rho_1 = 10$ mm, and the outer one is allowed to vary in the interval $\rho_s \in [10, 300]$ mm. Figure 19 shows the behavior of the PR as a function of ρ_2. Clearly, both the DPS-DPS and DPS-DNG structures exhibit resonances even though the ELS is located on the axis.

For the DPS-DPS structure the resonance is attained at $\rho_2 = 178.49$ mm and for the DPS-DNG structure at $\rho_2 = 208.36$ mm. The maximum value is PR $= 9.59$ dB for the DPS-DPS structure, and PR $= 9.72$ dB for the DPS-DNG structure. These results show that when the size of the cylinders is in the natural resonance regime, the DPS-DNG structures do not offer any advantage over the corresponding DPS-DPS structures. This is in agreement with the results given in [9] and [15]. This conclusion holds in fact for all locations of the ELS. This is in sharp contrast to the very electrically small MTM structures treated in this paper, which were found to have natural resonances that were caused by pairing ordinary DPS materials with specific MTMs and that led to the significant performance enhancements.

The wavelength-sized natural resonance phenomenon is familiar from wave guide and cavity theories where the natural modes occur if the structure has certain dimensions, e.g., see [29]. In particular, for TM polarization in a open circular dielectric resonator of radius a and wave number k, the first resonance

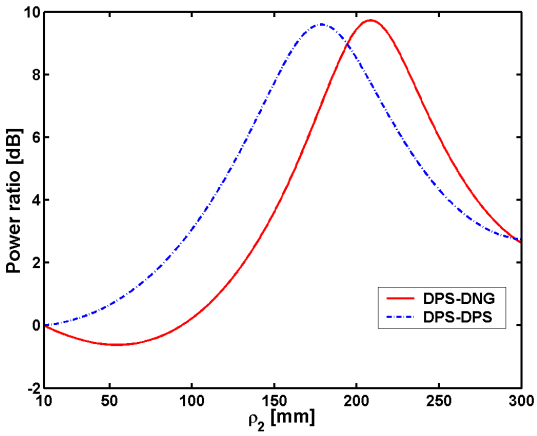

Figure 19: *Power ratio as a function of the outer shell radius ρ_2 for the DPS-DNG and DPS-DPS structures when the ELS is located on the axis of the cylinders. The values of ρ_2 are allowed to be large enough to capture the wavelength-sized natural resonances.*

occurs at $ka = 1.84$ [29, p. 472].

7 SNG structures

Although this manuscript has emphasized the use of DNG and DPS materials, a brief note on the use of SNG media, such as ENG or MNG media, is important. In Section 4 it was noted that electrically small resonant structures having the same properties as the DPS-DNG structures could be designed by using only MNG materials. This is due to the fact that the resonance condition (12) only includes the permeability of the three regions, and not the permittivity. Thus it can also be met simply with DPS-MNG structures. This is very interesting, particularly from a practical point of view, since a DPS-MNG structure may be much simpler to realize than the corresponding DPS-DNG one. Therefore, it is of interest to examine a configuration consisting of an ELS radiating in the presence of a DPS-MNG dipolar structure. The DPS-MNG dipolar structure introduced here has the same material and geometrical parameters as the DPS-DNG dipolar structure considered in Section 3, except that now the permittivity of region 2 is positive and equal to $\varepsilon_2 = \varepsilon_0$. For the sake of completeness, a DPS-ENG structure is likewise considered; it also has the same material and geometrical parameters as the DPS-DNG dipolar structure, except that now the permeability of region 2 is positive and equal to $\mu_2 = 4\mu_0$.

Figure 20 shows the PR as a function of the outer radius ρ_2 for the DPS-MNG and DPS-ENG dipolar structure when the ELS is located in region 1 at $\rho_s = 5.99$ mm.
A resonance peak with PR $\approx$ 23 dB is found in the PR values at $\rho_2 = 10.033$ mm for the DPS-MNG structure, which is extremely close to the value at which resonance was attained for the dipolar DPS-DNG structure. On the other hand, the PR for the corresponding DPS-ENG structure exhibits no enhancement of the total power; thus it resembles the behavior of the DPS-DPS structure. This confirms that a DPS-MNG structure can indeed replace the DPS-DNG structure while a DPS-ENG structure can not. It must be stressed that the underlying mechanism for the enhancement of the total power by the DPS-MNG structures is identical to that occurring in the DPS-DNG structure. As a consequence, the behavior of the near field, directivity, and total and differential cross sections of the DPS-MNG structures resembles that of the DPS-DNG structures, as does the influence of dispersion and losses present in MNG materials.

Another interesting point regards the use of TE polarization (e.g., with a magnetic line source), instead of the present TM polarization. In the TE case it can be shown that the resonance condition (12) includes the permittivity of the three regions, and not the permeability. Consequently, for the TE case it will be an ENG material, rather than a MNG one, that will provide a structure whose behavior is similar to the DPS-DNG and DPS-MNG structures treated here.

It must also be noted that when the ELS is located at the origin of a DPS-MNG structures whose size

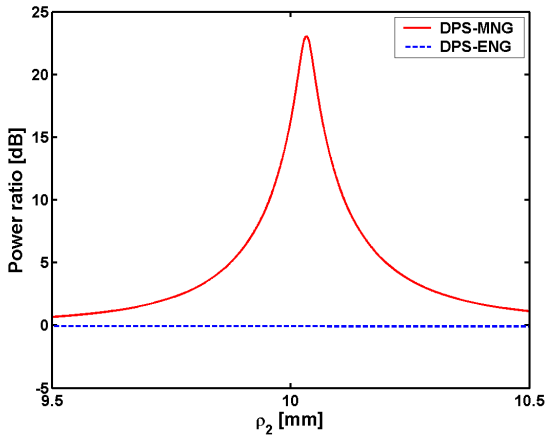

Figure 20: *Power ratio as a function of the outer shell radius ρ_2 for the dipolar DPS-MNG and DPS-ENG structures when the ELS is located in region 1 at $\rho_s = 5.99$ mm.*

is comparable to that of the DPS-DPS and DPS-DNG structures discussed in Section 6 and for which resonances were obtained at $\rho_2 = 178.49$ mm and at $\rho_s = 208.36$ mm, respectively, no enhancements of the total power can be observed. The explanation is straightforward. When the ELS is located at the origin, only the monopolar mode radiates. As discussed in Section 6, the size of the structure must be sufficiently large in order to obtain a resonance. However, for such a large DPS-MNG structure, the MNG shell will be quite thick. Consequently, this shell will not permit the passage of electromagnetic waves since the wave number inside it is imaginary; and thus the waves are evanescent rather than propagating in the shell [4]. Thus, no enhancements will result for DPS-MNG structures of that large size. Having the ELS displaced from the origin leads to enhancements only in the case where the DPS-MNG structure is electrically small, as well as in the case where the structure is electrically large and the MNG shell is simultaneously thin.

8 Conclusions

An antenna configuration consisting of an arbitrarily located ELS radiating in the presence of concentric MTM cylinders was solved analytically and investigated numerically for the particular case of either a DPS or a DNG shell. The near- and far-field properties of these structures were analysed through an investigation of various parameters including the total radiated power, directivity, and total and differential cross sections. The results for these MTM-based structures were compared to the corresponding structures made of conventional DPS materials.

In summary, it was shown that the electrically small MTM-based structures can be designed to possess resonances in the radiation and scattering characteristics, whereas such resonances do not exist for the corresponding DPS-based structures. In particular, significant enhancements of the total radiated power, as compared to the power radiated by the ELS in free space, as well as the total and differential cross section, were found by using specifically designed electrically small DPS-DNG structures. These enhancements were associated with the so-called subwavelength-sized natural resonances, also referred to as interface resonances in [10], that may occur in such small structures. The main characteristic of these enhancements, which are found for off-axis ELS locations, is that they are considerably larger when the ELS is located near the interfaces of the DNG layers, where it can directly drive these resonances. Both dipolar and quadrupolar resonant structures were designed, and the enhancements for the quadrupolar ones were shown to be significantly larger than those for the dipolar ones, but the resonances were also shown to be narrower, and more sensitive to even slight variations of the material as well as the geometrical parameters.

For both the dipolar and quadrupolar structures, the feasibility of controlling the directivity of the electrically small MTM-based structures through specific locations of the ELS was demonstrated. Even though a given resonant MTM-based structure was designed to be excited in a specific dominant mode,

other modes can be excited by proper locations of the ELS. Thus, it is possible to reshape the pattern to obtain desired radiation characteristics.

Frequency dispersion in the MTM material was shown to narrow the resonances significantly, while the inclusion of losses in the dispersion models decreased the peak values of those resonances. In addition, a separate analysis revealed that while small and moderate losses in the MTMs do not the make the enhancement of the quantities of interest disappear, large losses do so, this being caused by the suppressed excitation of the necessary higher order modes.

It was furthermore demonstrated that MNG, rather than DNG, materials can offer the same results for the ELS excitation (TM polarization) of these cylindrical structures, while it was noted that for the TE polarization case, e.g., obtained by using a magnetic line source excitation, ENG (or DNG) materials must be used. These observations on the use of SNG rather than DNG materials to realize the electrically small resonant structures are important, especially from the practical point of view, since the manufacturing of a SNG material may be easier than that of a DNG material.

It is worth emphasizing that the electrically small DPS-DNG structures investigated here possess enhanced radiation and scattering characteristics that are similar to those associated with an electrically large structure. When the size of the MTM-based structure is large enough for the wavelength-sized natural resonances to occur, it was shown that both the DPS-DNG and DPS-DPS structures (but not the DPS-SNG structures) possess resonances in the total radiated power, although smaller in amplitude, even when the ELS was located on the axis of the cylinders.

Acknowledgments

This work was supported in part by DARPA Contract number HR0011-05-C-0068

References

[1] V. G. Veselago, "The electrodynamics of substances with simultaneously negative values of ε and μ," *Sov. Phys. Usp.*, vol. 10, pp. 509-514, Jan.-Feb. 1968.

[2] G.V. Eleftheriades and K.G. Balmain (Eds.), *Negative-refraction metamaterials: fundamental principles and applications*, John Wiley & Sons, 2005.

[3] C. Caloz and T. Itoh (Eds.), *Electromagnetic metamaterials: transmission line theory and microwave applications*, John Wiley & Sons, 2006.

[4] N. Engheta and R.W. Ziolkowski (Eds.), *Metamaterials: physics and engineering explorations*, John Wiley & Sons, 2006.

[5] J. B. Pendry, "Negative refraction makes a perfect lens," *Phys. Rev. Let.*, vol. 85, pp. 3966-3969, Oct. 2000.

[6] A. Alú and N. Engheta, "Pairing an epsilon-negative slab with a mu-negative slab: resonance, tunneling, and transparency," *IEEE Trans. Antennas Propagat.*, vol. 51, no. 10, pp. 2558-2571, Oct. 2003.

[7] V. Kuzmiak, and A. A. Maradudin, "Scattering properties of a cylinder fabricated from a left-handed material," *Phys. Rev. B.*, vol. 66, pp. 1161-1167, July 2002.

[8] R. Ruppin, "Surface polaritons and extinction properties of a left-handed cylinder," *J. Phys.: Condens. Matter.*, vol. 16, pp. 5991-5998, Aug. 2004.

[9] Ma. M. Khodier, "Radiation characteristics of an infinite line source surrounded by concentric shells of metamaterials," emphIEEE Antennas and Propagation Society Symposium, Monterey, CA, June 20-26, 2004.

[10] A. Alú, and N. Engheta, "Resonances in sub-wavelength cylindrical structures made of pairs of double-negative and double-positive or epsilon-negative and mu-negative coaxial shells," in *Proc. of the International Electromagnetics and Advance Applications Conference*, Turin, Italy, Sep. 8-12, 2003, pp. 435-438.

[11] A. Alú, and N. Engheta, "Polarizabilities and effective parameters for collections of spherical nanoparticles formed by pairs of concentric double-negative (DNG), single-negative (SNG) and/or double-positive (DPS) metamaterial layers," *J. Appl. Phys.*, vol. 97, 094310, May 2005.

[12] R. W. Ziolkowski and A. Kipple, "Reciprocity between the effects of resonant scattering and enhanced radiated power by electrically small antennas in the presence of nested metamaterials shells," *Phys. Rev. E.*, vol. 72, 036602, Sept. 2005.

[13] C. Li, and Z. Shen, "Electromagnetic scattering by a conducting cylinder coated with metamaterials," in *Proc. of the Progress in Electromagnetic Research Society Meeting, PIERS'03*, Honolulu, Hawaii, 91-105, 2003.

[14] J. Sun, W. Sun, T. Jiang, and Y. Feng, "Directive electromagnetic radiation of a line source scattered by a conducting cylinder coated with left-handed material," *Microwave Opt. Technol. Lett.*, vol. 47, pp. 274-279, Nov. 2005.

[15] S. R. Nelatury, "Comparing double-negative and double-positive covers around a radiating line current," *Microwave Opt. Technol. Lett.*, vol. 48, pp. 250-252, Feb. 2006.

[16] S. Arslanagić, and O. Breinbjerg, "Electric line source illumination of a circular cylinder of lossless double negative material - An investigation of near field, directivity and radiation resistance," *IEEE Antennas and Propagat. Magazine*, vol. 48, no. 3, June 2006.

[17] R. Ruppin, "Extinction properties of a sphere with negative permittivity and permeability," *Solid State Commun.*, vol. 116, pp. 411-415, Aug. 2000.

[18] Z. Liu, Z. Lin, and S. T. Chui, "Electromagnetic scattering by spherical negative-refractive-index particles: low frequency resonance and localization parameters," *Phys. Rev. E.*, vol. 69, pp. 016 619/1-6, Jan. 2004.

[19] R. W. Ziolkowski and A. Kipple, "Application of double negative metamaterials to increase the power radiated by electrically small antennas," *IEEE Trans. Antennas Propagat.*, vol. 51, no. 10, pp. 2626-2640, Oct. 2003.

[20] R. W. Ziolkowski and A. Erentok, "Metamaterial-based efficient electrically small antennas," *IEEE Trans. Antennas Propagat.*, vol. 54, no. 7, pp. 2113-2130, July 2006.

[21] R. W. Ziolkowski and A. Erentok, "At and beyond the Chu limit: passive and active broad bandwidth metamaterial-based efficient electrically small antennas," submitted to *IEE Proceedings.*, Dec 2005.

[22] S. Arslanagić, R. W. Ziolkowski, and O. Breinbjerg, "Radiated power and total scattering cross section of multilayered cylinders excited by an electric line source," in *Proc. of Third Workshop on Metamaterials and Special Materials for Electromagnetic Applications and TLC*, p. 18, Rome, Italy, 2006.

[23] S. Arslanagić, R. W. Ziolkowski, and O. Breinbjerg, "Line source excitation of multilayered metamaterial cylinders: source and scattering results," *IEEE Antennas and Propagation Society Symposium*, Albuquerque, NM, USA, 2006.

[24] S. Arslanagić, R. W. Ziolkowski, and O. Breinbjerg, "Excitation of an electrically small metamaterial-coated cylinder by an arbitrarily located line source," *Microwave Opt. Technol. Lett.*, vol. 48, pp. 2598-

2605, Dec. 2006.

[25] S. Arslanagić, R. W. Ziolkowski, and O. Breinbjerg, "Near-field distribution, directivity and differential scattering cross section for a line source-excited metamaterial-coated electrically small cylinder," in *Proc. of EuCap*, Nice, France, November 2006.

[26] S. Arslanagić, R. W. Ziolkowski, and O. Breinbjerg, "Far-field properties of a line source-excited electrically small quadrupolar metamaterial cylindrical shell," accepted for presentation in *iWAT*, Cambridge, England, Mar. 2007.

[27] S. Arslanagić, R. W. Ziolkowski, and O. Breinbjerg, "Hertzian dipole excitation of higher order resonant modes in electrically small concentric metamaterial spheres: source and scattering structures," in *Proc. of IV Int. Workshop on Electromagnetic Wave Scattering*, Gebze, Turkey, Sept. 2006.

[28] S. A. Tretyakov, S. I. Maslovski, A. A. Sochava, and C. R. Simovski, "The influence of complex material coverings on the quality factor of simple radiating systems," *IEEE Trans. Antennas Propagat.*, vol. 53, pp. 965-970, Mar. 2005.

[29] C. A. Balanis, *Advanced engineering electromagnetics*, John Wiley & Sons, 1989.

[30] M. Abramowitz, and I. A. Stegun, *Handbook of mathematical functions*, Dover Publications, 1965.

APPENDIX B

MANUSCRIPT II

Electric line source illumination of a circular cylinder of lossless double-negative material - an investigation of near-field, directivity and radiation resistance[1]

Samel Arslanagić and Olav Breinbjerg

Ørsted•DTU, Electromagnetic Systems, Technical University of Denmark,
Building 348, Ørsteds Plads, DK-2800 Kgs. Lyngby, Denmark,
Tel: +45 4588 1444, Fax: +45 4593 1634,
E-mail: sar@oersted.dtu.dk, ob@oersted.dtu.dk

Key terms: *antennas*, *double-negative materials*, *cylinders*, *metamaterials*, *scattering*.

Abstract

The problem of scattering by a double negative circular cylinder illuminated by an exterior, close-by electric line source is considered. First, the exact, eigenfunction series based, analytical solution is derived. Second, this solution is used in the numerical calculations to investigate the properties of the near-field, inside as well as outside the cylinder, and the far-field. This is done for different geometrical and electrical parameters. The directivity and the radiation resistance are calculated and the variation of these with respect to various parameters is examined.

1 Introduction

Quite recently there has emerged a strong interest in exploring and exploiting the electromagnetic characteristics and properties of artificial materials, broadly referred to as metamaterials. A very interesting example of these materials is the so-called double negative (DNG) materials [1]-[3] in which the real part of both the permittivity and permeability are negative. The idea of DNG materials dates back to the late 1960s when the Russian physicist V. G. Veselago theoretically investigated the propagation of

[1] This manuscript is journal publication no. 4, see the list of publications on pages iv and v.

plane electromagnetic waves in lossless, isotropic DNG materials [1]. In such materials the electric and magnetic field intensity vectors of a plane wave form a left-handed set of vectors with its wave number vector. This is in contrast to double positive (DPS) materials, characterized by positive real parts of the permittivity and the permeability, in which these vectors form a right-handed set. In addition, the power flow density of a plane wave in DNG materials always forms a right-handed set of vectors with the electric and magnetic field intensity vectors, obviously implying that the phase and group velocities are oppositely directed. The reversal of the phase velocity direction relative to the direction of the power flow leads to some interesting physical phenomena such as the reversal of the Doppler effect, the reversal of the Vavilov-Čerenkov effect, and perhaps most importantly the negative refraction at a plane interface separating two DPS and DNG materials [1].

It is known that DNG materials are not found in nature and must therefore be made artificially. Recently, the feasibility of constructing negative permittivity materials on the one hand [4], and negative permeability materials on the other [5] was demonstrated. These two separate approaches were combined thereby providing the first realizations of DNG materials [2], [3] and the first experimental verifications followed briefly after [6], [7]. These first realizations of DNG materials were based on periodic arrangements of conducting wires and split-ring resonators (SRRs). However, other realizations exist and employ e.g., a parallel-plate waveguide filled by a two-dimensional (2D) array of broad-side coupled SRRs [8], transmission-line networks loaded with capacitors and inductors [9], [10], and magnetodielectric spherical particles embedded in a background matrix [11].

The strong interest in DNG materials is due to their unfamiliar electromagnetic properties and the potential applications due to these properties [1]. In particular, the lossless DNG slab has been of interest due to its so-called "perfect lens" property [12], but cylindrical [13]-[16] as well as spherical configurations [16]-[19] involving DNG materials have been investigated as well. A considerable amount of work with regard to the development and applications of DNG materials, and metamaterials in general, has already been accomplished as is evidenced by [20], [21]. Nevertheless, there is a continuing interest to further explore the properties and potential applications of these materials.

The purpose of the present work is to investigate the properties of a general antenna configuration with a DNG material. To this end, an infinitely long circular cylinder of lossless DNG material, henceforth referred to as simply a DNG cylinder, illuminated by a close-by electric line source (ELS) [2] is chosen. Though this 2D configuration does not constitute a practical antenna, it possesses a finite cross-section and a localized source and may thus reveal effects that are absent in configurations with one-dimensional (1D) slabs and/or plane wave illumination. Previous investigations of DNG cylinder configurations concerned evaluation of their scattering width under plane wave illumination [13]-[16], and their cavity and waveguide properties [14].

The present manuscript is organized as follows:

In Section 2 the exact analytical solutions for DPS and DNG cylinders are presented. The DNG cylinder solution is used in Section 3 in numerical calculations to investigate the influence of different geometrical and electromagnetic parameters such as cylinder radius, ELS position, cylinder permittivity and permeability, on the near-field, inside as well as outside the cylinder, and the far-field, in terms of the directivity and the radiation resistance. Throughout the investigations the case of a DPS cylinder is used as reference. The time factor $\exp(j\omega t)$, with ω being the angular frequency and t being the time, is assumed and suppressed throughout the manuscript.

2 Exact analytical solutions for DPS and DNG cylinders

In this section the analytical results for DPS and DNG cylinders are presented. The presentation comprises several steps. First, the antenna configuration is described. Second, the case of DPS cylinders is analyzed by employing the well-known eigenfunction expansion method and the expressions for both the scattered and transmitted fields are derived. Third, the considerations necessary to treat the corresponding DNG cylinders are outlined. In this respect the sign of various parameters in DNG materials is briefly discussed.

[2] This type of illumination corresponds to TM polarization. The results for TE polarization, i.e., the magnetic line source illumination, are easily obtained from the duality theorem, and are thus not included inhere.

2.1 Configuration

The configuration of interest is depicted in Figure 1.

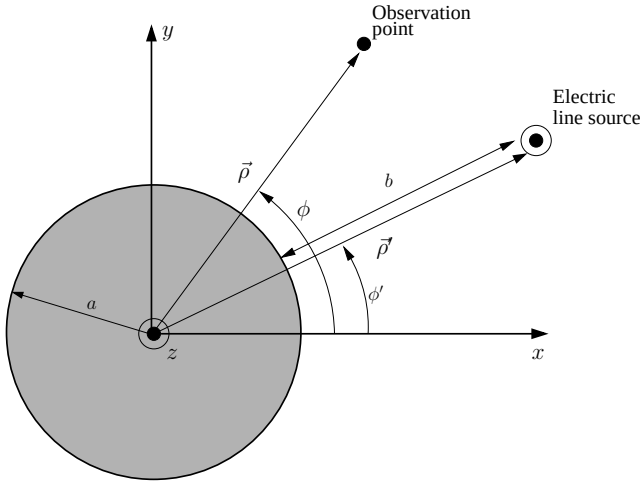

Figure 1: *Antenna configuration: a DPS or DNG cylinder illuminated by an ELS located in free space.*

It consists of a cylinder made of a lossless simple DPS or DNG material illuminated by an ELS of a constant electric current I_e [A] placed close and parallel to the cylinder. The ambient medium is free space, i.e., its material parameters are (ε_0, μ_0), where $\varepsilon_0 = 8.854 \cdot 10^{-12}$ [F/m] is the free-space permittivity, and $\mu_0 = 4\pi \cdot 10^{-7}$ [H/m] is the free-space permeability. The free-space wave number is $k_0 = \omega\sqrt{\varepsilon_0\mu_0} = 2\pi/\lambda_0$, with λ_0 being the free-space wavelength, and the free-space intrinsic impedance is $\eta_0 = \sqrt{\mu_0/\varepsilon_0}$. The cylinder is of infinite extent, and has a radius denoted by a. The permittivity and the permeability of the cylinder are real scalars denoted by $\varepsilon_c = \varepsilon_r\varepsilon_0$ and $\mu_c = \mu_r\mu_0$, respectively, where ε_r and μ_r, respectively, are its relative permittivity and permeability. The wave number inside the cylinder is denoted by k_c. For the DPS cylinder, $\varepsilon_r > 0$, $\mu_r > 0$, and $k_c = k_0\sqrt{\varepsilon_r\mu_r} > 0$. For the DNG cylinder $\varepsilon_r < 0$ and $\mu_r < 0$, and the sign of k_c will be chosen in Section 2.3.

A cylindrical coordinate system (ρ, ϕ, z) with the associated Cartesian coordinate system (x, y, z) is introduced such that the z-axis coincides with the cylinder axis, see Figure 1. The position vector of a given observation point is $\vec{\rho}$, and its coordinates are (ρ, ϕ), while the position vector of the ELS is $\vec{\rho}\,'$, and its coordinates are (ρ', ϕ'). The distance between the ELS and the cylinder surface is denoted by $b = \rho' - a$.

2.2 DPS cylinders

While the problem of plane wave illumination of DPS cylinders has been thoroughly treated, see e.g., the well-known textbook solutions [22, Ch. 17], [23, Ch. 6] and [24, Ch. 11], the problem of the ELS illumination is not as well-documented in the literature. In [25, Ch. 3], however, a general procedure of finding the solution to the problem of ELS illumination of DPS cylinders is given. The field expressions resulting from this procedure, which is based on an eigenfunction expansion method, can be manipulated to obtain the explicit expressions for the problem at hand. The eigenfunction expansion method has also been applied in [24, Ch. 11] to derive the explicit expressions for perfectly electric conducting (PEC) cylinders in the presence of an ELS, and this is easily extended to DPS cylinders, as shown below.

The incident field of the ELS is [24, p. 573]

$$\vec{E}^i(\vec{\rho}) = -\hat{z} I_e \frac{\omega\mu_0}{4} H_0^{(2)}(k_0|\vec{\rho} - \vec{\rho}\,'|), \tag{1}$$

where $H_0^{(2)}(\cdot)$ is the Hankel function of second kind and zeroth order. Note that $\vec{E}^i$ in (1) is given in terms of cylindrical wave functions which originate at the ELS. In order to facilitate the forthcoming analysis, the incident electric field (1) is expressed in terms of cylindrical wave functions which originate at the

origin of the coordinate system, i.e., at $\rho = 0$. Employing the addition theorem for Hankel functions, the incident electric field of the ELS takes the form of [24, p. 626]

$$\vec{E}^i(\rho,\phi) = -\hat{z} I_e \frac{\omega\mu_0}{4} \begin{cases} \sum_{n=-\infty}^{\infty} J_n(k_0\rho) H_n^{(2)}(k_0\rho') e^{jn(\phi-\phi')} & \text{for} \quad \rho \le \rho', \\ \sum_{n=-\infty}^{\infty} J_n(k_0\rho') H_n^{(2)}(k_0\rho) e^{jn(\phi-\phi')} & \text{for} \quad \rho \ge \rho'. \end{cases} \tag{2}$$

The function $J_n(\cdot)$ is the Bessel function of order n and is chosen to represent the field for $\rho \le \rho'$ due to its non-singular behavior at the origin, while $H_n^{(2)}(\cdot)$, which is the Hankel function of second kind and order n, is chosen for $\rho \ge \rho'$ due to its outward propagating nature in compliance with the radiation condition. Similarly, the scattered and the transmitted electric fields, respectively, are expanded as

$$\vec{E}^s(\rho,\phi) = -\hat{z} I_e \frac{\omega\mu_0}{4} \sum_{n=-\infty}^{\infty} \psi_n H_n^{(2)}(k_0\rho) e^{jn(\phi-\phi')} \quad \text{for} \quad \rho \ge a, \tag{3}$$

$$\vec{E}^t(\rho,\phi) = -\hat{z} I_e \frac{\omega\mu_0}{4} \sum_{n=-\infty}^{\infty} \chi_n J_n(k_c\rho) e^{jn(\phi-\phi')} \quad \text{for} \quad \rho \le a, \tag{4}$$

where ψ_n and χ_n are the unknown expansion coefficients. It is noted that outside the cylinder, the total field is the sum of the incident (2) and scattered (3) fields, while inside the cylinder, the total field equals the transmitted field (4). The associated incident, scattered, and transmitted magnetic fields, which are required in the determination of the expansion coefficients, are readily obtained from Faraday's law. The electromagnetic field boundary conditions, requiring the tangential components of the total electric and magnetic fields to be continuous at the cylinder surface, are then applied and it follows that the expansion coefficients can be expressed as

$$\psi_n = H_n^{(2)}(k_0\rho') \frac{J_n'(k_0a) J_n(k_ca) - \frac{\mu_0 k_c}{\mu_c k_0} J_n(k_0a) J_n'(k_ca)}{\frac{\mu_0 k_c}{\mu_c k_0} J_n'(k_ca) H_n^{(2)}(k_0a) - J_n(k_ca) H_n^{(2)\prime}(k_0a)}, \tag{5}$$

and

$$\chi_n = H_n^{(2)}(k_0\rho') \frac{J_n(k_0a) H_n^{(2)\prime}(k_0a) - J_n'(k_0a) H_n^{(2)}(k_0a)}{J_n(k_ca) H_n^{(2)\prime}(k_0a) - \frac{\mu_0 k_c}{\mu_c k_0} J_n'(k_ca) H_n^{(2)}(k_0a)}. \tag{6}$$

It is noted that all derivatives in the above equations, indicated by primed symbols, are to be taken with respect to the function's entire argument.

As regards the practical implementations of the field expressions, it is first noted that it is convenient to fold the summation over n employed in the exact solution, which ranges from $-\infty$ to ∞, to range from 0 to ∞. For the scattered electric field given by (3), it holds that

$$\vec{E}^s(\rho,\phi) = -\hat{z} I_e \frac{\omega\mu_0}{4} \sum_{n=-\infty}^{\infty} \psi_n H_n^{(2)}(k_0\rho) e^{jn(\phi-\phi')} = -\hat{z} I_e \frac{\omega\mu_0}{4} \sum_{n=0}^{\infty} \varepsilon_n \, \psi_n H_n^{(2)}(k_0\rho) \cos[n(\phi-\phi')], \tag{7}$$

where ε_n is the Neumann number, which equals 1 for $n = 0$, and 2 otherwise. Similar transformations are employed for the remaining field expressions (2) and (4). Second, the summations in use must be truncated at some $n = N_{max}$ chosen in a manner which ensures convergence. Experience has shown that, in general, this is accomplished by selecting $N_{max} = k_0\rho' + 20$ for all of the configurations treated in the present manuscript.

The far-field properties of the cylinders at hand are investigated through an examination of the two-dimensional directivity, henceforth referred to as simply the directivity, given by

$$D(\phi) = \frac{2\pi |\vec{E}_f^{tot}(\phi)|^2}{\int_{\phi=0}^{2\pi} |\vec{E}_f^{tot}(\phi)|^2 d\phi} = \frac{2\pi |\vec{E}_f^{i}(\phi) + \vec{E}_f^{s}(\phi)|^2}{\int_{\phi=0}^{2\pi} |\vec{E}_f^{i}(\phi) + \vec{E}_f^{s}(\phi)|^2 d\phi} = \frac{2\left| \sum_{n=0}^{N_{max}} j^n \varepsilon_n \alpha_n \cos[n(\phi-\phi')] \right|^2}{\sum_{n=0}^{N_{max}} \varepsilon_n^2 (3-\varepsilon_n) |\alpha_n|^2}, \tag{8}$$

where $\alpha_n = J_n(k_0\rho') + \psi_n$ with ψ_n given by (5). In (8) $\vec{E}_f^{tot}$ designates the total far-field pattern which is the sum of the incident, $\vec{E}_f^i$, and the scattered, $\vec{E}_f^s$, far-field patterns. These are easily obtained from (2) (the expression for $\rho \geq \rho'$) and (3), respectively, through a large argument expansion of the involved Hankel function [32, Ch. 10] and subsequent normalization with $\exp(-jk_0\rho)/\sqrt{\rho}$. In addition, the radiation resistance, R_{rad}^{tot}, of the system consisting of a given cylinder and the ELS is calculated and subsequently normalized to the radiation resistance, R_{rad}^i, due to the ELS alone. This normalized radiation resistance is denoted by R_{rad}^{norm} and is given by

$$R_{rad}^{norm} = \frac{R_{rad}^{tot}}{R_{rad}^i} = \frac{P_{rad}^{tot}}{P_{rad}^i}, \tag{9}$$

where

$$P_{rad}^{tot} = \frac{1}{2\eta_0}\int_{\phi=0}^{2\pi} |\vec{E}_f^{tot}(\phi)|^2 d\phi = \frac{{I_e}^2 k_0 \eta_0}{16} \sum_{n=0}^{N_{max}} \varepsilon_n^2 (3-\varepsilon_n)|\alpha_n|^2, \tag{10}$$

is the power radiated by the system, and

$$P_{rad}^i = \frac{1}{2\eta_0}\int_{\phi=0}^{2\pi} |\vec{E}_f^i(\phi)|^2 d\phi = \frac{{I_e}^2 k_0 \eta_0}{8}, \tag{11}$$

is the power radiated by the ELS alone.

2.3 DNG cylinders

In the following, two different ways of obtaining the solution to the DNG cylinder problem are presented. Since they essentially differ in the choice of signs for some important parameters for DNG materials, it is appropriate to briefly discuss the various choices of the signs as adopted in the literature.

The sign of such parameters for DNG materials as refractive index, wave number and intrinsic impedance, has been the subject of some discussion in the literature, see e.g., [1], [6]-[9], [12] and [26]-[31] for a few examples. Most of the works, including the pioneering work of Veselago [1], devote the majority of their discussion to the sign of the refractive index. In [1] it was argued that the refractive index must be negative in a DNG material in order to have a correct description of the plane wave refraction process taking place at a plane interface separating a DPS and a DNG material. No explicit mentioning of the sign of wave number and intrinsic impedance was made in [1]. The negative refractive index was later adopted among others by [6]-[9], [12], [26] and [27]. In [27], the negative refractive index implied also a negative wave number, and it was moreover argued that a positive intrinsic impedance of a DNG material must be used. The latter was also explicitly stated in [9], [12], and [26]. These findings were subsequently used to solve the problem of a DNG spherical shell surrounding an electrically small antenna [18] by simply using a negative wave number and a positive intrinsic impedance in the familiar expressions for the DPS spherical shell. Hence, in accordance with [27] the DNG cylinder solution can be obtained from the DPS cylinder solution derived in the previous section simply by inserting $\varepsilon_c < 0$, $\mu_c < 0$, and $k_c < 0$ at appropriate places in (1)-(10).

However, other works argue that a positive sign of the refractive index in a DNG material can likewise be used, see e.g., [28]-[31]. By considering plane wave propagation in an unbounded DNG material, [28] showed that the refractive index could be assumed positive if the unit propagation vector is defined in such a manner that it forms a left-handed set of vectors with the electric and magnetic field intensity vectors. In addition, [30], [31] have shown that in unbounded DNG materials, the sign of wave number merely depends on the choice of the partial solution to the wave equation, and that for either choice of the sign of wave number, the intrinsic impedance and the refractive index can be defined positive as well as negative. Regarding the problem of scattering from DPS and DNG cylinders, [30], [31] have moreover shown that the eigenfunction solution (1)-(6) applies to DPS as well as DNG cylinders. For the DNG cylinder one can choose $\varepsilon_r < 0$, $\mu_r < 0$, and $k_c > 0$, on the one hand, or, $\varepsilon_r < 0$, $\mu_r < 0$, and $k_c < 0$, on the other hand, and the two choices give the same result. This is easily verified by using the analytic continuation formula for the Bessel function of order n and negative argument, say $-x$ with $x > 0$, [32, p. 361]

$$J_n(-x) = (-1)^n J_n(x), \tag{12}$$

as well as the relation

$$J_n'(-x) = -(-1)^n \, J_n'(x), \tag{13}$$

at appropriate places in (1)-(10).

In summary, the results for the DNG cylinders are obtained from (1)-(10) with $\varepsilon_r < 0$ and $\mu_r < 0$, and with either positive or negative k_c.

3 Numerical results for DPS and DNG cylinders

The numerical calculations are performed for different geometrical and electromagnetic parameters such as cylinder radius, a, ELS position, b, cylinder permittivity, ε_c, and permeability, μ_c, see Figure 1. In all of the forthcoming calculations the coordinate system is aligned in such a manner that the ELS is placed along the positive x-axis at a distance b from the cylinder, see Figure 1. For easy reference, a cylinder having the material parameters $(\varepsilon_c, \mu_c) = (\varepsilon_r\varepsilon_0, \mu_r\mu_0)$ is referred to as a "$\varepsilon_r\varepsilon_0\mu_r\mu_0$" DPS cylinder for $\varepsilon_r > 0$, $\mu_r > 0$, and as a "$|\varepsilon_r|\varepsilon_0|\mu_r|\mu_0$" DNG cylinder for $\varepsilon_r < 0$, $\mu_r < 0$ [3].

3.1. Near-field properties

First, the near-field properties of DNG cylinders are investigated. This is done by calculating the total field, denoted by $\vec{E}(\rho, \phi)$, inside as well as outside the cylinder. More specifically, the quantity $20\log_{10}|\vec{E}(\rho, \phi)|$ [dB] [4] is shown in a circular region of radius $3\rho'$ centered at the cylinder axis (z-axis), see Figure 1. To facilitate comparison of the results, the dynamic range is kept constant throughout the forthcoming figures.

3.1.1 Results for "$1\varepsilon_0 1\mu_0$" DNG cylinders

The effect of the DNG material is particularly notable in the case of a "$1\varepsilon_0 1\mu_0$" cylinder. A few examples of such results are shown in figures 2 through 5, which depict the near-field distributions for the cylinders having radii $2\lambda_0$ through $10\lambda_0$, respectively. For all configurations the ELS is located at a distance $b = 1\lambda_0$ from the cylinder.

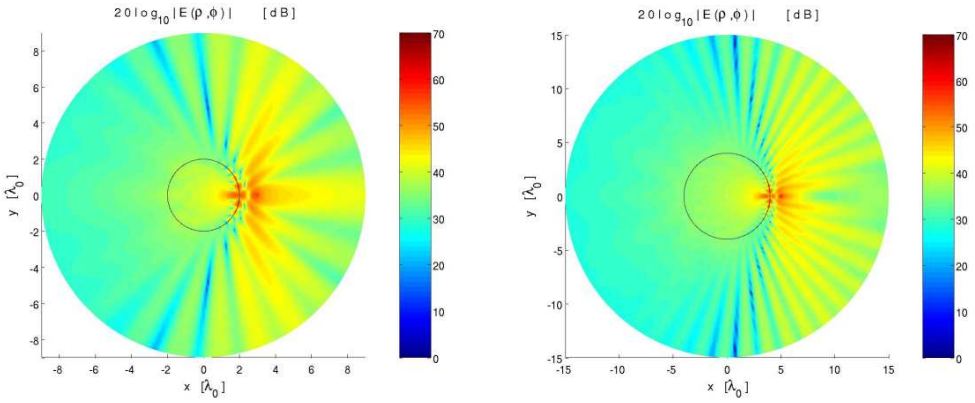

(a) (b)

Figure 2: *Electric field distribution for "$1\varepsilon_0 1\mu_0$" DNG cylinders having radii $a = 2\lambda_0$ (a) and $a = 4\lambda_0$ (b). The ELS is at a distance $b = 1\lambda_0$ from the cylinder.*

The "$1\varepsilon_0 1\mu_0$" DPS cylinder is clearly equivalent to the free-space case without any scattering of the ELS

[3] That is, a "$2\varepsilon_0 1\mu_0$" DPS cylinder is a cylinder for which $\varepsilon_r = 2$ and $\mu_r = 1$, while a "$2\varepsilon_0 1\mu_0$" DNG cylinder is a cylinder for which $\varepsilon_r = -2$ and $\mu_r = -1$.

[4] The near-field $\vec{E}(\rho, \phi)$ is normalized by 1 [V/m] prior taking the logarithm.

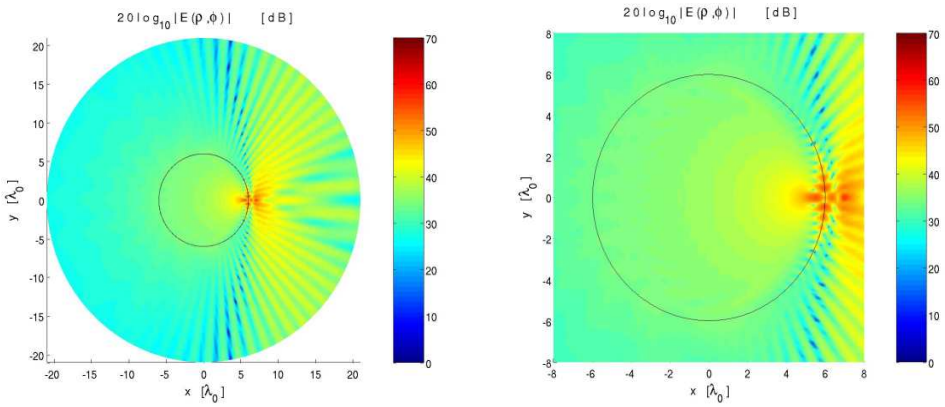

(a) (b)

Figure 3: *(a) Electric field distribution for "$1\varepsilon_0 1\mu_0$" DNG cylinder having radius $a = 6\lambda_0$ and the ELS at a distance $b = 1\lambda_0$ from the cylinder. (b) Selected region of (a) showing a closer look of the high field value formation.*

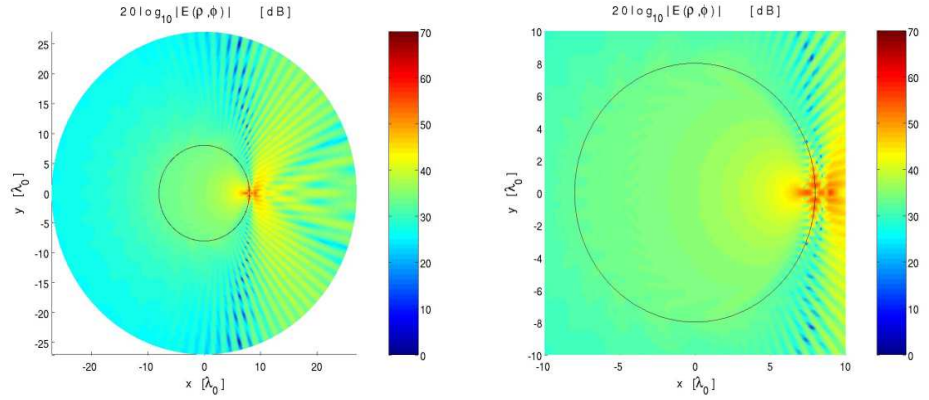

(a) (b)

Figure 4: *(a) Electric field distribution for "$1\varepsilon_0 1\mu_0$" DNG cylinder having radius $a = 8\lambda_0$ and the ELS at a distance $b = 1\lambda_0$ from the cylinder. (b) Selected region of (a) showing a closer look of the high field value formation.*

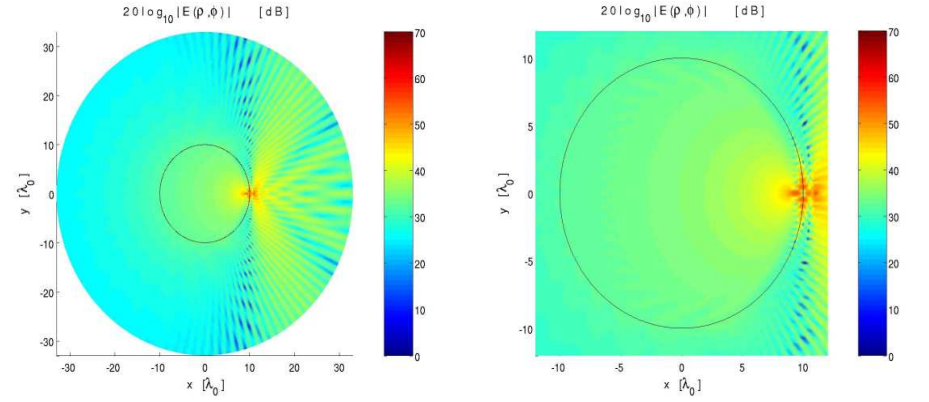

(a) (b)

Figure 5: *(a) Electric field distribution for "$1\varepsilon_0 1\mu_0$" DNG cylinder having radii $a = 10\lambda_0$ and the ELS at a distance $b = 1\lambda_0$ from the cylinder (a). (b) Selected region of (a) showing a closer look of the high field value formation.*

field which is thus omnidirectional. In comparison to this, the corresponding "$1\varepsilon_0 1\mu_0$" DNG cylinder of course has a significant effect on the field of the ELS by creating a field pattern with several lobes and a shadow region. It is observed that the variation of the field pattern is naturally more pronounced for the cylinders having larger radius. In all cases, there appears to be a formation of a point inside the cylinders at which the field assumes very high values. A similar effect was observed in [16] for the case of plane wave incidence. This formation, though less clear for the cylinder of radius $2\lambda_0$ than for the cylinders of larger radius, suggests that some focusing of the ELS field takes place inside the cylinders. Contrary to the well-known case of the lossless DNG slab configuration of the same material parameters, see e.g., [1] and [12], no high field values are observed in the region to the left of the cylinders along the negative x-axis. Moreover, the point inside the cylinders at which the field attains a high value does not represent an exact image of the ELS since the cylinder surface is curved and its aperture is finite. In addition to the high field value formation inside the cylinders, the field also attains rather high values along the part of the cylinder surface which is close to the ELS, see figures 3(b), 4(b) and 5(b).

3.1.2 Results for "$2\varepsilon_0 1\mu_0$" and "$1\varepsilon_0 2\mu_0$" DPS and DNG cylinders

Figures 6(a) and 7(a) show the field for "$2\varepsilon_0 1\mu_0$" DPS cylinders having radii $a = 2\lambda_0$ and $a = 4\lambda_0$, respectively, while figures 8(a) and 9(a) show the field for "$1\varepsilon_0 2\mu_0$" DPS cylinders having the same radii, respectively. In all cases, the ELS is located at $b = 1\lambda_0$. The results for the corresponding DNG cylinders are shown in figures 6(b) -7(b), and 8(b) - 9(b), respectively.

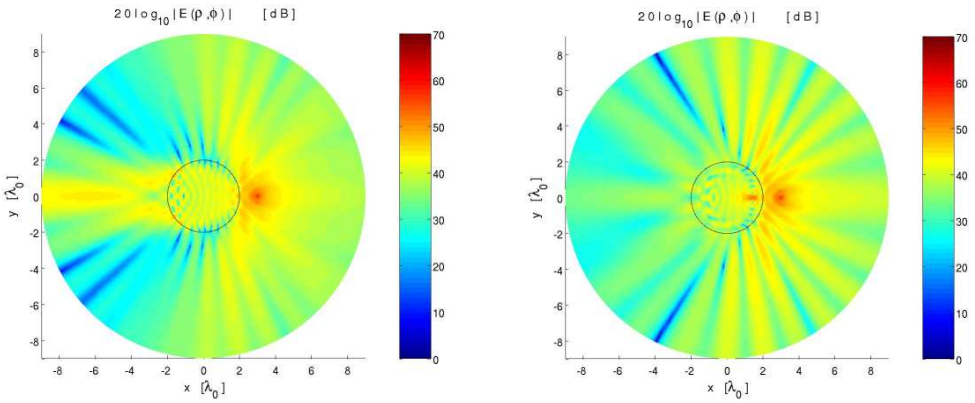

(a) (b)

Figure 6: *Electric field distribution for "$2\varepsilon_0 1\mu_0$" DPS (a) and DNG (b) cylinders having radius $a = 2\lambda_0$. The ELS is at a distance $b = 1\lambda_0$ from the cylinder.*

For the DPS cylinders a clear beam formation along the negative x-axis is observed, the beam being somewhat broader for the cylinders of larger radius. That is, the DPS cylinder configuration constitutes a lens-like antenna. Some field variation is observed in the half-space in which the ELS is located, and no shadow region is formed. For the DNG cylinder configurations, the field pattern exhibits rather large azimuthal variation, the variations being more pronounced for the cylinders of larger radius. The field outside the DNG cylinders is mainly confined to the half-space in which the ELS is located. Furthermore, the field variation is more pronounced for the DNG than for the DPS cylinders in the sense that much deeper zeros are observed in the pattern. Regarding the field transmitted into the DNG cylinders, a clear formation of a high field value is observed, this being more clear than with the previously shown results for "$1\varepsilon_0 1\mu_0$" DNG cylinders, again suggesting that some focusing of the ELS field is taking place. For both DPS and DNG cylinders, the field inside them is higher for the cylinders possessing the larger μ_c.

When the distance between the ELS and the cylinder is increased to $b = 2\lambda_0$, the field variation increases notably, and in the case of DNG cylinders, the formation of a high field value inside the cylinders is not as clear as with the $1\lambda_0$ distance considered previously. This is illustrated in Figure 10(a) and (b), respectively, which shows the results for "$2\varepsilon_0 1\mu_0$" and "$1\varepsilon_0 2\mu_0$" DNG cylinders having radius $a = 2\lambda_0$

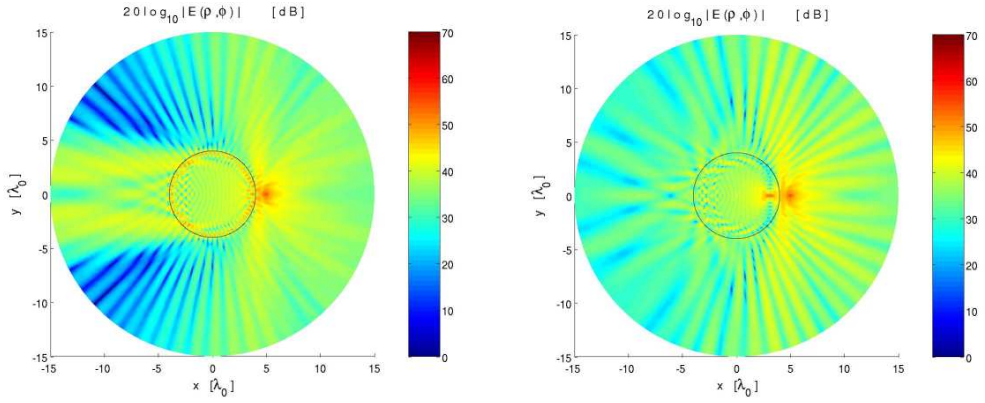

(a) (b)

Figure 7: *Electric field distribution for "*$2\varepsilon_0 1\mu_0$*" DPS (a) and DNG (b) cylinders having radius* $a = 4\lambda_0$*. The ELS is at a distance* $b = 1\lambda_0$ *from the cylinder.*

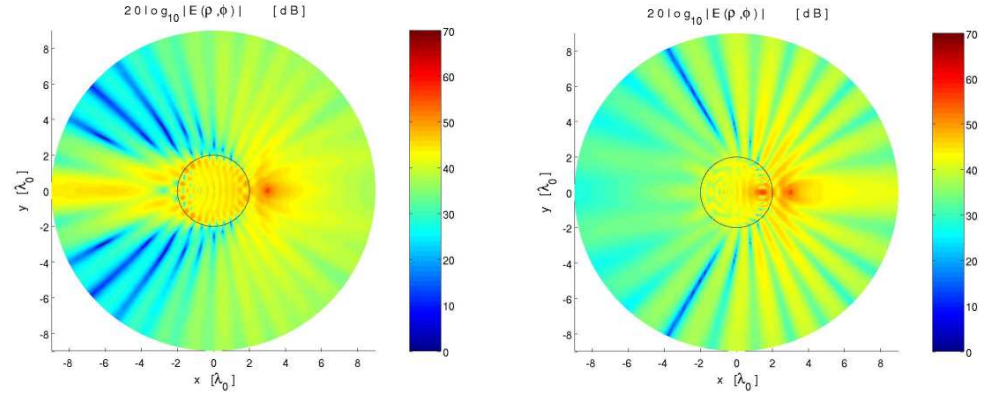

(a) (b)

Figure 8: *Electric field distribution for "*$1\varepsilon_0 2\mu_0$*" DPS (a) and DNG (b) cylinders having radius* $a = 2\lambda_0$*. The ELS is at a distance* $b = 1\lambda_0$ *from the cylinder.*

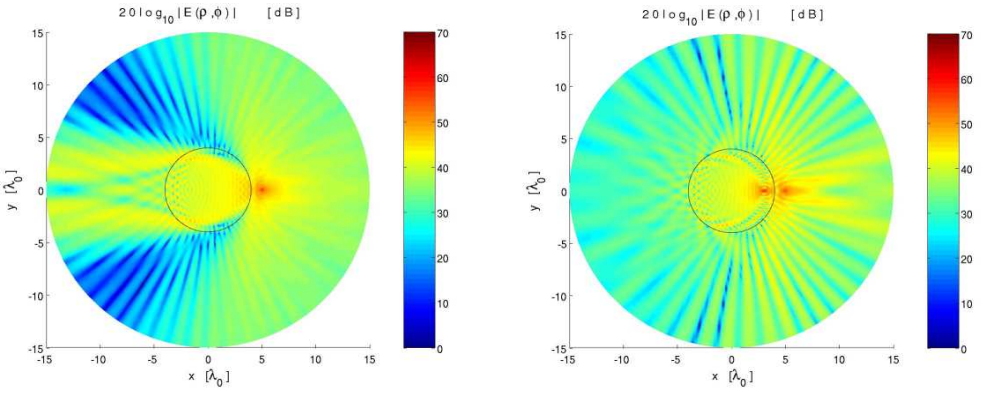

(a) (b)

Figure 9: *Electric field distribution for "*$1\varepsilon_0 2\mu_0$*" DPS (a) and DNG (b) cylinders having radius* $a = 4\lambda_0$*. The ELS is at a distance* $b = 1\lambda_0$ *from the cylinder.*

and the ELS located at $b = 2\lambda_0$. If the distance between the cylinder and the ELS is further increased, the field variation increases even further, and the high field value formation becomes very difficult to observe.

It is noted that DPS and DNG cylinders with various other combinations of the material parameters, investigated in our study but not included in this manuscript, give rise to the same observations as made above.

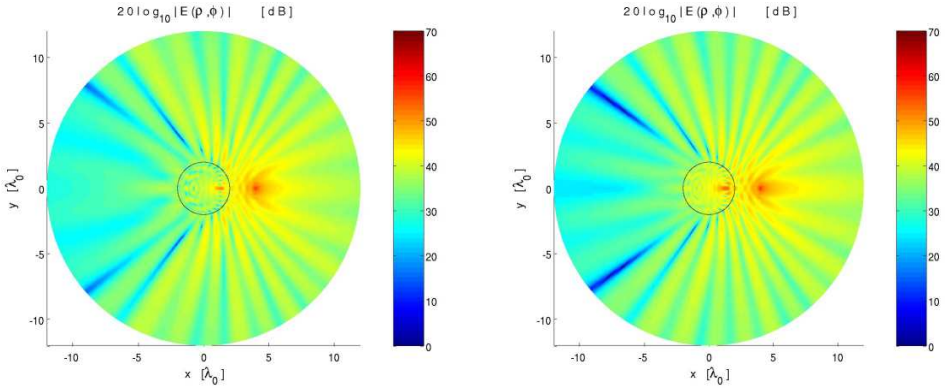

(a) (b)

Figure 10: *Electric field distribution for "$2\varepsilon_0 1\mu_0$" (a) and "$1\varepsilon_0 2\mu_0$" (b) DNG cylinders having radius $a = 2\lambda_0$. The ELS is at a distance $b = 2\lambda_0$ from the cylinder.*

In what follows, some results for DPS and DNG cylinders having a fairly small radius are shown. Figures 11(a) and 12(a), respectively, show the near-field distribution for "$2\varepsilon_0 1\mu_0$" and "$1\varepsilon_0 2\mu_0$" DPS cylinders, while figures 11(b) and 12(b) show the same results for the corresponding DNG cylinders. In all cases, the cylinder radius is $a = 0.1\lambda_0$, and the ELS is $0.3\lambda_0$ away from the cylinder surface. As can be observed the field patterns for DPS cylinders are very similar, while those for DNG cylinders differ considerably. In particular, very high field values are observed along the entire surface of the "$2\varepsilon_0 1\mu_0$" DNG cylinder, while this is not the case for the "$1\varepsilon_0 2\mu_0$" DNG cylinder. It is noted that the DNG cylinders have a much larger effect on the ELS field than the corresponding DPS cylinders.

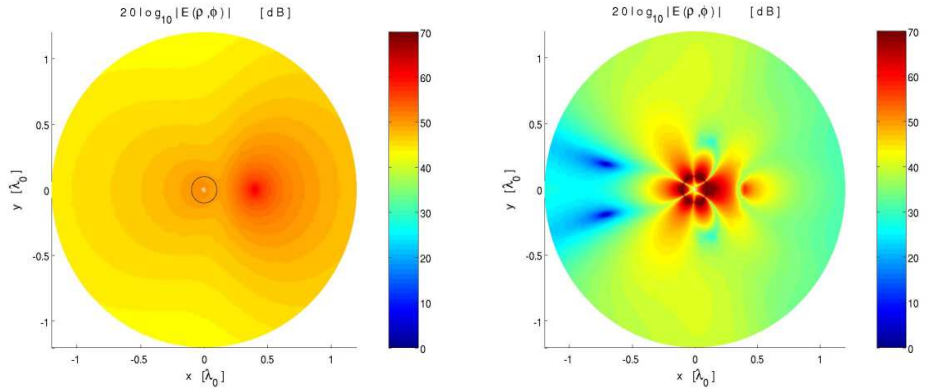

(a) (b)

Figure 11: *Electric field distribution for "$2\varepsilon_0 1\mu_0$" DPS (a) and DNG (b) cylinders having radius $a = 0.1\lambda_0$. The ELS is at a distance $b = 0.3\lambda_0$ from the cylinder.*

3.1.3 Results for different ELS positions

In the previous sections it was shown that the field pattern outside the DNG cylinders exhibits a significant variation with the azimuthal direction of observation for a fixed position of the ELS. Next, the variation

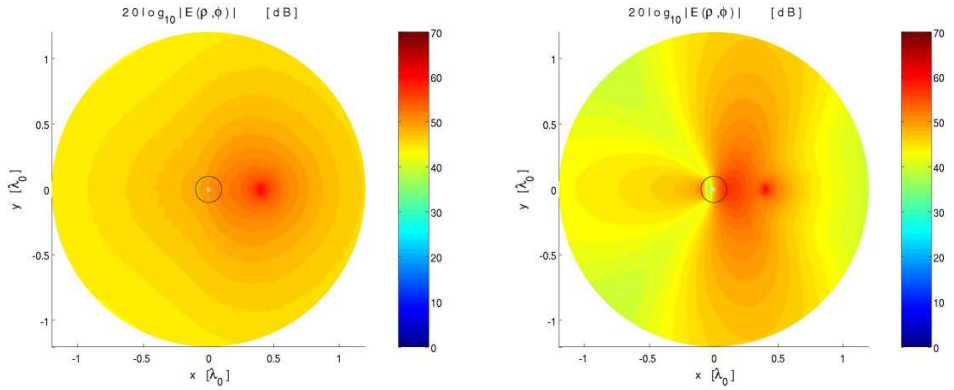

(a) (b)

Figure 12: *Electric field distribution for "*$1\varepsilon_0 2\mu_0$*" DPS (a) and DNG (b) cylinders having radius* $a = 0.1\lambda_0$*. The ELS is at a distance* $b = 0.3\lambda_0$ *from the cylinder.*

of the field pattern with different positions of the ELS is investigated to study the constructive/destructive interference of the incident and scattered fields.

To this end, the field patterns are recorded for a "$1\varepsilon_0 1\mu_0$" DNG cylinder of radius $a = 2\lambda_0$ and the ELS distances $b = [0.25, 0.40, 0.65, 0.75]\lambda_0$ [5], see Figure 13.
It is observed that the patterns shown in Figure 13(a) and (b), apart from being somewhat ripple-like, contain a sort of a main beam in the $\phi = 0^o$ direction. This can be explained by the constructive interference taking place in these two cases. However, the main beam is more clear for the distance $b = 0.40\lambda_0$ than for the $b = 0.25\lambda_0$ distance. In the case of the $b = 0.65\lambda_0$ distance, see Figure 13(c), the main beam is completely absent and this can be explained by the destructive interference. At the distance $b = 0.75\lambda_0$ the field begins to attain high field values in the $\phi = 0^o$ direction. However, due to a longer distance to the ELS, this formation does not merge in any sort of a main beam, and it is not nearly as pronounced as in the case of the two smaller distances giving rise to the constructive interference, see Figure 13(a) and (b). In addition, considerable sidelobes are present in the pattern of Figure 13(d).

Similar investigations as above were performed for the "$2\varepsilon_0 1\mu_0$" and "$1\varepsilon_0 2\mu_0$" DNG cylinders. The effects of constructive and destructive interference were observed, but they were far from being as pronounced as for the case of "$1\varepsilon_0 1\mu_0$" DNG cylinders shown here.

3.1.4 Results in terms of geometrical optics ray-tracing technique

It is interesting to note that the numerical results based on the eigenfunction solution technique presented inhere can be interpreted by means of the geometrical optics (GO) ray-tracing technique.

A number of incident rays launched from the ELS and forming angles $\alpha = \pm\ [0,\ 10,\ 20,\ 30,\ 35]^o$ with the x-axis are traced to their intersection points on the surface of the cylinder. At these points, Snell's law of refraction is then used to determine the directions of the corresponding refracted rays into the cylinder.

To exemplify the matters, the GO ray-tracing has been performed for the configuration of which the near-fields were shown in Figure 6, and the result is shown in Figure 14.
Comparing the results shown in figures 6 and 14, it is found that the GO ray-tracing results support the numerical results very well. The presence of a localized high field value for the DNG cylinder is also noted.

It is noted that the GO ray-tracing analysis was likewise performed, but not included inhere, for other configurations of which the near-fields were shown previously. In all cases, the GO ray-tracing results supported the numerical results very well. For the case of plane wave incidence [16] has reported a similar GO investigation.

[5] The field pattern was obtained for other distances as well. These are $b = [0.30, 0.35, 0.45, 0.50, 0.55, 0.60, 0.70]\lambda_0$. However, the effects explained in terms of constructive and destructive interferences are most in evidence for the distances $b = [0.25, 0.40, 0.65, 0.75]\lambda_0$. Therefore, only the results for the latter distances are included inhere.

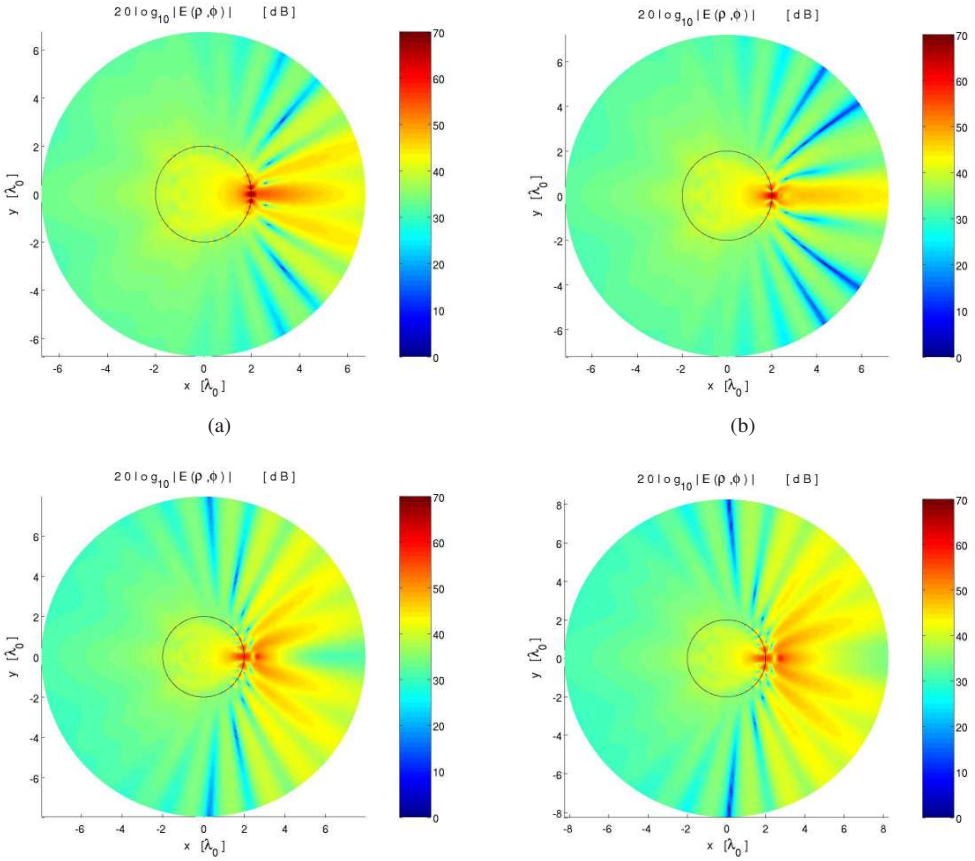

Figure 13: *Electric field distribution for "*$1\varepsilon_0 1\mu_0$*" DNG cylinder having radius* $a = 2\lambda_0$ *and the ELS placed at (a)* $b = 0.25\lambda_0$*, (b)* $b = 0.40\lambda_0$*, (c)* $b = 0.65\lambda_0$*, and (d)* $b = 0.75\lambda_0$*.*

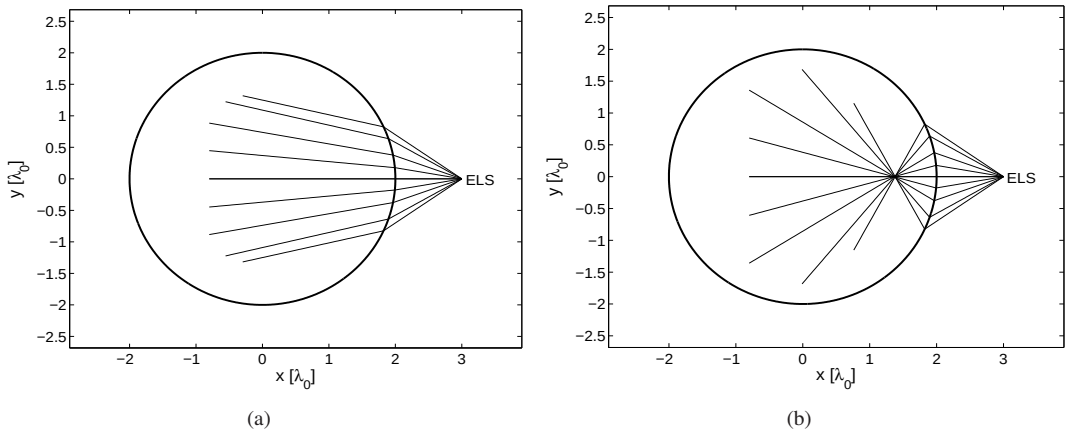

Figure 14: *GO ray-tracing results for "*$2\varepsilon_0 1\mu_0$*" DPS (a) and DNG (b) cylinders having radius* $a = 2\lambda_0$*. The ELS is at a distance* $b = 1\lambda_0$ *from the cylinder. The corresponding eigenfunction solution is shown in Figure 6.*

3.2 Far-field properties

Second, the far-field properties of DNG cylinders are investigated. This is done by examining their directivity and the normalized radiation resistance, both of which the analytical formulae were derived

in Section 2.2.

3.2.1 Directivity

Figure 15 shows the directivity for the "$1\varepsilon_0 1\mu_0$" DNG cylinder configuration for which the near-fields were depicted in Figure 2. The directivity for the corresponding DPS cylinder is shown as well and this is, of course, uniformly distributed.

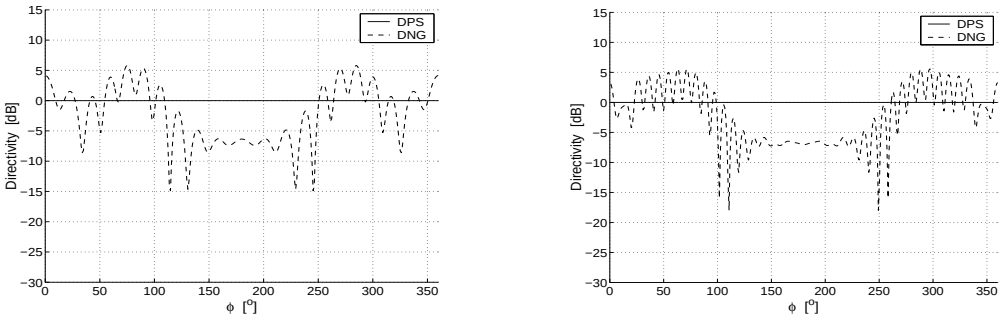

Figure 15: *Directivity for "$1\varepsilon_0 1\mu_0$" DPS and DNG cylinders having radii $a = 2\lambda_0$ (a) and $a = 4\lambda_0$ (b). The ELS is at a distance $b = 1\lambda_0$ from the cylinder.*

The DNG cylinders do not exhibit any main lobe formation, and the pattern contains a number of ripples, this being more pronounced for the cylinder of the larger radius. These observations are in accordance with the near-field results shown in Figure 2. The formation of a shadow region is obvious in both cases since the directivity attains much lower values for $\phi \in [125^o, 225^o]$ than for $\phi \in [0^o, 125^o[\cup]225^o, 360^o[$.

Similar observations apply for cylinders of other material parameters. Figure 16(a) and (b) show the directivity for DPS and DNG cylinders for which the near-fields were shown in figures 6 and 7, respectively. In addition, Figure 17(a) and (b) show the directivity for DPS and DNG cylinders for which the near-fields were shown in figures 8 and 9, respectively.

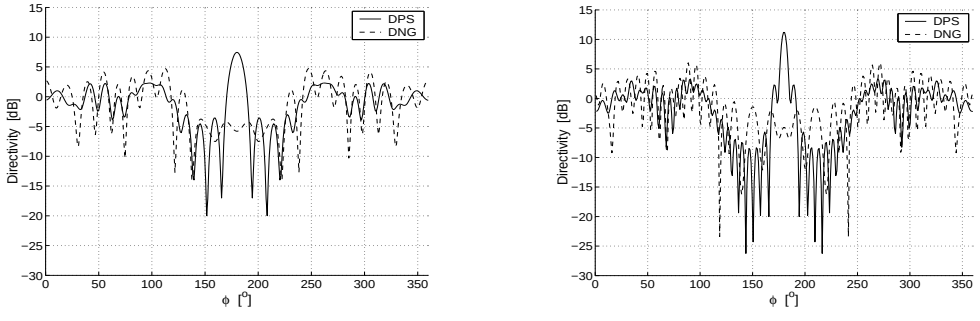

Figure 16: *Directivity for "$2\varepsilon_0 1\mu_0$" DPS and DNG cylinders having radii $a = 2\lambda_0$ (a) and $a = 4\lambda_0$ (b). The ELS is at a distance $b = 1\lambda_0$ from the cylinder.*

In all cases a clear lobe formation is observed for DPS cylinders in the angular region close to the $\phi = 180^o$ direction. As the observation point is moved away from this direction, the pattern becomes ripple-like, this again being more pronounced for the larger cylinder. The DNG cylinder directivity is observed to contain no distinct main lobe, but instead a number of ripples in the pattern. In these cases the shadow region around $\phi = 180^o$ is easily identified. As illustrated in Figure 18, this also holds for the "$2\varepsilon_0 1\mu_0$" and "$1\varepsilon_0 2\mu_0$" DNG cylinders having the ELS placed at $b = 2\lambda_0$ (see Figure 10 for the corresponding near-field results). In the case of the $2\lambda_0$ distance from the cylinder, the maximum

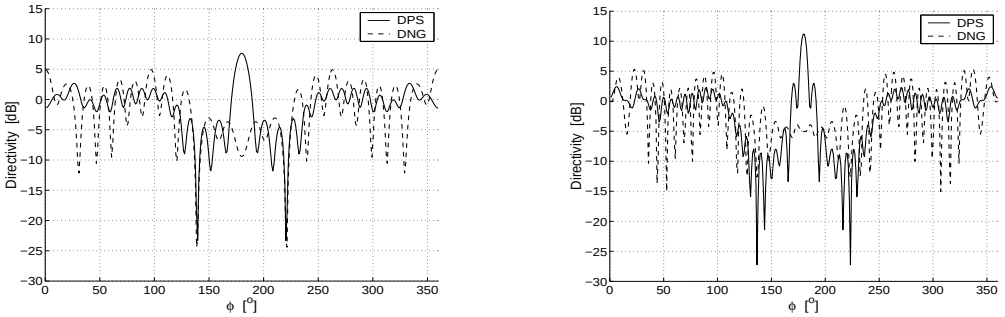

Figure 17: *Directivity for "$1\varepsilon_0 2\mu_0$" DPS and DNG cylinders having radii $a = 2\lambda_0$ (a) and $a = 4\lambda_0$ (b). The ELS is at a distance $b = 1\lambda_0$ from the cylinder.*

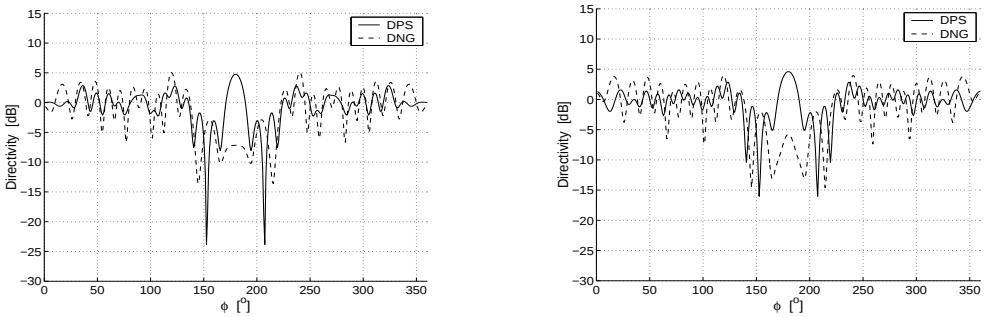

Figure 18: *Directivity for "$2\varepsilon_0 1\mu_0$" (a) and "$1\varepsilon_0 2\mu_0$" (b) DPS and DNG cylinders having radius $a = 2\lambda_0$. The ELS is at a distance $b = 2\lambda_0$ from the cylinder.*

directivity for the DPS cylinders is somewhat lower than in the case of the $1\lambda_0$ distance. Moreover, the shadow region for DNG cylinders is considerably narrowed, as expected, relative to the $1\lambda_0$ distance cases considered above.

For cylinders of other material parameters, of which the results are not included in this manuscript, the observations regarding the directivity resemble those presented above.

3.2.2 Radiation resistance

In Figure 19 the results for R_{rad}^{norm} are shown for "$1\varepsilon_0 1\mu_0$", "$2\varepsilon_0 1\mu_0$", and "$1\varepsilon_0 2\mu_0$" DPS and DNG cylinders as function of cylinder radius a, where $a \in [0.01, 10]\lambda_0$, for $b = 1\lambda_0$ location of the ELS. In Figure 20, the results for R_{rad}^{norm} are shown for "$1\varepsilon_0 1\mu_0$", "$2\varepsilon_0 1\mu_0$", and "$1\varepsilon_0 2\mu_0$" DPS and DNG cylinders of radius $a = 2\lambda_0$ as function of the distance to the ELS, b, where $b \in [0.25, 0.75]\lambda_0$.
As can observed, there is of course no variation for the "$1\varepsilon_0 1\mu_0$" DPS cylinders, see Figure 19(a), while the case of the "$1\varepsilon_0 1\mu_0$" DNG cylinders is seen to exhibit some variation of R_{rad}^{norm} as a changes. For the cylinders having the two other sets of material parameters, see Figure 19(b) and (c), R_{rad}^{norm} is seen to be slightly varying with a. However, the variation is somewhat more pronounced for DNG than for DPS cylinders.

The variation in R_{rad}^{norm} is also observed in the case of varying distance to the ELS. While the results for the "$1\varepsilon_0 1\mu_0$" DPS cylinder are as expected, the "$1\varepsilon_0 1\mu_0$" DNG cylinder exhibits a rather pronounced variation of R_{rad}^{norm} with b. In addition, the "$2\varepsilon_0 1\mu_0$" and "$1\varepsilon_0 2\mu_0$" DPS cylinders do not show as large variation as the corresponding DNG cylinder. However, the variation is more pronounced for the "$1\varepsilon_0 2\mu_0$" DNG cylinder than for the "$2\varepsilon_0 1\mu_0$" DNG cylinder, and in both cases the variation is larger for DNG than for DPS cylinders.

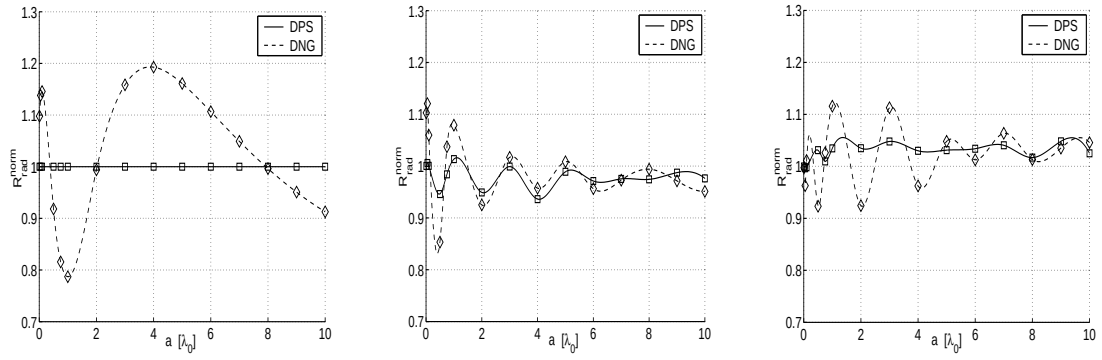

(a) "$1\varepsilon_0 1\mu_0$" cylinders. (b) "$2\varepsilon_0 1\mu_0$" cylinders. (c) "$1\varepsilon_0 2\mu_0$" cylinders.

Figure 19: *Variation of the normalized radiation resistance, R_{rad}^{norm}, as function of the cylinder radius, a, for DPS and DNG cylinders of various material parameters. The ELS is at a distance $b = 1\lambda_0$ from the cylinder. The markers indicate those radii for which R_{rad}^{norm} is calculated.*

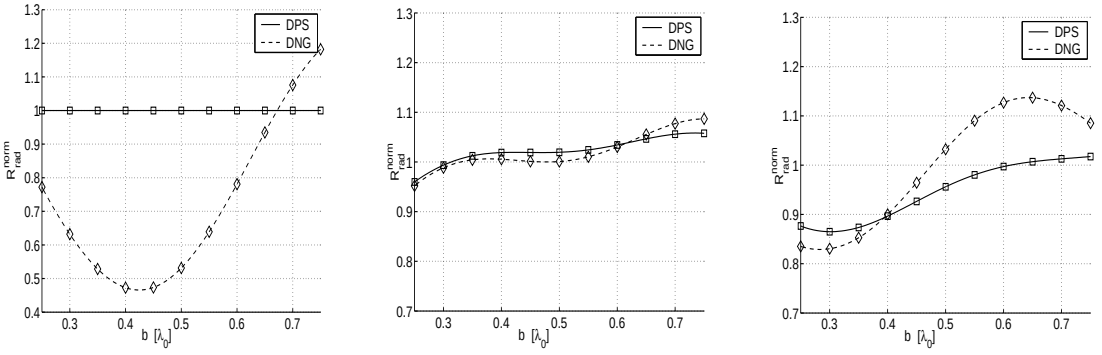

(a) "$1\varepsilon_0 1\mu_0$" cylinders. (b) "$2\varepsilon_0 1\mu_0$" cylinders. (c) "$1\varepsilon_0 2\mu_0$" cylinders.

Figure 20: *Variation of the normalized radiation resistance, R_{rad}^{norm}, as function of the distance to the cylinder, b, for DPS and DNG cylinders of radius $a = 2\lambda_0$ and various material parameters. The markers indicate those radii for which R_{rad}^{norm} is calculated.*

For cylinders of other material parameters, of which the results are not included in this manuscript, the observations regarding the radiation resistance resemble those presented above.

4 Conclusions

In the present work some properties of a general antenna configuration consisting of an infinitely long circular cylinder of lossless DNG material, illuminated by a close-by ELS, have been investigated. The analytical solution was first derived for the case of DPS cylinders and the steps necessary to obtain the solution for DNG cylinders were then outlined. In this regard the sign of some important parameters for DNG materials was briefly discussed. Subsequently, numerical calculations were performed to investigate the influence of different geometrical and electromagnetic parameters on the near-field, inside as well as outside the cylinder, and the far-field, in terms of the directivity and radiation resistance.

It was observed that, relative to the results of DPS cylinders, the effect of the DNG cylinder is most notable in the case of "$1\varepsilon_0 1\mu_0$" cylinders for which the near-field results revealed a formation of a field pattern with several lobes and a shadow region. Moreover, a high field value formation was observed at a point inside the DNG cylinders suggesting that some focusing of the field is taking place. It was furthermore noted that the point of the high field formation does not represent an exact image of the ELS due to the curved surface of the cylinder and its finite aperture. Similar features were observed for "$2\varepsilon_0 1\mu_0$" and "$1\varepsilon_0 2\mu_0$" DNG cylinders, but the high field value at a point inside the cylinders was found to be more clear. The presence of a localized high field value for the DNG cylinders was shown

to be supported by the GO ray-racing results. No distinct main lobe could be observed in the pattern for the "$2\varepsilon_0 1\mu_0$" and "$1\varepsilon_0 2\mu_0$" DNG cylinders, while the corresponding DPS cylinders were found to be directive with a clear main lobe. However, for specific small distances to the ELS, a constructive interference was observed in the pattern for "$1\varepsilon_0 1\mu_0$" DNG cylinders and this lead to a sort of a main lobe, while destructive interference was observed for some other distances. The same phenomena, but far less pronounced, was observed for the "$2\varepsilon_0 1\mu_0$" and "$1\varepsilon_0 2\mu_0$" DNG cylinders. It was furthermore shown that the near-field results are well in agreement with the directivity which is rather ripple-like and without a distinct main lobe for the DNG cylinders. In contrast to this, the directivity of the "$2\varepsilon_0 1\mu_0$" and "$1\varepsilon_0 2\mu_0$" DPS cylinders was observed to posses a clear main lobe, while, of course, being uniform for the "$1\varepsilon_0 1\mu_0$" DPS cylinders. The radiation resistance varied more for DNG cylinders than for DPS cylinders as function of their radius ("$1\varepsilon_0 1\mu_0$" DPS cylinders exhibited, of course, no variation) . This was also the case when the variation with the distance to the ELS was investigated.

In conclusion, the near- as well as far-field properties of DNG cylinders illuminated by an ELS were found to be vastly different from those of the corresponding DPS cylinders. While DPS cylinder can function as a lens and provide a directive pattern with a distinct main lobe, this is not the case for the DNG cylinder configurations investigated herein. Other antenna-like configurations have been investigated in the literature [12]-[19], and many more configurations are obviously possible. An extension of the present work will involve DNG materials which are lossy and dispersive. In addition, an investigation into the near-field, directivity and radiation resistance of PEC or DPS cylinders covered with lossless and lossy DNG cylindrical shells will be conducted.

References

[1] V. G. Veselago, "The electrodynamics of substances with simultaneously negative values of ε and μ," *Sov. Phys. Usp.*, vol. 10, pp. 509-514, Jan.-Feb. 1968.

[2] D. R. Smith, W. J. Padilla, D. C. Vier, S. C. Nemat-Nasser, and S. Schultz, "Composite medium with simultaneously negative permeability and permittivity," *Phys. Rev. Lett.*, vol. 84, pp. 4184-4187, May 2000.

[3] R. A. Shelby, D. R. Smith, S. C. Nemat-Nasser, and S. Schultz, "Microwave transmission through a two-dimensional, isotropic, left-handed metamaterial," *App. Phys. Lett.*, vol. 78, pp. 489-491, Jan. 2001.

[4] J. B. Pendry, A. J. Holden, W. J. Stewart, and I. Youngs, "Extremely low frequency plasmons in metallic meso structures," *Phys. Rev. Lett.*, vol. 76, pp. 4773-4776, June 1996.

[5] J. B. Pendry, A. J. Holden, D. J. Robbins, and W. J. Stewart, "Magnetism from conductors and enhanced nonlinear phenomena," *IEEE Trans. Microwave Theory Tech.*, vol. 47, pp. 2075-2084, Nov. 1999.

[6] R. A. Shelby, D. R. Smith, and S. Schultz, "Experimental verification of a negative index of refraction," *Science*, vol. 292, pp. 77-79, Apr. 2001.

[7] C. G. Parazzoli, R. B. Greegor, K. Li, B. E. C. Koltenbah, and M. Tanielian, "Experimental verification and simulation of negative index of refraction using Snell's Law," *Phys. Rev. Lett.*, vol. 90, pp. 4011-4014, Mar. 2003.

[8] R. Marques, J. Martel, F. Mesa, and F. Medina, "A new 2D isotropic left-handed metamaterial design: theory and experiment," *Microwave Opt. Tech. Lett.*, vol. 35, pp. 405-408, Dec. 2002.

[9] G. V. Eleftheriades, A. K. Iyer, and P. C. Kremer, "Planar negative refractive index media using

periodically L-C loaded transmission lines," *IEEE Trans. Microwave Theory Tech.*, vol. 50, pp. 2702-2712, Dec. 2002.

[10] C. Caloz, and T. Itoh, "Transmission line approach of left-handed (LH) materials and microstrip implementation of an artificial LH transmission line," *IEEE Trans. Antennas Propagat.*, vol. 52, pp. 1159-1166, May 2004.

[11] C. L. Holloway, E. F. Kuester, J. Baker-Jarvis, and P. Kabos, "A double negative (DNG) composite medium composed of magnetodielectric spherical particles embedded in a matrix," *IEEE Trans. Antennas Propagat.*, vol. 51, pp. 2596-2603, Oct. 2003.

[12] J. B. Pendry, "Negative refraction makes a perfect lens," *Phys. Rev. Let.*, vol. 85, pp. 3966-3969, Oct. 2000.

[13] V. Kuzmiak, and A. A. Maradudin, "Scattering properties of a cylinder fabricated from a left-handed material," *Phys. Rev. B.*, vol. 66, pp. 1161-1167, July 2002.

[14] A. Alù, and N. Engheta, "Resonances in sub-wavelength cylindrical structures made of pairs of double-negative and double-positive or ε-negative and μ-negative coaxial shells," *Dig. of ICEAA'03*, pp. 435-438, Turin, Italy, Sept. 8-12, 2003.

[15] R. Ruppin, "Surface polaritons and extinction properties of a left-handed cylinder," *J. Phys.: Condens. Matter.*, vol. 16, pp. 5991-5998, Aug. 2004.

[16] R. Ruppin, "Intensity distribution inside scatterers with negative-real permittivity and permeability," *Microwave Opt. Technol. Lett.*, vol. 36, pp. 150-154, Feb. 2003.

[17] R. Ruppin, "Extinction properties of a sphere with negative permittivity and permeability," *Solid State Commun.*, vol. 116, pp. 411-415, Aug. 2000.

[18] R. W. Ziolkowski, and A. Kipple, "Application of double negative materials to increase the power radiated by electrically small antennas," *IEEE Trans. Antennas Propagat.*, vol. 51, pp. 2626-2640, Oct. 2003.

[19] Z. Liu, Z. Lin, and S. T. Chui, "Electromagnetic scattering by spherical negative-refractive-index particles: low-frequency resonance and localization parameters," *Phys. Rev. E.*, vol. 69, pp. 016 619/1-6, Jan. 2004.

[20] M. Duncan (Editor-in-chief), "Focus issue: negative refraction and metamaterials," *Optic Express, on-line*, vol. 11, Apr. 2003.

[21] R. W. Ziolkowski, and N. Engheta (Eds.), "Special issue on metamaterials," *IEEE Trans. Antennas Propagat.*, vol. 51, Oct. 2003.

[22] J. R. Wait, *Electromagnetic radiation from cylindrical structures*, Pergamon Press, Inc., 1959.

[23] M. Kerker, *Scattering of light and other electromagnetic radiation*, Academic Press, Inc., 1969.

[24] C. A. Balanis, *Advanced engineering electromagnetics*, John Wiley & Sons, Inc., 1989.

[25] W. C. Chew, *Waves and fields in inhomogeneous media*, IEEE Press, Inc., 1995.

[26] D. R. Smith, and N. Kroll, "Negative refractive index in left-handed materials," *Phys. Rev. Lett.*, vol. 85, pp. 2933-2936, Oct. 2000.

[27] R. W. Ziolkowski, and E. Heyman, "Wave propagation in media having negative permittivity and permeability," *Phys. Rev. E.*, vol. 64, pp. 056 625/1-15, Oct. 2001.

[28] I. V. Lindell, S. A. Tretyakov, K. I. Nikoskinen, and S. Iivonen, "BW media - media with negative parameters, capable of supporting backward waves," *Microwave Opt. Technol. Lett.*, vol. 31, pp. 129-133, Oct. 2001.

[29] A. L. Pokrovsky, and A. L. Efros, "Sign of refractive index and group velocity in left-handed media ," *Solid State Commun.*, vol. 124, pp. 283-287, 2002.

[30] S. Arslanagić, and O. Breinbjerg, "A note on the sign of some important parameters for left-handed materials," Ørsted•DTU, Electromagnetic Systems, Technical University of Denmark, Internal Report, IR 781, July 2004.

[31] S. Arslanagić, and O. Breinbjerg, "Clarification of the sign of wave number, intrinsic impedance, and refractive index for simple lossless and lossy double negative materials," *Negative Refraction: revisiting electromagnetics from microwaves to optics*, p. 78, Laussane, Switzerland, Feb.-Mar. 2005.

[32] M. Abramowitz, and I. A. Stegun, *Handbook of mathematical functions*, Dover Publications, Inc., 1965.

APPENDIX C

MANUSCRIPT III

Analytical and numerical investigation of the radiation from concentric metamaterial spheres excited by an electric Hertzian dipole[1]

Samel Arslanagić[(1)], Richard W. Ziolkowski[(2)], and Olav Breinbjerg[(1)]

[(1)] Ørsted•DTU, ElectroScience Section, Technical University of Denmark,
Building 348, Ørsteds Plads, DK-2800 Kgs. Lyngby, Denmark,
Tel: +45 4588 1444, Fax: +45 4593 1634,
E-mail: sar@oersted.dtu.dk, ob@oersted.dtu.dk

[(2)] Department of Electrical and Computer Engineering, University of Arizona
1230 E. Speedway Blvd., Tucson, AZ, 85721-0104
Tel: (520) 621-6173, Fax: (520) 621-8076;
E-mail: ziolkowski@arizona.ece.edu

Key terms: *metamaterials*, *radiation*, *scattering*, *sub-wavelength resonances*.

Abstract

The canonical problem of an electric Hertzian dipole radiating in the presence of a pair of concentric double negative metamaterial spheres is investigated analytically and numerically. The spatial distribution of the near field as well as the total radiated power are examined. The results are compared to those for the corresponding structures made of conventional double positive materials. It is shown that electrically small concentric metamaterial spheres can be designed to be resonant and lead to significant changes of the field radiated by the electric Hertzian dipole and, in particular, to significant enhancements of the total radiated power. Furthermore, the influence of dispersion and loss is investigated. Finally, a few results for larger size metamaterial concentric spheres are given.

[1] This manuscript is journal publication no. 1, see the list of publications on pages iv and v.

1 Introduction

Recent years have witnessed an increased interest in various classes of metamaterials (MTMs), such as double-negative (DNG) and single-negative (SNG) materials, as well as interesting combinations of these with conventional double-positive (DPS) materials. A significant amount of work has already been performed on fundamental issues as well as potential applications, see e.g., [1]-[3] and the extensive list of works referenced therein.

The increased interest in MTMs is mainly due to the unusual properties of DNG materials [4] which are characterized by a negative real part of the permittivity as well as the permeability. The unusual properties are not present in conventional DPS materials which are characterized by a positive real part of these parameters. In particular, the concept of the so-called perfect lens [5], consisting of a specific DNG slab, has attracted much attention.. Moreover, combinations of DNG and DPS materials have lead to a new paradigm in the miniaturization of devices such as cavity resonators [6], waveguides [7], scatterers [8], [9], and antennas [9]-[14]. Many of these ideas were based on the observed properties of such electrically small MTM-based structures when illuminated by plane waves or by localized sources such as an electric Hertzian dipole (EHD) or an electric line source (ELS). In particular, it has been observed that such electrically small MTM-based structures can be designed to be resonant and thus provide significant enhancements of the total radiated power or the total scattering cross section. This is in contrast to structures made of only conventional DPS materials.

The purpose of this work is to further investigate the radiation properties of electrically small spherical MTM-based structures that are excited by an arbitrarily oriented and located EHD. In particular, it is shown that such structures can be designed to be resonant and thereby lead to significant enhancements of the total radiated power as compared to the power radiated by the EHD in free space. In extension of [10], [11], where the EHD is located at the origin, the present work investigates also other EHD locations and documents the properties and advantages of such configurations.

The present manuscript is organized as follows. In Section 2, the analytical solution is derived for the problem consisting of an arbitrarily located and oriented EHD radiating in the presence of a pair of concentric MTM spheres. This section also defines quantities which are used in subsequent numerical investigations of these structures. The condition for resonance in the electrically small designs is derived and discussed in Section 3, while Section 4 presents a detailed numerical investigation of the near-field spatial distribution and the total radiated power of these designs. Two types of structures, referred to as the dipolar and quadrupolar ones, are studied in Section 4. The influence of dispersion and loss, present in any realistic MTM, is taken into account in Section 5, while the properties of structures having larger electrical sizes are discussed in Section 6. The potential use of SNG materials in similar electrically small designs is clarified in Section 7. The entire work is summarized and concluded in Section 8.

Throughout this manuscript, the time factor $\exp(j\omega t)$, with ω being the angular frequency and t being the time, is assumed and suppressed.

2 Analytical solution

2.1 The configuration

The configuration of interest is depicted in Figure 1. A sphere (region 1) of radius r_1 is covered with a concentric spherical shell of radius r_2 (region 2) and immersed in an infinite ambient medium (region 3). The concentric MTM spheres are illuminated by an EHD possessing the dipole moment $\vec{p}_s = \hat{p}_s p_s$ with the orientation $\hat{p}_s$ and complex magnitude p_s [Am]. The EHD can be located in any of the three regions and can possess an arbitrary orientation and strength of the dipole moment. The EHD constitutes a model of an electrically short dipole with p_s being the product of the current and length of that dipole. Region i, with $i = 1$ and 2, is characterized by a permittivity and a permeability, denoted by $\varepsilon_i = \varepsilon_i' - j\varepsilon_i''$ and $\mu_i = \mu_i' - j\mu_i''$, respectively, while the wave number inside region i is $k_i = \omega\sqrt{\varepsilon_i \mu_i}$, where the branch of the square root is chosen such that $\mathcal{I}m\{k_i\} \leq 0$. Both region 1 and 2 can be composed of simple DPS, DNG and/or SNG materials. The exterior region, region 3, is free space with the permittivity ε_0 and permeability μ_0. Thus, its wave number is $k_0 = \omega\sqrt{\varepsilon_0 \mu_0}$ and intrinsic impedance

is $\eta_0 = \sqrt{\mu_0/\varepsilon_0}$. A spherical coordinate system (r, θ, ϕ) and the associated Cartesian coordinate system (x, y, z) are introduced such that the origin coincides with the common center of the spheres. The coordinates of the observation point and the EHD are (r, θ, ϕ) and (r_s, θ_s, ϕ_s), respectively.

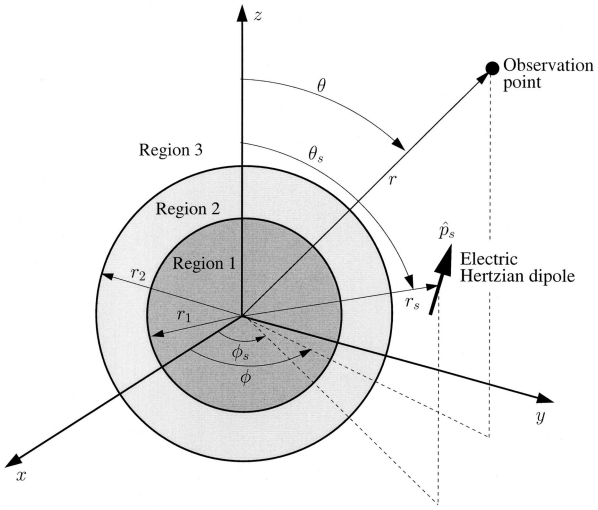

Figure 1: *The configuration of the EHD-excited concentric pair of MTM spheres.*

2.2 The field of the EHD

Following the approach of [15, Ch. 8], the electric field generated by the EHD in an infinite medium, characterized by ε_{EHD}, μ_{EHD} and k_{EHD}, can be expressed as an expansion of spherical transverse magnetic (TM) and transverse magnetic (TE) waves

$$\left\{ \begin{array}{c} \vec{E}_{\text{EHD}}(r,\theta,\phi) \\ \vec{H}_{\text{EHD}}(r,\theta,\phi) \end{array} \right\} = \sum_{n=1}^{N_{max}} \sum_{m=-n}^{m=+n} \left[\frac{1}{j\omega\varepsilon_{\text{EHD}}\mu_{\text{EHD}}} \left\{ \begin{array}{c} a_{nm}^{(c)} \vec{N}_{nm}^{(\text{TM}),(c)} \\ b_{nm}^{(c)} \vec{N}_{nm}^{(\text{TE}),(c)} \end{array} \right\} + \left\{ \begin{array}{c} (-1/\varepsilon_{\text{EHD}})\, b_{nm}^{(c)}\, \vec{M}_{nm}^{(\text{TE}),(c)} \\ (1/\mu_{\text{EHD}})\, a_{nm}^{(c)}\, \vec{M}_{nm}^{(\text{TM}),(c)} \end{array} \right\} \right], \tag{1}$$

where the familiar spherical vector wave functions (SVWFs) are

$$\vec{M}_{nm}^{(\Gamma),(c)}(r,\theta,\phi) = \gamma_{\text{EHD}}\, w_n^{(c)}(k_{\text{EHD}} r)\, e^{jm\phi} \left[\frac{jm}{\sin\theta} P_n^{|m|}(\cos\theta)\, \hat{\theta} - \frac{d}{d\theta} P_n^{|m|}(\cos\theta)\, \hat{\phi} \right], \tag{2}$$

$$\begin{aligned} \vec{N}_{nm}^{(\Gamma),(c)}(r,\theta,\phi) = {} & \gamma_{\text{EHD}}\, \frac{n(n+1)}{r} w_n^{(c)}(k_{\text{EHD}} r)\, P_n^{|m|}(\cos\theta)\, e^{jm\phi}\, \hat{r} \\ & + \gamma_{\text{EHD}}\, \frac{1}{r}\, \frac{d}{dr} \left\{ r w_n^{(c)}(k_{\text{EHD}} r) \right\} \frac{d}{d\theta} P_n^{|m|}(\cos\theta)\, e^{jm\phi}\, \hat{\theta} \\ & + \gamma_{\text{EHD}}\, \frac{1}{r}\, \frac{d}{dr} \left\{ r w_n^{(c)}(k_{\text{EHD}} r) \right\} \frac{jm}{\sin\theta} P_n^{|m|}(\cos\theta)\, e^{jm\phi}\, \hat{\phi}\,, \end{aligned} \tag{3}$$

with $\gamma_{\text{EHD}} = \varepsilon_{\text{EHD}}$ for $\Gamma = \text{TE}$, and $\gamma_{\text{EHD}} = \mu_{\text{EHD}}$ for $\Gamma = \text{TM}$, and with $w_n^{(c)}(\cdot)$ being a specific spherical special function to be introduced below. The quantities $a_{nm}^{(c)}$ and $b_{nm}^{(c)}$ are the TM and TE

expansion coefficients, respectively, of the EHD field which can be expressed as

$$a_{nm}^{(c)} = -jk_{\text{EHD}}\frac{p_s}{4\pi}\frac{1}{\mu_{\text{EHD}}}\frac{2n+1}{n(n+1)}\frac{(n-|m|)!}{(n+|m|)!}\left[\hat{p}_s \cdot \vec{N}_{n,-m}^{(\text{TM}),(5-c)}(r_s,\theta_s,\phi_s)\right] , \tag{4}$$

$$b_{nm}^{(c)} = \frac{k_{\text{EHD}}^3}{\omega}\frac{p_s}{4\pi}\frac{1}{\varepsilon_{\text{EHD}}^2}\frac{2n+1}{n(n+1)}\frac{(n-|m|)!}{(n+|m|)!}\left[\hat{p}_s \cdot \vec{M}_{n,-m}^{(\text{TE}),(5-c)}(r_s,\theta_s,\phi_s)\right] . \tag{5}$$

For $r < r_s$ c is equal to 1, and for $r > r_s$ c is equal to 4. The function $w_n^{(1)}(\cdot) = j_n(\cdot)$, where $j_n(\cdot)$ is the spherical Bessel function of order n, is chosen to represent the field for $r < r_s$ due to its non-singular behavior at the origin, while $w_n^{(4)}(\cdot) = h_n^{(2)}(\cdot)$, with $h_n^{(2)}(\cdot)$ being the spherical Hankel function of second kind and order n, is chosen for $r > r_s$ because it represents an outward propagating wave complying with the radiation condition. The function $P_n^{|m|}$ is the associated Legendre function of the first kind of degree n and order $|m|$. The symbol N_{max} is the truncation limit in a practical numerical implementation of the infinite summation in the exact solution and is chosen in a manner that ensures the convergence of this expansion. When the EHD is located in region 1 and 2, $\varepsilon_{\text{EHD}} = \varepsilon_i$, $\mu_{\text{EHD}} = \mu_i$, and $k_{\text{EHD}} = k_i$, for $i = 1$ and 2, respectively, while $\varepsilon_{\text{EHD}} = \varepsilon_0$, $\mu_{\text{EHD}} = \mu_0$, and $k_{\text{EHD}} = k_0$, when the EHD is in region 3.

2.3 Unknown fields

The unknown fields in each of the three regions, i.e., the scattered field in the region containing the EHD and the total fields in the other regions, are likewise expanded in terms of SVWFs. Therefore, these can be expressed as

$$\left\{ \begin{array}{c} \vec{E}_{1s}(r,\theta,\phi) \\ \vec{H}_{1s}(r,\theta,\phi) \end{array} \right\} = \sum_{n=1}^{N_{max}} \sum_{m=-n}^{m=+n} \left[\frac{1}{j\omega\varepsilon_1\mu_1} \left\{ \begin{array}{c} A_{1,nm}\vec{N}_{nm}^{(\text{TM}),(1)} \\ B_{1,nm}\vec{N}_{nm}^{(\text{TE}),(1)} \end{array} \right\} \right. \tag{6a}$$
$$\left. + \left\{ \begin{array}{c} (-1/\varepsilon_1)\, B_{1,nm}\, \vec{M}_{nm}^{(\text{TE}),(1)} \\ (1/\mu_1)\, A_{1,nm}\, \vec{M}_{nm}^{(\text{TM}),(1)} \end{array} \right\} \right] , \text{ for } r \le r_1$$

$$\left\{ \begin{array}{c} \vec{E}_{2s}(r,\theta,\phi) \\ \vec{H}_{2s}(r,\theta,\phi) \end{array} \right\} = \sum_{n=1}^{N_{max}} \sum_{m=-n}^{m=+n} \left[\frac{1}{j\omega\varepsilon_2\mu_2} \left\{ \begin{array}{c} A_{2,nm}\vec{N}_{nm}^{(\text{TM}),(1)} + A_{3,nm}\vec{N}_{nm}^{(\text{TM}),(2)} \\ B_{2,nm}\vec{N}_{nm}^{(\text{TE}),(1)} + B_{3,nm}\vec{N}_{nm}^{(\text{TE}),(2)} \end{array} \right\} \right. \tag{6b}$$
$$\left. + \left\{ \begin{array}{c} (-1/\varepsilon_2)\, [B_{2,nm}\, \vec{M}_{nm}^{(\text{TE}),(1)} + B_{3,nm}\, \vec{M}_{nm}^{(\text{TE}),(2)}] \\ (1/\mu_2)\, [A_{2,nm}\, \vec{M}_{nm}^{(\text{TM}),(1)} + A_{3,nm}\, \vec{M}_{nm}^{(\text{TM}),(2)}] \end{array} \right\} \right] , \text{ for } r_1 \le r \le r_2$$

$$\left\{ \begin{array}{c} \vec{E}_{3s}(r,\theta,\phi) \\ \vec{H}_{3s}(r,\theta,\phi) \end{array} \right\} = \sum_{n=1}^{N_{max}} \sum_{m=-n}^{m=+n} \left[\frac{1}{j\omega\varepsilon_0\mu_0} \left\{ \begin{array}{c} A_{4,nm}\vec{N}_{nm}^{(\text{TM}),(4)} \\ B_{4,nm}\vec{N}_{nm}^{(\text{TE}),(4)} \end{array} \right\} \right. \tag{6c}$$
$$\left. + \left\{ \begin{array}{c} (-1/\varepsilon_0)\, B_{4,nm}\, \vec{M}_{nm}^{(\text{TE}),(4)} \\ (1/\mu_0)\, A_{4,nm}\, \vec{M}_{nm}^{(\text{TM}),(4)} \end{array} \right\} \right] , \text{ for } r \ge r_2$$

where $A_{i,nm}$, $i = 1, \ldots, 4$ are the unknown expansion coefficients associated with the TM part of the fields, and, henceforth, are referred to as the TM coefficients, while $B_{i,nm}$, $i = 1, \ldots, 4$ are the unknown expansion coefficients associated with the TE part of the fields, and, henceforth, are referred to as the TE coefficients. It is noted that the expansion in (6b) also contains the function $w_n^{(2)}(\cdot) = y_n(\cdot)$, where $y_n(\cdot)$ is the spherical Neumann function of order n. The expressions (1) and (6a)-(6c) represent multipole expansions of the respective fields, i.e., the $n = 1$ term (for which $m = -1, 0$, and 1) corresponds to the dipolar mode, the $n = 2$ term (for which $m = -2, -1, 0, 1$, and 2) corresponds to the quadrupolar mode, and similarly for the other terms.

Enforcing the electromagnetic field boundary conditions, i.e., the continuity of the tangential components of the electric and magnetic fields at the interfaces r_1 and r_2, it can be shown that the unknown expansion coefficients are found from the following relation

$$\vec{D}_{nm} = \left[\bar{\bar{S}}_n\right]^{-1} \vec{\Omega}_{nm}, \quad n = 1, 2, \ldots N_{max}, \quad \text{and} \quad m = -n, \ldots n \tag{7}$$

where $\vec{D}_{nm} = [A_{1,nm}, \ldots, A_{4,nm}, B_{1,nm}, \ldots, B_{4,nm}]$ is the vector containing the eight unknown expansion coefficients, and $\vec{\Omega}_{nm} = [\Omega_{1,nm}, \ldots \Omega_{8,nm}]$ is the excitation vector, which depends on the location of the EHD. The elements of this excitation vector, when the EHD is located in regions 1, 2 or 3, are shown in Table 1.

$\Omega_{i,nm}$	EHD in region 1	EHD in region 2	EHD in region 3
$\Omega_{1,nm}$	$-a_{nm}^{(4)} h_n^{(2)}(k_1 r_1)$	$a_{nm}^{(1)} j_n(k_2 r_1)$	0
$\Omega_{2,nm}$	$-a_{nm}^{(4)} d'_{r=r_1}\{r h_n^{(2)}(k_1 r)\}$	$(\varepsilon_1/\varepsilon_2)\, a_{nm}^{(1)}\, d'_{r=r_1}\{r j_n(k_2 r)\}$	0
$\Omega_{3,nm}$	0	$-a_{nm}^{(4)} h_n^{(2)}(k_2 r_2)$	$a_{nm}^{(1)} j_n(k_0 r_2)$
$\Omega_{4,nm}$	0	$-a_{nm}^{(4)}\, d'_{r=r_2}\{r h_n^{(2)}(k_2 r)\}$	$(\varepsilon_2/\varepsilon_0)\, a_{nm}^{(1)}\, d'_{r=r_2}\{r j_n(k_0 r)\}$
$\Omega_{5,nm}$	$-b_{nm}^{(4)} h_n^{(2)}(k_1 r_1)$	$b_{nm}^{(1)} j_n(k_2 r_1)$	0
$\Omega_{6,nm}$	$-b_{nm}^{(4)} d'_{r=r_1}\{r h_n^{(2)}(k_1 r)\}$	$(\mu_1/\mu_2)\, b_{nm}^{(1)}\, d'_{r=r_1}\{r j_n(k_2 r)\}$	0
$\Omega_{7,nm}$	0	$-b_{nm}^{(4)} h_n^{(2)}(k_2 r_2)$	$b_{nm}^{(1)} j_n(k_0 r_2)$
$\Omega_{8,nm}$	0	$-b_{nm}^{(4)}\, d'_{r=r_2}\{r h_n^{(2)}(k_2 r)\}$	$(\mu_2/\mu_0)\, b_{nm}^{(1)}\, d'_{r=r_2}\{r j_n(k_0 r)\}$

Table 1: *The elements $\Omega_{i,nm}$, $i = 1, \ldots, 8$, of the excitation vector $\vec{\Omega}_{nm}$ when the EHD is located in regions 1, 2, or 3.*

In the table, as well as in certain forthcoming relations, use is made of the expression

$$d'_{r=r_k}\{r_k w_n^{(c)}(k_i r_k)\} = w_n^{(c)}(k_i r_k) + k_i r_k w_n^{(c)\prime}(k_i r_k), \tag{8}$$

where $w_n^{(c)\prime}(x) = dw_n^{(c)}/dx$.

The matrix $\bar{\bar{S}}_n$ is an eight-by-eight matrix that arises from the enforcement of the electromagnetic boundary conditions and, hence, depends on the values of the spherical waves at the two interfaces. The explicit form of this matrix is given by

$$\bar{\bar{S}} = \begin{bmatrix} \bar{\bar{A}}_n & \bar{\bar{0}} \\ \bar{\bar{0}} & \bar{\bar{B}}_n \end{bmatrix}, \tag{9}$$

where $\bar{\bar{0}}$ is a four-by-four zero matrix, $\bar{\bar{A}}_n = \bar{\bar{\Gamma}}_n(\gamma_i = \varepsilon_i,\ i = 1, 2\ ;\ \gamma_3 = \varepsilon_0)$ and $\bar{\bar{B}}_n = \bar{\bar{\Gamma}}_n(\gamma_i = \mu_i,\ i = 1, 2\ ;\ \gamma_3 = \mu_0)$, with the matrix $\bar{\bar{\Gamma}}_n$ having the form of

$$\bar{\bar{\Gamma}}_n = \begin{bmatrix} j_n(k_1 r_1) & j_n(k_2 r_1) & -y_n(k_2 r_1) & 0 \\ d'_{r=r_1}\{r j_n(k_1 r)\} & -\frac{\gamma_1}{\gamma_2} d'_{r=r_1}\{r j_n(k_2 r)\} & -\frac{\gamma_1}{\gamma_2} d'_{r=r_1}\{r y_n(k_2 r)\} & 0 \\ 0 & j_n(k_2 r_2) & y_n(k_2 r_2) & -h_n^{(2)}(k_0 r_2) \\ 0 & d'_{r=r_1}\{r j_n(k_2 r)\} & d'_{r=r_2}\{r y_n(k_2 r)\} & -\frac{\gamma_2}{\gamma_3} d'_{r=r_3}\{r h_n^{(2)}(k_0 r)\} \end{bmatrix}. \tag{10}$$

It is interesting to note that the first four elements of the excitation vector $\vec{\Omega}_{nm}$, i.e., $\Omega_{i,nm}$ with $i = 1, 2, 3$, and 4, see Table 1, are used only in the determination of the unknown TM coefficients $A_{i,nm}$, while the last four elements of this vector, i.e., $\Omega_{i,nm}$ with $i = 5, 6, 7$, and 8, are used in the determination of the unknown TE coefficients $B_{i,nm}$. This matrix structure is due to the fact that TM and TE spherical modes are linearly independent and, hence, their coefficients are uncoupled. In other words, the linear system of equations used to determine the TM coefficients, and the one used to determine the unknown TE coefficients, and vice versa, are uncoupled. As a consequence, relation (7) is split up into two relations for numerical convenience, each involving a four-by-four matrix of the form given by (10) to determine the $A_{i,nm}$ on the one hand, and $B_{i,nm}$ on the other. This fact will also be used in Section 3 in order to obtain conditions under which the two sets of coefficients become very large.

2.4 Total radiated power

In the numerical studies of several MTM-based structures conducted in Section 4 a thorough investigation of their spatial near-field distributions will be undertaken. Aside from these near-field investigations, significant attention will also be devoted to the total radiated power, P_t, henceforth termed the total power. The total power is given by the expression

$$P_t = \lim_{r\to\infty} \frac{1}{2} \int_{\theta=0}^{\pi} \int_{\phi=0}^{2\pi} \mathcal{R}e\{\vec{E}_t(r,\theta,\phi) \times \vec{H}_t^*(r,\theta,\phi)\} \cdot d\vec{s}, \tag{11}$$

where $*$ denotes the complex conjugate and $d\vec{s} = \hat{r}r^2 \sin\theta d\theta d\phi$ is the outward pointing surface differential element. In addition, $\vec{E}_t$ and $\vec{H}_t$ denote the total electric and magnetic field, respectively, in region 3. When the EHD is in region 3, these total fields are equal to the sum of the field generated by the EHD (1) defined for $r > r_s$ and the field (6c), while they equal the field (6c) when the EHD is located in either region 1 or 2. The expression for the total electric and magnetic fields in (11) is easily obtained for large r by introducing the large argument approximations of the involved spherical Hankel functions [16, Ch. 11]. The final expression for the total power then takes the form of

$$P_t = \frac{2\pi}{\omega k_0} \sum_{n=1}^{N_{max}} \sum_{m=-n}^{n} \frac{n(n+1)}{2n+1} \frac{(n+|m|)!}{(n-|m|)!} \left(\frac{|\alpha_{nm}|^2}{\varepsilon_0} + \frac{|\beta_{nm}|^2}{\mu_0} \right), \tag{12}$$

where $\alpha_{nm} = a_{nm}^{(4)} + A_{4,nm}$, $\beta_{nm} = b_{nm}^{(4)} + B_{4,nm}$ if the EHD is located in region 3, and $\alpha_{nm} = A_{4,nm}$, $B_{4,nm}$ if the EHD is located in either region 1 or 2.

The power radiated by the EHD, when situated alone in free space is denoted by P_i and is given by (12) with $\alpha_{nm} = a_{nm}^{(4)}$ and $\beta_{nm} = b_{nm}^{(4)}$. However, the power radiated by the EHD in free space has a considerably simpler and a well-known form if it is not expressed in terms of the SVWFs. In particular, with [17, p. 137] one finds that

$$P_i = \frac{\eta_0 \pi}{3} \left| \frac{p_s k_0}{2\pi} \right|^2. \tag{13}$$

Of particular interest to the present work is the comparison of the total power radiated in the presence of the concentric MTM spheres to that radiated by the EHD alone in free space. To this end, the quantity designated as the power ratio (PR) is introduced. It is given by

$$\text{PR} = \frac{P_t}{P_i}, \tag{14}$$

with P_t and P_i given by (12) and (13), respectively.

In the following sections numerical results for an EHD radiating in the presence of a concentric pair of MTM spheres are presented and discussed. Results for electrically small structures as well as those of larger size are discussed. In particular, if a is the radius of the smallest sphere enclosing the structure, then the term electrically small refers to a structure for which $k_0 a \leq 1$. Furthermore, throughout the forthcoming investigations, a structure is referred to by its properties in region 1 and 2. For instance, a DPS-MTM structure, where the MTM can be a DNG, ENG, or MNG material, indicates that region 1 consists of a DPS material while region 2 consists of the selected MTM.

3 Resonance condition - discussion and derivation

Prior to presenting the results for specifically designed electrically small structures, it is useful to derive the conditions for which they provide enhancements of the total power. To this end it is important to note that specific details on how to find these conditions have already been reported in e.g., [8], [9], [11] for cylindrical and spherical structures. Therefore, only the main points associated with the spherical structures are included below.

With the objective of making the total power in (12) and, hence, the PR in (14) large, the amplitudes of the coefficients $A_{4,nm}$ and/or $B_{4,nm}$ must likewise be large. When the spheres are made of DPS

materials only, these coefficients become large, i.e., they exhibit a resonant behavior, only when the sizes of the spheres are on the order of, or larger, than the wavelengths in the materials [3, Ch. 2]. These resonances are referred to as the wavelength-sized natural resonances of the structure [9]. As the size of the object becomes electrically small, these resonances are lost since no natural modes may exist below a certain cut-off size [3, Ch. 2]. In contrast to this, the unknown coefficients may exhibit a resonance when the structure is made of a specific combination of DPS, DNG, and/or SNG materials, even if the structure is electrically small. These features result due to the presence of the so-called subwavelength-sized natural resonances (also termed interface resonances in [3, Ch. 2] and [8]) in such electrically small structures, see [3, Ch. 2], [8], [9], and [11].

In order to find the condition for which the amplitudes of $A_{4,nm}$ and $B_{4,nm}$ become large, it is first recalled that these coefficients are determined independently of each other. The TM coefficients $A_{4,nm}$ are proportional to the product of the inverse of the matrix $\bar{\bar{A}}_n$ and the first four elements of the excitation vector Ω_{nm}, i.e., $\Omega_{i,nm}$ with $i = 1, 2, 3$, and 4, while the TE coefficients $B_{i,nm}$ are proportional to the product of the inverse of the matrix $\bar{\bar{B}}_n$ and the last four elements of the excitation vector Ω_{nm}, i.e., $\Omega_{i,nm}$ with $i = 5, 6, 7$, and 8. Then, in similitude with the procedure outlined in [9] for the case of concentric MTM-based cylinders illuminated by an ELS, it is found that $A_{4,nm}$ and $B_{4,nm}$ become large, and hence a resonance occurs, when the magnitudes of the determinants of $\bar{\bar{A}}_n$ and $\bar{\bar{B}}_n$, respectively, attain a minimum. As the structures of interest inhere are electrically small, the small argument expansions of the functions in $\bar{\bar{A}}_n$ and $\bar{\bar{B}}_n$, which hold when the products $|k_1|r_1$, $|k_2|r_1$, $|k_2|r_2$, and $|k_0|r_2$ are much smaller than unity, are used to derive the approximate analytical expressions for which the resonances will occur. The derivation of these resonance conditions is facilitated significantly by assuming that the materials in regions 1 and 2 are lossless. For the range of parameters to be investigated here, it can be shown that the TM coefficients $A_{4,nm}$ exhibit a resonance when the approximate condition

$$\frac{r_1}{r_2} \simeq \sqrt[2n+1]{\frac{[(n+1)\varepsilon_0 + n\varepsilon_2][(n+1)\varepsilon_2 + n\varepsilon_1]}{n(n+1)(\varepsilon_2 - \varepsilon_0)(\varepsilon_2 - \varepsilon_1)}}\,, \tag{15a}$$

is met, while the TE coefficients $B_{4,nm}$ exhibit a resonance when the approximate condition

$$\frac{r_1}{r_2} \simeq \sqrt[2n+1]{\frac{[(n+1)\mu_0 + n\mu_2][(n+1)\mu_2 + n\mu_1]}{n(n+1)(\mu_2 - \mu_0)(\mu_2 - \mu_1)}}\,, \tag{15b}$$

is met.

The conditions (15a)-(15b) are used to determine, for a given set of material parameters, the approximate ratio of r_1 and r_2 that will yield a resonant, concentric pair of lossless MTM spheres. The condition for the electrically small resonant structure given by (15) depends on the mode number, n, the values of the permittivity and permeability of the three regions, and, most importantly, on the ratio of the inner and outer radii of region 2. The resonance condition therefore does not depend on the absolute size of these radii. A given resonant structure is defined on the basis of (15), e.g., by first selecting the material parameters and the mode number that is to be excited as the dominant mode, and then selecting the inner (outer) radius. Subsequently, (15) gives the outer (inner) radius of the structure at which the resonance occurs. It is stressed that certain small terms have been neglected in the derivation of (15). Thus, as will be demonstrated below, this condition only constitutes an approximation for the radii ratio at resonance and serves as a guideline to estimate the resonant configuration, i.e., as a starting point for the numerical analysis. Since it is implemented without the use of any small argument expansions, the numerical solution will, of course, be exact. The values of r_1 and r_2 so obtained will be the ones used to define the resonant structures that lead to the performance enhancements demonstrated below. It must be noted that relation (15) has also been derived in [3, Ch.2] and [8] for plane wave scattering from similar spherical structures. Furthermore, the condition (15a) for the $n = 1$ term has likewise been derived and discussed in [18].

As noted in the beginning of this section, large values of the total power, and hence, the PR may result if either $A_{4,nm}$ or $B_{4,nm}$, exhibit a resonance. In this regard, only (15a) or (15b), depending on the specific configuration, needs to be satisfied. According to [3, Ch. 2] and [8], at least one of the parameters, ε_1 or ε_2 for (15a), and μ_1 or μ_2 for (15b), must be negative in order to satisfy the resonance conditions (15a) or (15b). In [15] it has also been pointed out that for (15a) with $n = 1$, the permittivities

of regions 1 and 2 must be of opposite signs to fulfill the condition. Thus, in this case, an ENG or MNG material, respectively, is needed in at least one of the regions 1 or 2. On the other hand, the simultaneous fulfillment of (15a) and (15b) requires either that at least one of the regions, 1 or 2, be a DNG material or that an ENG-MNG or MNG-ENG structures be used. A resonance for the n'th mode in both the $A_{4,nm}$ and $B_{4,nm}$ coefficients requires ε_i and μ_i, $i = 1$ and 2, to be selected such as to insure the same radii ratio for the same mode number n. As will be illustrated in Section 6, the EHD-driven DPS-ENG structures may possess resonant features in the quantities of interest similar to those exhibited by the DPS-DNG ones.

4 Numerical results

4.1 Resonant configurations - definition

The resonant configurations that have been selected to illustrate the results of interest are summarized in Table 2. Two different structures, namely those for which the dominant modes of radiation are the dipolar and the quadrupolar ones, are chosen.

Structure	ε_1	μ_1	ε_2	μ_2	r_1 [mm]	r_2 [mm]
Dipolar	ε_0	μ_0	$\pm 3\varepsilon_0$	$\pm 3\mu_0$	10	18.57
Quadrupolar	ε_0	μ_0	$\pm 3\varepsilon_0$	$\pm 3\mu_0$	10	13.55

Table 2: *Material and approximate geometrical parameters of the electrically small resonant dipolar and quadrupolar configurations.*

Region 1 is assumed to be free space, while region 2 is taken to be a DNG medium. Region 3 is, as noted before, free space. The positive material parameters in region 2 of the corresponding reference DPS-DPS structures are also included in the table. For these fixed materials and the specified value of the radius of region 1 the resonance conditions (15a) and (15b) were used to obtain the approximate value of the radius of region 2 for the structures that excite the dipolar and the quadrupolar modes, respectively, as the dominant ones. These structures are referred to as the dipolar and quadrupolar structures, respectively. Throughout the following discussion, the frequency of operation is $f_0 = 300$ MHz, implying that the free-space wavelength is $\lambda_0 = 1$ m. Although the outer radius of region 2 given in Table 2 is approximate, the forthcoming numerical investigations used the full solution to determine the exact value of this radius. This exact value of the outer radius was subsequently used in the analysis of the relevant figures of merit. The approximate analytical value basically acted as a guide for the numerical determination of the exact value.

The numerical results are illustrated for the following configuration. The EHD is taken to be z-oriented, i.e., $\hat{p}_s = \hat{z}$, and is located on the positive x-axis, i.e., with the coordinates $(r_s, \theta_s = 90^o, \phi_s = 0^o)$. The magnitude of the dipole moment is $p_s = 0.01$ Am. Thus, the structures under examination are either a DPS or a DNG spherical shell in the presence of a z-oriented EHD that is located at an arbitrary distance on the positive x-axis.

It is furthermore interesting to note, as observed from (15a), (15b) and Table 2, that for fixed material parameters, a considerably thinner structure is needed to excite the quadrupolar mode than the dipolar one. This behavior is similar to that found for the cylindrical structures treated in [9]. In addition, the diameter of the resonant dipolar structure is close to 37 mm , or $\lambda_0/27$ (which means $k_0 r_2 = 0.116$), while that of the quadrupolar structure is 27 mm, or $\lambda_0/37$ (which means $k_0 r_2 = 0.085$). This shows that the designed structures are indeed electrically small.

4.2 Electrically small dipolar structures

Presently, the electrically small resonant dipolar DPS-DNG structure is examined and compared to the corresponding DPS-DPS structure.

4.2.1 Total power

Figure 2 shows the PR as a function of the outer shell radius r_2 for the dipolar DPS-DNG and DPS-DPS structures, when the inner radius is $r_1 = 10$ mm and the EHD is in region 1 at $r_s = 5$ mm.

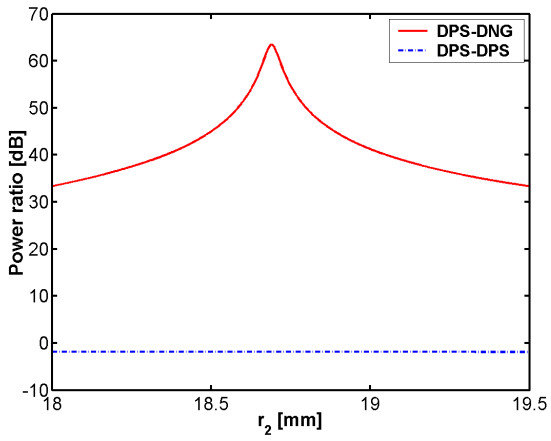

Figure 2: *Power ratio as a function of the outer shell radius r_2 for the dipolar DPS-DNG and DPS-DPS structures. The EHD is in region 1 at $r_s = 5$ mm.*

As can be seen in Figure 2, a resonance in the PR with a maximum value PR $\simeq$ 63 dB or PR $\simeq 1.99\times10^6$ occurs for the DPS-DNG structure at $r_2 = 18.69$ mm. This value is very close to the approximate value $r_2 = 18.57$ mm obtained from (15). In contrast, no resonance in the PR is found for the corresponding DPS-DPS structure; in fact, the PR is somewhat below 0 dB for all considered values of r_2. These results clearly show the advantage of the electrically small dipolar DPS-DNG structure over the corresponding DPS-DPS one. Similar results, not included here, have been obtained for the same structures when the EHD is located in regions 2 and 3. The peak at $r_2 = 18.69$ mm for the DPS-DNG structure is rather broad for this lossless and non-dispersive case. Large PRs are obtained for a range of outer radius values, e.g., PR $>$ 30 dB for $r_2 \in [18, 19.5]$ mm. Furthermore, it is of interest to note that the value of r_2 and the peak value of the PR at $r_2 = 18.69$ mm for the DPS-DNG structure agree very well with the corresponding peak value of the PR for the same radius reported in [10], but for the EHD located at the center of the spheres.

To investigate the effect of the EHD location on the enhancement of the total power, Figures 3(a), 3(b), and 3(c) show, respectively, the PR as a function of the EHD location, r_s, when the EHD is located in regions 1, 2, and 3 for the DPS-DNG and DPS-DPS structures with $r_1 = 10$ mm and $r_2 = 18.69$ mm. The location of the EHD varies in the interval $r_s \in [0.01-9.99]$ mm in Figure 3(a), in $r_s \in [10.1-18.68]$ mm for Figure 3(b), and in $r_s \in [18.7 - 30]$ mm for Figure 3(c).
For all locations, the DPS-DPS structure gives no enhancement, while the corresponding DPS-DNG structure gives very large values of the PR. As the EHD moves through region 1, the PR is approximately constant and equal to PR $\simeq$ 63 dB. As the EHD traverses region 2, a very small decrease of the PR is observed. For the case of the EHD in region 3, it is found that the PR values are diminished as the EHD is moved further away. However, for the considered EHD locations, significant enhancements of the total power are still in evidence as the source moves a significant distance away from the structure.

It is interesting to note that the largest PR values are obtained for EHD locations very close to the origin. One finds that the PR values are falling off slowly as the EHD moves away from the origin through regions 1, 2 and 3. However, the PR values in these three regions are not significantly affected by changing the EHD locations, this being particularly the case when the EHD is in regions 1 and 2. These findings are very interesting and are in sharp contrast to those obtained for the corresponding cylindrical structures excited by an electric line source. For those cylindrical cases the PR values vary significantly when the source is located in the different regions [9]. In particular, these cylindrical counterparts offer no enhancements when the source is located close to and at the origin, and at a specific location inside region 2, while the largest enhancements are found when the source is located near the interfaces of the cylindrical

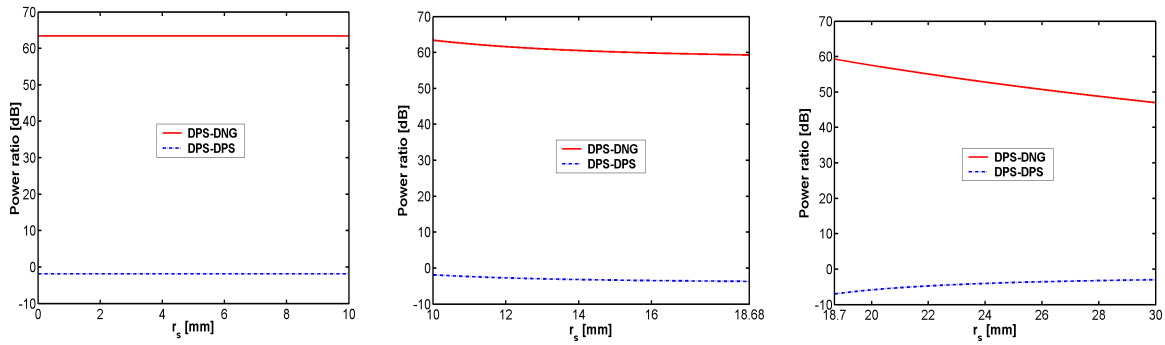

Figure 3: *Power ratio as a function of the EHD location r_s for the dipolar DPS-DNG and DPS-DPS structures when the EHD is located in region 1 (a), region 2 (b), and region 3 (c).*

shell. The differences in the behavior of the spherical and cylindrical structures, as explained in [9], are caused by the fact that the latter allows the monopolar mode. The monopolar mode, which dominates for source locations close to and at the origin, and at a specific location inside region 2, produces no PR enhancements. As the source approaches the interfaces of the cylindrical MTM shell, the dipolar mode is emphasized strongly. As a consequence, large variations in the PR values for the corresponding cylindrical structures occur as the source location varies. In the spherical case, however, there is no monopolar mode regardless of the EHD location. The dipolar mode dominates the radiating/scattering processes when it is excited, and the corresponding enhancement is on the same order of magnitude for all of the considered EHD locations.

4.2.2 Near Field

In order to investigate further the presence of the enhanced PR values when the EHD is radiating in the presence of the DPS-DNG structure, and their absence in the presence of the DPS-DPS structure, near-field investigations are performed next. For the near-field plots the quantity given by $20\log_{10}|E_{t,\theta}|$, where $E_{t,\theta}$ is the θ-component of the total electric field normalized by 1 V/m, is shown. The plane of observation is the xz-plane, and the field is shown in a circular region with a radius of 30 mm.

Figure 4(a) shows the near field of the EHD in free spaca; Figure 4(b) shows the near field of the DPS-DPS structure for which $r_2 = 18.69$ mm (curves representing the spherical surfaces of the DPS-DPS structure are also shown).

The near field of the EHD in free space would, of course, have a dipolar form in a coordinate system centered at the EHD. However, it is seen to be asymmetric in Figure 4(a) due to the displacement of the EHD from the origin. The near field in Figure 4(b) is very similar to the field in Figure 4(a), implying that the present DPS-DPS structure does not affect the field of the EHD. Therefore, such a structure is not expected to lead to any enhancement of the total power, this being in line with the results presented in Figures 2 and 3. Similar results, not included here, have been obtained for DPS-DPS structures with the EHD located in any of the three regions.

The near field of the resonant dipolar DPS-DNG structure with $r_2 = 18.69$ mm is depicted in Figure 4(c). It is clear from comparisons of Figures 4(a)-(c) that the DNG structure has significantly affected the near field of the EHD. More specifically, the near field in Figure 4(c) has a dipolar form. This result indicates that an EHD in the presence of a DPS-DNG structure having these specific geometry and material parameters will excite a dominant dipolar mode. These results agree with those predicted by the approximate resonance conditions (15).

An additional insight into the resonance behavior can be observed from Figure 4(d) where the total power spectrum of the n'th mode for this DPS-DNG structure is found. More specifically, the total power in the n'th mode, $n = 1, 2$, and 3, normalized by the total power in the dipolar mode is depicted. As observed, the vast majority of the total power is contained in the dipolar mode, while only a negligible amount is contained in the next two higher order modes. In particular, $P_t(n = 2)$ and $P_t(n = 3)$ are more than 80 dB below the total power in the dipolar mode, and essentially no power is contained in the

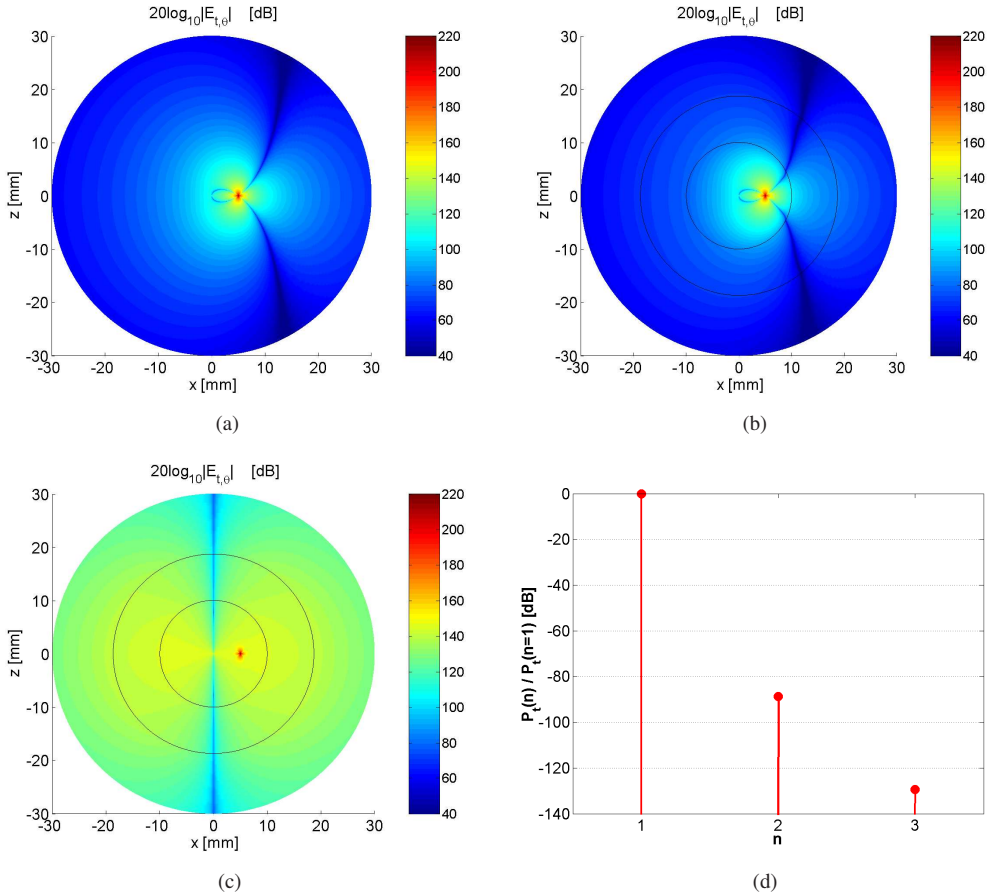

Figure 4: *Electric near field of the EHD in free space (a), in the presence of the DPS-DPS structure (b), and in the presence of the resonant dipolar DPS-DNG structure (c). The EHD is in region 1 at* $r_s = 5$ *mm. (d) The total power of the DPS-DNG structure contained in the* n*'th mode,* $n = 1, 2,$ *and 3, normalized by the total power in the dipolar mode. The plane of observation is the* xz*-plane, and the field is shown in a circular region with a radius of* 30 *mm.*

$n > 3$ modes.

Before closing this section, several remarks are in order. Although not included here, it was verified that the near field of the electrically small resonant dipolar DPS-DNG structure for other locations of the EHD in regions 1, 2, and 3 (provided that moderate distances between the EHD and the structure are considered when the EHD is in region 3) is very similar to the near field shown in Figure 4(c). This means that the excited resonant dipolar mode is the natural dipolar mode of this structure. Consequently, the strongest (weakest) excitation of this mode is obtained by placing the EHD at locations where the field is a maximum (minimum). These findings are general and, therefore, also apply for the quadrupolar (and even higher order) structures considered next.

The strength of the near field in Figure 4(c) is rather constant for those locations of the EHD used in the examination of the PR, see Figures 3 and 4(c), i.e., along the positive x-axis throughout the three regions. Therefore, it is clear that the enhancements observed in Figure 3 are comparable in amplitude.

4.3 Electrically small quadrupolar structures

Next, the results for the quadrupolar DPS-DNG structures are illustrated and compared to the results of the corresponding DPS-DPS structures.

Figure 5 shows the PR as a function of the outer shell radius for quadrupolar DPS-DNG and DPS-DPS structures having $r_1 = 10$ mm and for the EHD being located in region 1 at $r_s = 5$ mm.

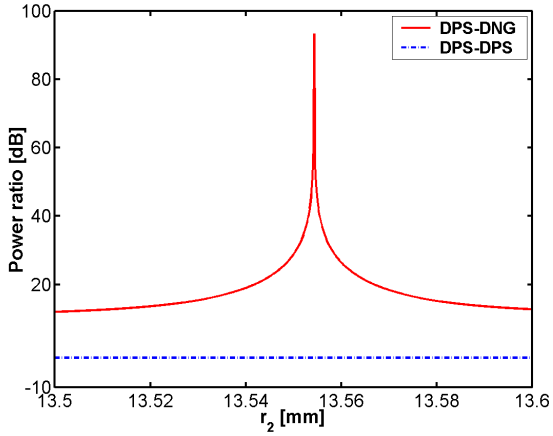

Figure 5: *Power ratio as a function of the outer shell radius r_2 for the quadrupolar DPS-DNG and DPS-DPS structures when the EHD is in region 1 at $r_s = 5$ mm.*

As with the dipolar mode, the present DPS-DPS structure does not offer any enhancements of the total power. On the other hand, a resonance peak and, thus, a significant enhancement of the total power is observed in Figure 5 for the DPS-DNG structure. The maximum PR of the DPS-DNG structure is approximately PR $\simeq$ 93 dB at $r_2 = 13.55$ mm which agrees with the value in Table 2 predicted by the resonance condition (15). It is also found that the resonant enhancements reported in Figure 5 are larger, but extremely narrower than those occurring in the corresponding dipolar DPS-DNG structure. This difference between the dipolar and quadrupolar spherical structures is in line with the differences observed for the dipolar and quadrupolar cylindrical structures in [9].

To verify that these results are due to the resonant excitation of the quadrupolar mode, the near-field and the total power spectra of the n'th mode are again considered. The electric near field for the quadrupolar DPS-DNG structure for which $r_2 = 13.55$ is depicted in Figure 6(a) for the case where the EHD is located at $r_s = 5$ mm (curves representing the spherical surfaces of the DPS-DNG structure are also shown).

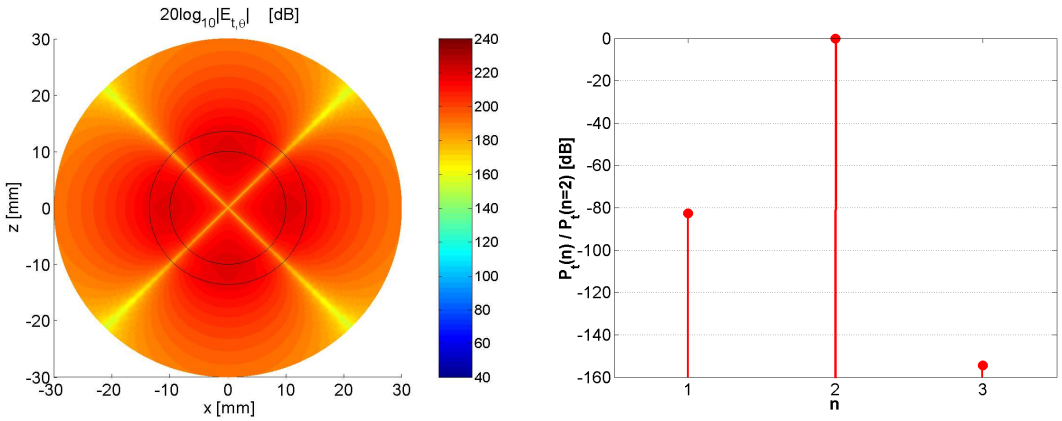

(a) (b)

Figure 6: *Quadrupolar DPS-DNG structure: (a) the electric near field when the EHD is in region 1 at $r_s = 5$ mm, and (b) the total power in the n'th mode, $n = 1, 2$, and 3, normalized by the total power in the quadrupolar mode. In (a), the plane of observation is the xz-plane, and the field is shown in a circular region of radius 30 mm.*

Since the near field has a clear quadrupolar form, it follows that the EHD in the presence of this DPS-

DNG structure excites the quadrupolar mode, and the enhancements of the total power result from this dominant mode. These findings are confirmed with the results given in Figure 6(b), where the total power spectrum of the n'th mode, $n = 1, 2$, and 3, normalized by the total power in the quadrupolar mode, is shown. The largest part of the total power is contained in the quadrupolar mode, while only an extremely small amount is contained in the other modes. Again, essentially no total power is contained in the $n > 3$ modes. Results similar to those reported in Figure 6 are obtained for the quadrupolar DPS-DNG structure when the EHD is located in regions 2 and 3. One also notes from Figure 6(a) that this near field, evaluated at a given distance and direction, is larger (as the dynamic range is larger) than the near field of the corresponding dipolar structure depicted in Figure 4(c). These differences in the near-field values for the dipolar and quadrupolar structures explain why the PR values are higher for the quadrupolar cases.

Additional near-field results for the quadrupolar DPS-DNG structure are shown in Figure 7(a) and (b) for the EHD located at $r_s = 1$ mm and $r_s = 9$ mm, respectively.

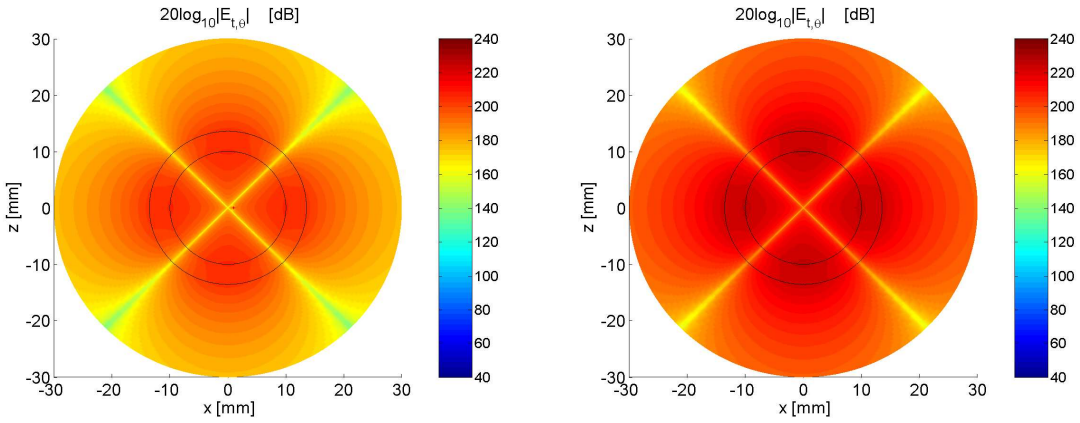

(a) (b)

Figure 7: *Electric near field of the quadrupolar DPS-DNG structure when the EHD is in region 1 at* $r_s = 1$ *mm (a) and* $r_s = 9$ *mm (b).*

From these results and the one shown in Figure 6(a), it is clear that once the resonant quadrupolar mode is excited, its form is, apart from the field strength, rather unaffected of the location of the EHD. Thus, similar to the previously considered dipolar mode, the excited quadrupolar mode is a natural mode of the structure. As a consequence, placing the EHD at locations where the field is very small (large) leads to a weak (strong) excitation of this mode. With reference to Figures 6(a) and 7, the small field locations are, amongst others, near the origin. The locations of the largest fields are near the interfaces of the DNG shell along the x- and z-axes. Thus, the excitation of the resonant quadrupolar mode is very weak when the EHD is near the origin, while it is very strong when it is close to the interfaces of the DNG shell along the x-and z-axes.

With these results in hand, it is next of interest to address the influence of the location of the EHD in the presence of a quadrupolar structure on the resonant enhancement of the total power. Figures 8(a), 8(b) and 8(c) show, respectively, the PR as a function of the EHD location, r_s, in regions 1, 2, and 3 for the DPS-DNG and DPS-DPS quadrupolar structures having the fixed radii: $r_1 = 10$ mm and $r_2 = 13.55$ mm. The EHD varies through the interval $r_s \in [0.01 - 9.99]$ mm in Figure 8(a), $r_s \in [10.01 - 13.54]$ mm in Figure 8(b), and $r_s \in [13.56 - 30]$ mm in Figure 8(c).

While no enhancements are in evidence for the DPS-DPS structures, the DPS-DNG ones produce very large values of the PR for most of the considered EHD locations. Aside from the fact that the enhancements of the total power in the quadrupolar cases are larger than those for the dipolar cases for the majority of the EHD locations, the overall behavior of the results given in Figure 8(b) and (c) resembles that of the corresponding dipolar DPS-DNG structures. Nonetheless, there are some differences between the PR results in Figures 8(a) and 3(a). In the former, the PR $\in [39.3 - 99.3]$ dB when the EHD location traverses region 1 from the origin towards the DNG shell. This is in contrast to the dipolar DPS-DNG structure results given in Figure 3(a), where the PR is nearly constant in this region. This behavior of

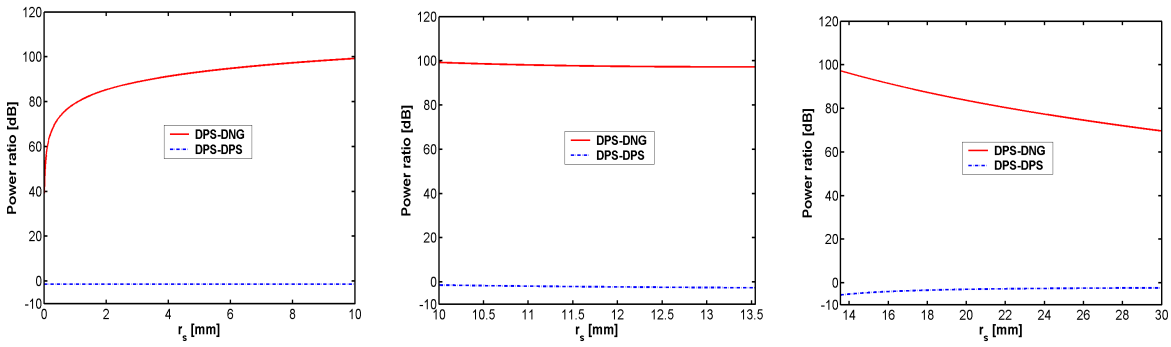

Figure 8: *Power ratio as a function of the EHD location r_s for the quadrupolar DPS-DNG and DPS-DPS structures when the EHD is located in region 1 (a), region 2 (b), and region 3 (c).*

the quadrupolar DPS-DNG structure is not surprising. One recalls that the resonant structure has been designed so that the EHD will dominantly excite the quadrupolar mode. Moreover, with reference to the above discussion on the near-field behavior and the characterization of the excited quadrupolar mode as the natural mode, it is recalled that this mode is excited most strongly (weakly) when the EHD is located near to the interfaces (origin) of the DNG shell. In particular, it is well known that only the dipolar mode exists at the origin, e.g., see [10] and [15, Ch. 8]. As a consequence, the enhancements of the total power are diminished significantly as the EHD location is moved near the origin; and they are completely absent when the EHD is located at the common center of the structure. On the other hand, they are significantly increased as the EHD approaches the surface of the DNG shell. This behavior is clarified further by the results shown in Figure 9, where the total power spectrum in the n'th mode, $n = 1, 2$, and 3, is shown for three representative locations of the EHD (note that in Figure 9(a) only the values for $n = 1$ and 2 modes are given since essentially no power is contained in the $n > 2$ modes). While the total power in the dipolar mode is almost constant in the three cases, an increase in the total power in the quadrupolar mode is noted as the location of the EHD changes from $r_s = 1$ mm in Figure 9(a) to $r_s = 9$ mm in Figure 9(c). Although not included in the figure, it has been verified that at a distance of $r_s = 0.0001$ mm, the total power in the quadrupolar mode is close to the total power in the dipolar mode. Thus, for such small distances from the origin, no enhancements can occur since the structure has *a priori* been designed to excite the quadrupolar mode as the dominant one.

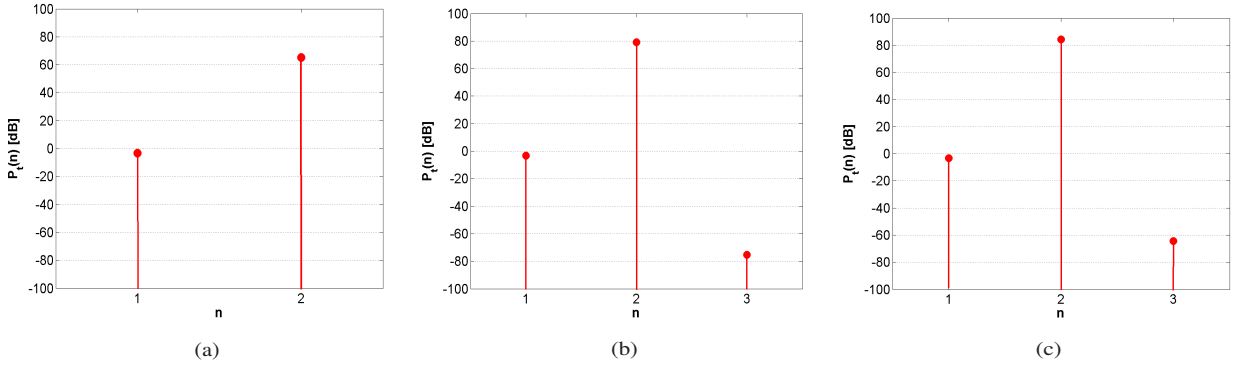

Figure 9: *The total power contained in the n'th mode for the quadrupolar DPS-DNG structure when the EHD is in region 1 at $r_s = 1$ mm (a), $r_s = 5$ mm (b), and $r_s = 9$ mm (c).*

5 Effects of dispersion and losses

Next, dispersion and losses are introduced in the DNG shell in order to examine the effects of these two factors on the overall behavior of the resonant DPS-DNG structures considered in Section 4. To this end, the well-known Drude and Lorentz lossy dispersion models of the permittivity and permeability are used. Mathematically, the lossy Drude models of the permittivity and permeability read

$$\varepsilon_2(\omega) = \varepsilon_0 \left(1 - \frac{\omega_{pe}^2}{\omega(\omega - j\Gamma_e)}\right), \tag{16a}$$

$$\mu_2(\omega) = \mu_0 \left(1 - \frac{\omega_{pm}^2}{\omega(\omega - j\Gamma_m)}\right), \tag{16b}$$

while the lossy Lorentz models of these two material parameters take on the form

$$\varepsilon_2(\omega) = \varepsilon_0 \left(1 - \frac{\omega_{pe}^2}{\omega^2 - j\Gamma_e\omega - \omega_{er}^2}\right), \tag{17a}$$

$$\mu_2(\omega) = \mu_0 \left(1 - \frac{\omega_{pm}^2}{\omega^2 - j\Gamma_m\omega - \omega_{mr}^2}\right). \tag{17b}$$

In (16) and (17), the quantities ω_{pe} and ω_{pm} represent the electric and magnetic plasma frequencies, Γ_e and Γ_m represent the electric and magnetic collision frequencies, while ω_{er} and ω_{mr} in (17) represent the resonance frequencies of the permittivity and permeability, respectively. The two models are designed to recover, at the angular frequency of operation, $\omega_0 = 2\pi f_0$ with $f_0 = 300$ MHz, the lossless permittivity and permeability values given in Table 2, which were used in Section 3 to define the resonant DPS-DNG structures. For the Drude model, the values of ω_{pe}^2 and ω_{pm}^2 are determined from the real part of (16a) and (16b), respectively, evaluated at ω_0 to recover the desired lossless material parameter values. For the Lorentz model, with the assumption that the losses are small, the frequency of operation f_0 must lie above the resonance frequency to obtain the required negative lossless material parameter values. Since the angular frequencies of the permittivity and permeability at resonance are given by $\omega_{er} = 2\pi f_{er}$ and $\omega_{mr} = 2\pi f_{mr}$, we set $f_{er} = f_{mr} = f_r = 290$ MHz, and subsequently determine the values of ω_{pe}^2 and ω_{pm}^2 for the Lorentz model from the required values of the real parts of (17a) and (17b).

To investigate the effects of the dispersion and loss, two specific cases are first considered. In the first case, $\Gamma_e = \Gamma_m = 0$ for both models, and in the second case, $\Gamma_e = \Gamma_m = 10^{-3}\omega_0$. Thus, the DNG shell in the first case is dispersive and lossless, while it is both dispersive and lossy in the second case. The influence of these two cases on the performance of the electrically small dipolar DPS-DNG structure with the EHD located in region 1 at $r_s = 5$ mm is shown in Figure 10[2]. The results for the reference case, in which no dispersion occurs, are likewise included in the figure.

As can be observed from the figure, the PR is almost constant in the depicted frequency range when the DNG shell is treated as lossless and non-dispersive, and, hence, the response is broadband. In contrast to these non-dispersive results, the bandwidth of the resonance attained at $f_0 = 300$ MHz is narrowed considerably when either of the two dispersion models is introduced into the DNG shell. Moreover, the Lorentz model results are characterized by an even narrower bandwidth than those obtained with the Drude model, this being particularly the case in the absence of losses as illustrated in Figure 10(a). In the lossless dispersion cases it is important to note that the maxima of their PR values, which occur at the resonance frequency $f_0 = 300$ MHz, attain the same value as predicted for the non-dispersive case. The inclusion of loss has two basic impacts on the PR values. With reference to Figure 10(b) it is first noted that the resonances remain at $f_0 = 300$ MHz, but they are broadened considerably relative to the lossless cases. Secondly, the maxima of the PR values at the resonance frequency $f_0 = 300$ MHz for the lossy dispersive models are significantly lower than the non-dispersive case value. In particular, the PR value at $f_0 = 300$ MHz in the non-dispersive case is 63.43 dB, while it is 57.44 dB for the Drude dispersion model and 39.55 dB for the Lorentz dispersion model. Again, this decrease is most

[2]The PR values given in this section are calculated for the same resonant dipolar configuration that was treated in Section 4.2, with the exception that dispersion or/and loss are now included.

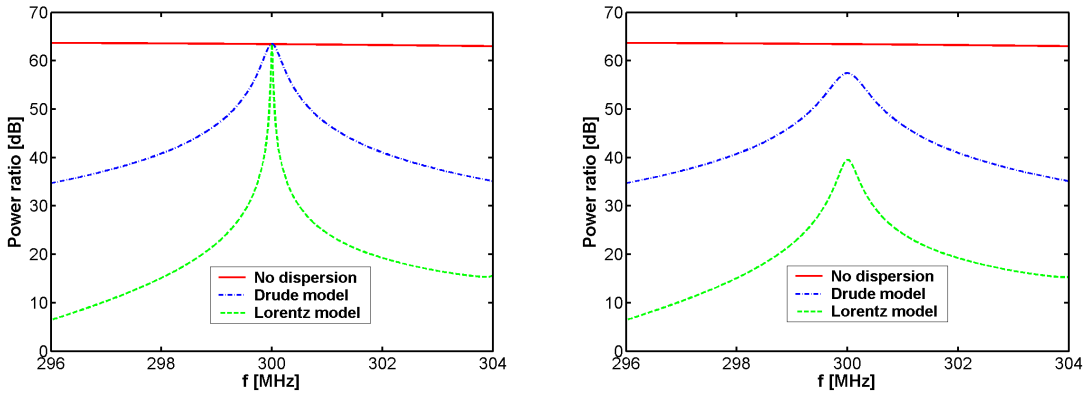

Figure 10: *Power ratio as a function of the frequency for the dipolar DPS-DNG structure in which the DNG shell is described by non-dispersive, Drude and Lorentz material models. The Drude and Lorentz dispersion models are lossless in (a) and lossy in (b). The EHD is located in region 1 at* $r_s = 5$ *mm.*

profound for the Lorentz dispersion model. The difference in the PR behavior between the two dispersion models was expected. The Lorentz model, which has a faster frequency variation than the Drude model near the specified negative material values, has a much narrower bandwidth. The losses associated with the Lorentz model are also more severe (for the same collision frequencies) than those with the Drude model because the required negative values occur near its resonance frequency, where its losses are largest. In fact the values of the permittivity and the permeability in the lossy dispersion models evaluated at $f_0 = 300$ MHz are $\varepsilon_2 = \varepsilon_0(-3 - j0.004)$, $\mu_2 = \mu_0(-3 - j0.004)$ for the Drude model, and $\varepsilon_2 = \varepsilon_0(-3 - j0.059)$, $\mu_2 = \mu_0(-3 - j0.059)$ for the Lorentz model. As a consequence, the electric and magnetic loss tangents at this frequency, denoted and given by $LT_e = \varepsilon_2''/\varepsilon_2'$ and $LT_e = \mu_2''/\mu_2'$, respectively, are $LT_e = LT_m = 0.0013$ for the Drude model and $LT_e = LT_m = 0.019$ for the Lorentz model. Thus, the loss in the Lorentz model is indeed more severe than that in the Drude mode, even though their collision frequency values are the same. Similar results are obtained for the dipolar DPS-DNG structure when the EHD is located in regions 2 and 3.

To further illustrate the effects of loss on the overall performance of the resonant dipolar DPS-DNG structure, several additional lossy, dispersionless cases were considered. In particular, five lossy cases whose permittivity and permeability values (at $f_0 = 300$ MHz) are shown in Table 3, along with the associated electric and magnetic loss tangent values, were chosen for the investigation. The real parts of the material parameters were fixed at the same value, while the amount of loss was varied from a very small to a very large value. In each of these cases, identical values of the relative permittivity and permeability were selected, thus yielding the same electric and magnetic loss tangents. The PR as a function of the EHD location, r_s, is shown in Figure 11(a) for these five lossy cases. The reference lossless case, treated in Section 4.2, is likewise included for comparison purposes.

Parameter	Case 1	Case 2	Case 3	Case 4	Case 5
$\varepsilon_2/\varepsilon_0 = \mu_2/\mu_0$	$-3 - j0.0003$	$-3 - j0.003$	$-3 - j0.03$	$-3 - j0.3$	$-3 - j3$
$LT_e = LT_m$	0.0001	0.001	0.01	0.1	1

Table 3: *Five lossy cases for the additional investigation on the effects of loss.*

While there is almost no difference between the lossless case and the very small loss Case 1, there is reduction of the PR in Case 2. As more loss is included in Cases 3 and 4, the PR values are lowered even further. They attain their lowest values for Case 5 when the largest amount of loss is included. One finds that an appreciable amount of loss in the DNG shell suppresses the excitation of the resonant dipolar mode. More loss further suppresses the interaction of the EHD with the DPS-DNG structure. Consequently, the inclusion of loss has the effect of lowering the enhancement of the total power. These

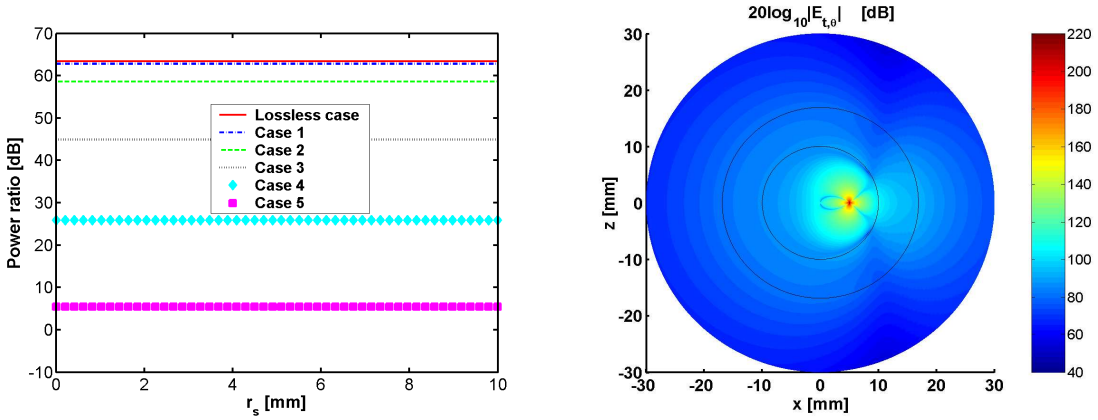

(a) (b)

Figure 11: *Impact of the DNG material losses: (a) Power ratio as a function of the EHD location, r_s, when the EHD is in region 1 for the lossless and the lossy (Cases 1-5) dipolar DPS-DNG structures. (b) Total electric near field of the dipolar DPS-DNG structure in which the DNG shell is modeled by Case 5 and the EHD is in region 1 at $r_s = 5$ mm. In (b), the plane of observation is the xz-plane, and the field is shown in a circular region of radius 30 mm.*

observations are illustrated in Figure 11(b), where the electric near field is given for the Case 5 lossy DPS-DNG structure when the EHD is in region 1 at $r_s = 5$ mm. Comparing the results in Figure 11(b) with the electric near field for the EHD in free space given in Figure 4(a), it is found that they are very similar, i.e., the Case 5 lossy DPS-DNG structure does not have any influence on the field radiated by the EHD, this being similar to the effect of the corresponding lossless DPS-DPS structure, see also Figure 4(b). In other words, the Case 5 lossy DPS-DNG structure is at most only very weakly resonant and, therefore, it can not lead to any appreciable enhancement of the total power.

It must be emphasized that only the results for the dipolar DPS-DNG structures have been presented in this section. Similar behavior is obtained when lossless and lossy dispersive quadrupolar, or even higher-order, DPS-DNG structures are considered. Although not included inhere, it has been shown that these higher-order structures have significantly narrower bandwidths and are, therefore, even more easily affected by the presence of dispersion and losses than the dipolar DPS-DNG structures are. These features observed for the concentric sphere geometry treated in this manuscript are also in evidence when the corresponding cylindrical structures are considered, see e.g., [9].

6 Wavelength-sized natural resonances

In the previous sections it was emphasized that DNG materials offer advantages over the usual DPS materials in the design of resonant electrically small MTM layered spheres, with significant enhancement of the total power. The existence of these resonances, despite the electrically small size, was attributed to the excitation of the necessary resonant mode, which was shown to be possible because of the presence of the DNG material. It will be demonstrated below that as the size of the structure is increased to be on the order of a wavelength, the advantages of the DNG materials disappear, e.g., the same order of magnitude of the PR values are obtained for both DPS-DNG and DPS-DPS structures. This behavior is expected and occurs when the size of the structure enters the natural resonance regime, e.g., see [3, Ch. 2], [8] and [10] for detailed explanations.

To illustrate this point, a DPS-DPS and a DPS-DNG structure with the material parameters given in Table 2 are considered. The frequency of operation is $f_0 = 300$ MHz and the location, as well as the orientation, of the EHD is the same as in Section 3. The inner radius of region 2 is set to $r_1 = 10$ mm, and the outer radius is allowed to vary in the interval $r_2 \in [19.5, 300]$ mm, corresponding to r_2 values much larger than those investigated previously. Figure 12 shows the PR values as a function of these r_2 values. For r_2 approximately greater than 150 mm, comparable values of the PR are obtained in this wavelength-sized natural resonance regime for both the DPS-DPS and DPS-DNG structures. However,

for the majority of the investigated r_2 values, the PR values for the DPS-DNG structure are slightly above those for the DPS-DPS structure. Nonetheless, none of the PR values in Figure 12 are on the order of the very large PRs obtained with the electrically small resonant dipolar, as well as quadrupolar structures, considered in Section 4.

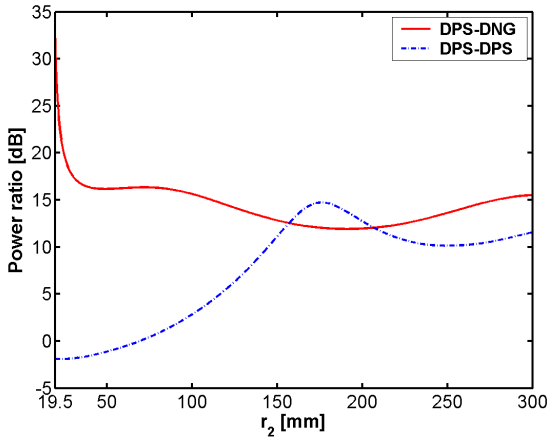

Figure 12: *Power ratio as a function of the outer shell radius r_2 for the DPS-DNG and DPS-DPS spherical structures when the size of the structures is in the wavelength-sized natural resonance regime.*

7 SNG structures

While the emphasis so far has been on the use of DNG versus DPS materials, it is possible, as noted in Section 3, to use SNG materials to achieve subwavelength-sized natural resonances. More specifically, depending on the specific configuration under examination, satisfaction of either of the two resonance conditions, i.e., (15a) or (15b), can still lead to electrically small resonant structures having the same enhancement properties as those discussed with the DPS-DNG structures. It is recalled that this occurs because the total power in (12) has resonant features when either $A_{4,nm}$ or $B_{4,nm}$ have resonant behaviors.

To illustrate this behavior it is useful to examine configurations consisting of an EHD radiating in the presence of a dipolar DPS-ENG structure and a dipolar DPS-MNG structure. These structures are chosen to have the same material and geometrical parameters as the dipolar DPS-DNG structure considered in Section 4, except that for the DPS-ENG structure, the permeability in region 2 is positive and equal to $\mu_2 = 3\mu_0$, while for the DPS-MNG structure, the permittivity in region 2 is positive and equal to $\varepsilon_2 = 3\varepsilon_0$.

Figure 13(a) shows the PR as a function of the outer radius r_2 for the dipolar DPS-ENG and DPS-MNG structures having the EHD located in region 1 at $r_s = 5$ mm. The results reported in Section 4 for the DPS-DNG and DPS-DPS structures are likewise included.

The resonance peaks, at which significant enhancements of the total power are obtained, are found for the DPS-ENG and DPS-MNG structures at the same outer radius value $r_2 = 18.84$ mm. These peaks clearly show that ENG and MNG materials may be used in the design of electrically small resonant MTM-based designs with the aim of obtaining significant enhancements of the quantities of interest. These finding are important and of direct practical interest since it may be much simpler to realize a SNG material rather than a DNG material.

It is also interesting to note that the amplitude of the resonance peak for the DPS-ENG structure is PR $\simeq$ 63 dB, and is thus identical to the peak value of PR dB obtained for the DPS-DNG structure in Section 4.2. However, the peak PR value, PR $=$ 21.04 dB, for the resonant DPS-MNG structure is significantly lower than those obtained for the corresponding resonant DPS-DNG and DPS-ENG structures. Nonetheless, it is still considerably higher that the PR values generated by the DPS-DPS structures. These results show that the dominant field structure in the spherical vector wave expansions of the fields present in the electrically small cases is, as expected, TM. Thus, a DPS-ENG structure is favored in the

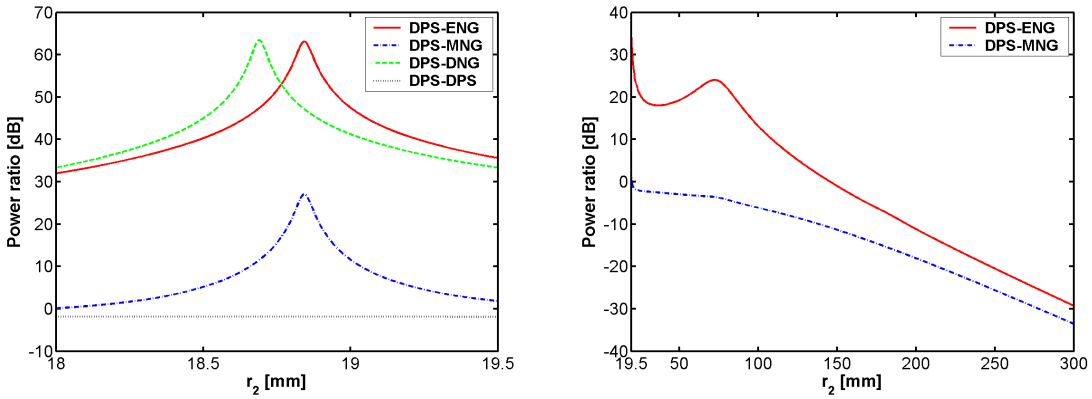

(a) (b)

Figure 13: *(a) Power ratio as a function of the outer shell radius r_2 for the electrically small dipolar DPS-ENG, DPS-MNG, DPS-DNG and DPS-DPS structures. (b) Power ratio as a function of the outer shell radius as it varies in the interval $r_2 \in [19.5, 300]$ MHz for the DPS-ENG and DPS-MNG structures. In both (a) and (b), the EHD is in region 1 at $r_s = 5$ mm.*

presence of an EHD. Note that if the source of electromagnetic radiation is a magnetic Hertzian dipole, the DPS-MNG structure would be naturally favored, since the dominant term is TE in that case. It must be stressed that the underlying mechanism for obtaining the enhancement of the total power when an EHD radiates in the presence of DPS-ENG structures resembles the previously treated DPS-DNG structure. Moreover, the resonant peaks for the two DPS-SNG cases, found at $r_2 = 18.84$ mm, are attained at a somewhat larger value of the outer radius $r_2 = 18.69$ mm, than is the case for the DPS-DNG structure.

For the SNG-based structures of larger size, the PR as a function of $r_2 \in [19.5, 300]$ mm is shown in Figure 13(b) for both DPS-ENG and DPS-MNG structures. For the former, PR values above 10 dB are obtained up to the outer radius of $r_2 = 100$ mm, while beyond this radius the PR falls rapidly off, as expected, since the waves from the EHD cannot penetrate through an electrically large ENG shell in which the wave number is purely imaginary. This is also the case for the DPS-MNG structure, for which the blockage of the waves is emphasized at even smaller r_2 values and, thus, no enhancements are observed. As a consequence, the significant enhancements of the total power by use of DPS-ENG and DPS-MNG structures are only obtained if they are electrically small.

8 Summary and conclusions

The investigation presented in this work concerned specific properties of the canonical configuration consisting of an arbitrarily oriented and located EHD radiating in the presence of a pair of concentric MTM spheres. An analytical solution in terms of spherical vector wave functions was first derived, and this was subsequently employed in a numerical investigation of electrically small, as well as large, MTM-based structures. Particular emphasis was put on the electrically small dipolar and quadrupolar structures. In the numerical investigations, the near field spatial distribution and the total radiated power were examined. The results for the MTM-based designs were compared to the corresponding DPS-based designs.

It was found that the electrically small MTM-based structures, such as the DPS-DNG structures, can be designed to be resonant and thereby lead to significant changes of the field radiated by the EHD as well as significant enhancements of the total radiated power. These enhancements were found to be due to the so-called subwavelength-sized natural resonances of the MTM-based structures. Their existence was predicted analytically, and it was demonstrated that they do not exist for the corresponding DPS-DPS structures. It was also shown that changing the location of the EHD within the DPS-DNG structure had little impact on the total radiated power. This is in distinct contrast to the analogous cylindrically-shaped configurations [9] for which, as an example, the total radiated power of the DPS-DNG dipolar structure

exhibits large variations with the ELS location. Nonetheless, the spherical electrically small resonant quadrupolar DPS-DNG structure was found to exhibit some variation of the total radiated power with the EHD location. In particular, when the EHD is located near the center of the concentric spheres because the dipolar mode then dominates the interaction process. Thus, although such a resonant DPS-DNG structure was designed to excite the quadrupolar mode as the dominant one, it was found that other modes, such as the dipolar mode, could be excited for specific source locations and could, thereby, lead to pattern reshaping with the changing source location; this was also found for the cylindrical cases in [9]. Moreover, it was found that the enhancements, although significantly narrower and more sensitive to variations of the material and geometrical parameters, are considerably larger for the quadrupolar structures than for the dipolar ones. This feature was also recognized with the corresponding cylindrical designs in [9].

The dispersive nature of the MTM material was shown to lead to a considerable narrowing in frequency of the resonances. Small and moderate losses did not make the resonances disappear but were found to lower the peak amplitudes of the resonant enhancements. However, the inclusion of very large losses did make the resonances disappear because of the suppression of the required resonant modes.

Furthermore, it was demonstrated that ENG and MNG materials can offer results similar to those obtained with DNG materials. With the EHD, the exciting field is predominantly TM and for this case it was found that the DPS-ENG structure posses properties comparable to those of the DPS-DNG structure.

It is important to emphasize that the electrically small resonant DPS-DNG structures investigated in this work give rise to a total radiated power comparable to and even exceeding those of electrically larger structures. For the latter, it was found that both DPS-DPS and DPS-DNG structures lead to resonant behaviors.

References

[1] G. V. Eleftheriades and K. G. Balmain (Eds.), *Negative-refraction metamaterials: fundamental principles and applications*, John Wiley & Sons, 2005.

[2] C. Caloz and T. Itoh (Eds.), *Electromagnetic metamaterials: transmission line theory and microwave applications*, John Wiley & Sons, 2006.

[3] N. Engheta and R.W. Ziolkowski (Eds.), *Metamaterials: physics and engineering explorations*, John Wiley & Sons, 2006.

[4] V. G. Veselago, "The electrodynamics of substances with simultaneously negative values of ε and μ," *Sov. Phys. Usp.*, vol. 10, pp. 509-514, Jan.-Feb. 1968.

[5] J. B. Pendry, "Negative refraction makes a perfect lens," *Phys. Rev. Let.*, vol. 85, pp. 3966-3969, Oct. 2000.

[6] N. Engheta, "An idea for thin subwavelength cavity resonators using metamaterials with negative permittivity and permeability," *IEEE Antennas Wireless Propag. Lett.*, vol. 1, no.1., pp. 10-13, 2002.

[7] A. Alú, and N. Engheta, "Guided modes in a waveguide filled with a pair of single-negative (SNG), double-negative (DNG) and/or double-positive (DPS) layers," *IEEE Trans. Microwave Theory Tech.*, vol. 52, no. 1, pp. 199-210, Jan. 2004.

[8] A. Alú, and N. Engheta, "Polarizabilities and effective parameters for collections of spherical nanoparticles formed by pairs of concentric double-negative (DNG), single-negative (SNG) and/or double-positive (DPS) metamaterial layers," *J. Appl. Phys.*, vol. 97, 094310, May 2005.

[9] S. Arslanagic, R. W. Ziolkowski, and O. Breinbjerg, "Excitation of an electrically small metamaterial-coated cylinder by an arbitrarily located line source," *Microwave Opt. Technol. Lett.*, vol. 48, pp. 2598-2605, Dec. 2006.

[10] R. W. Ziolkowski and A. Kipple, "Application of double negative metamaterials to increase the power radiated by electrically small antennas," *IEEE Trans. Antennas Propagat.*, vol. 51, no. 10, pp. 2626-2640, Oct. 2003.

[11] R. W. Ziolkowski and A. Kipple, "Reciprocity between the effects of resonant scattering and enhanced radiated power by electrically small antennas in the presence of nested metamaterials shells," *Phys. Rev. E.*, vol. 72, 036602, Sept. 2005.

[12] H. Stuart, and A. Pidwerbetsky, "Electrically small antenna elements using negative permittivity and permeability resonators," *IEEE Trans. Antennas Propag.*, vol. 54, no. 6, pp. 1644-1654, June 2006.

[13] R. W. Ziolkowski and A. Erentok, "Metamaterial-based efficient electrically small antennas," *IEEE Trans. Antennas Propagat.*, Vol. 54, No. 7, pp. 2113-2130, July 2006.

[14] A. Alú, F. Bilotti, N. Engheta, and L. Vegni, "Subwavelength, compact, resonant patch antennas loaded with metamaterials," *IEEE Trans. Antennas Propag.*, vol. 55, no. 1, pp. 13-25, Jan. 2007.

[15] D.S. Jones, *The Theory of Electromagnetism*, Oxford: Pergamon Press, 1964.

[16] M. Abramowitz, and I. A. Stegun, *Handbook of mathematical functions*, Dover Publications, Inc., 1965.

[17] C. A. Balanis, *Antenna theory: analysis and design*, John Wiley & Sons, Inc., 1997.

[18] M. Kerker, and C. G. Blatchford, "Elastic scattering, absorption, and surface-enhanced Raman scattering by concentric spheres comprised of a metallic and a dielectric region," *Phys. Rev. B.*, vol. 26, pp. 4052-4063, Oct. 1982.

Part III

Complete derivations

APPENDIX D

2D CANONICAL CONFIGURATIONS - DETAILED CALCULATIONS

This appendix presents the details of the analytical results which form the background of Chapter 4. First, the problem of concentric cylinders is treated, and second, the steps necessary to reduce this problem to that of a single cylinder are outlined. For both of these configurations the relevant resonance conditions are derived in the electrically small limit. Moreover, the details of the geometrical optics (GO) ray-tracing technique, which is applied to the configuration of a single cylinder, are elucidated.

D.1 Concentric cylinders - ELS results

The configuration of interest is depicted in Figure 4.1 in Chapter 4.

D.1.1 The ELS field

The electric field generated by the ELS in an infinite medium characterized by ε_{ELS}, μ_{ELS}, and k_{ELS} is given by the expression [117, p. 573]

$$\vec{E}_{\text{ELS}}(\,\vec{\rho}\,) = -\hat{z}\; I_e\; \frac{\omega\mu_{\text{ELS}}}{4}\; H_0^{(2)}(k_{\text{ELS}}|\vec{\rho}-\vec{\rho}_s|)\;, \tag{D.1}$$

where $H_0^{(2)}(\cdot)$ is the Hankel function of second kind and zero'th order, while $\vec{\rho}$ and $\vec{\rho}_s$ are the position vectors of a given observation point (with coordinates (ρ,ϕ)) and the ELS (with coordinates (ρ_s,ϕ_s)), respectively. The expression in (D.1) represents cylindrical waves that are centered on the ELS. In order to facilitate the following analysis, the electric field is expressed in terms of cylindrical wave functions which originate at the origin of the coordinate system, i.e., at $\rho = 0$. Employing the addition theorem for Hankel functions, one can write the electric field generated by the ELS in the form [117, p. 626]

$$\vec{E}_{\text{ELS}}(\rho,\phi) = -\hat{z}\; I_e \frac{\omega\mu_{\text{ELS}}}{4} \begin{cases} \sum_{n=-\infty}^{\infty} J_n(k_{\text{ELS}}\rho)\; H_n^{(2)}(k_{\text{ELS}}\rho_s)\; e^{jn(\phi-\phi_s)} & \text{for } \rho \le \rho_s\;, \\ \sum_{n=-\infty}^{\infty} J_n(k_{\text{ELS}}\rho_s)\; H_n^{(2)}(k_{\text{ELS}}\rho)\; e^{jn(\phi-\phi_s)} & \text{for } \rho \ge \rho_s\;. \end{cases} \tag{D.2}$$

For implementation purposes it is convenient to fold the summation over n, which ranges from $-\infty$ to ∞, to the range from 0 to ∞. This is done by first noting that

$$\sum_{n=-\infty}^{\infty} e^{jn(\phi-\phi')} = \sum_{n=0}^{\infty} \tau_n\; \cos[n(\phi-\phi')], \tag{D.3}$$

where the symbol τ_n is the Neumann number, i.e., $\tau_n = 1$, for $n = 0$, and $\tau_n = 2$ otherwise. Consequently, the ELS electric field in (D.2) reads

$$\vec{E}_{\text{ELS}}(\rho,\phi) = -\hat{z}\; I_e \frac{\omega\mu_{\text{ELS}}}{4} \begin{cases} \sum_{n=0}^{\infty} \tau_n\; J_n(k_{\text{ELS}}\rho)\; H_n^{(2)}(k_{\text{ELS}}\rho_s)\; \cos[n(\phi-\phi_s)] & \text{for } \rho \le \rho_s\;, \\ \sum_{n=0}^{\infty} \tau_n\; J_n(k_{\text{ELS}}\rho_s)\; H_n^{(2)}(k_{\text{ELS}}\rho)\; \cos[n(\phi-\phi_s)] & \text{for } \rho \ge \rho_s\;, \end{cases} \tag{D.4}$$

The corresponding magnetic field generated by the ELS is obtained from Faraday's law [64, Ch. 1]

$$\nabla \times \vec{E} = -j\omega\mu\vec{H} \; . \tag{D.5}$$

Since the electric field in (D.4) only has a z-component, its curl, as expressed in cylindrical coordinates, will only result in a ϕ-component of the corresponding magnetic field. More specifically,

$$\vec{H} = -\frac{1}{j\omega\mu}\Big[\hat{\rho}\,\frac{1}{\rho}\frac{\partial E_z}{\partial \phi} - \hat{\phi}\,\frac{\partial E_z}{\partial \rho}\Big] \; , \tag{D.6}$$

and thus the magnetic field generated by the EHD is

$$\vec{H}_{\text{ELS}}(\rho,\phi) = j\frac{I_e}{4}\begin{cases} \hat{\rho}\,\frac{1}{\rho}\sum_{n=0}^{\infty}\tau_n\, n\, J_n(k_{\text{ELS}}\rho)\, H_n^{(2)}(k_{\text{ELS}}\rho_s)\, \sin[n(\phi-\phi_s)] \\ \quad +\hat{\phi}\, k_{\text{ELS}}\, \sum_{n=0}^{\infty}\epsilon_n\, J_n'(k_{\text{ELS}}\rho)\, H_n^{(2)}(k_{\text{ELS}}\rho_s)\, \cos[n(\phi-\phi_s)] & \text{for } \rho \le \rho_s \; , \\ \hat{\rho}\,\frac{1}{\rho}\sum_{n=0}^{\infty}\tau_n\, n\, J_n(k_{\text{ELS}}\rho_s)\, H_n^{(2)}(k_{\text{ELS}}\rho)\, \sin[n(\phi-\phi_s)] \\ \quad +\hat{\phi}\, k_{\text{ELS}}\, \sum_{n=0}^{\infty}\tau_n\, J_n(k_{\text{ELS}}\rho_s)\, H_n^{(2)\prime}(k_{\text{ELS}}\rho)\, \cos[n(\phi-\phi_s)] & \text{for } \rho \ge \rho_s \; . \end{cases} \tag{D.7}$$

In the above expressions, the index ELS $= 1$ or 2 when the ELS is in region 1 or 2, respectively, while ELS $= 0$ when the ELS is in region 3, which is free space. Furthermore, the prime denotes the derivative with respect to the argument; e.g., $J_n'(x) = dJ_n(x)/dx$, which also is the case in the following.

D.1.2 Unknown fields

The unknown scattered field in the region containing the ELS and the unknown total fields in the other regions are also expanded in terms of cylindrical wave functions. In this regard it is first useful to note the following. In Region 1, the electric and magnetic fields, denoted by $\vec{E}_{1s}$ and $\vec{H}_{1s}$, are composed of standing waves, and thus their radial dependencies are properly described by the Bessel function of order n, i.e., $J_n(\cdot)$. In Region 2, the electric and magnetic fields, denoted by $\vec{E}_{2s}$ and $\vec{H}_{2s}$, are composed of standing waves (or, alternatively, as a superposition of cylindrical waves propagating in the $+\rho$ - direction and those propagating in the $-\rho$ - direction). Therefore, the radial dependence of the field in Region 2 is properly described by the Bessel, $J_n(\cdot)$, and Neumann, $Y_n(\cdot)$, functions of order n. In Region 3, the electric and magnetic fields, denoted by $\vec{E}_{3s}$ and $\vec{H}_{3s}$, are composed of outward propagating spherical waves, and thus their radial dependencies are properly described by the Hankel functions of the second kind and order n, i.e., $H_n^{(2)}(\cdot)$. Thus, the resulting expansions of these fields read

$$\vec{E}_{1s}(\rho,\phi) = -\hat{z}I_e\frac{\omega\mu_1}{4}\sum_{n=0}^{\infty}\tau_n C_{1n} J_n(k_1\rho)\cos[n(\phi-\phi_s)] \quad \text{for} \quad \rho \le \rho_1 \; , \tag{D.8a}$$

$$\vec{E}_{2s}(\rho,\phi) = -\hat{z}I_e\frac{\omega\mu_2}{4}\sum_{n=0}^{\infty}\tau_n \left[C_{2n} J_n(k_2\rho) + C_{3n} Y_n(k_2\rho)\right]\cos[n(\phi-\phi_s)] \quad \text{for} \quad \rho_1 \le \rho \le \rho_2 \; , \tag{D.8b}$$

$$\vec{E}_{3s}(\rho,\phi) = -\hat{z}I_e\frac{\omega\mu_0}{4}\sum_{n=0}^{\infty}\tau_n C_{4n} H_n^{(2)}(k_0\rho)\cos[n(\phi-\phi_s)] \quad \text{for} \quad \rho \ge \rho_2 \; , \tag{D.8c}$$

where C_{in}, with $i = 1, \ldots, 4$ and $n = 0, 1, 2, \ldots$, are the unknown expansion coefficients which must

be determined. The associated magnetic fields are

$$\vec{H}_{1s}(\rho,\phi) = j\frac{I_e}{4}\Big\{\hat{\rho}\,\frac{1}{\rho}\sum_{n=0}^{\infty}\tau_n\, jn\, C_{1n}\, J_n(k_1\rho)\,\sin[n(\phi-\phi_s)] + \hat{\phi}\,k_1\sum_{n=0}^{\infty}\epsilon_n\, C_{1n}\, J_n'(k_1\rho)\,\cos[n(\phi-\phi_s)]\Big\}, \tag{D.9a}$$

$$\vec{H}_{2s}(\rho,\phi) = j\frac{I_e}{4}\Big\{\hat{\rho}\,\frac{1}{\rho}\sum_{n=0}^{\infty}\tau_n\, jn\,\left[C_{2n}\, J_n(k_2\rho) + C_{3n}\, Y_n(k_2\rho)\right]\,\sin[n(\phi-\phi_s)] + \hat{\phi}\,k_2\sum_{n=0}^{\infty}\tau_n\,\left[C_{2n}\, J_n'(k_2\rho) + C_{3n}\, Y_n'(k_2\rho)\right]\,\cos[n(\phi-\phi_s)]\Big\}, \tag{D.9b}$$

$$\vec{H}_{3s}(\rho,\phi) = j\frac{I_e}{4}\Big\{\hat{\rho}\,\frac{1}{\rho}\sum_{n=0}^{\infty}\tau_n\, jn\, C_{4n}\, H_n^{(2)}(k_0\rho)\,\sin[n(\phi-\phi_s)] + \hat{\phi}\,k_0\sum_{n=0}^{\infty}\tau_n\, C_{4n}\, H_n^{(2)\prime}(k_0\rho)\,\cos[n(\phi-\phi_s)]\Big\}. \tag{D.9c}$$

The above expressions for the unknown electric and magnetic fields hold true irrespective of the location of the ELS. By taking into account the location of the ELS, the equations that are used to determine the unknown expansion coefficients are obtained.

D.1.3 Expansion coefficients

In order to determine the unknown expansion coefficients C_{in}, $i = 1,\ldots,4$, the electromagnetic boundary conditions, which require the continuity of the tangential components of the total electric and magnetic fields at the cylindrical interfaces $\rho = \rho_1$ and $\rho = \rho_2$, must be applied. The component of the total electric field which is tangential at the said interfaces is denoted by $E_{z,it}$, while that of the total magnetic field is denoted by $H_{\phi,it}$. The index $i = 1, 2$ and 3, for the total fields in regions 1,2 and 3, respectively. In mathematical terms, the boundary conditions read

$$E_{z,1t}(\rho=\rho_1) = E_{z,2t}(\rho=\rho_1), \tag{D.10}$$
$$H_{\phi,1t}(\rho=\rho_1) = H_{\phi,2t}(\rho=\rho_1), \tag{D.11}$$

and

$$E_{z,2t}(\rho=\rho_2) = E_{z,3t}(\rho=\rho_2), \tag{D.12}$$
$$H_{\phi,2t}(\rho=\rho_2) = H_{\phi,3t}(\rho=\rho_2), \tag{D.13}$$

Depending on the location of the ELS, the expressions for the total fields in the three regions will be different. Thus, a different system of equations is obtained for the ELS being located in regions 1, 2 and 3. However, by treating all of the possible ELS locations separately, it is easily observed that the system of equations for the unknown expansion coefficients, which is obtained from the boundary conditions (D.10)-(D.13), always takes on the form

$$\vec{\Lambda}_n = \bar{\bar{M}}_n\vec{C}_n\,, \quad n = 0, 1, 2, \ldots\,, \tag{D.14}$$

where $\vec{C}_n = [C_{1n}, C_{2n}, C_{3n}, C_{4n}]$ is the vector containing the four expansion coefficients and $\vec{\Lambda}_n = [\Lambda_{1n}, \Lambda_{2n}, \Lambda_{3n}, \Lambda_{4n}]$ is the so-called excitation vector, which depends on the location of the ELS. The matrix $\bar{\bar{M}}_n$ is a four-by-four matrix that depends on the values of the cylindrical waves at the two interfaces and is given by

$$\bar{\bar{M}}_n = \begin{bmatrix} -\mu_1 J_n(k_1\rho_1) & \mu_2 J_n(k_2\rho_1) & \mu_2 Y_n(k_2\rho_1) & 0 \\ -k_1 J_n'(k_1\rho_1) & k_2 J_n'(k_2\rho_1) & k_2 Y_n'(k_2\rho_1) & 0 \\ 0 & \mu_2\, J_n(k_2\rho_2) & \mu_2\, Y_n(k_2\rho_2) & -\mu_0\, H_n^{(2)}(k_0\rho_2) \\ 0 & k_2\, J_n'(k_2\rho_2) & k_2\, Y_n'(k_2\rho_2) & -k_0\, H_n^{(2)\prime}(k_0\rho_2) \end{bmatrix}. \tag{D.15}$$

The relation (D.14) can be solved for the unknown coefficients as

$$\vec{C}_n = \left[\bar{\bar{M}}_n\right]^{-1} \vec{\Lambda}_n \, . \tag{D.16}$$

This form of the solution allows one to account for the various ELS locations in a very simple manner and, therefore, is very convenient from an understanding and implementation point of view. The only thing that changes in (D.16) as the ELS changes its location is the excitation vector $\vec{\Lambda}_n$. The elements of the excitation vector, when the ELS is located in regions 1, 2 and 3, are shown in Table D.2.

Λ_{in}	ELS in region 1	ELS in region 2	ELS in region 3
Λ_{1n}	$\mu_1 J_n(k_1\rho_s)H_n^{(2)}(k_1\rho_1)$	$-\mu_2 J_n(k_2\rho_1)H_n^{(2)}(k_2\rho_s)$	0
Λ_{2n}	$k_1 J_n(k_1\rho_s)H_n^{(2)\prime}(k_1\rho_1)$	$-k_2 J_n'(k_2\rho_1)H_n^{(2)}(k_2\rho_s)$	0
Λ_{3n}	0	$-\mu_2 J_n(k_2\rho_s)H_n^{(2)}(k_2\rho_2)$	$\mu_0 J_n(k_0\rho_2)H_n^{(2)}(k_0\rho_s)$
Λ_{4n}	0	$-k_2 J_n(k_2\rho_s)H_n^{(2)\prime}(k_2\rho_2)$	$k_0 J_n'(k_0\rho_2)\ H_n^{(2)}(k_0\rho_s)$

Table D.1: *The elements Λ_{in}, $i = 1, \ \ldots \ , 4$, of the excitation vector $\vec{\Lambda}_n$ when the ELS is located in regions 1, 2, and 3.*

In the numerical implementation of (D.4) and (D.7), as well as the electric, (D.8a)-(D.8c), and magnetic, (D.9a)-(D.9c), unknown fields, the employed summations must be truncated to some finite truncation limit N_{max} chosen in a manner which ensures their convergence. In the forthcoming sections, the employed summations are truncated to the truncation limit N_{max}.

D.1.4 Derived quantities

The figures of merit employed in the numerical investigations found in Chapter 4, as well as in Manuscript I (Appendix A) and Manuscript II (Appendix B), include

- the total average radiated power, P_t, henceforth termed the total power;
- the directivity, D;
- the total scattering cross section, σ_t, henceforth termed the total cross section; and
- the differential scattering cross section, σ_d, henceforth termed the differential cross section.

Since the configuration at hand is infinite in the z-direction, all of these quantities are determined on a *per unit length* basis.

D.1.4.1 Total power

The total power P_t is given by the expression

$$P_t = \frac{1}{2}\int_{\phi=0}^{2\pi} \mathcal{R}e\{\vec{E}_t^f \times \vec{H}_t^{f*}\} \cdot d\vec{s}, \tag{D.17}$$

where $\vec{E}_t^f$ and $\vec{H}_t^f$ are the total electric and magnetic far fields, respectively, in region 3, $*$ denotes the complex conjugate, and $d\vec{s} = \hat{\rho}\ \rho\ d\phi$ is the outward pointing differential element of the integration path. Due to the form of the electric and magnetic fields in the present problem, the only component of the total magnetic field that contributes to the total power is its ϕ-component, see also Sections D.1.1 and D.1.2. Therefore, the relation (D.17) can be rewritten as

$$P_t = \frac{1}{2\eta_0}\int_{\phi=0}^{2\pi} |\vec{E}_t^f(\rho,\phi)|^2 \rho d\phi, \tag{D.18}$$

where $\eta_0 = \sqrt{\mu_0/\varepsilon_0}$ is the intrinsic impedance of free space (region 3).

When the ELS is in region 1 or 2, $\vec{E}_t^f$ equals the far-field version of (D.8c), i.e., $\vec{E}_t^f = \vec{E}_{3s}^f$. On the other hand, when the ELS is in region 3, it equals the sum of the far-field versions of the incident field (D.4) for $\rho \geq \rho_s$ and the field (D.8c), i.e., $\vec{E}_t^f = \vec{E}_{\text{ELS}}^{f,\,\rho\geq\rho_s} + \vec{E}_{3s}^f$. The relevant expression of these fields is easily obtained by using the large argument approximation of the Hankel function [119, Ch.10]

$$H_n^{(2)}(x) \sim \sqrt{\frac{2}{\pi x}}\, e^{-j\,\left[x - n\frac{\pi}{2} - \frac{\pi}{4}\right]}, \quad |x| \to \infty\,. \tag{D.19}$$

Consequently

$$\begin{aligned}
\vec{E}_{\text{ELS}}^{f,\,\rho\geq\rho_s} &= \lim_{\rho\to\infty} \vec{E}_{\text{ELS}}^{\rho\geq\rho_s}(\rho,\phi) \\
&= \Big\{ -\hat{z}\, I_e \frac{\omega\mu_0}{4} \sqrt{\frac{2}{\pi k_0}}\, e^{j\pi/4} \sum_{n=0}^{N_{max}} \tau_n\, j^n\, J_n(k_0\rho_s)\, \cos[n(\phi-\phi_s)] \Big\} \frac{e^{-jk_0\rho}}{\sqrt{\rho}}\,. \qquad \text{(D.20)} \\
\vec{E}_{3s}^f &= \lim_{\rho\to\infty} \vec{E}_{3s}(\rho,\phi) \\
&= \Big\{ -\hat{z}\, I_e \frac{\omega\mu_0}{4} \sqrt{\frac{2}{\pi k_0}}\, e^{j\pi/4} \sum_{n=0}^{N_{max}} C_{4n}\,\tau_n\, j^n\, \cos[n(\phi-\phi_s)] \Big\} \frac{e^{-jk_0\rho}}{\sqrt{\rho}}\,, \qquad \text{(D.21)}
\end{aligned}$$

and thus

$$\begin{aligned}
\vec{E}_t^f = \lim_{\rho\to\infty} \vec{E}_t(\rho,\phi) &= \lim_{\rho\to\infty} \Big[\vec{E}_{\text{ELS}}^{\rho\geq\rho_s}(\rho,\phi) + \vec{E}_{3s}(\rho,\phi) \Big] \\
&= \Big\{ -\hat{z}\, I_e \frac{\omega\mu_0}{4} \sqrt{\frac{2}{\pi k_0}}\, e^{j\pi/4} \sum_{n=0}^{N_{max}} \tau_n\, j^n\, \alpha_n\, \cos[n(\phi-\phi_s)] \Big\} \frac{e^{-jk_3\rho}}{\sqrt{\rho}}\,, \qquad \text{(D.22)}
\end{aligned}$$

where the quantity

$$\alpha_n = \begin{cases} C_{4n} & \text{when the ELS is in region 1 or 2}\,, \\ J_n(k_0\rho_s) + C_{4n} & \text{when the ELS is in region 3}\,. \end{cases} \tag{D.23}$$

The total power in (D.18) thus reads

$$\begin{aligned}
P_t &= \frac{1}{2\eta_0} \int_{\phi=0}^{2\pi} |\vec{E}_t^f(\rho,\phi)|^2 \rho\, d\phi \\
&= \frac{1}{2\eta_0} \left(I_e \frac{\omega\mu_0}{4} \right)^2 \frac{2}{k_0\pi} \sum_{n=0}^{N_{max}} \tau_n^2\, |\alpha_n|^2 \int_{\phi=0}^{2\pi} \left(\frac{1}{\sqrt{\rho}} \right)^2 \cos^2[n(\phi-\phi_s)]\, \rho\, d\phi \\
&= \frac{1}{2\eta_0} \left(I_e \frac{\omega\mu_0}{4} \right)^2 \frac{2}{k_0} \sum_{n=0}^{N_{max}} \tau_n^2\, |\alpha_n|^2 \begin{cases} 2 & \text{for} \quad n=0 \\ 1 & \text{otherwise} \end{cases} \\
&= \frac{1}{2\eta_0} \left(I_e \frac{\omega\mu_0}{4} \right)^2 \frac{2}{k_0} \sum_{n=0}^{N_{max}} \tau_n^2\, (3-\epsilon_n)\, |\alpha_n|^2 \\
&= \left(\frac{1}{4}\eta_0 I_e^2 \right) \left[\frac{k_0}{4} \sum_{n=0}^{N_{max}} \tau_n^2 (3-\tau_n) |\alpha_n|^2 \right]\,, \qquad \text{(D.24)}
\end{aligned}$$

where use has been made of the orthogonality of the $\cos[n(\phi-\phi_s)]$ functions, as well as of the relation $\omega\mu_0 = k_0\mu_0/\sqrt{\varepsilon_0\mu_0} = k_0\eta_0$.

In Chapter 4 particular attention was devoted to the so-called power ratio (PR), which is the ratio of the total power in (D.24) to the power radiated by the ELS in free space. This latter quantity, denoted by P_i, is actually given by (D.18) with $\vec{E}_t^f$ replaced by $\vec{E}_{\text{ELS}}^{f,\ \rho\geq\rho_s}$. In this case N_{max} can be set to infinity and it is found that

$$P_i = P_i = \left(\frac{1}{4}\eta_0 I_e^2\right)\left[\frac{k_0}{4}\sum_{n=0}^{N_{max}}\tau_n^2(3-\tau_n)|J_n(k_0\rho_s)|^2\right]_{N_{max}=\infty} . \tag{D.25}$$

According to [119, Ch. 10]

$$[J_0(x)]^2 + 2\sum_{n=1}^{\infty}[J_n(x)]^2 \ = \ 1\,. \tag{D.26}$$

Thus, the power radiated by the ELS in free space (D.25) becomes

$$P_i = \left(\frac{1}{4}\eta_0 I_e^2\right)\left[\frac{k_0}{2}\right]. \tag{D.27}$$

It is noted that P_i in (D.27) also follows from (D.24) with $\alpha_n = J_n(k_0\rho_s)$. As a consequence, the PR reads

$$\text{PR} = \frac{P_t}{P_i} = \frac{1}{2}\sum_{n=0}^{N_{max}}\tau_n^2(3-\tau_n)|\alpha_n|^2\,. \tag{D.28}$$

D.1.4.2 Directivity

In order to determine the directivity, one must first find the radiation intensity, denoted by U, and the total power per unit angle. The radiation intensity, U, is

$$U(\phi) = \frac{1}{2}\,\rho\,\mathcal{R}e\{\vec{E}_t^f(\rho,\phi)\times\vec{H}_t^{f*}(\rho,\phi)\}\cdot\hat{\rho} = \frac{1}{2\eta_0}\,\rho\,|E_t^f(\rho,\phi)|^2\,. \tag{D.29}$$

Since the total angle subtended by a full circle is 2π radians, the total power per unit angle is $P_t/2\pi$, where P_t is given by (D.24). Thus, the directivity is

$$\begin{aligned} D(\phi) &= \frac{U(\phi)}{P_t/2\pi} = \frac{2\pi\rho\,|\vec{E}_t^f(\rho,\phi)|^2}{\int_{\phi=0}^{2\pi}|\vec{E}_t^f(\rho,\phi)|^2\rho\,d\phi} \\ &= \frac{2\pi\rho\,\left(I_e\frac{\omega\mu_0}{4}\right)^2\,\frac{2}{\pi\,k_0}\left|\sum_{n=0}^{N_{max}}\tau_n\,j^n\,\alpha_n\,\cos[n(\phi-\phi_s)]\right|^2\,\left(\frac{1}{\sqrt{\rho}}\right)^2}{\left(I_e\frac{\omega\mu_0}{4}\right)^2\,\frac{2}{k_0}\sum_{n=0}^{N_{max}}\tau_n^2\,(3-\tau_n)\,|\alpha_n|^2} \\ &= \frac{2\left|\sum_{n=0}^{N_{max}}\tau_n\,j^n\,\alpha_n\,\cos[n(\phi-\phi_s)]\right|^2}{\sum_{n=0}^{N_{max}}\tau_n^2\,(3-\tau_n)\,|\alpha_n|^2}\,. \end{aligned} \tag{D.30}$$

D.1.4.3 Cross sections

When the ELS is located in region 3 and is moved infinitely far away from the cylinders, it is of interest to investigate the behaviour of the differential and total cross section.

Differential cross section

In the framework of the formulation of the present problem, the differential cross section, σ_d, is defined by the square of the ratio of the magnitude of the scattered electric field in the far-field region (i.e., in region 3) to the magnitude of the incident electric field at the origin, both evaluated when the ELS is moved infinitely far away from the cylinders (i.e., for $\rho_s \to \infty$) along an arbitrary direction ϕ_s. Thus, σ_d is given by

$$\sigma_d = \lim_{\rho\to\infty}\lim_{\rho_s\to\infty\ ;\ \phi_s}\left[2\pi\rho\frac{|\vec{E}_{3s}(\rho,\phi)|^2}{|\vec{E}_{\text{ELS}}(\rho=0)|^2}\right]. \tag{D.31}$$

For convenience, the expressions for $\vec{E}_{\text{ELS}}$ and $\vec{E}_{3s}$ are rewritten into the forms given by

$$\vec{E}_{\text{ELS}} = -\hat{z} I_e \frac{\omega\mu_0}{4} \, H_0^{(2)}(k_0|\vec{\rho} - \vec{\rho}_s|) \, , \tag{D.32a}$$

$$\vec{E}_{3s} = -\hat{z} I_e \frac{\omega\mu_0}{4} \sum_{n=0}^{N_{max}} \tau_n \, C_{4n} \, H_n^{(2)}(k_0\rho) \, \cos[n(\phi - \phi_s)] \, . \tag{D.32b}$$

It is recalled that the C_{4n} are given by (D.16), i.e., $\vec{C}_n = \left[\bar{\bar{M}}_n\right]^{-1} \vec{\Lambda}_n$, where the excitation vector is

$$\vec{\Lambda}_n = H_n^{(2)}(k_0\rho_s) \begin{bmatrix} 0 \\ 0 \\ \mu_0 \, J_n(k_0\rho_2) \\ k_0 \, J_n'(k_0\rho_2) \end{bmatrix} = H_n^{(2)}(k_0\rho_s)\vec{\Lambda}_n' \, , \tag{D.33}$$

when the ELS is in region 3. Therefore, one can also write that $\vec{C}_n = \left[\bar{\bar{M}}_n\right]^{-1} \vec{\Lambda}_n' \, H_n^{(2)}(k_0\rho_s)$. Introducing a new vector $\vec{C}_n'$, which is defined as $\vec{C}_n' = \left[\bar{\bar{M}}_n\right]^{-1} \vec{\Lambda}_n'$, it thus follows that $C_{4n} = C_{4n}' H_n^{(2)}(k_0\rho_s)$, where C_{4n}' is contained in $\vec{C}_n'$. As a consequence, C_{4n} depends on ρ_s only through the term $H_n^{(2)}(k_0\rho_s)$ in (D.33) since both $\bar{\bar{M}}_n$ and $\vec{\Lambda}_n'$ are independent of ρ_s.

As to the numerator of (D.31), one therefore first writes

$$\vec{E}_{3s} = -\hat{z} I_e \frac{\omega\mu_0}{4} \sum_{n=0}^{N_{max}} \tau_n \, \left[C_{4n}' H_n^{(2)}(k_0\rho_s)\right] \, H_n^{(2)}(k_0\rho) \, \cos[n(\phi - \phi_s)] \, , \tag{D.34}$$

and subsequently obtains

$$\begin{aligned} \lim_{\rho\to\infty} \lim_{\rho_s\to\infty \, ; \, \phi_s} \vec{E}_{3s} &= -\hat{z} I_e \frac{\omega\mu_0}{4} \sum_{n=0}^{N_{max}} \tau_n \, \left[C_{4n}' \sqrt{\frac{2}{\pi k_0\rho_s}} e^{-jk_0\rho_s} e^{j\pi/4} j^n\right] \\ &\qquad \times \left[\sqrt{\frac{2}{\pi k_0\rho}} e^{-jk_0\rho} e^{j\pi/4} j^n\right] \cos[n(\phi - \phi_s)] \\ &= -\hat{z} I_e \frac{\omega\mu_0}{4} \frac{2}{\pi k_0} \frac{e^{-jk_0\rho_s}}{\sqrt{\rho_s}} \frac{e^{-jk_0\rho}}{\sqrt{\rho}} \sum_{n=0}^{N_{max}} \tau_n \, C_{4n}' \, (-1)^n \, \cos[n(\phi - \phi_s)] \, . \end{aligned} \tag{D.35}$$

As to the denumerator of (D.31), one first notes that [117, Ch. 10]

$$|\vec{\rho} - \vec{\rho}_s| = \sqrt{\rho^2 + \rho_s^2 - 2\rho\rho_s \cos(\phi - \phi_s)} \, . \tag{D.36}$$

When the ELS is moved toward infinity ($\rho_s \to \infty$, or $\rho_s >> \rho$) along the ϕ_s direction, the square root in (D.36) can be approximated as [117, Ch. 10]

$$\begin{aligned} |\vec{\rho} - \vec{\rho}_s| &\simeq \sqrt{\rho_s^2 - 2\rho\rho_s \cos(\phi - \phi_s)} \\ &= \rho_s \sqrt{1 - 2\left(\frac{\rho}{\rho_s}\right) \cos(\phi - \phi_s)} \\ &\simeq \rho_s \left(1 - \frac{\rho}{\rho_s} \cos(\phi - \phi_s)\right) = \rho_s - \rho \cos(\phi - \phi_s) \, , \end{aligned} \tag{D.37}$$

where the terms in ρ/ρ_s higher than the first order have been discarded and only the first two terms in the Taylor expansion for $\sqrt{1+x}$ have been retained. Using this result one thus obtains

$$\lim_{\rho_s\to\infty \, ; \, \phi_s} \vec{E}_{\text{ELS}} = -\hat{z} \frac{I_e \omega\mu_0}{4} \sqrt{\frac{2}{\pi k_0\rho_s}} \, e^{-jk_0\rho_s} e^{j\pi/4} e^{jk_0\rho\cos(\phi - \phi_s)} \, . \tag{D.38}$$

Using (D.35) and (D.38) in (D.31), the following explicit expression for σ_d is obtained

$$\begin{aligned}\sigma_d &= 2\pi\rho\frac{\left(\frac{I_e\omega\mu_0}{4}\right)^2\left(\frac{2}{\pi k_0}\right)^2\frac{1}{\rho_s\rho}\left|\sum_{n=0}^{N_{max}}\tau_n\,C'_{4n}\,(-1)^n\,\cos[n(\phi-\phi_s)]\right|^2}{\left(\frac{I_e\omega\mu_0}{4}\right)^2\frac{2}{\pi k_0}\frac{1}{\rho_s}} \\ &= \frac{4}{k_0}\left|\sum_{n=0}^{N_{max}}\tau_n\,C'_{4n}\,(-1)^n\,\cos[n(\phi-\phi_s)]\right|^2 . \end{aligned} \tag{D.39}$$

Total cross section

The total cross section σ_t is defined by the ratio of the power P_s contained in the scattered far field to the incident power density S_i at the origin, both again evaluated when the ELS is moved infinitely far away from the cylinders along an arbitrary direction ρ_s. Mathematically,

$$\sigma_t = \lim_{\rho_s\to\rho_s\,;\,\phi_s}\frac{P_s}{S_i(\rho=0)} = \lim_{\rho\to\infty}\lim_{\rho_s\to\rho_s\,;\,\phi_s}\frac{\frac{1}{2\eta_0}\int_{\phi=0}^{2\pi}|\vec{E}_{3s}(\rho,\phi)|^2\rho d\phi}{\frac{1}{2\eta_0}|\vec{E}_{\text{ELS}}(\rho=0)|^2} . \tag{D.40}$$

Using the same procedure as in the determination of the total power P_t in (D.24), and recalling the result derived in (D.35), the explicit expression for σ_t becomes

$$\begin{aligned}\sigma_t &= \frac{\left(\frac{I_e\omega\mu_0}{4}\right)^2\left(\frac{2}{\pi k_0}\right)^2\frac{1}{\rho_s}\sum_{n=0}^{N_{max}}\tau_n^2\,|C'_{4n}|^2\int_{\phi=0}^{2\pi}\left(\frac{1}{\sqrt{\rho}}\right)^2\cos^2[n(\phi-\phi_s)]\,\rho\,d\phi}{\left(\frac{I_e\omega\mu_0}{4}\right)^2\frac{2}{\pi k_0}\frac{1}{\rho_s}} \\ &= \frac{2}{k_0}\sum_{n=0}^{N_{max}}\tau_n^2\,(3-\tau_n)\,|C'_{4n}|^2 . \end{aligned} \tag{D.41}$$

When the ELS is moved infinitely far away from the concentric cylinders, the field generated by the ELS constitutes locally a plane wave. Thus, the cross sections in (D.39) and (D.41) recover the usual plane wave cross sections, as demonstrated in Section D.2, where the corresponding geometry under the illumination of a TM polarized plane wave has been considered and its results compared to those derived presently.

D.2 Concentric cylinders - plane wave results

The derivation of the explicit expressions for the differential and total cross sections, σ_d and σ_t, respectively, in Section D.1.4 assumed that the ELS is moved infinitely far away from the concentric cylinders. It was in this connection noted that the so-derived cross sections recover those obtained when the source of illumination is, from the outset of the solution process, taken to be a TM polarized plane wave impinging on the structure. Presently, these statements are confirmed by deriving the respective usual plane wave cross sections under the TM plane wave incidence, and subsequently comparing them numerically with the expressions derived in Section D.1.4.

Without loss of generality, it is assumed that a uniform TM polarized plane wave having a real amplitude E_0 is incident on the structure comprised of concentric cylinders, see Figure 4.1 in Chapter 4, along the positive x-axis, i.e., along the direction $\phi_s = 0$. In this case, the electric field is given by [117, Ch. 11]

$$\vec{E}_{\text{PW}} = \hat{z}E_0e^{jk_0x} = \hat{z}E_0e^{jk_0\cos\phi} = \hat{z}E_0\sum_{n=0}^{N_{max}}\tau_n\,j^n\cos n\phi . \tag{D.42}$$

In similitude to this field, the unknown fields in the three regions are expanded as

$$\vec{E}_{1s,\text{PW}}(\rho,\phi) = \hat{z}\sum_{n=0}^{N_{max}} \tau_n C_{1n,\text{PW}} J_n(k_1\rho)\cos(n\phi) \quad \text{for} \quad \rho \le \rho_1 \,, \tag{D.43a}$$

$$\vec{E}_{2s,\text{PW}}(\rho,\phi) = \hat{z}\sum_{n=0}^{N_{max}} \tau_n \left[C_{2n,\text{PW}} J_n(k_2\rho) + C_{3n,\text{PW}} Y_n(k_2\rho)\right]\cos(n\phi) \quad \text{for} \quad \rho_1 \le \rho \le \rho_2 \,, \tag{D.43b}$$

$$\vec{E}_{3s,\text{PW}}(\rho,\phi) = \hat{z}\sum_{n=0}^{N_{max}} \tau_n C_{4n,\text{PW}} H_n^{(2)}(k_0\rho)\cos(n\phi), \quad \text{for} \quad \rho \ge \rho_2 \,, \tag{D.43c}$$

From (D.6) the incident magnetic field is

$$\vec{H}_{\text{PW}}(\rho,\phi) = \frac{E_0}{j\omega\mu_0}\Big\{\hat{\rho}\sum_{n=0}^{N_{max}} \tau_n\, n\, j^n\, J_n(k_0\rho)\, \sin(n\phi) + \hat{\phi}\, k_0 \sum_{n=0}^{N_{max}} \tau_n\, j^n\, J_n'(k_0\rho)\, \cos(n\phi)\Big\} \,, \tag{D.44a}$$

while the unknown magnetic fields in the three regions are

$$\vec{H}_{1s,\text{PW}}(\rho,\phi) = \frac{E_0}{j\omega\mu_1}\Big\{\hat{\rho}\sum_{n=0}^{N_{max}} \tau_n\, n\, C_{1n,\text{PW}}\, J_n(k_1\rho)\, \sin(n\phi) + \hat{\phi}\, k_1 \sum_{n=0}^{N_{max}} \tau_n\, C_{1n,\text{PW}}\, J_n'(k_1\rho)\, \cos(n\phi)\Big\}, \tag{D.44b}$$

$$\vec{H}_{2s,\text{PW}}(\rho,\phi) = \frac{E_0}{j\omega\mu_2}\Big\{\hat{\rho}\sum_{n=0}^{N_{max}} \tau_n\, n\, \left[C_{2n,\text{PW}}\, J_n(k_2\rho) + C_{3n,\text{PW}}\, Y_n(k_2\rho)\right]\, \sin(n\phi) + \hat{\phi}\, k_2 \sum_{n=0}^{N_{max}} \tau_n\, \left[C_{2n,\text{PW}}\, J_n'(k_2\rho) + C_{3n,\text{PW}}\, Y_n'(k_2\rho)\right]\, \cos(n\phi)\Big\}, \tag{D.44c}$$

$$\vec{H}_{3s,\text{PW}}(\rho,\phi) = \frac{E_0}{j\omega\mu_0}\Big\{\hat{\rho}\sum_{n=0}^{N_{max}} \tau_n\, n\, C_{4n,\text{PW}}\, H_n^{(2)}(k_0\rho)\, \sin(n\phi) + \hat{\phi}\, k_0 \sum_{n=0}^{N_{max}} \tau_n\, C_{4n,\text{PW}}\, H_n^{(2)\prime}(k_0\rho)\, \cos(n\phi)\Big\} \,, \tag{D.44d}$$

where $C_{in,\text{PW}}$, with $i = 1,\ldots 4$, are the unknown expansion coefficients which must be determined. Applying the electromagnetic boundary conditions at the interfaces $\rho = \rho_1$ and $\rho = \rho_2$, it follows easily that the continuity of the tangential components of the total electric and magnetic fields at $\rho = \rho_1$ gives the following relations

$$-C_{1n,\text{PW}} J_n(k_1\rho_1) + C_{2n,\text{PW}} J_n(k_2\rho_1) - C_{3n,\text{PW}} Y_n(k_2\rho_1) = 0 \,, \tag{D.45a}$$

$$-\frac{k_1}{\mu_1} C_{1n,\text{PW}} J_n'(k_1\rho_1) + \frac{k_2}{\mu_2} C_{2n,\text{PW}} J_n'(k_2\rho_1) + \frac{k_2}{\mu_2} C_{3n,\text{PW}} Y_n'(k_2\rho_1) = 0 \,, \tag{D.45b}$$

while the continuity of the same field components at the interface $\rho = \rho_2$ gives

$$C_{2n,\text{PW}} J_n(k_2\rho_2) + C_{3n,\text{PW}} Y_n(k_2\rho_2) - C_{4n,\text{PW}} H_n^{(2)}(k_0\rho_2) = j^n J_n(k_0\rho_2) \,, \tag{D.45c}$$

$$\frac{k_2}{\mu_2} C_{2n,\text{PW}} J_n'(k_2\rho_2) + \frac{k_2}{\mu_2} C_{3n,\text{PW}} Y_n'(k_2\rho_2) - \frac{k_0}{\mu_0} C_{4n,\text{PW}} H_n^{(2)\prime}(k_0\rho_2) = \frac{k_0}{\mu_0} j^n J_n'(k_0\rho_2) \,. \tag{D.45d}$$

These relations, which hold for $n = 0, 1, 2, \ldots, N_{max}$, can be written more compactly as

$$\vec{\Lambda}_{n,\text{PW}} = \bar{\bar{M}}_{n,\text{PW}}\, \vec{C}_{n,\text{PW}} \,, \quad n = 0, 1, 2, \ldots N_{max} \tag{D.46}$$

where $\vec{C}_{n,\text{PW}} = [C_{1n,\text{PW}},\ C_{2n,\text{PW}}, C_{3n,\text{PW}},\ C_{4n,\text{PW}}]$ is the vector containing the four expansion coefficients and $\vec{\Lambda}_{n,\text{PW}} = [\Lambda_{1n\text{PW}} = 0,\ \Lambda_{2n\text{PW}} = 0,\ \Lambda_{3n\text{PW}} = j^n J_n(k_0\rho_2),\ \Lambda_{4n\text{PW}} = (k_0/\mu_0) j^n J_n'(k_0\rho_2)]$ is the so-called excitation vector. The matrix $\bar{\bar{M}}_{n,\text{PW}}$ is a four-by-four matrix that depends on the values of the cylindrical waves at the two interfaces and is given by

$$\bar{\bar{M}}_{n,\text{PW}} = \begin{bmatrix} -J_n(k_1\rho_1) & J_n(k_2\rho_1) & Y_n(k_2\rho_1) & 0 \\ -\frac{k_1}{\mu_1} J_n'(k_1\rho_1) & \frac{k_2}{\mu_2} J_n'(k_2\rho_1) & \frac{k_2}{\mu_2} Y_n'(k_2\rho_1) & 0 \\ 0 & J_n(k_2\rho_2) & Y_n(k_2\rho_2) & -H_n^{(2)}(k_0\rho_2) \\ 0 & \frac{k_2}{\mu_2}\, J_n'(k_2\rho_2) & \frac{k_2}{\mu_2}\, Y_n'(k_2\rho_2) & -\frac{k_0}{\mu_0}\, H_n^{(2)\prime}(k_0\rho_2) \end{bmatrix} \tag{D.47}$$

The relation (D.46) can be solved for the unknown coefficients as

$$\vec{C}_{n,\text{PW}} = \left[\bar{\bar{M}}_{n,\text{PW}}\right]^{-1}\ \vec{\Lambda}_{n,\text{PW}}\ , \tag{D.48}$$

which is identical in form to the relation by which the unknown expansion coefficients are determined in the ELS illumination case, see Section D.1.3.

The derived solution is next used to determine the differential cross section, $\sigma_{d,\text{PW}}$, as well as the total cross section, $\sigma_{t,\text{PW}}$. The definitions of these quantities are the same as those used in Section D.1.4, except that now the corresponding plane wave based quantities are used. In the framework of the plane wave incidence, $\sigma_{d,\text{PW}}$ is given by

$$\sigma_{d,\text{PW}} = \lim_{\rho\to\infty}\left[2\pi\rho\ \frac{|\vec{E}_{3s,\text{PW}}(\rho,\phi)|^2}{|\vec{E}_{\text{PW}}(\rho=0)|^2}\right]\ . \tag{D.49}$$

while $\sigma_{t,\text{PW}}$ is

$$\sigma_{t,\text{PW}} = \frac{P_{s,\text{PW}}}{S_{i,\text{PW}}(\rho=0)} = \frac{\lim_{\rho\to\infty}\frac{1}{2\eta_0}\int_{\phi=0}^{2\pi}|\vec{E}_{3s,\text{PW}}(\rho,\phi)|^2\rho d\phi}{\frac{1}{2\eta_0}|\vec{E}_{\text{PW}}(\rho=0)|^2}\ . \tag{D.50}$$

With reference to (D.19) it is easily deduced that

$$\lim_{\rho\to\infty}\vec{E}_{3s,\text{PW}} = \left\{\hat{z}\ E_0\ \sqrt{\frac{2}{\pi k_0}}\ e^{j\pi/4}\sum_{n=0}^{N_{max}} C_{4n,\text{PW}}\ \tau_n\ j^n\ \cos(n\phi)\right\}\frac{e^{-jk_0\rho}}{\sqrt{\rho}}\ , \tag{D.51}$$

and thus

$$\begin{aligned}\sigma_{d,\text{PW}} &= 2\pi\rho\ \frac{\frac{2}{\pi k_0}|E_0|^2\left|\sum_{n=0}^{N_{max}} C_{4n,\text{PW}}\ \tau_n\ j^n\cos(n\phi)\right|^2}{|E_0 e^{jk_0x}|^2} \\ &= \frac{4}{k_0}\left|\sum_{n=0}^{N_{max}} C_{4n,\text{PW}}\ \tau_n j^n\cos(n\phi)\right|^2\ .\end{aligned} \tag{D.52}$$

Moreover, owing to the intermediate calculations of (D.24), it is straightforward to demonstrate that

$$\sigma_{t,\text{PW}} = \frac{2}{k_0}\sum_{n=0}^{N_{max}}\tau_n^2(3-\tau_n)|C_{4n,\text{PW}}|^2\ . \tag{D.53}$$

Having derived the respective cross section for the case of TM plane wave illumination, it is next of interest to compare these expressions with those obtained by moving the ELS to infinity along an arbitrary direction ϕ_s, see Section D.1.4. To perform the comparison, the same dipolar DPS-DNG structure as the one included in Chapter 4 is chosen, i.e, regions 1 and 3 are free space, while $\varepsilon_2 = -\varepsilon_0$ and $\mu_2 = -4\mu_0$. Moreover, the inner radius of the DNG shell is $\rho_1 = 6$ mm.

Figure D.1(a) shows σ_t given by (D.41) and $\sigma_{t,\text{PW}}$ given by (D.53) as a function of the outer shell radius ρ_2 for the dipolar DPS-DNG and DPS-DPS structures. From the figure it follows that σ_t indeed recovers $\sigma_{t,\text{PW}}$. This also holds for the corresponding differential cross sections, as is confirmed by Figure D.1(b), which shows σ_d given by (D.39), and $\sigma_{d,\text{PW}}$ given by (D.52) for the dipolar DPS-DNG structure having $\rho_1 = 6$ mm and $\rho_1 = 10.03$ mm.

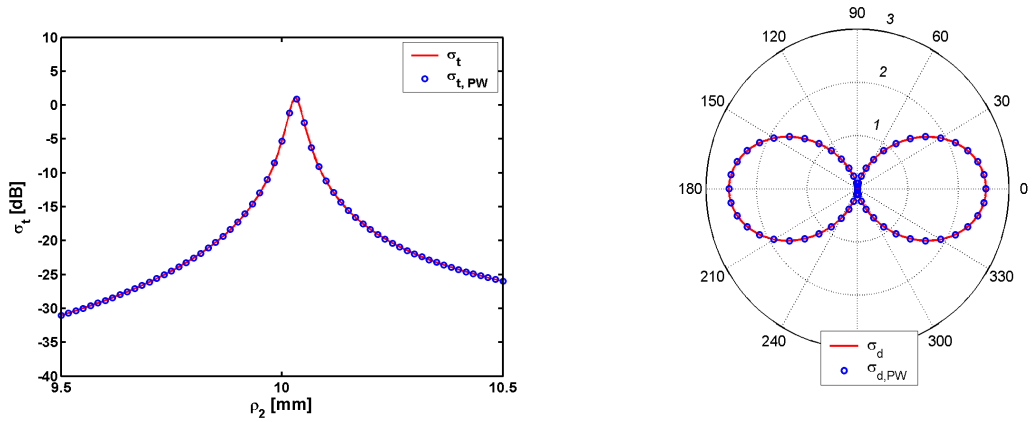

(a) (b)

Figure D.1: (a) *The total cross sections σ_t and $\sigma_{t,PW}$ as a function of the outer shell radius ρ_2, and* (b) *the differential cross sections σ_d and $\sigma_{d,PW}$, for the dipolar DPS-DNG structures. See the main text for explanation.*

D.3 Single cylinder - ELS results

D.3.1 Exact solution

The single cylinder configuration is obtained from that of the concentric cylinders shown in Figure 4.1 by simply removing the outer layer, e.g., region 2, while retaining region 1 and the exterior free-space region. Hence, the cylinder under examination is the core cylinder of radius ρ_1 in Figure 4.1, embedded into free space. Only the case in which the ELS is located outside the cylinder is considered here (a similar procedure is, of course, applied to obtain the solution when the ELS is located inside the cylinder), since it is the only one that pertains to the results presented in Chapter 4.

From Section D.1 it follows that the electric field generated by the ELS is given by (D.4) with $\mu_{\text{ELS}} = \mu_0$, $\varepsilon_{\text{ELS}} = \varepsilon_0$, and $k_{\text{ELS}} = k_0$. The unknown total electric field inside the cylinder, $\vec{E}^{sc}_{1s}$, and the scattered field outside of it, $\vec{E}^{sc}_{2s}$, are given by the expressions

$$\vec{E}^{sc}_{1s}(\rho,\phi) = -\hat{z} I_e \frac{\omega\mu_1}{4} \sum_{n=0}^{N_{max}} \tau_n C^{sc}_{1n} J_n(k_1\rho)\cos[n(\phi-\phi_s)] \quad \text{for} \quad \rho \le \rho_1 \,, \tag{D.54a}$$

$$\vec{E}^{sc}_{2s}(\rho,\phi) = -\hat{z} I_e \frac{\omega\mu_0}{4} \sum_{n=0}^{N_{max}} \tau_n C^{sc}_{2n} H^{(2)}_n(k_0\rho_1)\cos[n(\phi-\phi_s)] \quad \text{for} \quad \rho \ge \rho_2 \,, \tag{D.54b}$$

where C^{sc}_{1n} and C^{sc}_{2n} are the unknown expansion coefficients. The corresponding magnetic fields, which are required in the boundary conditions that lead to the determination of these coefficients, are obtained by Faraday's law (D.5). Using the electromagnetic boundary conditions at $\rho = \rho_1$, the following system of equations is obtained

$$\vec{\Lambda}^{sc}_n = \bar{\bar{M}}^{sc}_n \vec{C}^{sc}_n \,, \tag{D.55}$$

where

$$\vec{\Lambda}^{sc}_n = \begin{bmatrix} \Lambda^{sc}_{1n} \\ \Lambda^{sc}_{2n} \end{bmatrix} = \begin{bmatrix} \mu_0\, J_n(k_0\rho_1) H^{(2)}_n(k_0\rho_s) \\ k_0\, J'_n(k_0\rho_1) H^{(2)}_n(k_0\rho_s) \end{bmatrix} \,, \tag{D.56}$$

is the excitation vector, and $\vec{C}^{sc}_n = [C^{sc}_{1n},\ C^{sc}_{2n}]$ is the vector containing the two unknown expansion coefficients. The matrix $\bar{\bar{M}}^{sc}_n$ is a two-by-two matrix which contains the values of the cylindrical waves

at the interface $\rho = \rho_1$ and is given by

$$\bar{\bar{M}}_n^{sc} = \begin{bmatrix} \mu_1 J_n(k_1\rho_1) & -\mu_0 H_n^{(2)}(k_0\rho_1) \\ k_1 J_n'(k_1\rho_1) & -k_0 H_n^{(2)\prime}(k_0\rho_1) \end{bmatrix} = \begin{bmatrix} a & b \\ c & d \end{bmatrix}. \tag{D.57}$$

The unknown expansion coefficients are thus determined as

$$\vec{C}_n^{sc} = \left[\bar{\bar{M}}_n^{sc}\right]^{-1} \vec{\Lambda}_n^{sc}\,. \tag{D.58}$$

The inverse of the matrix $\bar{\bar{M}}_n^{sc}$ is of the form [123, Ch. 1]

$$\left[\bar{\bar{M}}_n^{sc}\right]^{-1} = \frac{1}{\det \bar{\bar{M}}_n^{sc}} \begin{bmatrix} d & -b \\ -c & a \end{bmatrix}, \tag{D.59}$$

where the determinant of the matrix $\bar{\bar{M}}_n^{sc}$, $\det \bar{\bar{M}}_n^{sc}$, is [123, Ch. 1]

$$\begin{aligned} \det \bar{\bar{M}}_n^{sc} &= ad \;-\; bc \\ &= -\mu_1 k_0 J_n(k_1\rho_1) H_n^{(2)\prime}(k_0\rho_1) + \mu_0 k_1 J_n'(k_1\rho_1) H_n^{(2)}(k_0\rho_1)\,. \end{aligned} \tag{D.60}$$

Using (D.56) and (D.58) one obtains

$$\begin{aligned} \begin{bmatrix} C_{1n}^{sc} \\ C_{2n}^{sc} \end{bmatrix} &= \frac{1}{-\mu_1 k_0 J_n(k_1\rho_1) H_n^{(2)\prime}(k_0\rho_1) + \mu_0 k_1 J_n'(k_1\rho_1) H_n^{(2)}(k_0\rho_1)} \\ &\quad \times \begin{bmatrix} -k_0 H_n^{(2)\prime}(k_0\rho_1) & \mu_0 H_n^{(2)}(k_0\rho_1) \\ -k_1 J_n'(k_1\rho_1) & \mu_1 J_n(k_1\rho_1) \end{bmatrix} \begin{bmatrix} \mu_0\; J_n(k_0\rho_1) H_n^{(2)}(k_0\rho_s) \\ k_0\; J_n'(k_0\rho_1) H_n^{(2)}(k_0\rho_s) \end{bmatrix}, \end{aligned} \tag{D.61}$$

which readily yields the coefficients

$$C_{1n}^{sc} = \mu_0 k_0\; H_n^{(2)}(k_0\rho_s) \frac{J_n'(k_0\rho_1) H_n^{(2)\prime}(k_0\rho_1) - J_n(k_0\rho_1) H_n^{(2)\prime}(k_0\rho_1)}{\det \bar{\bar{M}}_n^{sc}}\,, \tag{D.62}$$

and

$$C_{2n}^{sc} = H_n^{(2)}(k_0\rho_s) \frac{\mu_1 k_0 J_n'(k_0\rho_1) J_n(k_1\rho_1) - \mu_0 k_1 J_n(k_0\rho_1) J_n'(k_1\rho_1)}{\det \bar{\bar{M}}_n^{sc}}\,. \tag{D.63}$$

Once these coefficients are known, the various near- and far-field quantities considered in Chapter 4 and Manuscript II (Appendix B) for a single DPS or a DNG cylinder are easily obtained from the corresponding relations derived in Section D.1 for the concentric cylinders.

D.3.2 GO ray-tracing technique

This section details the GO ray-tracing technique applied to DPS or DNG cylinders to support the exact derived in Section D.3.1.

The configuration of interest is shown in Figure D.2. It is comprised of a DPS or a DNG cylinder, treated in Section D.3.1. The cylinder is illuminated by an exterior ELS which is located at a distance b from the cylinder surface along the positive x-axis. The GO ray-tracing technique requires a number of incident rays to be launched from the ELS toward the cylinder. These rays are launched at an angle α measured clockwise from the positive x-axis. Upon hitting the cylinder surface, some of the rays are reflected while some are refracted into the cylinder. It is of interest to examine the behaviour of the refracted rays in order to investigate the approximate field behaviour inside the DNG cylinders, and in particular to demonstrate the focusing of the ELS field as noted in Chapter 4 and Manuscript II (Appendix B).

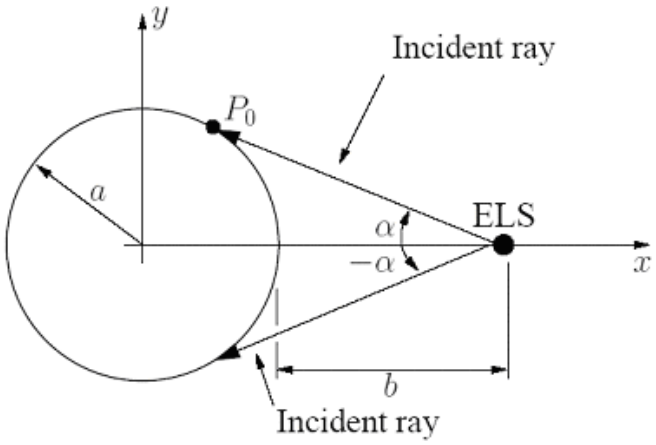

Figure D.2: *A DPS or a DNG cylinder illuminated by incident rays emanating from the ELS at an angle α, and hitting the cylinder at a point P_0*

D.3.2.1 Incident rays

An incident ray emanates from the ELS at an angle α. This ray hits the cylinder surface at a point P_0, referred to as the refraction point (since only the refracted rays are of interest inhere). In order to determine the refraction point one must first determine the equation of a straight line that represents a given incident ray. The maximum angle at which rays that emanate from the ELS will hit the surface of the cylinder is denoted by α_{max} and is given by

$$\alpha_{max} = \sin^{-1} \frac{a}{a+b} \,, \tag{D.64}$$

while the corresponding minimum angle, $\alpha_{min} = -\alpha_{max}$. An arbitrary line (i.e., a ray) that emanates from the ELS with an angle α ($\alpha_{min} \leq \alpha \leq \alpha_{max}$) has the equation

$$y = -x \tan\alpha + (a+b)\tan\alpha \,. \tag{D.65}$$

The intersection of this ray with the surface of the cylinder is found as the solution to the following two relations

$$x = (a+b) - \frac{y}{\tan\alpha} \,, \tag{D.66a}$$

$$x^2 + y^2 = a^2 \,, \tag{D.66b}$$

which can be combined to yield

$$x = (a+b) \mp \frac{\sqrt{a^2 - x}}{\tan\alpha} \,, \tag{D.67}$$

with $\alpha > 0$ and $\alpha < 0$. Carrying out the calculation, one obtains

$$\begin{aligned}
&[x - (a+b)]\tan\alpha = \mp\sqrt{a^2 - x^2} \quad \Rightarrow \\
&\left[x^2 + (a+b)^2 - 2x(a+b)\right]\tan^2\alpha = a^2 - x^2 \quad \Rightarrow \\
&x^2(1+\tan^2\alpha) - 2x(a+b)\tan^2\alpha + (a+b^2)\tan^2\alpha - a^2 = 0 \,.
\end{aligned} \tag{D.68}$$

The determinant of (D.68) is

$$\begin{aligned} D &= 4(a+b)^2\tan^4\alpha - 4(1+\tan^2\alpha)((a+b)^2\tan^2\alpha - a^2) \\ &= -4\left[(a+b)^2\tan^2\alpha - a^2 - a^2\tan^2\alpha\right] \\ &= -4\left[(a^2+b^2+2ab)\tan^2\alpha - a^2 - a^2\tan^2\alpha\right] \\ &= -4\left[(b^2+2ab)\tan^2\alpha - a^2\right] \\ &= 4a^2 - 4(b^2+2ab)\tan^2\alpha\,. \end{aligned} \tag{D.69}$$

Thus, the solution to (D.68), denoted by x_0, is

$$\begin{aligned} x_0 &= \frac{2(a+b)\tan^2\alpha \pm \sqrt{4a^2 - (b^2+2ab)\tan^2\alpha}}{2(1+\tan^2\alpha)} \\ &= \left[(a+b)\tan\alpha^2\alpha \pm \sqrt{a^2 - b(b+2a)}\right]\,\cos^2\alpha\,. \end{aligned} \tag{D.70}$$

Disregarding the "$-$" sign in front of the square root in (D.70), the coordinates (x_0, y_0) of the intersection point P_0 thus read

$$x_0 = \left[(a+b)\tan\alpha^2\alpha + \sqrt{a^2 - b(b+2a)}\right]\,\cos^2\alpha\,, \tag{D.71a}$$

$$y_0 = -x_0\tan\alpha + (a+b)\tan\alpha\,. \tag{D.71b}$$

The incident rays can now be easily depicted in the range $x_0 \le x \le (a+b)$.

D.3.2.2 Refracted rays

Next, the rays which are refracted into the cylinder at the point P_0 are determined. To this end, it is useful to consider Figure D.3 where all of the symbols are introduced that are used in the following derivation of the equation for the refracted rays.

At P_0, a local Cartesian coordinate system (x', y') is introduced, i.e., P_0 is located at the origin of this local coordinate system. The unit vector pointing from P_0 towards the ELS is

$$\hat{p} = \hat{x}\,\sin\beta\;-\;\hat{y}\,\cos\beta\,, \tag{D.72}$$

with $\beta = (\pi/2) - \alpha$. The unit vector normal to the cylinder surface at P_0 is

$$\hat{n} = \hat{x}\,\cos\Phi\;+\;\hat{y}\,\sin\Phi\,, \tag{D.73}$$

with

$$\Phi = \tan^{-1}\frac{y_0}{x_0}\,, \tag{D.74}$$

which is positive for $\alpha > 0$ and negative for $\alpha < 0$.

The angle of incidence θ_i is

$$\theta_i = \cos^{-1}(\hat{p}\cdot\hat{n}) = \cos^{-1}\left(\sin\beta\cos\Phi - \cos\beta\sin\Phi\right)\,. \tag{D.75}$$

Furthermore, it is noted that $\theta_i \in [0 - (\pi/2)]$ for $\alpha > 0$.

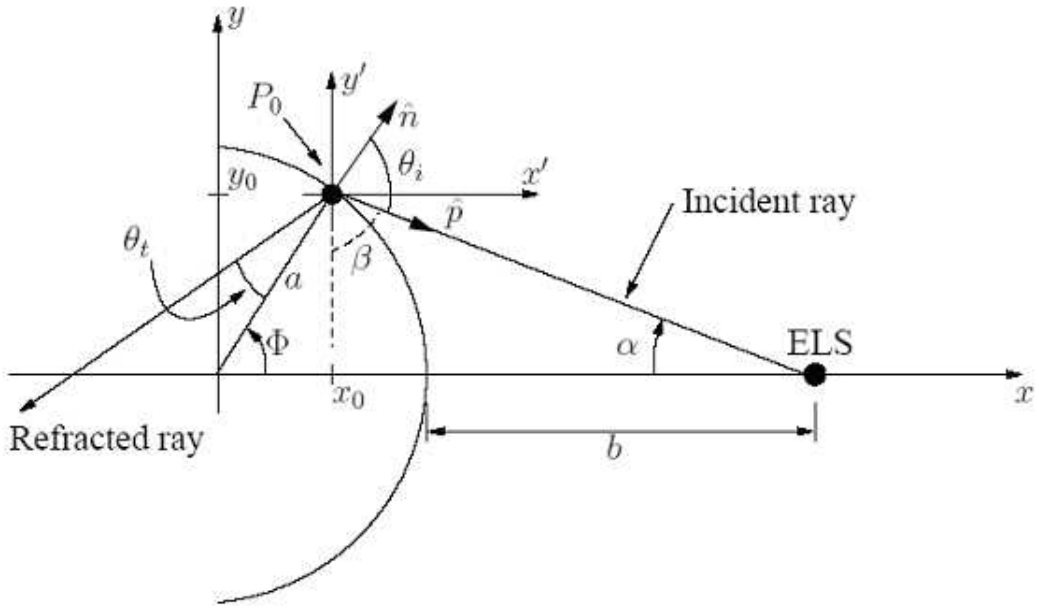

Figure D.3: *Determination of the equations for the refracted rays.*

The angle of refraction θ_t is determined by use of Snell's law of refraction. With reference to Chapter 3, this law is given by

$$\frac{\sin\theta_t}{\sin\theta_i} = \frac{k_0}{k_1}\,, \tag{D.76}$$

with $k_0 > 0$ being the free space wave number and k_1 being the wave number inside the cylinder. It is assumed that $k_1 > 0$ in a DPS cylinder and $k_1 < 0$ in a DNG cylinder, this implying that the angle of refraction θ_t is negative for a DNG cylinder. This is in agreement with the results given in Chapter 3. Thus, in a DNG cylinder, the angle of refraction, θ_t, is negative, which agrees with the results of Chapter 3. Relation (D.76) yields

$$\theta_t = \sin^{-1}\left[\frac{k_0}{k_1}\sin\theta_i\right]\,, \tag{D.77}$$

At this point all of the ingredients for the determination of the equation for the refracted rays have been gathered. In the local coordinate system the refracted rays have the equation

$$y' = x'\,\frac{1}{\tan\left(\frac{\pi}{2} - \Phi + \theta_t\right)}\,, \tag{D.78}$$

which, when transformed to the xy-coordinate system, gives the final result

$$y = y_0 \;+\; \frac{x - x_0}{\tan\left(\frac{\pi}{2} - \Phi + \theta_t\right)}\,. \tag{D.79}$$

The refracted rays are now easily depicted in the range $-a \le x \le x_0$.

D.4 Resonance conditions

D.4.1 Single cylinder

Using the results of Sections D.1.4 and D.3, it is found, e.g., that the total power is maximized when the quantity $|C_{2n}^{sc}|$ attains a maximum. In order to determine the condition for which this occurs, the

expansion coefficient C_{2n}^{sc} derived in Section D.3.1 is rewritten as

$$C_{2n}^{sc} = H_n^{(2)}(k_0\rho_s)\,\frac{\mu_1 k_0\; J_n'(k_0\rho_1)J_n(k_1\rho_1) - \mu_0 k_1\; J_n(k_0\rho_1)J_n'(k_1\rho_1)}{\det \bar{\bar{M}}_n^{sc}}\;. \tag{D.80}$$

From this expression it follows that the magnitude of C_{2n}^{sc} is maximized, i.e., a resonance occurs, when a minimum in the magnitude of $\det \bar{\bar{M}}_n^{sc}$ is attained. The derivation of the resonance condition depends on the material that constitutes the cylinder. Two cases, which are of interest to the present work, are considered. In the first case, the cylinder is either a DPS or a DNG material, and in the second case it is a SNG material.

D.4.1.1 DPS and DNG cylinders

The derivation of the condition for which the magnitude of the coefficient $|C_{2n}^{sc}|$ is maximized is greatly facilitated by assuming that the material parameters are lossless, i.e., that they are real numbers. This implies that the wave number k_1 is also a real number.

The determinant $\det \bar{\bar{M}}_n^{sc}$ is given by (D.60), which can be rewritten as

$$\begin{aligned}\det \bar{\bar{M}}_n^{sc} &= \mu_0 k_1 J_n'(k_1\rho_1)H_n^{(2)}(k_0\rho_1) - \mu_1 k_0 J_n(k_1\rho_1)H_n^{(2)}(k_0\rho_1)\\ &= \mu_0 k_1 J_n'(k_1\rho_1)J_n(k_0\rho_1) - \mu_1 k_0 J_n(k_1\rho_1)J_n'(k_0\rho_1)\\ &\qquad + j\left[\mu_1 k_0 J_n(k_1\rho_1)Y_n'(k_0\rho_1) - \mu_0 k_1 J_n'(k_1\rho_1)Y_n(k_0\rho_1)\right]\\ &= R_n + jS_n\;.\end{aligned} \tag{D.81}$$

where

$$R_n = \mathcal{R}e\{\det \bar{\bar{M}}_n^{sc}\} = \mu_0 k_1 J_n'(k_1\rho_1)J_n(k_0\rho_1) - \mu_1 k_0\; J_n(k_1\rho_1)J_n(k_0\rho_1)\;, \tag{D.82a}$$

$$S_n = \mathcal{I}m\{\det \bar{\bar{M}}_n^{sc}\} = \mu_1 k_0 J_n(k_1\rho_1)Y_n'(k_0\rho_1) - \mu_0 k_1 J_n'(k_1\rho_1)Y_n(k_0\rho_1)\;. \tag{D.82b}$$

This allows one to rewrite C_{2n}^{sc} as

$$C_{2n}^{sc} = -H_n^{(2)}(k_0\rho_s)\,\frac{R_n}{R_n + jS_n}\;. \tag{D.83}$$

from which it is clear that the magnitude $|C_{2n}^{sc}|$ attains a maximum, i.e., a resonance occurs, at the frequencies for which

$$S_n = \mathcal{I}m\{\det \bar{\bar{M}}_n^{sc}\} = \mu_1 k_0\; J_n(k_1\rho_1)Y_n'(k_0\rho_1) - \mu_0 k_1\; J_n'(k_1\rho_1)Y_n(k_0\rho_1) = 0\;. \tag{D.84}$$

This condition is referred to as the resonance condition. A similar resonance condition was derived in [122] for the case of a TM polarized plane wave incident on a single DPS cylinder. It was concluded there that the peaks in the expansion coefficient for the scattered field occur at the frequencies of the natural modes of the structure, i.e., the resonances are due to the excitation of the natural modes.

Apart for being exact, the resonance condition in (D.84) is general in the sense that it applies for DPS or DNG cylinders of arbitrary size. It is very interesting to note that for lossless DPS or DNG cylinders, the resonance condition is given by setting the imaginary part of the determinant of the matrix $\bar{\bar{M}}_n$ to zero.

Next, the approximate resonance condition for electrically small cylinders is derived. In this case one must evaluate (D.84) for $|k_1|\rho_1 << 1$ and $k_0\rho_1 << 1$. To this end one recalls the small argument expansion formulas [119, Ch. 10]

$$J_n(x) = \frac{1}{n!}\,\frac{1}{2^n}\,x^n\;, \tag{D.85a}$$

$$Y_n(x) = -\frac{(n-1)!}{\pi}\,2^n\,\frac{1}{x^n}\;, \tag{D.85b}$$

which hold for $n \geq 1$ as $x \to 0$. The derivatives of these functions are evaluated by first noting that [119, Ch. 10]

$$B_n'(x) = \frac{n}{x} B_n(x) - B_{n+1}(x) \; , \tag{D.86}$$

where $B_n(x)(\cdot)$ denotes either $J_n(\cdot)$ or $Y_n(\cdot)$, and the prime denotes the derivative with respect to the entire argument. Consequently,

$$J_n'(x) = \frac{1}{x} \; \frac{n}{n!} \; \frac{1}{2^n} \; x^n - \frac{1}{(n+1)!} \; \frac{1}{2^{n+1}} \; x^{n+1}, \tag{D.87a}$$

$$\begin{aligned} Y_n'(x) &= -\frac{n}{x} \; \frac{(n-1)!}{\pi} \; 2^n \; \frac{1}{x^n} + \frac{n!}{\pi} \; 2^{n+1} \; \frac{1}{x^{n+1}} \\ &= \frac{1}{x^{n+1}} \; \frac{2^n}{\pi} \; n!, \end{aligned} \tag{D.87b}$$

as $x \to 0$. Therefore, the resonance condition in (D.84) gives

$$\begin{aligned} \mathcal{I}m\{\det \bar{\bar{M}}_n^{sc}\} \simeq \; & \mu_1 k_0 \; \frac{1}{n!} \; \frac{1}{2^n} \; k_1^n \rho_1^n \; \frac{1}{k_0^n k_0 \; \rho_1^n \rho_1} \; \frac{2^n}{\pi} \; n! \\ & + \mu_0 k_1 \; \left[\frac{1}{k_1 \rho_1} \; \frac{n}{n!} \; \frac{1}{2^n} \; k_1^n \rho_1^n - \frac{1}{(n+1)!} \; \frac{1}{2^{n+1}} k_1^n \rho_1^n \; k_1 \rho_1 \right] \times \; \frac{(n-1)!}{\pi} \; 2^n \; \frac{1}{k_0^n \rho_1^n} \\ = \; & \mu_1 \; \frac{k_1^n}{k_0^n} \; \frac{1}{\pi} \; \frac{1}{\rho_1} + \mu_0 \; \frac{k_1^n}{k_0^n} \; \frac{1}{\pi} \; \frac{1}{\rho_1} \; \frac{n(n-1)!}{n!} - \mu_0 \; \frac{(n-1)!}{(n+1)!} \; \frac{1}{2} \; \frac{k_1^n}{k_0^n} \; \frac{1}{\pi} \; k_1^2 \rho_1 = 0 \; . \end{aligned} \tag{D.88}$$

Since $n(n-1)!/n! = 1$ the last expression reduces to

$$(\mu_1 + \mu_0) - \frac{1}{2} \; \mu_0 \; \frac{(n-1)!}{(n+1)!} \; (k_1 \rho_1)^2 = 0 \; , \tag{D.89}$$

upon the cancelation of the common terms in (D.88) and multiplication by ρ_1. Obviously, the first term on the left-hand side in (D.89) is significantly larger than the second one since $|k_1|\rho_1 << 1$. Thus, the resonance condition for a lossless DPS or DNG cylinder is

$$\mu_1 = -\mu_0 \; , \tag{D.90}$$

which thus holds for any radius, ρ_1, and permeability, μ_1, as long as $|k_1|\rho_1 << 1$. One notes that this condition requires a DNG cylinder (or as will be shown below, an MNG cylinder). In particular, it means that electrically small DPS cylinders will not exhibit a resonant behaviour.

The resonance condition in (D.90) was obtained by inserting the small argument expansions (D.85a)-(D.85b) and (D.87a)-(D.87b) in the general relation (D.84). As noted above, these expansions are valid for $n \geq 1$, and thus the relation in (D.90) is valid only for these modes. In the case of the monopolar mode, i.e., for $n = 0$, different small argument expansions must be used, e.g., see [119, Ch. 10]. It was not possible to find a relation similar to (D.90) for the monopolar mode.

D.4.1.2 SNG cylinders

In a SNG cylinder one has either $\varepsilon_1 > 0$ and $\mu_1 < 0$ or $\varepsilon_1 < 0$ and $\mu_1 > 0$. In both of these cases, the wave number k_1 is imaginary. For the discussion below it is written as $k_1 = j|k_1|$. In this SNG case one then finds

$$\det \bar{\bar{M}}_n^{sc} = R_n + jS_n \; , \tag{D.91}$$

where

$$R_n = j\mu_0|k_1|J_n'(j|k_1|\rho_1)J_n(k_0\rho_1) - \mu_1 k_0 J_n(j|k_1|\rho_1)J_n'(k_0\rho_1)\ , \tag{D.92a}$$

$$S_n = \mu_1 k_0 J_n(i|k_1|\rho_1)Y_n'(k_0\rho_1) - j\mu_0|k_1|J_n'(i|k_1|\rho_1)Y_n(k_0\rho_1)\ . \tag{D.92b}$$

Since [119, Ch. 10]

$$J_n(jx) = j^n I_n(x), \tag{D.93}$$

$$J_n'(jx) = -jj^n I_n'(x), \tag{D.94}$$

where $I_n(\cdot)$ is the modified Bessel function of the first kind and order n, and $I_n'(\cdot)$ is its derivative with respect to the entire argument, the expressions in (D.92a) and (D.92a) can be written as

$$R_n = j^n\left[\mu_0|k_1|I_n'(|k_1|\rho_1)J_n(k_0\rho_1) - \mu_1 k_0 I_n(|k_1|\rho_1)J_n'(k_0\rho_1)\right] \equiv j^n\ r_n\ , \tag{D.95a}$$

$$S_n = j^n\left[\mu_1 k_0 I_n(|k_1|\rho_1)Y_n'(k_0\rho_1) - \mu_0|k_1|I_n'(|k_1|\rho_1)Y_n(k_0\rho_1)\right] \equiv j^n\ s_n\ . \tag{D.95b}$$

As a consequence, C_{2n}^{sc} becomes

$$C_{2n}^{sc} = -H_n^{(2)}(k_0\rho_s)\ \frac{r_n}{r_n + js_n}\ . \tag{D.96}$$

Since $I_n(|k_1|\rho_1)$ and $I_n'(|k_1|\rho)$ are real numbers, it is found that r_n and s_n are real. From (D.96) is clear that the magnitude $|C_{2n}^{sc}|$ attains a maximum, i.e., a resonance occurs, at the frequencies that satisfy the condition

$$s_n = \mu_1 k_0\ I_n(|k_1|\rho_1)Y_n'(k_0\rho_1) - \mu_0|k_1|\ I_n'(|k_1|\rho_1)Y_n(k_0\rho_1) = 0\ , \tag{D.97}$$

which is the resonance condition for a single SNG cylinder for any mode number n.

It is interesting to note that since the small argument expansion of $J_n(\cdot)$ and $I_n(\cdot)$ are identical, see e.g., [119, Ch. 10], the condition in (D.97) is identical to the one given by (D.84) for lossless DPS and DNG cylinders when electrically small sizes are utilized[D.1]. Thus, the resonance condition $\mu_1 = -\mu_0$ in (D.90) for electrically small lossless DPS and DNG cylinders, also holds true for electrically small SNG cylinders. In fact, since the condition implies that $\mu_1 = -\mu_0$, these findings are only applicable to MNG materials.

Having determined the resonance condition in the case of a single cylinder, the same procedure is applied next to determine the resonance condition for the case of concentric cylinders treated extensively in Section D.1.

D.4.2 Concentric cylinders

Presently, the resonance condition for the case of concentric cylinders is derived. In this case, the relevant matrix, which is to be inverted to determine the unknown expansion coefficients, is now a four-by-four

[D.1] It is, however, noted that since the recurrence relation for Bessel functions in (D.86) differs from that of the modified Bessel functions of the first kind, which reads [119, Ch. 10] $I_n'(x) = (n/x)I_n(x) + I_{n+1}(x)$, the general resonance condition (D.97) for SNG cylinders yields

$$(\mu_1 + \mu_0) + \underbrace{\frac{1}{2}\ \mu_0\ \frac{(n-1)!}{(n+1)!}\ (|k_1|\rho_1)^2}_{\text{Term 1}} = 0\ , \tag{D.98}$$

in the limit of electrically small sizes. This expression differs from (D.89) by the sign in front of term 1. However, for $|k_1|\rho_1 << 1$ it recovers the final resonance condition in (D.90) for electrically small lossless DPS and DNG cylinders.

matrix $\bar{\bar{M}}_n$, which is rewritten below for convenience as

$$\bar{\bar{M}}_n = \begin{bmatrix} a = -\mu_1 J_n(k_1\rho_1) & b = \mu_2 J_n(k_2\rho_1) & c = \mu_2 Y_n(k_2\rho_1) & d = 0 \\ e = -k_1 J_n'(k_1\rho_1) & f = k_2 J_n'(k_2\rho_1) & g = k_2 Y_n'(k_2\rho_1) & h = 0 \\ i = 0 & \jmath = \mu_2\, J_n(k_2\rho_2) & k = \mu_2\, Y_n(k_2\rho_2) & l = -\mu_0\, H_n^{(2)}(k_0\rho_2) \\ m = 0 & n = k_2\, J_n'(k_2\rho_2) & o = k_2\, Y_n'(k_2\rho_2) & p = -k_0\, H_n^{(2)\prime}(k_0\rho_2) \end{bmatrix} . \tag{D.99}$$

The determinant of this matrix is [123, Ch. 1]

$$\begin{aligned} \det \bar{\bar{M}}_n &= a\ [f(kp - lo) - g(\jmath p - ln)] - e\,[b(kp - lo) - c(\jmath p - ln)] \\ &= (af - eb)(kp - lo) + (ec - ag)(\jmath p - ln)\ . \end{aligned} \tag{D.100}$$

The case of DPS- or DNG-based concentric cylinders is first considered in terms of both analytical and numerical investigations. Subsequently, the SNG-based concentric cylinder configurations are mentioned briefly.

D.4.2.1 DPS- and DNG-based concentric cylinders

The derivation of the resonance condition is greatly facilitated by assuming that the material parameters of the various regions are lossless, in which case the wave numbers k_1 and k_2 are real. In this case, only the terms l and p in (D.100) are complex and one has

$$\begin{aligned} \det \bar{\bar{M}}_n &= (af - eb)(k\mathcal{R}e\{p\} - \mathcal{R}e\{l\}o) + (ec - ag)(\jmath\mathcal{R}e\{p\} - \mathcal{R}e\{l\}n) \\ &\quad + j\,[(af - eb)(k\mathcal{I}m\{p\} - \mathcal{I}m\{l\}o) + (ec - ag)(\jmath\mathcal{I}m\{p\} - \mathcal{I}m\{l\}n)] \\ &= \mathcal{R}e\{\det \bar{\bar{M}}_n\} + j\mathcal{I}m\{\det \bar{\bar{M}}_n\}\ . \end{aligned} \tag{D.101}$$

From Section D.1.3 the following system of equations is recalled

$$\vec{\Lambda}_n = \bar{\bar{M}}_n \vec{C}_n\ , \quad n = 0, 1, 2, \ldots N_{max}\ , \tag{D.102}$$

where $\vec{C}_n = [C_{1n}, C_{2n}, C_{3n}, C_{4n}]$ is the vector containing the four expansion coefficients and $\vec{\Lambda}_n = [\Lambda_{1n}, \Lambda_{2n}, \Lambda_{3n}, \Lambda_{4n}]$ is the excitation vector, which depends on the location of the ELS. With reference to (D.102) and Cramers's theorem [123, Ch. 1], the explicit expression for C_{4n} can be obtained as

$$C_{4n} = \frac{\det \bar{\bar{\Upsilon}}_{4n}}{\det \bar{\bar{M}}_n}\ , \tag{D.103}$$

where $\det \bar{\bar{\Upsilon}}_{4n}$ is the determinant of the matrix $\bar{\bar{\Upsilon}}_{4n}$, which is obtained by replacing the fourth column of $\bar{\bar{M}}_n$ by $\vec{\Lambda}_n$. From (D.103) it is clear that C_{4n} is maximized when $|\det \bar{\bar{M}}_n|$ is minimized. Since different $\vec{\Lambda}_n$ are used when the ELS is in region 1, 2, or 3, it is clear that different expressions for C_{4n} will result for ELS locations in region 1, 2, or 3. The case in which the ELS is in region 3 is considered first.

ELS in region 3:

With reference to Section D.1.3, the excitation vector is

$$\vec{\Lambda}_n = \begin{bmatrix} 0 \\ 0 \\ \mu_0\, J_n(k_0\rho_2) H_n^{(2)}(k_0\rho_s) \\ k_0\, J_n'(k_0\rho_2) H_n^{(2)}(k_0\rho_s) \end{bmatrix}\ , \tag{D.104}$$

when the ELS is in region 3. Thus, the matrix $\bar{\bar{\Upsilon}}_{4n}$ is identical to the matrix $\bar{\bar{M}}_n$ in (D.99) except that the

fourth column of the latter is replaced by (D.104). Specifically,

$$\bar{\bar{\Upsilon}}_{4n} = \begin{bmatrix} a = -\mu_1 J_n(k_1\rho_1) & b = \mu_2 J_n(k_2\rho_1) & c = \mu_2 Y_n(k_2\rho_1) & d = 0 \\ e = -k_1 J_n'(k_1\rho_1) & f = k_2 J_n'(k_2\rho_1) & g = k_2 Y_n'(k_2\rho_1) & h = 0 \\ i = 0 & \jmath = \mu_2\, J_n(k_2\rho_2) & k = \mu_2\, Y_n(k_2\rho_2) & l_1 = \mu_0\, J_n(k_0\rho_2)\, H_n^{(2)}(k_0\rho_s) \\ m = 0 & n = k_2\, J_n'(k_2\rho_2) & o = k_2\, Y_n'(k_2\rho_2) & p_1 = k_0\, J_n'(k_0\rho_2)\, H_n^{(2)}(k_0\rho_s) \end{bmatrix} , \tag{D.105}$$

and the associated determinant reads

$$\begin{aligned} \det \bar{\bar{\Upsilon}}_{4n} &= a\ [f(kp_1 - l_1 o) - g(jp_1 - l_1 n)] - e\,[b(kp_1 - l_1 o) - c(jp_1 - l_1 n)] \\ &= (af - eb)(kp_1 - l_1 o) + (ec - ag)(jp_1 - l_1 n)\ . \end{aligned} \tag{D.106}$$

All of the terms in (D.105) and (D.106), except l_1 and p_1, are identical to those in (D.99) and (D.100), respectively. Since both l_1 and p_1 include the factor $H_n^{(2)}(k_0\rho_s)$, the relation in (D.106) can be written as

$$\det \bar{\bar{\Upsilon}}_{4n} = H_n^{(2)}(k_0\rho_s)\,[(af - eb)(kp_{11} - l_{11} o) + (ec - ag)(jp_{11} - l_{11} n)]\ , \tag{D.107}$$

where

$$l_{11} = \mu_0 J_n(k_0\rho_2)\ , \tag{D.108}$$

$$p_{11} = k_0 J_n'(k_0\rho_2)\ . \tag{D.109}$$

However, recalling that the terms l and p in $\bar{\bar{M}}_n$, and thereby in its determinant, are given by

$$l = -\mu_0 H_n(k_0\rho_2) = -\mu_0\,(J_n(k_0\rho_2) - jY_n(k_0\rho_2))\,, \tag{D.110}$$

$$p = -k_0 H_n^{(2)}(k_0\rho_2) = k_0\,(J_n'(k_0\rho_2) - jY_n'(k_0\rho_2))\ , \tag{D.111}$$

it is found that l_{11} and p_{11} in (D.108) and (D.109), respectively, can also be expressed as

$$l_{11} = -\,(-\mu_0 J_n(k_0\rho_2)) = -\mathcal{R}e\{l\}\,, \tag{D.112}$$

$$p_{11} = -\,(-k_0 J_n'(k_0\rho_2)) = -\mathcal{R}e\{p\}\ . \tag{D.113}$$

As a consequence, $\det \bar{\bar{\Upsilon}}_{4n}$ in (D.107) can now be expressed as

$$\begin{aligned} \det \bar{\bar{\Upsilon}}_{4n} &= -H_n^{(2)}(k_0\rho_s)\ [(af - eb)(k\mathcal{R}e\{p\} - \mathcal{R}e\{l\}o) + (ec - ag)(j\mathcal{R}e\{p\} - \mathcal{R}e\{l\}n)] \\ &= -H_n^{(2)}(k_0\rho_s)\ \mathcal{R}e\{\det \bar{\bar{M}}_n\}\ . \end{aligned} \tag{D.114}$$

Inserting (D.101) and (D.114) in (D.103), the expansion coefficient C_{4n} now takes the form

$$C_{4n} = -H_n^{(2)}(k_0\rho_s)\ \frac{\mathcal{R}e\{\det \bar{\bar{M}}_n\}}{\mathcal{R}e\{\det \bar{\bar{M}}_n\} + j\mathcal{I}m\{\det \bar{\bar{M}}_n\}}\ . \tag{D.115}$$

The coefficient C_{4n} in (D.115) is now expressed in terms of the same functional form as the coefficient C_{2n}^{sc} in (D.83) for the single cylinder. It is clear that $|C_{4n}|$ is maximum, and thus the resonance occurs, when $\mathcal{I}m\{\det \bar{\bar{M}}_n\} = 0$, i.e., when the condition

$$\mathcal{I}m\{\det \bar{\bar{M}}_n\} = (af - eb)(k\mathcal{I}m\{p\} - \mathcal{I}m\{l\}o) + (ec - ag)(j\mathcal{I}m\{p\} - \mathcal{I}m\{l\}n) = 0\ , \tag{D.116}$$

is met.

In the limit of electrically small designs, where the products $|k_1|\rho_1$, $|k_2|\rho_1$, $|k_2|\rho_2$ and $k_0\rho_2$ are much smaller than unity, the small argument expansions of the different terms in (D.116) are used to obtain

$$\begin{aligned}
\mathcal{I}m\{\det \bar{\bar{M}}_n^{sc}\} \simeq \Big[& -\mu_1 \, \frac{n}{(n!)^2} \, \frac{1}{2^{2n}} \, \frac{1}{\rho_1} \, k_1^n k_2^n \rho_1^{2n} + \mu_2 \, \frac{n}{(n!)^2} \, \frac{1}{2^{2n}} \, \frac{1}{\rho_1} \, k_2^n k_1^n \rho_1^{2n} \\
& + \mu_1 k_2 \, \frac{1}{n!(n+1)!} \, \frac{1}{2^{2n}} \, \frac{1}{2} \, k_1^n k_2^n k_2 \rho_1^{2n} \rho_1 \\
& - \mu_2 k_1 \, \frac{1}{n!(n+1)!} \, \frac{1}{2^{2n}} \, \frac{1}{2} \, k_2^n k_1^n k_1 \rho_1^{2n} \rho_1 \Big] \\
\times \Big[& -\mu_2 k_0 \, \frac{(n-1)!}{\pi} \, 2^n \, \frac{1}{(k_2\rho_2)^n} \, \frac{1}{(k_0\rho_2)^{n+1}} \, \frac{2^n}{\pi} \, n! \\
& + \mu_0 k_2 \, \frac{(n-1)!}{\pi} \, 2^n \, \frac{1}{(k_0\rho_2)^2} \, \frac{1}{(k_2\rho_2)^{n+1}} \, \frac{2^n}{\pi} \, n! \Big] \\
+ \Big[& \mu_2 \, \frac{(n-1)!}{\pi} \, \frac{k_1^n}{k_2^n} \, \frac{1}{\rho_1} \, \frac{n}{n!} - \mu_2 k_1 \, \frac{(n-1)!}{(n+1)!} \, \frac{1}{\pi} \, \frac{1}{2} \, \frac{k_1^n}{k_2^n} \, k_1\rho_1 + \mu_1 \, \frac{k_1^n}{k_2^n} \, \frac{1}{\rho_1} \, \frac{1}{\pi} \Big] \\
\times \Big[& \mu_2 \, \frac{k_2^n}{k_0^n} \, \frac{1}{\rho_2} \, \frac{1}{\pi} + \mu_0 k_2 \, \frac{(n-1)!}{\pi} \, 2^n \, \frac{1}{(k_0\rho_2)^n} \\
& \times \Big(\frac{1}{k_2\rho_2} \, \frac{n}{n!} \, \frac{1}{2^n} \, (k_2\rho_2)^n - \frac{1}{(n+1)!} \, \frac{1}{2^{n+1}} \, (k_2\rho_2)^{n+1} \Big) \Big] \\
= 0 \, . &
\end{aligned} \tag{D.117}$$

The expression in (D.117) can be rearranged into the following form

$$\begin{aligned}
& (\mu_2-\mu_1)\,(\mu_2-\mu_0) \, \frac{1}{\rho_1\rho_2} \, \frac{\rho_1^{2n}}{\rho_2^{2n}} + (\mu_1 k_2^2 - \mu_2 k_1^2)\,(\mu_2-\mu_0) \, \frac{(n-1)!}{(n+1)!} \, \frac{1}{2} \, \frac{\rho_1}{\rho_2} \, \frac{\rho_1^{2n}}{\rho_2^{2n}} \\
= \quad & (\mu_2+\mu_1)\,(\mu_2+\mu_0) \, \frac{1}{\rho_1\rho_2} \; - \; \mu_0 k_2^2 \,(\mu_2+\mu_1) \, \frac{(n-1)!}{(n+1)!} \, \frac{1}{2} \, \frac{\rho_2}{\rho_1} \\
& - \mu_2 k_1^2 \,(\mu_2+\mu_0) \, \frac{(n-1)!}{(n+1)!} \, \frac{1}{2} \, \frac{\rho_1}{\rho_2} \\
& + \mu_2\mu_0 k_1^2 k_2^2 \, \frac{(n-1)!}{(n+1)!} \, \frac{1}{4} \, \rho_1\rho_2 \, ,
\end{aligned} \tag{D.118}$$

which upon multiplication by $\rho_1\rho_2$ gives

$$\begin{aligned}
& (\mu_2-\mu_1)\,(\mu_2-\mu_0) \, \frac{\rho_1^{2n}}{\rho_2^{2n}} - (\mu_2+\mu_1)\,(\mu_2+\mu_0) \\
= \quad & \mu_2\mu_0 k_1^2 k_2^2 \, \frac{(n-1)!}{(n+1)!} \, \frac{1}{4} \, (\rho_1\rho_2)^2 - \mu_2 k_1^2 \,(\mu_2+\mu_0) \, \frac{(n-1)!}{(n+1)!} \, \frac{1}{2} \, \rho_1^2 \\
& - \mu_0 k_2^2 \,(\mu_2+\mu_1) \, \frac{(n-1)!}{(n+1)!} \, \frac{1}{2} \, \rho_2^2 - (\mu_1 k_2^2 - \mu_2 k_1^2)\,(\mu_2-\mu_0) \, \frac{(n-1)!}{(n+1)!} \, \frac{1}{2} \, \rho_1^2 \, \frac{\rho_1^{2n}}{\rho_2^{2n}}
\end{aligned}$$

$$= \underbrace{\mu_2\mu_0 \frac{(n-1)!}{(n+1)!}\frac{1}{4}(k_1\rho_1)^2(k_2\rho_2)^2}_{\text{Term 1}} - \underbrace{\mu_2(\mu_2+\mu_0)\frac{(n-1)!}{(n+1)!}\frac{1}{2}(k_1\rho_1)^2}_{\text{Term 2}}$$

$$- \underbrace{\mu_0(\mu_2+\mu_1)\frac{(n-1)!}{(n+1)!}\frac{1}{2}(k_2\rho_2)^2}_{\text{Term 3}}$$

$$- \underbrace{(\mu_1\frac{k_2^2}{k_1^2}-\mu_2)(\mu_2-\mu_0)\frac{(n-1)!}{(n+1)!}\frac{1}{2}\frac{\rho_1^{2n}}{\rho_2^{2n}}(k_1\rho_1)^2}_{\text{Term 4}} . \qquad \text{(D.119)}$$

Since $|k_1|\rho_1 << 1$ and $|k_2|\rho_2 << 1$, it is found that the terms 1, 2, 3, and 4 in (D.119) are negligible as compared to both of the terms on the left-hand side of (D.119), and thus this relation reduces to

$$\frac{\rho_1}{\rho_2} \simeq \sqrt[2n]{\frac{(\mu_2+\mu_1)(\mu_2+\mu_0)}{(\mu_2-\mu_1)(\mu_2-\mu_0)}} , \qquad \text{(D.120)}$$

which is the resonance condition for lossless DPS- or DNG-based concentric cylinders when the ELS is in region 3.

This resonance condition becomes more accurate as the mode number increases since the factor $(n-1)!/(n+1)! = 1/(n(n+1))$ included in terms 1 through 4 in (D.119) diminishes rapidly as n increases. Nonetheless, as the analysis in Chapter 4 and Manuscript I (Appendix A) revealed, the resonance condition is very accurate also in the case of e.g., the dipolar mode.

The resonance condition given by (D.120) has been used in Chapter 4 and Manuscript I (Appendix A), e.g., to determine the approximate value of the outer radius ρ_2 of the electrically small structures which excite the dominant mode of order $n \geq 1$ for various material parameters and values of the inner radius ρ_1.

The above derivation assumed $n \geq 1$. As with the single cylinder cases, it was not possible to obtain a monopolar mode resonance condition.

ELS in region 1 or 2:

In order to obtain the analytical expression for the expansion coefficient C_{4n} in (D.103) when the ELS is in region 1 or 2, the matrix $\bar{\bar{\Upsilon}}_{4n}$, whose determinant is the numerator of (D.103), is constructed by replacing the fourth column of the matrix $\bar{\bar{M}}_n$ with the appropriate excitation vector, $\vec{\Lambda}_n$, for these two regions. As noted above, the excitation vector differs for the ELS locations in regions 1, 2 and 3. As a consequence, the matrix $\bar{\bar{\Upsilon}}_{4n}$ and thus the numerator of (D.103) is different when the ELS is located in region 1, 2, or 3. Although not included inhere, it was verified analytically that the C_{4n} can not be written in the form given by (D.115) when the ELS is in region 1 or 2. In these cases it is difficult to predict analytically the resonance condition, as both the numerator and denominator of the expressions derived for the C_{4n} depend on essentially the same parameters. However, in the electrically small limit and for the range of parameters of interest here, it was verified numerically that the resonance condition in (D.120) also holds when the ELS is in region 1 or 2. This is confirmed though the following numerical calculations, where several DPS-DNG structures were considered. These cases are denoted structures 1, 2, and 3; they were designed to excite the resonant dipolar mode. Their material and approximate geometrical parameters are summarized in Table D.2. In all cases, the resonance condition in (D.120) was used for $n = 1$, and the material parameters and the value of the inner radius ρ_1 were chosen to obtain the approximate value of the outer radius ρ_2 at which a resonance is expected. In principle, since (D.120) only holds for the ELS in region 3, the definitions of the structure in Table D.2 hold only when the ELS is in region 3. However, as the results below will reveal, the resonance in $|C_{4n}|$ occurs at the same value of ρ_2 when the ELS is in region 1 or 2.

Structure no.	ε_1	μ_1	ε_2	μ_2	ρ_1 [mm]	ρ_2 [mm]
1	ε_0	μ_0	$-\varepsilon_0$	$-4\mu_0$	6	10
2	ε_0	$-1.5\mu_0$	ε_0	$-0.5\mu_0$	6	7.35
3	ε_0	$-2\mu_0$	ε_0	$2.5\mu_0$	6	11.78

Table D.2: *Material and approximate geometrical parameters of the electrically small resonant dipolar DPS-DNG structures.*

Figures D.4(a), (b) and (c) show the magnitude $|C_{4n}|$ of the expansion coefficient C_{4n} as a function of ρ_2 for structures 1, 2, and 3, respectively, when the ELS is in regions 1, 2, and 3. More specifically, the ELS is in regions 1 and 2 at $\rho_s = 5.99$ mm and $\rho_s = 6.01$ mm, respectively, for all of these structures. On the other hand, when the ELS is in region 3 it is located at $\rho_s = 10.51$ mm for structure 1, $\rho_s = 8.01$ mm for structure 2, $\rho_s = 12.1$ mm for structure 3.

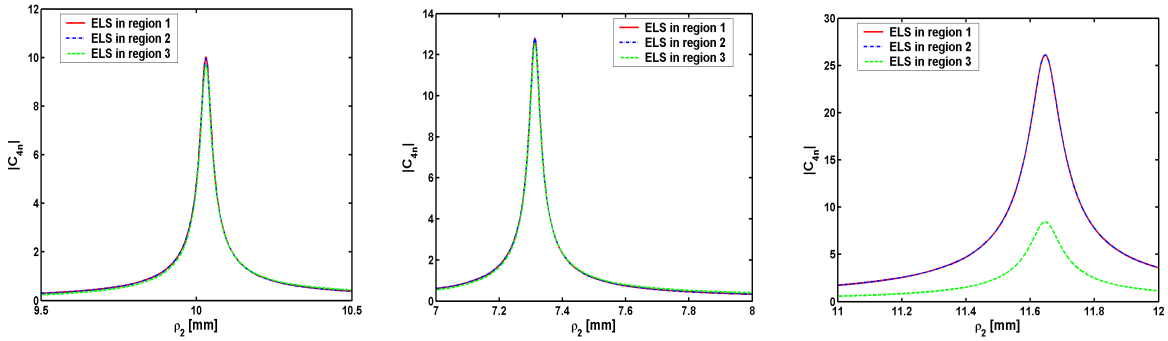

(a) (b) (c)

Figure D.4: *The magnitude $|C_{4n}|$ of the expansion coefficient C_{4n} for structure 1 (a), 2 (b), and (3) (c). When the ELS is in regions 1 and 2 it is located at $\rho_s = 5.99$ mm and $\rho_s = 6.01$ mm, respectively, for all structures. When the ELS is in region 3 it is located at $\rho_s = 10.51$ mm for structure 1, and at $\rho_s = 8.01$ mm for structure 2, and at $\rho_s = 12.1$ mm for structure 3.*

In Figure D.4(a), a resonant peak is found at $\rho = 10.03$ mm for the ELS locations in regions 1, 2, and 3. This value of ρ_2 is very close to the approximate value of 10 mm given in Table D.2 obtained by the resonance condition (D.120). Therefore, this condition, which was derived for the ELS in region 3, also holds for the ELS locations in the two other regions since resonances are obtained at the same value of ρ_2 regardless of the location of the ELS. This is also the case with the other two structures where the resonant peaks are found at $\rho = 7.32$ mm and $\rho_2 = 11.65$ mm, respectively, regardless of the location of the ELS. These values are very close to the approximate values of $\rho_2 = 7.35$ mm and $\rho_2 = 11.78$ mm, respectively, predicted by the resonance condition (D.120) and given in Table D.2. Consequently, for the range of parameters investigated here and of interest to this work, the resonance condition in (D.120) applies to ELS locations in all three regions.

The fact that the resonance condition in (D.120), derived for ELS locations in region 3, also holds when the ELS is in region 1 or 2 means that the expressions for C_{4n} for those cases, which are not included inhere, are dominated by the behaviour of their respective denominators because the resulting numerators do not produce a zero for the same combination of parameters that produce the minima in the denominators.

D.4.2.2 SNG-based concentric cylinders

Several numerical investigations, not included here, confirmed that resonances for the SNG-based structures were found to occur at those values of ρ_2 which were very accurately predicted by the resonance condition for the electrically small DPS- and DNG-based concentric cylinders. Thus, it is concluded that the resonance condition in (D.120) also applies to electrically small SNG-based structures, this being in line with the results for single SNG cylinders in Section D.4.1. This has also been confirmed in

Manuscript I (Appendix A) where it is shown that (D.120) can be satisfied if at least one of the parameters, μ_1 or μ_2, is negative, while the sign of the respective permittivities does not matter since these do not appear in (D.120).

APPENDIX E

3D CANONICAL CONFIGURATIONS - DETAILED CALCULATIONS

The detailed calculations of the near- and far-field quantities that form the background of Chapter 5 are presented in this appendix. The configuration of interest is comprised of a set of concentric spheres which are excited by an arbitrarily located and oriented electric Hertzian dipole (EHD), see Figure 5.1 in Chapter 5.

E.1 The EHD field

In order to solve the problem illustrated in Figure 5.1 in Chapter 5 it is convenient to employ the notion of spherical vector wave function (SVWF) expansions. This approach, inhere referred to as the SVWF approach, is first used to determine the field generated by the EHD, and subsequently to determine the unknown fields scattered by a given material structure. Several approaches and notations to this end exist, and the one used here is adopted from [118, Ch. 8][E.1]. In order to derive the appropriate SVWF expansion, use is made also of the field expressions that do not exploit SVWFs. Therefore, an account on the field generated by the EHD as obtained by such an approach, inhere referred to as the simple approach, is also included.

E.1.1 Introduction

An EHD, which is located at an arbitrary location (r_s, θ_s, ϕ_s) (with the the position vector $\vec{r}_s$), has the dipole moment $\vec{p}_s = \hat{p}_s p_s$, has the arbitrary orientation $\hat{p}_s$, and has the complex magnitude p_s [Am], is characterized by the volume current density [64, Ch. 4]

$$\vec{J}_{\text{EHD}}(\vec{r}, \vec{r}_s) = \vec{p}_s \; \delta(\vec{r} - \vec{r}_s) = \vec{p}_s \; \frac{\delta(r - r_s)\delta(\theta - \theta_s)\delta(\phi - \phi_s)}{r^2 \sin\theta} \; , \tag{E.1}$$

where the single three-dimensional (3D) Dirac delta function is replaced by three one-dimensional (1D) delta functions, see e.g., [117, p. 903] for relations between 1D and 3D delta functions. The observation coordinates are (r, θ, ϕ) with the associated position vector $\vec{r}$. The EHD constitutes a model of an electrically short dipole with p_s being the product of the current and the length of that dipole. It is furthermore assumed that the EHD is radiating in a source-free and simple medium characterized by a permittivity ε_{EHD}, permeability μ_{EHD}, and wave number k_{EHD}.

The volume current density in (E.1) gives rise to the vector magnetic potential, $\vec{A}_{\text{EHD}}$, given by [64, Ch. 4]

$$\vec{A}_{\text{EHD}}(\vec{r}) = \mu_{\text{EHD}} \int_V G(\vec{r}, \vec{r}_s) \; \vec{J}_{\text{EHD}}(\vec{r}, \vec{r}_s) \; dv' = \mu_{\text{EHD}} \; \vec{p}_s \; G(\vec{r}, \vec{r}_s) \; , \tag{E.2}$$

where the integration region V is the source region, and the quantity $G(\vec{r}, \vec{r}_s)$ is the 3D scalar Green's function given by

[E.1] It is understood that the various general relations associated with the SVWFs, which are included in the following are likewise found in [118].

$$G(\vec{r},\vec{r}_s) = \frac{e^{-jk_{\text{EHD}}|\vec{r}-\vec{r}_s|}}{4\pi|\vec{r}-\vec{r}_s|}. \tag{E.3}$$

E.1.2 Simple approach

When the EHD fields are expressed in terms of the SVWFs, their expressions contain expansion coefficients which must be determined in order to determine the fields. In order to determine these expansion coefficients, use is made of the general field expressions obtained on the basis of the Green's function given by (E.3). In a source-free and simple region, these expressions take the form [117, Ch. 6]

$$\begin{aligned}
\vec{E}_{\text{EHD}} &= \frac{1}{j\omega\varepsilon_{\text{EHD}}\mu_{\text{EHD}}}\,\nabla\times\nabla\times\vec{A}_{\text{EHD}} - \frac{1}{\varepsilon_{\text{EHD}}}\,\nabla\times\vec{F}_{\text{EHD}} \\
&= -j\omega\vec{A}_{\text{EHD}} + \frac{\nabla\left(\nabla\cdot\vec{A}_{\text{EHD}}\right)}{j\omega\varepsilon_{\text{EHD}}\mu_{\text{EHD}}} - \frac{1}{\varepsilon_{\text{EHD}}}\,\nabla\times\vec{F}_{\text{EHD}}\,, \qquad \text{(E.4a)} \\
\vec{H}_{\text{EHD}} &= \frac{1}{j\omega\varepsilon_{\text{EHD}}\mu_{\text{EHD}}}\,\nabla\times\nabla\times\vec{F}_{\text{EHD}} + \frac{1}{\mu_{\text{EHD}}}\,\nabla\times\vec{A}_{\text{EHD}} \\
&= -j\omega\vec{F}_{\text{EHD}} + \frac{\nabla\left(\nabla\cdot\vec{F}_{\text{EHD}}\right)}{j\omega\varepsilon_{\text{EHD}}\mu_{\text{EHD}}} + \frac{1}{\mu_{\text{EHD}}}\,\nabla\times\vec{A}_{\text{EHD}}\,, \qquad \text{(E.4b)}
\end{aligned}$$

for the electric, $\vec{E}_{\text{EHD}}$, and magnetic, $\vec{H}_{\text{EHD}}$, fields, respectively. In these expressions, the function $\vec{A}_{\text{EHD}}$ is the previously introduced vector magnetic potential, while $\vec{F}_{\text{EHD}}$ is the electric vector potential. These potentials are also commonly referred to as the magnetic and electric Lorentz potentials, respectively. In the present problem $\vec{F}_{\text{EHD}} = 0$, while $\vec{A}_{\text{EHD}}$ satisfies the homogeneous vector Helmholtz equation

$$\nabla^2\,\vec{A}_{\text{EHD}} + k_{\text{EHD}}^2\,\vec{A}_{\text{EHD}} = 0\,. \tag{E.5}$$

As a consequence, for the present problem, (E.4a) gives

$$\begin{aligned}
j\omega\varepsilon_{\text{EHD}}\mu_{\text{EHD}}\,\vec{E}_{\text{EHD}} &= k_{\text{EHD}}^2\vec{A}_{\text{EHD}} + \nabla\left(\nabla\cdot\vec{A}_{\text{EHD}}\right) \\
\frac{j\omega\varepsilon_{\text{EHD}}}{p_s}\,\vec{E}_{\text{EHD}} &= k_{\text{EHD}}^2 G(\vec{r},\vec{r}_s)\;\hat{p}_s + \nabla\,[\,\hat{p}_s\cdot\nabla G(\vec{r},\vec{r}_s)\,] \\
&= k_{\text{EHD}}^2 G(\vec{r},\vec{r}_s)\;\hat{p}_s - \nabla\,[\,\hat{p}_s\cdot\nabla_s G(\vec{r},\vec{r}_s)\,] \\
&= k_{\text{EHD}}^2 G(\vec{r},\vec{r}_s)\;\hat{p}_s - (\hat{p}_s\cdot\nabla)\,[\,\nabla_s\,G(\vec{r},\vec{r}_s)\,] \\
&= k_{\text{EHD}}^2 G(\vec{r},\vec{r}_s)\;\hat{p}_s + (\hat{p}_s\cdot\nabla_s)\,[\,\nabla_s\,G(\vec{r},\vec{r}_s)\,] \qquad \text{(E.6)}
\end{aligned}$$

while (E.4b) gives

$$\begin{aligned}
\mu_{\text{EHD}}\,\vec{H}_{\text{EHD}} &= \nabla\times\vec{A}_{\text{EHD}} \\
\frac{1}{p_s}\,\vec{H}_{\text{EHD}} &= \nabla\times[\,G(\vec{r},\vec{r}_s)\,\hat{p}_s\,] \;=\; -\nabla_s\times[\,G(\vec{r},\vec{r}_s)\,\hat{p}_s\,] \\
&= -\hat{p}_s\times\nabla G(\vec{r},\vec{r}_s) \\
&= \hat{p}_s\times\nabla_s G(\vec{r},\vec{r}_s)\,, \qquad \text{(E.7)}
\end{aligned}$$

where ∇_s denotes the gradient with respect to the source coordinates, i.e., the coordinates of the EHD. The derivative with respect to the source coordinates can be introduced because the Green's function depends only on the distance between the EHD and the observation point, so that $\nabla\, G(\vec{r},\vec{r}_s) = -\nabla_s\, G(\vec{r},\vec{r}_s)$. In the derivation of (E.6) and (E.7) the arbitrarily oriented unit vector $\hat{p}_s$ is assumed to be constant.

E.1.3 SVWF approach - derivation

E.1.3.1 General relations

In order to determine the field generated by the EHD in terms of the SVWFs, it is useful first to note that the space in which the EHD radiates is divided in two spherical regions. One region is defined for $r < r_s$ and the other for $r > r_s$. In both regions, proper expansions of the field must be established. These are given by

$$\left\{ \begin{array}{c} \vec{E}_{\text{EHD}}(r,\theta,\phi) \\ \vec{H}_{\text{EHD}}(r,\theta,\phi) \end{array} \right\} = \sum_{n=1}^{\infty} \sum_{m=-n}^{m=+n} \left[\frac{1}{j\omega\varepsilon_{\text{EHD}}\mu_{\text{EHD}}} \left\{ \begin{array}{c} a_{nm}^{(c)} \vec{N}_{nm}^{(\text{TM}),(c)} \\ b_{nm}^{(c)} \vec{N}_{nm}^{(\text{TE}),(c)} \end{array} \right\} + \left\{ \begin{array}{c} (-1/\varepsilon_{\text{EHD}})\, b_{nm}^{(c)}\, \vec{M}_{nm}^{(\text{TE}),(c)} \\ (1/\mu_{\text{EHD}})\, a_{nm}^{(c)}\, \vec{M}_{nm}^{(\text{TM}),\,(c)} \end{array} \right\} \right], \tag{E.8}$$

where the SVWFs are

$$\vec{M}_{nm}^{(\Gamma),(c)}(r,\theta,\phi) = \gamma_{\text{EHD}}\, w_n^{(c)}(k_{\text{EHD}} r)\, e^{jm\phi} \left[\frac{jm}{\sin\theta}\, P_n^{|m|}(\cos\theta)\, \hat{\theta} - \frac{d}{d\theta} P_n^{|m|}(\cos\theta)\, \hat{\phi} \right], \tag{E.9}$$

$$\begin{aligned} \vec{N}_{nm}^{(\Gamma),(c)}(r,\theta,\phi) = {} & \gamma_{\text{EHD}}\, \frac{n(n+1)}{r} w_n^{(c)}(k_{\text{EHD}} r)\, P_n^{|m|}(\cos\theta)\, e^{jm\phi}\, \hat{r} \\ & + \gamma_{\text{EHD}}\, \frac{1}{r}\, \frac{d}{dr} \left\{ r w_n^{(c)}(k_{\text{EHD}} r) \right\}\, \frac{d}{d\theta} P_n^{|m|}(\cos\theta)\, e^{jm\phi}\, \hat{\theta} \\ & + \gamma_{\text{EHD}}\, \frac{1}{r}\, \frac{d}{dr} \left\{ r w_n^{(c)}(k_{\text{EHD}} r) \right\}\, \frac{jm}{\sin\theta}\, P_n^{|m|}(\cos\theta)\, e^{jm\phi}\, \hat{\phi}\,, \end{aligned} \tag{E.10}$$

with $\gamma_{\text{EHD}} = \varepsilon_{\text{EHD}}$ for $\Gamma = \text{TE}$, and $\gamma_{\text{EHD}} = \mu_{\text{EHD}}$ for $\Gamma = \text{TM}$, and with $w_n^{(c)}(\cdot)$ being a specific spherical special function to be specified below. The quantities $a_{nm}^{(c)}$ and $b_{nm}^{(c)}$, respectively, are the unknown transverse magnetic (TM) and transverse electric (TE) expansion coefficients of the EHD field which are derived below[E.2].

For $r < r_s$ c is equal to 1, and for $r > r_s$ c is equal to 4. The function $w_n^{(1)}(\cdot) = j_n(\cdot)$, where $j_n(\cdot)$ is the spherical Bessel function of order n, is chosen to represent the field for $r < r_s$ due to its non-singular behaviour at the origin, while $w_n^{(4)}(\cdot) = h_n^{(2)}(\cdot)$, where $h_n^{(2)}(\cdot)$ is the spherical Hankel function of second kind and order n, is chosen for $r > r_s$ because it represents an outward propagating wave complying with the radiation condition. The function $P_n^{|m|}$ is the associated Legendre function of the first kind of degree n and order $|m|$.

In order to determine the unknown TM and TE expansion coefficients, $a_{nm}^{(c)}$ and $b_{nm}^{(c)}$, respectively, one

[E.2] The derivation of the coefficients $a_{nm}^{(c)}$ and $b_{nm}^{(c)}$ for $r > r_s$ is due to [124].

first notes that the SVWFs in (E.9) and (E.10) satisfy the orthogonality relations

$$\int_0^{2\pi} d\phi \int_0^{\pi} d\theta \, \sin\theta \; \vec{M}_{nm}^{(\Gamma)\,(c)} \cdot \vec{N}_{st}^{(\Gamma)\,(c)} = 0, \tag{E.11}$$

$$\int_0^{2\pi} d\phi \int_0^{\pi} d\theta \, \sin\theta \; \vec{M}_{nm}^{(\Gamma)\,(c)} \cdot \vec{M}_{s,-t}^{(\Gamma)\,(c)} = \delta_{ns}\,\delta_{mt}\,A_{nm}^{(\Gamma),(c)}, \tag{E.12}$$

$$\int_0^{2\pi} d\phi \int_0^{\pi} d\theta \, \sin\theta \; \vec{N}_{nm}^{(\Gamma)\,(c)} \cdot \vec{N}_{s,-t}^{(\Gamma)\,(c)} = \delta_{ns}\,\delta_{mt}\,B_{nm}^{(\Gamma),(c)}, \tag{E.13}$$

where δ_{XY} is the Kronecker delta, i.e., $\delta_{XY} = 1$ for $X = Y$ and $\delta_{XY} = 0$ for $X \neq Y$, and furthermore

$$A_{nm}^{(\Gamma),(c)} = \gamma_{\text{EHD}}^2 \, \frac{4\pi\, n(n+1)}{2n+1} \, \frac{(n+|m|)!}{(n-|m|)!} \, [w_n^{(c)}(k_{\text{EHD}} r)]^2 \,, \tag{E.14}$$

$$B_{nm}^{(\Gamma),(c)} = \gamma_{\text{EHD}}^2 \, \frac{4\pi\, n(n+1)}{2n+1} \, \frac{(n+|m|)!}{(n-|m|)!} \times \left\{ \frac{n(n+1)\,[w_n^{(c)}(k_{\text{EHD}} r)]^2}{r^2} + \left[\frac{1}{r} \, \frac{d}{dr} \left(r w_n^{(c)}(k_{\text{EHD}} r) \right) \right]^2 \right\} . \tag{E.15}$$

The unknown coefficients are therefore given by the relations

$$a_{nm}^{(c)} = \frac{1}{A_{nm}^{(\text{TM}),(c)}} \int_0^{2\pi} d\phi \int_0^{\pi} d\theta \, \sin\theta \; \vec{M}_{n,-m}^{(\text{TM}),(c)}(r,\theta,\phi) \cdot \left[\, \mu_{\text{EHD}} \, \vec{H}_{\text{EHD}} \, \right]$$
$$= \frac{1}{B_{nm}^{(\text{TM}),(c)}} \int_0^{2\pi} d\phi \int_0^{\pi} d\theta \, \sin\theta \; \vec{N}_{n,-m}^{(\text{TM}),(c)}(r,\theta,\phi) \cdot \left[\, j\omega\varepsilon_{\text{EHD}}\mu_{\text{EHD}} \, \vec{E}_{\text{EHD}} \, \right] , \tag{E.16}$$

$$b_{nm}^{(c)} = -\frac{1}{A_{nm}^{(\text{TE}),(c)}} \int_0^{2\pi} d\phi \int_0^{\pi} d\theta \, \sin\theta \; \vec{M}_{n,-m}^{(\text{TE}),(c)}(r,\theta,\phi) \cdot \left[\, \varepsilon_{\text{EHD}} \, \vec{E}_{\text{EHD}} \right]$$
$$= \frac{1}{B_{nm}^{(\text{TE}),(c)}} \int_0^{2\pi} d\phi \int_0^{\pi} d\theta \, \sin\theta \; \vec{N}_{n,-m}^{(\text{TE}),(c)}(r,\theta,\phi) \cdot \left[\, j\omega\varepsilon_{\text{EHD}}\mu_{\text{EHD}} \, \vec{H}_{\text{EHD}} \right] . \tag{E.17}$$

E.1.3.2 TM coefficients $a_{nm}^{(c)}$; $c = 4$

Using (E.7), evaluated for $r > r_s$, which is based on the simple approach, the TM coefficients, $a_{nm}^{(4)}$, of the field generated by the EHD can be acquired through the following rather involved, but well defined, manner

$$a_{nm}^{(4)} = \frac{1}{A_{nm}^{(\text{TM},(c)}} \int_0^{2\pi} d\phi \int_0^{\pi} d\theta \, \sin\theta \; \vec{M}_{n,-m}^{(\text{TM}),(4)}(r,\theta,\phi) \cdot \left[\, \mu_{\text{EHD}} \, \vec{H}_{\text{EHD}} \, \right]$$
$$= -\frac{\chi}{A_{nm}^{(\text{TM}),(4)}} \int_0^{2\pi} d\phi \int_0^{\pi} d\theta \, \sin\theta \; \vec{M}_{n,-m}^{(\text{TM}),(4)}(r,\theta,\phi) \cdot \left\{ \, \nabla_s \times \left[\, G^{(4)}(\vec{r},\vec{r}_s) \, \hat{p}_s \, \right] \right\}$$
$$= -\frac{\chi}{A_{nm}^{(\text{TM}),(4)}} \, \nabla_s \cdot \left\{ \hat{p}_s \times \int_0^{2\pi} d\phi \int_0^{\pi} d\theta \, \sin\theta \; \left[\, G^{(4)}(\vec{r},\vec{r}_s) \, \vec{M}_{n,-m}^{(\text{TM}),(4)}(r,\theta,\phi) \, \right] \right\}$$
$$= -\frac{\chi}{A_{nm}^{(\text{TM}),(4)}} \, \nabla_s \cdot \left[\, \hat{p}_s \times \vec{W}_{nm}^{(\text{TM}),(4)}(\vec{r},\vec{r}_s) \, \right] , \tag{E.18}$$

where the symbol $\chi = \mu_{\text{EHD}} p_s$ and the function

$$\vec{W}_{nm}^{(\text{TM}),(4)}(\vec{r},\vec{r}_s) = \int_0^{2\pi} d\phi \int_0^{\pi} d\theta \, \sin\theta \; G^{(4)}(\vec{r},\vec{r}_s) \, \vec{M}_{n,-m}^{(\text{TM}),(4)}(r,\theta,\phi) \,, \tag{E.19}$$

have been introduced. In the above relations $G^{(4)}(\vec{r},\vec{r}_s)$ is the Green's function evaluated for $r > r_s$.

It is clear that the crucial step in the determination of the coefficients $a_{nm}^{(4)}$ is the evaluation of the integral in (E.19). To this end it is useful to recall the addition theorem for the Green's function in terms of the spherical wave functions

$$G^{(4)}(\vec{r},\vec{r}_s) = -jk_{\text{EHD}}\,\frac{1}{4\pi}\,\sum_{\ell=0}^{\infty}(2\ell+1)\,\sum_{q=-\ell}^{\ell}\frac{(\ell-|q|)!}{(\ell+|q|)!}\,j_\ell(k_{\text{EHD}}r_s)\,h_\ell^{(2)}(k_{\text{EHD}}r) \times P_\ell^{|q|}(\cos\theta)\,P_\ell^{|q|}(\cos\theta_s)\;\;e^{jq(\phi-\phi_s)}\,. \quad \text{(E.20)}$$

As a consequence, $\vec{W}_{nm}^{(\text{TM}),(4)}$ in (E.19) becomes (in what follows the arguments of $\vec{M}_{n,-m}^{(\text{TM}),(4)}$ have been omitted for simplicity)

$$\begin{aligned}
\vec{W}_{nm}^{(\text{TM}),(4)}(\vec{r},\vec{r}_s) &= \int_0^{2\pi}d\phi\,\int_0^{\pi}d\theta\,\sin\theta\;G^{(4)}(\vec{r},\vec{r}_s)\,\vec{M}_{n,-m}^{(\text{TM}),(4)}\\
&= \int_0^{2\pi}d\phi\,\int_0^{\pi}d\theta\,\sin\theta\,\Big[-\frac{jk_{\text{EHD}}}{4\pi}\,\sum_{\ell=0}^{\infty}(2\ell+1)\,\sum_{q=-\ell}^{\ell}\frac{(\ell-|q|)!}{(\ell+|q|)!}\\
&\qquad\times P_\ell^{|q|}(\cos\theta)\,P_\ell^{|q|}(\cos\theta_s)j_\ell(k_{\text{EHD}}r_s)\,h_\ell^{(2)}(k_{\text{EHD}}r)\;\;e^{jq(\phi-\phi_s)}\;\;\vec{M}_{n,-m}^{(\text{TM}),(4)}\Big]\\
&= -\frac{jk_{\text{EHD}}}{4\pi}\,\sum_{\ell=0}^{\infty}(2\ell+1)\,\sum_{q=-\ell}^{\ell}\frac{(\ell-|q|)!}{(\ell+|q|)!}\;j_\ell(k_{\text{EHD}}r_s)\,h_\ell^{(2)}(k_{\text{EHD}}r)\\
&\quad\times\int_0^{2\pi}d\phi\,\int_0^{\pi}d\theta\,\sin\theta\;\Big[\,P_\ell^{|q|}(\cos\theta)\,P_\ell^{|q|}(\cos\theta_s)\;\;e^{jq(\phi-\phi_s)}\;\vec{M}_{n,-m}^{(\text{TM}),(4)}\Big]\,. \quad \text{(E.21)}
\end{aligned}$$

Since

$$\begin{aligned}
\vec{M}_{nm}^{(\text{TM}),(4)} &= \mu_{\text{EHD}}\,h_n^{(2)}(k_{\text{EHD}}r)\,e^{jm\phi}\,\Big[\frac{jm}{\sin\theta}\,P_n^{|m|}(\cos\theta)\,\hat{\theta}-d'_\theta P_n^{|m|}(\cos\theta)\,\hat{\phi}\Big]\\
&= \mu_{\text{EHD}}\,h_n^{(2)}(k_{\text{EHD}}r)\,e^{jm\phi}\,\Big\{\frac{jm}{\sin\theta}\,P_n^{|m|}(\cos\theta)\;[\,\cos\theta\cos\phi\,\hat{x}+\cos\theta\sin\phi\,\hat{y}-\sin\theta\,\hat{z}\,]\\
&\quad -d'_\theta P_n^{|m|}(\cos\theta)\;[\,-\sin\phi\,\hat{x}+\cos\phi\,\hat{y}\,]\Big\}\\
&= \mu_{\text{EHD}}\,h_n^{(2)}(k_{\text{EHD}}r)\,e^{jm\phi}\,\Big\{\Big[\frac{jm}{\sin\theta}\,P_n^{|m|}(\cos\theta)\;\cos\theta\cos\phi\;+d'_\theta P_n^{|m|}(\cos\theta)\;\sin\phi\Big]\,\hat{x}\\
&\qquad+\Big[\frac{jm}{\sin\theta}\,P_n^{|m|}(\cos\theta)\;\cos\theta\sin\phi\;-d'_\theta P_n^{|m|}(\cos\theta)\;\cos\phi\Big]\,\hat{y}\\
&\qquad-\Big[\frac{jm}{\sin\theta}\,P_n^{|m|}(\cos\theta)\Big]\;\sin\theta\,\hat{z}\Big\}\\
&= \mu_{\text{EHD}}\,h_n^{(2)}(k_{\text{EHD}}r)\,e^{jm\phi}\,\Big\{\Big[jm\;\cot\theta\,P_n^{|m|}(\cos\theta)\;\cos\phi+d'_\theta P_n^{|m|}(\cos\theta)\;\sin\phi\Big]\,\hat{x}\\
&\qquad+\Big[jm\;\cot\theta\,P_n^{|m|}(\cos\theta)\;\sin\phi-d'_\theta P_n^{|m|}(\cos\theta)\;\cos\phi\Big]\,\hat{y}\\
&\qquad-jm\,P_n^{|m|}(\cos\theta)\,\hat{z}\Big\}\,, \quad \text{(E.22)}
\end{aligned}$$

where the notation

$$d'_\theta P_n^{|m|}(\cos\theta) = \frac{dP_n^{|m|}(\cos\theta)}{d\theta}\,, \quad \text{(E.23)}$$

has been introduced, the relation (E.21) now reads

$$\left[\vec{W}_{nm}^{(\mathrm{TM}),(4)}(\vec{r},\vec{r}_s)\right]_x = -\mu_{\mathrm{EHD}}\,\frac{jk_{\mathrm{EHD}}}{4\pi}\,\sum_{\ell=0}^{\infty}(2\ell+1)\,\sum_{q=-\ell}^{\ell}\frac{(\ell-|q|)!}{(\ell+|q|)!}\,j_\ell(k_{\mathrm{EHD}}r_s)\,\left[\,h_\ell^{(2)}(k_{\mathrm{EHD}}r)\,\right]^2\,e^{-jq\phi_s}$$
$$\times P_\ell^{|q|}(\cos\theta_s)\,\int_0^{2\pi}d\phi\,\int_0^{\pi}d\theta\,\sin\theta\,\Big\{\,e^{j(q-m)\phi}\,P_\ell^{|q|}(\cos\theta)$$
$$\times\Big[\,-jm\,\cot\theta\,P_n^{|m|}(\cos\theta)\,\cos\phi\,+d'_\theta P_n^{|m|}(\cos\theta)\,\sin\phi\,\Big]\,\Big\}, \tag{E.24}$$

$$\left[\vec{W}_{nm}^{(\mathrm{TM}),(4)}(\vec{r},\vec{r}_s)\right]_y = -\mu_{\mathrm{EHD}}\,\frac{jk_{\mathrm{EHD}}}{4\pi}\,\sum_{\ell=0}^{\infty}(2\ell+1)\,\sum_{q=-\ell}^{\ell}\frac{(\ell-|q|)!}{(\ell+|q|)!}\,j_\ell(k_{\mathrm{EHD}}r_s)\,\left[\,h_\ell^{(2)}(k_{\mathrm{EHD}}r)\,\right]^2\,e^{-jq\phi_s}$$
$$\times P_\ell^{|q|}(\cos\theta_s)\,\int_0^{2\pi}d\phi\,\int_0^{\pi}d\theta\,\sin\theta\,\Big\{\,e^{j(q-m)\phi}\,P_\ell^{|q|}(\cos\theta)$$
$$\times\Big[\,-jm\,\cot\theta\,P_n^{|m|}(\cos\theta)\,\sin\phi\,-d'_\theta P_n^{|m|}(\cos\theta)\,\cos\phi\,\Big]\,\Big\}, \tag{E.25}$$

$$\left[\vec{W}_{nm}^{(\mathrm{TM}),(4)}(\vec{r},\vec{r}_s)\right]_z = -\mu_{\mathrm{EHD}}\,\frac{jk_{\mathrm{EHD}}}{4\pi}\,\sum_{\ell=0}^{\infty}(2\ell+1)\,\sum_{q=-\ell}^{\ell}\frac{(\ell-|q|)!}{(\ell+|q|)!}\,j_\ell(k_{\mathrm{EHD}}r_s)\,\left[\,h_\ell^{(2)}(k_{\mathrm{EHD}}r)\,\right]^2\,e^{-jq\phi_s}$$
$$\times P_\ell^{|q|}(\cos\theta_s)\,\int_0^{2\pi}d\phi\,\int_0^{\pi}d\theta\,\sin\theta\,\Big\{\,e^{j(q-m)\phi}\,P_\ell^{|q|}(\cos\theta)$$
$$\times\Big[\,+jm\,P_n^{|m|}(\cos\theta)\,\Big]\,\Big\}. \tag{E.26}$$

The x-component of $\vec{W}_{nm}^{(\mathrm{TM}),(4)}$, given by (E.24), can be rewritten as

$$\left[\vec{W}_{nm}^{(\mathrm{TM}),(4)}(\vec{r},\vec{r}_s)\right]_x = -\mu_{\mathrm{EHD}}\,\frac{jk_{\mathrm{EHD}}}{4\pi}\,\sum_{\ell=0}^{\infty}(2\ell+1)\,\sum_{q=-\ell}^{\ell}\frac{(\ell-|q|)!}{(\ell+|q|)!}\,j_\ell(k_{\mathrm{EHD}}r_s)\,\left[\,h_\ell^{(2)}(k_{\mathrm{EHD}}r)\,\right]^2\,e^{-jq\phi_s}$$
$$\times P_\ell^{|q|}(\cos\theta_s)\int_0^{2\pi}d\phi\,\int_0^{\pi}d\theta\,\sin\theta\,\Big\{\,P_\ell^{|q|}(\cos\theta)$$
$$\times\,\Big[\,-jm\,\cot\theta\,P_n^{|m|}(\cos\theta)\,e^{j(q-m)\phi}\,\cos\phi$$
$$+\,d'_\theta P_n^{|m|}(\cos\theta)\,e^{j(q-m)\phi}\,\sin\phi\,\Big]\,\Big\}. \tag{E.27}$$

Using the orthogonality relations

$$\int_0^{2\pi}d\phi\;e^{j(q-m)\phi}\,\cos\phi=\pi\,\left[\,\delta_{q,m+1}+\delta_{q,m-1}\,\right], \tag{E.28}$$

$$\int_0^{2\pi}d\phi\;e^{j(q-m)\phi}\,\sin\phi=j\pi\,\left[\,\delta_{q,m+1}-\delta_{q,m-1}\,\right], \tag{E.29}$$

relation (E.27) becomes

$$\left[\vec{W}_{nm}^{(\mathrm{TM}),(4)}(\vec{r},\vec{r}_s)\right]_x = -\mu_{\mathrm{EHD}}\,\frac{jk_{\mathrm{EHD}}}{4\pi}\,\pi\,\sum_{\ell=0}^{\infty}(2\ell+1)\,\sum_{q=-\ell}^{\ell}\frac{(\ell-|q|)!}{(\ell+|q|)!}\,j_\ell(k_{\mathrm{EHD}}r_s)\,\left[\,h_\ell^{(2)}(k_{\mathrm{EHD}}r)\,\right]^2\,e^{-jq\phi_s}$$

$$
\begin{aligned}
&\times P_\ell^{|q|}(\cos\theta_s) \\
&\qquad \times \int_0^\pi d\theta\ \sin\theta\ \Big\{ P_\ell^{|q|}(\cos\theta)\Big[-jm\ \cot\theta\, P_n^{|m|}(\cos\theta)\ (\delta_{q,m+1}+\delta_{q,m-1}) \\
&\qquad\qquad +j\ d'_\theta P_n^{|m|}(\cos\theta)\ (\delta_{q,m+1}-\delta_{q,m-1})\Big]\Big\} \\
&= \mu_{\text{EHD}}\ \frac{k_{\text{EHD}}}{4}\ \sum_{\ell=0}^{\infty}(2\ell+1)\ \frac{(\ell-|m+1|)!}{(\ell+|m+1|)!}\ j_\ell(k_{\text{EHD}}r_s)\ \Big[\, h_\ell^{(2)}(k_{\text{EHD}}r)\,\Big]^2\ e^{-j(m+1)\phi_s} \\
&\times P_\ell^{|m+1|}(\cos\theta_s) \\
&\qquad \times \int_0^\pi d\theta\ \ \sin\theta\ \ P_\ell^{|m+1|}(\cos\theta)\ \Big[\ d'_\theta P_n^{|m|}(\cos\theta) - m\ \cot\theta\, P_n^{|m|}(\cos\theta)\ \Big] \\
&- \mu_{\text{EHD}}\ \frac{k_{\text{EHD}}}{4}\sum_{\ell=0}^{\infty}(2\ell+1)\ \frac{(\ell-|m-1|)!}{(\ell+|m-1|)!}\ j_\ell(k_{\text{EHD}}r_s)\ \Big[\, h_\ell^{(2)}(k_{\text{EHD}}r)\,\Big]^2\ e^{-j(m-1)\phi_s} \\
&\times P_\ell^{|m-1|}(\cos\theta_s)\int_0^\pi d\theta\ \ \sin\theta\ \ P_\ell^{|m-1|}(\cos\theta) \\
&\qquad\qquad \times\Big[\ d'_\theta P_n^{|m|}(\cos\theta) + m\ \cot\theta\, P_n^{|m|}(\cos\theta)\ \Big]\,. \qquad \text{(E.30)}
\end{aligned}
$$

Making use of the relations [118, p. 493]

$$d'_\theta\ P_n^m(\cos\theta) - m\ \cot\theta\, P_n^m(\cos\theta) = P_n^{m+1}(\cos\theta)\,, \qquad \text{(E.31)}$$

$$d'_\theta\ P_n^m(\cos\theta) + m\ \cot\theta\, P_n^m(\cos\theta) = -(n+m)(n-m+1)\ P_n^{m-1}(\cos\theta)\,, \qquad \text{(E.32)}$$

when m is positive, relation (E.30) reduces to

$$
\begin{aligned}
\Big[\vec{W}_{nm}^{(\text{TM}),(4)}(\vec{r},\vec{r}_s)\Big]_x \quad &= \quad \mu_{\text{EHD}}\ \frac{k_{\text{EHD}}}{4}\sum_{\ell=0}^{\infty}(2\ell+1)\ \frac{(\ell-|m+1|)!}{(\ell+|m+1|)!}\ j_\ell(k_{\text{EHD}}r_s)\ \Big[\, h_\ell^{(2)}(k_{\text{EHD}}r)\,\Big]^2 \\
&\qquad \times e^{-j(m+1)\phi_s}\ P_\ell^{|m+1|}(\cos\theta_s)\int_0^\pi d\theta\ \ \sin\theta\ \ P_\ell^{|m+1|}(\cos\theta)\ P_n^{m+1}(\cos\theta) \\
&+ \quad \mu_{\text{EHD}}\ \frac{k_{\text{EHD}}}{4}\sum_{\ell=0}^{\infty}(2\ell+1)\ \frac{(\ell-|m-1|)!}{(\ell+|m-1|)!}\ j_\ell(k_{\text{EHD}}r_s)\ \Big[\, h_\ell^{(2)}(k_{\text{EHD}}r)\,\Big]^2 \\
&\qquad \times e^{-j(m-1)\phi_s}\ \ P_\ell^{|m-1|}(\cos\theta_s)\ \ (n+m)(n-m+1) \\
&\qquad\qquad \times\int_0^\pi d\theta\ \ \sin\theta\ \ P_\ell^{|m-1|}(\cos\theta)\ P_n^{m-1}(\cos\theta)\,. \qquad \text{(E.33)}
\end{aligned}
$$

Using the orthogonality relation [118, p. 489]

$$\int_0^\pi d\theta\ \ \sin\theta\ \ P_\ell^m(\cos\theta)\ P_n^m(\cos\theta) = \frac{2}{2n+1}\ \frac{(n+m)!}{(n-m)!}\ \delta_{\ell n}\,, \qquad \text{(E.34)}$$

in (E.33), one obtains

$$
\begin{aligned}
\Big[\vec{W}_{nm}^{(\text{TM}),(4)}(\vec{r},\vec{r}_s)\Big]_x \quad &= \quad \mu_{\text{EHD}}\ \frac{k_{\text{EHD}}}{4}\sum_{\ell=0}^{\infty}(2\ell+1)\ \frac{(\ell-|m+1|)!}{(\ell+|m+1|)!}\ j_\ell(k_{\text{EHD}}r_s)\ \Big[\, h_\ell^{(2)}(k_0 r)\,\Big]^2 \\
&\qquad \times e^{-j(m+1)\phi_s}\ P_\ell^{|m+1|}(\cos\theta_s)\ \frac{2}{2n+1}\ \frac{(n+|m+1|)!}{(n-|m+1|)!}\ \delta_{\ell n}
\end{aligned}
$$

$$
\begin{aligned}
&+ \quad \mu_{\text{EHD}}\,\frac{k_{\text{EHD}}}{4}\sum_{\ell=0}^{\infty}(2\ell+1)\,\frac{(\ell-|m-1|)!}{(\ell+|m-1|)!}\;j_\ell(k_{\text{EHD}}r_s)\left[\,h_\ell^{(2)}(k_{\text{EHD}}r)\,\right]^2 \\
&\qquad \times e^{-j(m-1)\phi_s}\;P_\ell^{|m-1|}(\cos\theta_s)\;\;(n+m)(n-m+1) \\
&\qquad\qquad \times\frac{2}{2n+1}\,\frac{(n+|m-1|)!}{(n-|m-1|)!}\,\delta_{\ell n} \\
&= \quad \mu_{\text{EHD}}\,\frac{k_{\text{EHD}}}{2}\;j_n(k_{\text{EHD}}r_s)\left[\,h_n^{(2)}(k_{\text{EHD}}r)\,\right]^2\;e^{-jm\phi_s} \\
&\times\Big[e^{-j\phi_s}P_n^{|m+1|}(\cos\theta_s)+e^{j\phi_s}P_n^{|m-1|}(\cos\theta_s)\;(n+m)(n-m+1)\Big]\,. \qquad \text{(E.35)}
\end{aligned}
$$

Similarly, it can be shown that

$$
\begin{aligned}
\Big[\vec{W}_{nm}^{(\text{TM}),(4)}(\vec{r},\vec{r}_s)\Big]_y \quad &= \quad -j\mu_{\text{EHD}}\,\frac{k_{\text{EHD}}}{2}\;j_n(k_{\text{EHD}}r_s)\left[\,h_n^{(2)}(k_{\text{EHD}}r)\,\right]^2\;e^{-jm\phi_s} \\
&\times\Big[-e^{-j\phi_s}P_n^{|m+1|}(\cos\theta_s)+e^{j\phi_s}P_n^{|m-1|}(\cos\theta_s)\;(n+m)(n-m+1)\Big]\,, \qquad \text{(E.36)}
\end{aligned}
$$

$$
\Big[\vec{W}_{nm}^{(\text{TM}),(4)}(\vec{r},\vec{r}_s)\Big]_z \quad = \quad \mu_{\text{EHD}}\;k_{\text{EHD}}\;j_n(k_{\text{EHD}}r_s)\left[\,h_n^{(2)}(k_{\text{EHD}}r)\,\right]^2\;e^{-jm\phi_s}\;m\;P_n^{|m|}(\cos\theta_s) \qquad \text{(E.37)}
$$

Thus,

$$
\begin{aligned}
\vec{W}_{nm}^{(\text{TM}),(4)}(\vec{r},\vec{r}_s) \quad &= \quad \mu_{\text{EHD}}\,\frac{k_{\text{EHD}}}{2}\;j_n(k_{\text{EHD}}r_s)\;\left[\,h_n^{(2)}(k_{\text{EHD}}r)\,\right]^2\;\;e^{-jm\phi_s} \\
&\times \quad \Big\{\Big[\;e^{-j\phi_s}\;P_n^{|m+1|}(\cos\theta_s)+e^{+j\phi_s}\;P_n^{|m-1|}(\cos\theta_s)\;\;(n+m)(n-m+1)\;\Big]\,\hat{x} \\
&\qquad -j\;\Big[\;-e^{-j\phi_s}\;P_n^{|m+1|}(\cos\theta_s)+e^{+j\phi_s}\;P_n^{|m-1|}(\cos\theta_s)\;\;(n+m)(n-m+1)\;\Big]\,\hat{y} \\
&\qquad +2\;m\;P_n^{|m|}(\cos\theta_s)\,\hat{z}\Big\}. \qquad \text{(E.38)}
\end{aligned}
$$

Next, the result in (E.38) can be written such that only an m dependence, and thus not the $m\pm1$ dependence, is retained by using (E.31) and (E.32) with the $\cos\theta_s$ argument. One readily finds that

$$
\begin{aligned}
\vec{W}_{nm}^{(\text{TM}),(4)}(\vec{r},\vec{r}_s) \quad &= \quad \mu_{\text{EHD}}\,\frac{k_{\text{EHD}}}{2}\;j_n(k_{\text{EHD}}r_s)\;\;\Big[\,h_n^{(2)}(k_{\text{EHD}}r)\,\Big]^2\;\;e^{-jm\phi_s} \\
&\times \quad \Big\{\Big\{\;e^{-j\phi_s}\;\Big[\;d'_{\theta=\theta_s}P_n^{|m|}(\cos\theta)-m\;\cot\theta_s\;P_n^{|m|}(\cos\theta_s)\;\Big] \\
&\qquad\quad -e^{j\phi_s}\;\Big[\;d'_{\theta=\theta_s}P_n^{|m|}(\cos\theta)+m\;\cot\theta_s\;P_n^{|m|}(\cos\theta_s)\;\Big]\;\Big\}\,\hat{x} \\
&- \quad j\Big\{-e^{-j\phi_s}\;\Big[\;d'_{\theta=\theta_s}P_n^{|m|}(\cos\theta)-m\;\cot\theta_s\;P_n^{|m|}(\cos\theta_s)\;\Big] \\
&\qquad\quad -e^{j\phi_s}\;\Big[\;d'_{\theta=\theta_s}P_n^{|m|}(\cos\theta)+m\;\cot\theta_s\;P_n^{|m|}(\cos\theta_s)\;\Big]\;\Big\}\,\hat{y} \\
&\qquad +2\;m\;P_n^{|m|}(\cos\theta_s)\,\hat{z}\;\Big\} \\
&= \quad \mu_{\text{EHD}}\,\frac{k_{\text{EHD}}}{2}\;j_n(k_{\text{EHD}}r_s)\;\;\Big[\,h_n^{(2)}(k_{\text{EHD}}r)\,\Big]^2\;\;e^{-jm\phi_s}
\end{aligned}
$$

$$
\begin{aligned}
\times \quad & \Big\{ -2j \Big[d'_{\theta=\theta_s} P_n^{|m|}(\cos\theta)\ \sin\phi_s\ - jm\ \cot\theta_s\ P_n^{|m|}(\cos\theta_s)\ \cos\phi_s \Big]\ \hat{x} \\
& +2j\ \Big[d'_{\theta=\theta_s} P_n^{|m|}(\cos\theta) \cos\phi_s + jm\ \cot\theta_s\ P_n^{|m|}(\cos\theta_s)\ \sin\phi_s \Big]\ \hat{y} \\
& +2\,m\ P_n^{|m|}(\cos\theta_s)\ \hat{z}\ \Big\} \\
= \quad & -j\mu_{\text{EHD}}\ k_{\text{EHD}}\ j_n(k_{\text{EHD}} r_s)\ \Big[h_n^{(2)}(k_{\text{EHD}} r) \Big]^2\ e^{-jm\phi_s} \\
\times \quad & \Big\{ \Big[d'_{\theta=\theta_s} P_n^{|m|}(\cos\theta)\ \sin\phi_s\ - jm\ \cot\theta_s\ P_n^{|m|}(\cos\theta_s)\ \cos\phi_s \Big]\ \hat{x} \\
& - \Big[d'_{\theta=\theta_s} P_n^{|m|}(\cos\theta) \cos\phi_s + jm\ \cot\theta_s\ P_n^{|m|}(\cos\theta_s)\ \sin\phi_s \Big]\ \hat{y} \\
& +j\,m\ P_n^{|m|}(\cos\theta_s)\ \hat{z}\ \Big\}\,, \qquad \text{(E.39)}
\end{aligned}
$$

where

$$
d'_{\theta=\theta_s} P_n^{|m|}(\cos\theta) \quad = \quad \frac{dP_n^{|m|}(\cos\theta)}{d\theta}\Big|_{\theta=\theta_s}\,. \qquad \text{(E.40)}
$$

It is useful to recall that

$$
\begin{aligned}
\vec{M}_{n,-m}^{(\text{TM}),(1)}(r_s,\theta_s,\phi_s) \quad = \quad & \mu_{\text{EHD}}\ j_n(k_{\text{EHD}} r_s)\ e^{-jm\phi_s} \\
\times \quad & \Big\{ \Big[d'_{\theta=\theta_s} P_n^{|m|}(\cos\theta)\ \sin\phi_s\ - jm\ \cot\theta_s\ P_n^{|m|}(\cos\theta_s)\ \cos\phi_s \Big]\ \hat{x} \\
& - \Big[d'_{\theta=\theta_s} P_n^{|m|}(\cos\theta) \cos\phi_s + jm\ \cot\theta_s\ P_n^{|m|}(\cos\theta_s)\ \sin\phi_s \Big]\ \hat{y} \\
& +j\,m\ P_n^{|m|}(\cos\theta_s)\ \hat{z}\ \Big\} \qquad \text{(E.41)}
\end{aligned}
$$

One thus finds that (E.39) reduces to

$$
\vec{W}_{nm}^{(\text{TM}),(4)}(\vec{r},\vec{r}_s) \quad = \quad -jk_{\text{EHD}}\ \Big[h_n^{(2)}(k_{\text{EHD}} r) \Big]^2\ \vec{M}_{n,-m}^{(\text{TM}),(1)}(r_s,\theta_s,\phi_s)\,. \qquad \text{(E.42)}
$$

From (E.14) it follows that

$$
A_{nm}^{(\text{TM}),(4)} \quad = \quad \mu_{\text{EHD}}^2\ \frac{4\pi\ n(n+1)}{2n+1}\ \frac{(n+|m|)!}{(n-|m|)!}\ [h_n^{(2)}(k_{\text{EHD}} r)]^2\,, \qquad \text{(E.43)}
$$

and the coefficients $a_{nm}^{(4)}$ thus become

$$
\begin{aligned}
a_{nm}^{(4)} \quad & = \quad -\frac{\chi}{A_{nm}^{(\text{TM}),(4)}}\ \nabla_s \cdot \Big[\hat{p}_s \times \vec{W}_{nm}^{(\text{TM}),(4)}(\vec{r},\vec{r}_s) \Big] \\
& = \quad \frac{jk_{\text{EHD}}\chi}{\mu_{\text{EHD}}^2} \left[\frac{2n+1}{4\pi\ n(n+1)} \frac{(n-|m|)!}{(n+|m|)!} \right] \Big\{ \nabla_s \cdot \Big[\hat{p}_s \times \vec{M}_{n,-m}^{(\text{TM}),(1)}(r_s,\theta_s,\phi_s) \Big] \Big\}\,. \qquad \text{(E.44)}
\end{aligned}
$$

Recalling the general relation

$$
\nabla \cdot \Big(\vec{A} \times \vec{B} \Big) \quad = \quad \vec{B} \cdot \Big(\nabla \times \vec{A} \Big) - \vec{A} \cdot \Big(\nabla \times \vec{B} \Big)\,, \qquad \text{(E.45)}
$$

one notes that

$$\begin{aligned}\nabla_s \cdot \Big(\hat{p}_s \times \vec{M}^{(\text{TM}),(1)}_{n,-m}(r_s,\theta_s,\phi_s) \Big) &= \vec{M}^{(\text{TM}),(1)}_{n,-m}(r_s,\theta_s,\phi_s) \cdot (\nabla_s \times \hat{p}_s) \\ &\quad -\hat{p}_s \cdot \Big(\nabla_s \times \vec{M}^{(\text{TM}),(1)}_{n,-m}(r_s,\theta_s,\phi_s) \Big) \\ &= -\hat{p}_s \cdot \vec{N}^{(\text{TM}),(1)}_{n,-m}(r_s,\theta_s,\phi_s) \,, \end{aligned} \tag{E.46}$$

and thus

$$\begin{aligned} a^{(4)}_{nm} &= -jk_{\text{EHD}} \frac{\chi}{4\pi} \frac{1}{\mu^2_{\text{EHD}}} \frac{2n+1}{n(n+1)} \frac{(n-|m|)!}{(n+|m|)!} \Big\{ \hat{p}_s \cdot \vec{N}^{(\text{TM}),(1),}_{n,-m}(r_s,\theta_s,\phi_s) \Big\} \\ &= -jk_{\text{EHD}} \frac{p_s}{4\pi} \frac{1}{\mu_{\text{EHD}}} \frac{2n+1}{n(n+1)} \frac{(n-|m|)!}{(n+|m|)!} \Big\{ \hat{p}_s \cdot \vec{N}^{(\text{TM}),(1),}_{n,-m}(r_s,\theta_s,\phi_s) \Big\} \,, \end{aligned} \tag{E.47}$$

since $\chi = \mu_{\text{EHD}}\, p_s$.

E.1.3.3 TE coefficients $b^{(c)}_{nm}$; $c = 4$

Next, the TE coefficients $b^{(4)}_{nm}$ are determined. For clarity, the general relation (E.17) is rewritten. This relation reads

$$b^{(4)}_{nm} = -\frac{1}{A^{(\text{TE}),(4)}_{nm}} \int_0^{2\pi} d\phi \int_0^{\pi} d\theta \, \sin\theta \; \vec{M}^{(\text{TE}),(4)}_{n,-m} \cdot \Big[\varepsilon_{\text{EHD}} \, \vec{E}_{\text{EHD}} \Big] \,. \tag{E.48}$$

where

$$A^{(\text{TE}),(4)}_{nm} = \varepsilon^2_{\text{EHD}} \frac{4\pi\, n(n+1)}{2n+1} \frac{(n+|m|)!}{(n-|m|)!} \Big[h^{(2)}_n(k_{\text{EHD}} r) \Big]^2 \,, \tag{E.49}$$

as obtained from (E.14). Substituting the Green's function based result given by (E.6) into (E.48), one obtains

$$\begin{aligned} b^{(4)}_{nm} &= -\frac{p_s}{j\omega A^{(\text{TE}),(4)}_{nm}} \int_0^{2\pi} d\phi \int_0^{\pi} d\theta \, \sin\theta \; \vec{M}^{(\text{TE}),(4)}_{n,-m} \\ &\qquad \cdot \Big[k^2_{\text{EHD}} G^{(4)}(\vec{r},\vec{r}_s) \; \hat{p}_s + (\hat{p}_s \cdot \nabla_s) \; \nabla_s \, G^{(4)}(\vec{r},\vec{r}_s) \Big] \\ &= -\frac{p_s}{j\omega A^{(\text{TE}),(4)}_{nm}} \, k^2_{\text{EHD}} \, \hat{p}_s \cdot \underbrace{\int_0^{2\pi} d\phi \int_0^{\pi} d\theta \, \sin\theta \; G^{(4)}(\vec{r},\vec{r}_s) \; \vec{M}^{(\text{TE}),(4)}_{n,-m}}_{\vec{W}^{(\text{TE}),(4)}_{nm}} \\ &\quad -\frac{p_s}{j\omega A^{(\text{TE}),(4)}_{nm}} \int_0^{2\pi} d\phi \int_0^{\pi} d\theta \, \sin\theta \Big\{ \vec{M}^{(\text{TE}),(4)}_{n,-m} \cdot \Big[(\hat{p}_s \cdot \nabla_s) \, \nabla_s G^{(4)}(\vec{r},\vec{r}_s) \Big] \Big\} \,. \end{aligned} \tag{E.50}$$

Using (E.42) with the superscript TM replaced by TE, the term $\vec{W}^{(\text{TE}),(4)}_{nm}$ in (E.50) can be straightforwardly evaluated. Furthermore, rearranging the second term in (E.50), the following expressions are obtained

$$b^{(4)}_{nm} = -\frac{p_s}{j\omega A^{(\text{TE}),(4)}_{nm}} \, k^2_{\text{EHD}} \, \hat{p}_s \cdot \Big[-jk_{\text{EHD}} \Big[\, h^{(2)}_n(k_{\text{EHD}} r) \, \Big]^2 \; \vec{M}^{(\text{TE}),(1)}_{n,-m}(r_s,\theta_s,\phi_s) \Big]$$

$$
\begin{aligned}
& -\frac{p_s}{j\omega A_{nm}^{(\mathrm{TE}),(4)}} \int_0^{2\pi} d\phi \int_0^{\pi} d\theta \, \sin\theta \;\; (\hat{p}_s \cdot \nabla_s) \left\{ \vec{M}_{n,-m}^{(\mathrm{TE}),(4)} \cdot \nabla_s \, G(\vec{r},\vec{r}_s) \right\} \\
= \;\; & -\frac{p_s}{j\omega A_{nm}^{(\mathrm{TE}),(4)}} \, k_{\mathrm{EHD}}^2 \, \hat{p}_s \cdot \left[-jk_{\mathrm{EHD}} \left[h_n^{(2)}(k_{\mathrm{EHD}} r) \right]^2 \vec{M}_{n,-m}^{(\mathrm{TE}),(1)}(r_s,\theta_s,\phi_s) \right] \\
& -\frac{p_s}{j\omega A_{nm}^{(\mathrm{TE}),(4)}} \int_0^{2\pi} d\phi \int_0^{\pi} d\theta \, \sin\theta \;\; (\hat{p}_s \cdot \nabla_s) \left\{ \nabla_s \cdot \left[G^{(4)}(\vec{r},\vec{r}_s) \, \vec{M}_{n,-m}^{(\mathrm{TE}),(4)} \right] \right\} \\
= \;\; & -\frac{p_s}{j\omega A_{nm}^{(\mathrm{TE}),(4)}} \, k_{\mathrm{EHD}}^2 \, \hat{p}_s \cdot \left[-jk_{\mathrm{EHD}} \left[h_n^{(2)}(k_{\mathrm{EHD}} r) \right]^2 \vec{M}_{n,-m}^{(\mathrm{TE}),(1)}(r_s,\theta_s,\phi_s) \right] \\
& -\frac{p_s}{j\omega A_{nm}^{(\mathrm{TE}),(4)}} \, (\hat{p}_s \cdot \nabla_s) \left\{ \nabla_s \cdot \left[\underbrace{\int_0^{2\pi} d\phi \int_0^{\pi} d\theta \, \sin\theta \; G^{(4)}(\vec{r},\vec{r}_s) \, \vec{M}_{n,-m}^{(\mathrm{TE}),(4)}}_{\vec{W}_{nm}^{(\mathrm{TE}),(4)}} \right] \right\} \\
= \;\; & -\frac{p_s}{j\omega A_{nm}^{(\mathrm{TE}),(4)}} \, k_{\mathrm{EHD}}^2 \, \hat{p}_s \cdot \left[-jk_{\mathrm{EHD}} \left[h_n^{(2)}(k_{\mathrm{EHD}} r) \right]^2 \vec{M}_{n,-m}^{(\mathrm{TE}),(1)}(r_s,\theta_s,\phi_s) \right] \\
& -\frac{p_s}{j\omega A_{nm}^{(\mathrm{TE}),(4)}} \, (\hat{p}_s \cdot \nabla_s) \left\{ \nabla_s \cdot \left[-jk_{\mathrm{EHD}} \left[h_n^{(2)}(k_{\mathrm{EHD}} r) \right]^2 \vec{M}_{n,-m}^{(\mathrm{TE}),(1)}(r_s,\theta_s,\phi_s) \right] \right\} \\
= \;\; & -\frac{p_s}{j\omega A_{nm}^{(\mathrm{TE}),(4)}} \, k_{\mathrm{EHD}}^2 \, \hat{p}_s \cdot \left[-jk_{\mathrm{EHD}} \left[h_n^{(2)}(k_{\mathrm{EHD}} r) \right]^2 \vec{M}_{n,-m}^{(\mathrm{TE}),(1)}(r_s,\theta_s,\phi_s) \right] , \qquad \text{(E.51)}
\end{aligned}
$$

since $\vec{M}_{nm}^{(\mathrm{TE}),(1)}$ is, of course, divergence-free. Thus,

$$
b_{nm}^{(4)} = \frac{k_{\mathrm{EHD}}^3}{\omega} \, \frac{p_s}{4\pi} \, \frac{1}{\varepsilon_{\mathrm{EHD}}^2} \, \frac{2n+1}{n(n+1)} \, \frac{(n-|m|)!}{(n+|m|)!} \left\{ \hat{p}_s \cdot \vec{M}_{n,-m}^{(\mathrm{TE}),(1)}(r_s,\theta_s,\phi_s) \right\} , \qquad \text{(E.52)}
$$

which is the final result.

E.1.3.4 The TM and TE coefficients $a_{nm}^{(c)}$ and $b_{nm}^{(c)}$; $c = 1$

In regards to the calculation of the corresponding coefficients for $r < r_s$, it follows the one outlined above. The main difference is that for $c = 1$, the addition theorem of the Green's function in terms of the spherical wave functions is

$$
\begin{aligned}
G^{(1)}(\vec{r},\vec{r}_s) = \; & -jk_{\mathrm{EHD}} \, \frac{1}{4\pi} \sum_{\ell=0}^{\infty} (2\ell+1) \sum_{q=-\ell}^{\ell} \frac{(\ell-|q|)!}{(\ell+|q|)!} \, j_\ell(k_{\mathrm{EHD}} r) \, h_\ell^{(2)}(k_{\mathrm{EHD}} r_s) \\
& \times P_\ell^{|q|}(\cos\theta) \, P_\ell^{|q|}(\cos\theta_s) \;\; e^{jq(\phi-\phi_s)} \, . \qquad \text{(E.53)}
\end{aligned}
$$

One then has to evaluate the integral

$$
\vec{W}_{nm}^{(\Gamma),(1)}(\vec{r},\vec{r}_s) = \int_0^{2\pi} d\phi \int_0^{\pi} d\theta \, \sin\theta \; G^{(1)}(\vec{r},\vec{r}_s) \, \vec{M}_{n,-m}^{(\Gamma),(1)}(r,\theta,\phi) \, , \qquad \text{(E.54)}
$$

where $\Gamma = \mathrm{TM}$ in the determination of $a_{nm}^{(1)}$, and $\Gamma = \mathrm{TE}$ in the determination of $b_{nm}^{(1)}$. Moreover, it is important to note here that from (E.14) one has the terms

$$
A_{nm}^{(\Gamma),(1)} = \gamma_{\mathrm{EHD}}^2 \, \frac{4\pi \, n(n+1)}{2n+1} \, \frac{(n+|m|)!}{(n-|m|)!} \left[j_n(k_{\mathrm{EHD}} r) \right]^2 , \qquad \text{(E.55)}
$$

which also is used in the expressions for the coefficients. In (E.55), $\gamma_{\text{EHD}} = \varepsilon_{\text{EHD}}$ in the determination of $a_{nm}^{(1)}$, while $\gamma_{\text{EHD}} = \mu_{\text{EHD}}$ in the determination of $b_{nm}^{(1)}$. This is in line with the use of either the TM or TE based SVWFs.

With these slight changes relative to the calculations included in Section E.1.3.2, it is first found that

$$\vec{W}_{nm}^{(\Gamma),(1)}(\vec{r},\vec{r}_s) \;=\; -jk_{\text{EHD}}\,\left[\,j_n(k_{\text{EHD}}r)\,\right]^2\;\vec{M}_{n,-m}^{(\Gamma),(4)}(r_s,\theta_s,\phi_s)\,. \tag{E.56}$$

and thus that

$$\begin{aligned} a_{nm}^{(1)} &= -jk_{\text{EHD}}\frac{p_s}{4\pi}\,\frac{1}{\mu_{\text{EHD}}}\,\frac{2n+1}{n(n+1)}\,\frac{(n-|m|)!}{(n+|m|)!}\,\left\{\hat{p}_s\cdot\vec{N}_{n,-m}^{(\text{TM}),(4),}(r_s,\theta_s,\phi_s)\right\}\,, \\ b_{nm}^{(1)} &= \frac{k_{\text{EHD}}^3}{\omega}\,\frac{p_s}{4\pi}\,\frac{1}{\varepsilon_{\text{EHD}}^2}\,\frac{2n+1}{n(n+1)}\,\frac{(n-|m|)!}{(n+|m|)!}\,\left\{\hat{p}_s\cdot\vec{M}_{n,-m}^{(\text{TE}),(4)}(r_s,\theta_s,\phi_s)\,\right\}\,. \end{aligned} \tag{E.57}$$

As expected, the coefficients for $r < r_s$ can be obtained from those for $r > r_s$, and vice versa, simply by using the proper radial functions, i.e., by using the proper value of c.

This concludes the derivation of the TE and TM expansion coefficients of the electromagnetic field generated by the the arbitrarily oriented and located EHD.

E.1.4 SVWF approach - summary

The electric and magnetic fields generated by the EHD in an infinite medium, characterized by ε_{EHD}, μ_{EHD} and k_{EHD}, can thus be expressed as an expansion of spherical TM and TE waves

$$\begin{aligned} \left\{\begin{array}{c}\vec{E}_{\text{EHD}}(r,\theta,\phi)\\ \vec{H}_{\text{EHD}}(r,\theta,\phi)\end{array}\right\} = \sum_{n=1}^{\infty}\sum_{m=-n}^{m=+n}\Bigg[\frac{1}{j\omega\varepsilon_{\text{EHD}}\mu_{\text{EHD}}}\left\{\begin{array}{c}a_{nm}^{(c)}\vec{N}_{nm}^{(\text{TM}),(c)}\\ b_{nm}^{(c)}\vec{N}_{nm}^{(\text{TE}),(c)}\end{array}\right\} \\ +\left\{\begin{array}{c}(-1/\varepsilon_{\text{EHD}})\,b_{nm}^{(c)}\,\vec{M}_{nm}^{(\text{TE}),(c)}\\ (1/\mu_{\text{EHD}})\,a_{nm}^{(c)}\,\vec{M}_{nm}^{(\text{TM}),\,(c)}\end{array}\right\}\Bigg]\,, \end{aligned} \tag{E.58}$$

where the SVWFs are

$$\vec{M}_{nm}^{(\Gamma),(c)}(r,\theta,\phi) = \gamma_{\text{EHD}}\,w_n^{(c)}(k_{\text{EHD}}r)\,e^{jm\phi}\left[\,\frac{jm}{\sin\theta}\,P_n^{|m|}(\cos\theta)\,\hat{\theta} - \frac{d}{d\theta}P_n^{|m|}(\cos\theta)\,\hat{\phi}\,\right]\,, \tag{E.59}$$

$$\begin{aligned} \vec{N}_{nm}^{(\Gamma),(c)}(r,\theta,\phi) = \gamma_{\text{EHD}}\,&\frac{n(n+1)}{r}w_n^{(c)}(k_{\text{EHD}}r)\,P_n^{|m|}(\cos\theta)\,e^{jm\phi}\,\hat{r} \\ &+\gamma_{\text{EHD}}\,\frac{1}{r}\,\frac{d}{dr}\left\{rw_n^{(c)}(k_{\text{EHD}}r)\right\}\,\frac{d}{d\theta}P_n^{|m|}(\cos\theta)\,e^{jm\phi}\,\hat{\theta} \\ &+\gamma_{\text{EHD}}\,\frac{1}{r}\,\frac{d}{dr}\left\{rw_n^{(c)}(k_{\text{EHD}}r)\right\}\,\frac{jm}{\sin\theta}\,P_n^{|m|}(\cos\theta)\,e^{jm\phi}\,\hat{\phi}\,, \end{aligned} \tag{E.60}$$

with $\gamma_{\text{EHD}} = \varepsilon_{\text{EHD}}$ for $\Gamma = \text{TE}$, and $\gamma_{\text{EHD}} = \mu_{\text{EHD}}$ for $\Gamma = \text{TM}$, and with $w_n^{(c)}(\cdot) = j_n(\cdot)$ for $c = 1$ (which applies for $r < r_s$), and $w_n^{(c)} = h_n^{(2)}(\cdot)$ for $c = 4$ (which applies for $r > r_s$). The quantities $a_{nm}^{(c)}$ and $b_{nm}^{(c)}$, respectively, are given by

$$a_{nm}^{(c)} = -jk_{\text{EHD}}\frac{p_s}{4\pi}\,\frac{1}{\mu_{\text{EHD}}}\,\frac{2n+1}{n(n+1)}\,\frac{(n-|m|)!}{(n+|m|)!}\left[\hat{p}_s\cdot\vec{N}_{n,-m}^{(\text{TM}),(5-c)}(r_s,\theta_s,\phi_s)\right]\,, \tag{E.61a}$$

$$b_{nm}^{(c)} = \frac{k_{\text{EHD}}^3}{\omega}\,\frac{p_s}{4\pi}\,\frac{1}{\varepsilon_{\text{EHD}}^2}\,\frac{2n+1}{n(n+1)}\,\frac{(n-|m|)!}{(n+|m|)!}\left[\hat{p}_s\cdot\vec{M}_{n,-m}^{(\text{TE}),(5-c)}(r_s,\theta_s,\phi_s)\right]\,. \tag{E.61b}$$

Before proceeding with the determination of the unknown fields in the three regions of interest it is worth remarking that the SVWFs in (E.59) and (E.60) are related to the multipole TE and TM Debye potentials, denoted by $\Phi_{nm}^{(c)}$ and $\Psi_{nm}^{(c)}$, in the following simple manner

$$\vec{M}_{nm}^{(\mathrm{TE}),(c)} = \nabla \times \Phi_{nm}^{(c)} \,, \tag{E.62a}$$

$$\vec{N}_{nm}^{(\mathrm{TE}),(c)} = \nabla \times \vec{M}_{nm}^{(\mathrm{TE}),(c)} \,. \tag{E.62b}$$

and

$$\vec{M}_{nm}^{(\mathrm{TM}),(c)} = \nabla \times \Psi_{nm}^{(c)} \,, \tag{E.62c}$$

$$\vec{N}_{nm}^{(\mathrm{TM}),(c)} = \nabla \times \vec{M}_{nm}^{(\mathrm{TM}),(c)} \,, \tag{E.62d}$$

where

$$\Phi_{nm}^{(c)} = \varepsilon_{\mathrm{EHD}}\, w_n^{(c)}(k_{\mathrm{EHD}} r)\, P_n^{|m|}(\cos\theta)\, e^{jm\phi} \,, \tag{E.63a}$$

$$\Psi_{nm}^{(c)} = \mu_{\mathrm{EHD}}\, w_n^{(c)}(k_{\mathrm{EHD}} r)\, P_n^{|m|}(\cos\theta)\, e^{jm\phi} \,, \tag{E.63b}$$

from which the total TE and TM Debye potentials are constructed, respectively, as

$$\Phi_{\mathrm{EHD}}^{(c)} = \sum_{n=1}^{\infty} \sum_{m=-n}^{m=+n} b_{nm}^{(c)}\, \Phi_{nm}^{(c)} \,, \tag{E.64a}$$

$$\Psi_{\mathrm{EHD}}^{(c)} = \sum_{n=1}^{\infty} \sum_{m=-n}^{m=+n} a_{nm}^{(c)}\, \Psi_{nm}^{(c)} \,. \tag{E.64b}$$

The expressions for the total TE and TM Debye potentials in (E.64a) and (E.64b), as well as those associated with the unknown fields in the three regions, allow an easy process to determine the unknown field expansion coefficients as will be demonstrated in Section E.2.

E.1.5 SVWF approach - convergence problem

In this section, some issues related to the convergence of the expressions for the electric and magnetic fields generated by the EHD, as expressed in terms of SVWFs, are discussed. These expressions have been derived in Section E.1.3 and summarized in Section E.1.4, see (E.58). Since the summations employed in (E.58) are infinite, the resulting electric and magnetic fields are exact. However, as with the corresponding cylindrical case also investigated in this work, the infinite summations must be truncated to some finite truncation limit N_{max}, which in the case of (E.58) means that $n = 1, 2, \ldots, N_{max}$, and $m = -n, \ldots, n$. The truncation limit N_{max} must be chosen such as to ensure the convergence of the employed expansions, and it is therefore of interest to examine the behaviour of the resulting expressions with respect to N_{max}. To this end, the SVWF-based results are compared the field expressions based on the simple approach, which does not use SVWFs, see Section E.1.2.

The expressions for the electric and magnetic fields radiated by an arbitrarily located and oriented EHD, as obtained by the simple approach, are given by (E.6) and (E.7), respectively. Performing the indicated differentiation in these expressions, it can be shown that the electric and magnetic fields read [125]

$$\begin{aligned}\vec{E}_{\mathrm{EHD}} = \frac{-j\eta_{\mathrm{EHD}}}{k_{\mathrm{EHD}}}\, G(\vec{r},\vec{r}_s) \\ \cdot\Big[\left(-k_{\mathrm{EHD}}^2 + 3jk_{\mathrm{EHD}}|\vec{r}-\vec{r}_s|^{-1} + 3|\vec{r}-\vec{r}_s|^{-2}\right) \vec{p}_s \cdot \frac{\vec{r}-\vec{r}_s}{|\vec{r}-\vec{r}_s|}\, \frac{\vec{r}-\vec{r}_s}{|\vec{r}-\vec{r}_s|} \\ + \left(k_{\mathrm{EHD}}^2 - jk_{\mathrm{EHD}}|\vec{r}-\vec{r}_s|^{-1} - |\vec{r}-\vec{r}_s|^{-2}\right) \vec{p}_s \Big] \,,\end{aligned} \tag{E.65a}$$

$$\vec{H}_{\mathrm{EHD}} = G(\vec{r},\vec{r}_s)\, \left(jk_{\mathrm{EHD}} + |\vec{r}-\vec{r}_s|^{-1}\right) \vec{p}_s \times \frac{\vec{r}-\vec{r}_s}{|\vec{r}-\vec{r}_s|} \,, \tag{E.65b}$$

where η_{EHD} is the intrinsic impedance of the material in which the EHD is radiating. The expressions in (E.65a) and (E.65b) are the exact electric and magnetic fields, respectively, for all observation points, except for the source point itself, where they are not defined.

For the purpose of comparing the electric and magnetic fields based on the SVWF approach given by (E.58) with (E.65a) and (E.65b), the EHD is taken to be z-directed, i.e., $\hat{p}_s = \hat{z}$, and located on the positive x-axis at a distance of 5 mm from the origin, i.e., it has the coordinates $(r_s = 5 \text{ mm}, \theta_s = 90^o, \phi_s = 0^o)$. The magnitude of the dipole moment is $p_s = 0.01$ Am. Throughout the following comparisons, the frequency of operation is $f_0 = 300$ MHz, and the electric and magnetic fields are shown as a function of $r \in [0, 4r_s]$, for the angular observation coordinates equal to $\theta = \phi = 45^o$.

Figures E.1, E.2, and E.3 show, respectively, the amplitude of the r-, θ-, and ϕ-components of the electric and magnetic fields, as obtained by the simple approach as well as the SVWF approach with $N_{max} = 10,\ 20$, and 40, for the configuration outlined above.

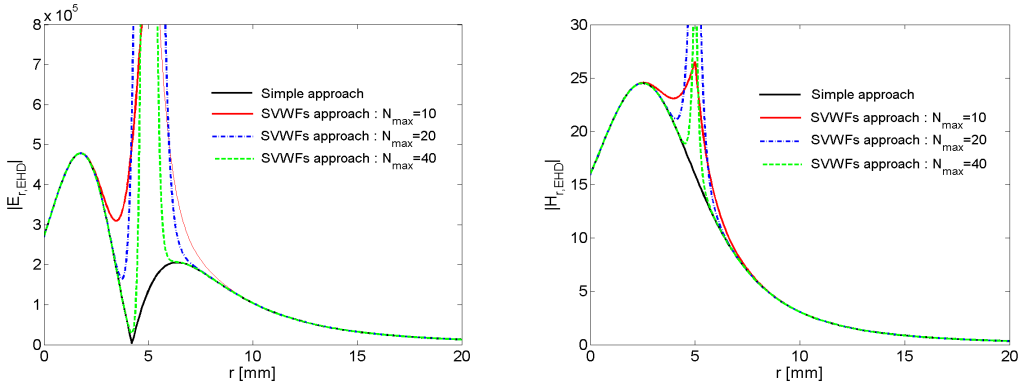

(a) (b)

Figure E.1: *The amplitude of the r-component of the electric (a) and magnetic (b) fields as a function of $r \in [0, 4r_s]$, with $r_s = 5$ mm, for $\theta = \phi = 45^o$. The results for both the simple approach, and the SVWF approach with $N_{max} = 10,\ 20$, and 40 modes, are shown.*

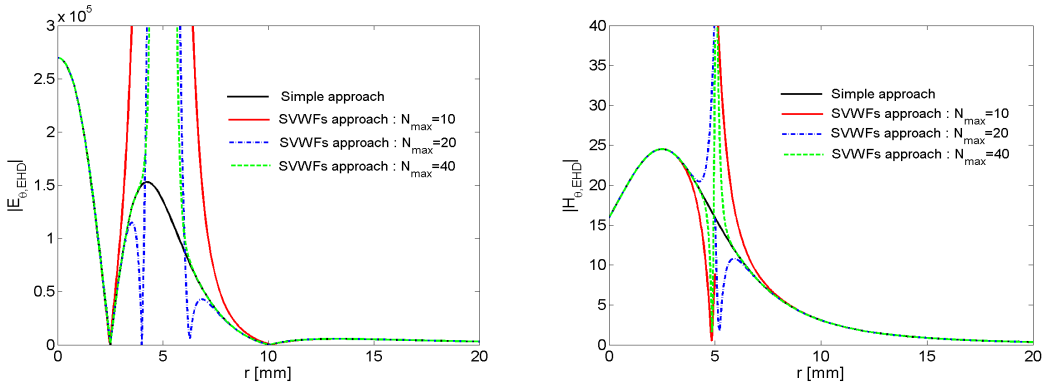

(a) (b)

Figure E.2: *The amplitude of the θ-component of the electric (a) and magnetic (b) fields as a function of $r \in [0, 4r_s]$, with $r_s = 5$ mm, for $\theta = \phi = 45^o$. The results for both the simple approach, and the SVWF approach with $N_{max} = 10,\ 20$, and 40 modes, are shown.*

The general characteristics of these results are the following. The simple approach, which does not use the SVWFs, gives, of course, in all cases a well-behaved, exact result for all r. As to the SVWF approach, it is found that the respective fields for $r < 5$ mm and $r > 5$ mm are in excellent agreement with the simple approach provided that the observation point, r, is sufficiently far away from $r = 5$ mm.

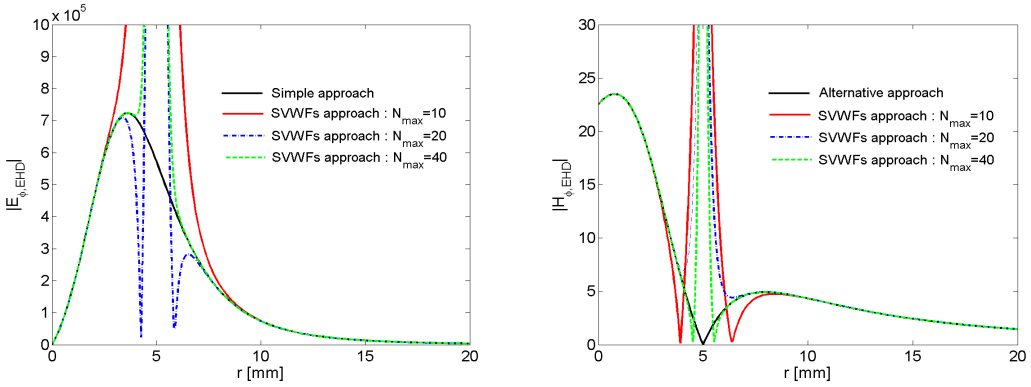

(a) (b)

Figure E.3: *The amplitude of the ϕ-component of the electric (a) and magnetic (b) fields as a function of $r \in [0, 4r_s]$, with $r_s = 5$ mm, for $\theta = \phi = 45^o$. The results for both the simple approach, and the SVWF approach with $N_{max} = 10,\ 20$, and 40 modes, are shown.*

In the vicinity of this point, the SVWF-based results deviate from the exact results. In fact, although not shown inhere, excellent agreement between the two approaches is found for all observation points which are sufficiently away from the surface of the sphere with radius $r = r_s = 5$ mm, while the opposite is true for the observation points near this surface. The radius of this sphere is, as noted above, equal to the radial distance to the EHD, i.e., its location. The sphere with this radius is referred to as the minimum sphere [126]. It is thus concluded that the SVWF approach yields excellent results for observation points sufficiently away from the surface of the minimum sphere (SMS), while less accurate results are obtained for observation points in the vicinity of the SMS[E.3] [126].

However, as the results in Figures E.1 to E.3 show, the region around $r = 5$ mm, in which the deviation is found between the two approaches, is narrowed as the truncation limit, N_{max}, in the SVWF approach increases from 10 to 40. In other words, the accuracy of the SVWF approach in the critical region around the SMS increases as the higher-order modes are included. It is moreover clear that many modes are needed to obtain a good representation of the EHD field near the SMS than away from it. Thus, the observed differences are of a numerical, rather than an analytical nature of the derived expressions. The SVWF approach indeed calculates the contribution in the separate modes correctly, and the correct representation of the EHD field is thus obtained for all observation points, except the source point itself, provided that the employed summations are convergent (which surely is the case in the limit of infinitely many modes, i.e., for $N_{max} = \infty$).

These remarks thus imply that the SVWF-based expressions in (E.58) can be used in the solution of the scattering problem depicted in Figure 5.1 in Chapter 5, i.e., for the determination of the unknown fields, see also Section E.2, which are due to a given material structure. However, the observed numerical deviation between the SVWF-based approach and the exact results, which means that the former gives a non-smooth and incorrect EHD field behaviour close to the SMS, obviously renders the SVWF-based expressions impractical for e.g., plotting purposes of the EHD field[E.4]. Moreover, it is expected that the unknown fields due to a give material structure will be slightly inaccurate if the EHD is located close to the SMS, since in that case a slightly inaccurate EHD field will illuminate the material structure in the first place. However, the location of the EHD, as well as the deviation of the SVWF-based results from the exact ones which is due to the lack of higher-order modes, does not have any effect on e.g., total power and directivity determined in Section E.3, since only the lower-order modes contribute in the far field [126].

In consequence of these findings, and in order to obtain a smooth and correct field behaviour across

[E.3] Since the SVWF approach gives very high field values near the SMS, the ordinate axes in Figures E.1 to E.3 have been adjusted such that the details around the critical point $r = 5$ mm are clearly illustrated.

[E.4] Although it is not visible in Figures E.1 to E.3, except in Figures E.1(b) and E.2(b) for $N_{max} = 10$, some SVWF-based field components are, apart from being somewhat inaccurate, moreover discontinuous, while others are continuous across the SMS for the selected N_{max}. These effects are also due to the impossibility of having $N_{max} = \infty$ in the practical implementation of the SVWF-based fields.

the SMS, the SVFW-based expressions for the electric and magnetic fields in (E.58) are replaced by the corresponding simple approach expressions (E.65a) and (E.65b), whenever a graphical illustration of the EHD or the total fields is needed, as was the case in Chapter 5. As explained in Section E.2.3, such a procedure is theoretically expected to give rise to a discontinuity in the total field, but now across the physical interface of a given material structure illuminated by the EHD, rather than across the SMS. However, as noted further in Section E.2.3, this discontinuity is negligible and is, in fact, difficult to observe in the numerical results for the total fields of the resonant electrically small MTM-based structures, such as those considered in Chapter 5.

E.2 Unknown fields

E.2.1 Field expansions

The unknown scattered field in the region containing the EHD and the unknown total fields in the other regions are also expanded in terms of SVWFs. In this regard it is first useful to note the following. In Region 1, the electric and magnetic fields, denoted by $\vec{E}_{1s}$ and $\vec{H}_{1s}$, are composed of standing waves, and thus their radial dependencies are properly described by the spherical Bessel function of order n, i.e., $j_n(\cdot)$. In Region 2, the electric and magnetic fields, denoted by $\vec{E}_{2s}$ and $\vec{H}_{2s}$ are composed of standing waves (i.e., as a superposition of spherical waves propagating in the $+r$-direction and those propagating in the $-r$-direction). Therefore, the radial dependence of the field in Region 2 is properly described by the spherical Bessel, $j_n(\cdot)$, and Neumann, $y_n(\cdot)$, functions of order n. In Region 3, the electric and magnetic fields, denoted by $\vec{E}_{3s}$ and $\vec{H}_{3s}$ are composed of outward propagating spherical waves, and, thus, their radial dependencies are properly described by the spherical Hankel functions of the second kind and order n, i.e., $h_n^{(2)}(\cdot)$. With these remarks in hand, the relevant expansions of these field take on the following form

$$\left\{ \begin{array}{c} \vec{E}_{1s}(r,\theta,\phi) \\ \vec{H}_{1s}(r,\theta,\phi) \end{array} \right\} = \sum_{n=1}^{\infty} \sum_{m=-n}^{m=+n} \left[\frac{1}{j\omega\varepsilon_1\mu_1} \left\{ \begin{array}{c} A_{1,nm}\vec{N}_{nm}^{(\mathrm{TM}),(1)} \\ B_{1,nm}\vec{N}_{nm}^{(\mathrm{TE}),(1)} \end{array} \right\} \right. \tag{E.66a}$$
$$\left. + \left\{ \begin{array}{c} (-1/\varepsilon_1)\, B_{1,nm}\, \vec{M}_{nm}^{(\mathrm{TE}),(1)} \\ (1/\mu_1)\, A_{1,nm}\, \vec{M}_{nm}^{(\mathrm{TM}),(1)} \end{array} \right\} \right], \text{ for } r \leq r_1$$

$$\left\{ \begin{array}{c} \vec{E}_{2s}(r,\theta,\phi) \\ \vec{H}_{2s}(r,\theta,\phi) \end{array} \right\} = \sum_{n=1}^{\infty} \sum_{m=-n}^{m=+n} \left[\frac{1}{j\omega\varepsilon_2\mu_2} \left\{ \begin{array}{c} A_{2,nm}\vec{N}_{nm}^{(\mathrm{TM}),(1)} + A_{3,nm}\vec{N}_{nm}^{(\mathrm{TM}),(2)} \\ B_{2,nm}\vec{N}_{nm}^{(\mathrm{TE}),(1)} + B_{3,nm}\vec{N}_{nm}^{(\mathrm{TE}),(2)} \end{array} \right\} \right. \tag{E.66b}$$
$$\left. + \left\{ \begin{array}{c} (-1/\varepsilon_2)\, [B_{2,nm}\, \vec{M}_{nm}^{(\mathrm{TE}),(1)} + B_{3,nm}\, \vec{M}_{nm}^{(\mathrm{TE}),(2)}] \\ (1/\mu_2)\, [A_{2,nm}\, \vec{M}_{nm}^{(\mathrm{TM}),(1)} + A_{3,nm}\, \vec{M}_{nm}^{(\mathrm{TM}),(2)}] \end{array} \right\} \right], \text{ for } r_1 \leq r \leq r_2$$

$$\left\{ \begin{array}{c} \vec{E}_{3s}(r,\theta,\phi) \\ \vec{H}_{3s}(r,\theta,\phi) \end{array} \right\} = \sum_{n=1}^{\infty} \sum_{m=-n}^{m=+n} \left[\frac{1}{j\omega\varepsilon_0\mu_0} \left\{ \begin{array}{c} A_{4,nm}\vec{N}_{nm}^{(\mathrm{TM}),(4)} \\ B_{4,nm}\vec{N}_{nm}^{(\mathrm{TE}),(4)} \end{array} \right\} \right. \tag{E.66c}$$
$$\left. + \left\{ \begin{array}{c} (-1/\varepsilon_0)\, B_{4,nm}\, \vec{M}_{nm}^{(\mathrm{TE}),(4)} \\ (1/\mu_0)\, A_{4,nm}\, \vec{M}_{nm}^{(\mathrm{TM}),(4)} \end{array} \right\} \right], \text{ for } r \geq r_2$$

where $A_{i,nm}$ and $B_{i,nm}$, $i = 1, \ldots, 4$, are the unknown expansion coefficients associated, respectively, with the TM and TE parts of the fields. In similitude to the field generated by the EHD, the multipole TE and TM Debye potentials associated with the above unknown fields are

$$\Phi_{nm}^{(c)} = \varepsilon_i\, w_n^{(c)}(k_i r)\, P_n^{|m|}(\cos\theta)\, e^{jm\phi}\,, \tag{E.67}$$

$$\Psi_{nm}^{(c)} = \mu_i\, w_n^{(c)}(k_i r)\, P_n^{|m|}(\cos\theta)\, e^{jm\phi}\,, \tag{E.68}$$

with ε_i, μ_i, and k_i being the permittivity, permeability, and wave number in region 1 and 2 for $i = 1$ and 2, while they represent the corresponding free-space quantities, that apply for region 3, when $i = 0$. The

expansions in (E.66b) also contain the function $y_n(\cdot)$, i.e., the spherical Neumann function of order n. It thus follows that the explicit form of the SVWFs in (E.66a)-(E.66c) is the same as those given by (E.9) and (E.10), except that the proper material parameters must be used when expanding the unknown field in any given region.

To facilitate the procedure by which the unknown expansion coefficients $A_{i,nm}$ and $B_{i,nm}$, $i = 1, \ldots, 4$, are found, it is useful to write the expressions for the total TE and TM Debye potentials associated with the unknown fields (E.66a)-(E.66c). These expressions are

$$\Phi_{1s} = \sum_{n=1}^{\infty} \sum_{m=-n}^{m=+n} B_{1,nm}\, \Phi_{nm}^{(1)}\,, \tag{E.69a}$$

$$\Psi_{1s} = \sum_{n=1}^{\infty} \sum_{m=-n}^{m=+n} A_{1,nm}\, \Psi_{nm}^{(1)}\,, \tag{E.69b}$$

in region 1, and

$$\Phi_{2s} = \sum_{n=1}^{\infty} \sum_{m=-n}^{m=+n} \left[B_{2,nm}\, \Phi_{nm}^{(1)} + B_{3,nm}\, \Phi_{nm}^{(2)} \right], \tag{E.70a}$$

$$\Psi_{2s} = \sum_{n=1}^{\infty} \sum_{m=-n}^{m=+n} \left[A_{2,nm}\, \Psi_{nm}^{(1)} + A_{3,nm}\, \Psi_{nm}^{(2)} \right], \tag{E.70b}$$

in region 2, and

$$\Phi_{3s} = \sum_{n=1}^{\infty} \sum_{m=-n}^{m=+n} B_{4,nm}\, \Phi_{3,nm}\,, \tag{E.71a}$$

$$\Psi_{3s} = \sum_{n=1}^{\infty} \sum_{m=-n}^{m=+n} A_{4,nm}\, \Psi_{3,nm}\,, \tag{E.71b}$$

in region 3.

E.2.2 Expansion coefficients

The unknown expansion coefficients $A_{i,nm}$ and $B_{i,nm}$, $i = 1, \ldots, 4$, are determined by imposing the electromagnetic boundary conditions, which require the continuity of the tangential components of the total electric and magnetic fields at the spherical interfaces $r = r_1$ and $r = r_2$. The components of the total tangential electric and magnetic fields at these interfaces are the θ- and ϕ- components. These are denoted by $E_{\theta,\, it}$ and $E_{\phi,\, it}$, for the total electric field, and $H_{\theta,\, it}$ and $H_{\phi,\, it}$, for the total magnetic field. The index $i = 1, 2$ and 3, denotes the total fields in regions 1,2 and 3, respectively. The total TE and TM potentials associated with the total fields in regions 1 through 3 are denoted by Φ_{it} and Ψ_{it}, $i = 1, \ldots, 3$; and, as seen below, these depend on the location of the EHD. From the TE and TM representations of the various fields one finds that satisfying the below given set equations for the total TE and TM potentials in the various regions guarantees continuity of the tangential field components

across the spherical interfaces at $r = r_1$ and r_2[E.5].

Applying the electromagnetic boundary conditions, one then finds that at $r = r_1$ the following is required

$$\frac{1}{\varepsilon_1}\,\Phi_{1t}(r=r_1) = \frac{1}{\varepsilon_2}\,\Phi_{2t}(r=r_1)\,, \tag{E.76a}$$

$$\frac{1}{\varepsilon_1\mu_1}\,d'_{r=r_1}\left(\,r\,\Phi_{1t}\,\right) = \frac{1}{\varepsilon_2\mu_2}\,d'_{r=r_1}\left(\,r\,\Phi_{2t}\,\right)\,, \tag{E.76b}$$

$$\frac{1}{\mu_1}\,\Psi_{1t}(r=r_1) = \frac{1}{\mu_2}\,\Psi_{2t}(r=r_1), \tag{E.76c}$$

$$\frac{1}{\mu_1\varepsilon_1}\,d'_{r=r_1}\left(\,r\,\Psi_{1t}\,\right) = \frac{1}{\mu_2\varepsilon_2}\,d'_{r=r_1}\left(\,r\,\Psi_{2t}\,\right)\,, \tag{E.76d}$$

while at $r = r_2$ the following is required

$$\frac{1}{\varepsilon_2}\,\Phi_{2t}(r=r_2) = \frac{1}{\varepsilon_0}\,\Phi_{3t}(r=r_2)\,, \tag{E.77a}$$

$$\frac{1}{\varepsilon_2\mu_2}\,d'_{r=r_2}\left(\,r\,\Phi_{2t}\,\right) = \frac{1}{\varepsilon_0\mu_0}\,d'_{r=r_2}\left(\,r\,\Phi_{3t}\,\right)\,, \tag{E.77b}$$

$$\frac{1}{\mu_2}\,\Psi_{2t}(r=r_2) = \frac{1}{\mu_0}\,\Psi_{3t}(r=r_2), \tag{E.77c}$$

$$\frac{1}{\mu_2\varepsilon_2}\,d'_{r=r_2}\left(\,r\,\Psi_{2t}\,\right) = \frac{1}{\mu_0\varepsilon_0}\,d'_{r=r_2}\left(\,r\,\Psi_{2t}\,\right)\,. \tag{E.77d}$$

The equations (E.76a)-(E.77d) must be solved in the three cases for which the EHD is located in region 1,2 or 3.

When the EHD is in Region 1, the total potentials Φ_{1t} and Ψ_{1t} (to be matched at the interface $r = r_1$) in Region 1 are

$$\Phi_{1t} = \Phi^{(4)}_{\text{EHD}} + \Phi_{1s}\,, \tag{E.78}$$

$$\Psi_{1t} = \Psi^{(4)}_{\text{EHD}} + \Psi_{1s}\,, \tag{E.79}$$

Moreover, the total potentials in Region 2, Φ_{2t} and Ψ_{2t}, are given by (E.70a) and (E.70b), respectively, while the total potentials in Region 3, Φ_{3t} and Ψ_{3t}, are given by (E.71a) and (E.71b), respectively.

[E.5] This can be inferred from the expressions for the fields already presented. However, rewriting the tangential components of these fields as [117, Ch. 10]

$$E_{\theta,it}(r,\theta,\phi) = \frac{1}{j\omega\varepsilon_i\mu_i}\,\frac{1}{r}\,\frac{\partial^2}{\partial r\partial\theta}\left(r\,\Psi_{it}\right) - \frac{1}{\varepsilon_i}\,\frac{1}{r\sin\theta}\,\frac{\partial}{\partial\phi}\left(r\,\Phi_{it}\right)\,, \tag{E.72}$$

$$E_{\phi,it}(r,\theta,\phi) = \frac{1}{j\omega\varepsilon_i\mu_i}\,\frac{1}{r\,\sin\theta}\,\frac{\partial^2}{\partial r\partial\phi}\left(r\,\Psi_{it}\right) + \frac{1}{\varepsilon_i}\,\frac{1}{r}\frac{\partial}{\partial\theta}\left(r\,\Phi_{it}\right)\,, \tag{E.73}$$

$$H_{\theta,it}(r,\theta,\phi) = \frac{1}{j\omega\varepsilon_i\mu_i}\,\frac{1}{r}\,\frac{\partial^2}{\partial r\partial\theta}\left(r\,\Phi_{it}\right) + \frac{1}{\mu_i}\,\frac{1}{r\sin\theta}\,\frac{\partial}{\partial\phi}\left(r\,\Psi_{it}\right)\,, \tag{E.74}$$

$$H_{\phi,it}(r,\theta,\phi) = \frac{1}{j\omega\varepsilon_i\mu_i}\,\frac{1}{r\,\sin\theta}\,\frac{\partial^2}{\partial r\partial\phi}\left(r\,\Phi_{it}\right) - \frac{1}{\mu_i}\,\frac{1}{r}\frac{\partial}{\partial\theta}\left(r\,\Psi_{it}\right)\,, \tag{E.75}$$

the equations satisfied by the potentials to achieve the continuity of the fields at $r = r_1$ and $r = r_2$ can be identified more easily.

When the EHD is in Region 2, the total potentials (to be matched at the interface $r = r_1$) in Region 2 now become

$$\Phi_{2t} = \Phi^{(1)}_{\text{EHD}} + \Phi_{2s} \,, \tag{E.80}$$

$$\Psi_{2t} = \Psi^{(1)}_{\text{EHD}} + \Psi_{2s} \,, \tag{E.81}$$

while those to be matched at the interface $r = r_2$ are

$$\Phi_{2t} = \Phi^{(4)}_{\text{EHD}} + \Phi_{2s} \,, \tag{E.82}$$

$$\Psi_{2t} = \Psi^{(4)}_{\text{EHD}} + \Psi_{2s} \,, \tag{E.83}$$

In addition, Φ_{1t} and Ψ_{1t} are now given by (E.69a) and (E.69b), respectively, while Φ_{3t} and Ψ_{3t} are now given by (E.71a) and (E.71b), respectively.

Finally, when the EHD is in Region 3, the total potentials Φ_{1t} and Ψ_{1t} in Region 1 are given by (E.69a) and (E.69b), respectively. The total potentials Φ_{2t} and Ψ_{2t} in Region 2 are given by (E.70a) and (E.70b), respectively. The total potentials Φ_{3t} and Ψ_{3t} (to be matched at the interface $r = r_2$) in Region 3 are

$$\Phi_{3t} = \Phi^{(1)}_{\text{EHD}} + \Phi_{3s} \,, \tag{E.84}$$

$$\Psi_{3t} = \Psi^{(1)}_{\text{EHD}} + \Psi_{3s} \,. \tag{E.85}$$

Thus, depending on the location of the EHD, the total Debye potentials and, hence, the total fields in the various regions will be different. As a consequence, different systems of equations are obtained for the EHD being located in Region 1,2, or 3. However, by treating all of the possible EHD locations on a separate basis, it is easily observed that the system of equations for the unknown expansion coefficients, which is obtained from the boundary conditions (E.76a)-(E.77d), always takes the following form

$$\vec{\Omega}_{nm} = \bar{\bar{S}}_n \vec{D}_{nm}, \quad n = 1, 2, \ldots N_{max}, \quad \text{and} \quad m = -n, \ldots n \tag{E.86}$$

where $\vec{D}_{nm} = [A_{1,nm}, \ldots, A_{4,nm}, B_{1,nm}, \ldots, B_{4,nm}]$ is the vector containing the eight unknown expansion coefficients and $\vec{\Omega}_{nm} = [\Omega_{1,nm}, \ldots \Omega_{8,nm}]$ is the excitation vector, which depends on the location of the EHD. The elements of this excitation vector, when the EHD is located in regions 1, 2 or 3, are shown in Table E.1.

$\Omega_{i,nm}$	EHD in region 1	EHD in region 2	EHD in region 3
$\Omega_{1,nm}$	$-a^{(4)}_{nm} h^{(2)}_n(k_1 r_1)$	$a^{(1)}_{nm} j_n(k_2 r_1)$	0
$\Omega_{2,nm}$	$-a^{(4)}_{nm} d'_{r=r_1}\{r h^{(2)}_n(k_1 r)\}$	$(\varepsilon_1/\varepsilon_2)\, a^{(1)}_{nm}\, d'_{r=r_1}\{r j_n(k_2 r)\}$	0
$\Omega_{3,nm}$	0	$-a^{(4)}_{nm} h^{(2)}_n(k_2 r_2)$	$a^{(1)}_{nm} j_n(k_0 r_2)$
$\Omega_{4,nm}$	0	$-a^{(4)}_{nm}\, d'_{r=r_2}\{r h^{(2)}_n(k_2 r)\}$	$(\varepsilon_2/\varepsilon_0)\, a^{(1)}_{nm}\, d'_{r=r_2}\{r j_n(k_0 r)\}$
$\Omega_{5,nm}$	$-b^{(4)}_{nm} h^{(2)}_n(k_1 r_1)$	$b^{(1)}_{nm} j_n(k_2 r_1)$	0
$\Omega_{6,nm}$	$-b^{(4)}_{nm} d'_{r=r_1}\{r h^{(2)}_n(k_1 r)\}$	$(\mu_1/\mu_2)\, b^{(1)}_{nm}\, d'_{r=r_1}\{r j_n(k_2 r)\}$	0
$\Omega_{7,nm}$	0	$-b^{(4)}_{nm} h^{(2)}_n(k_2 r_2)$	$b^{(1)}_{nm} j_n(k_0 r_2)$
$\Omega_{8,nm}$	0	$-b^{(4)}_{nm}\, d'_{r=r_2}\{r h^{(2)}_n(k_2 r)\}$	$(\mu_2/\mu_0)\, b^{(1)}_{nm}\, d'_{r=r_2}\{r j_n(k_0 r)\}$

Table E.1: The elements $\Omega_{i,nm}$, $i = 1, \ldots, 8$, of the excitation vector $\vec{\Omega}_{nm}$ when the EHD is located in regions 1, 2, or 3.

The matrix $\bar{\bar{S}}_n$ is an eight-by-eight matrix that arises from the enforcement of the electromagnetic boundary conditions and, hence, depends on the values of the spherical wave functions at the two interfaces.

The explicit form of this matrix is given by

$$\bar{\bar{S}} = \begin{bmatrix} \bar{\bar{A}}_n & \bar{\bar{0}} \\ \bar{\bar{0}} & \bar{\bar{B}}_n \end{bmatrix}, \tag{E.87}$$

where

$$\bar{\bar{A}}_n = \begin{bmatrix} j_n(k_1 r_1) & j_n(k_2 r_1) & -y_n(k_2 r_1) & 0 \\ d'_{r=r_1}\{r j_n(k_1 r)\} & -\frac{\varepsilon_1}{\varepsilon_2} d'_{r=r_1}\{r j_n(k_2 r)\} & -\frac{\varepsilon_1}{\varepsilon_2} d'_{r=r_1}\{r y_n(k_2 r)\} & 0 \\ 0 & j_n(k_2 r_2) & y_n(k_2 r_2) & -h_n^{(2)}(k_0 r_2) \\ 0 & d'_{r=r_1}\{r j_n(k_2 r)\} & d'_{r=r_2}\{r y_n(k_2 r)\} & -\frac{\varepsilon_2}{\varepsilon_0} d'_{r=r_3}\{r h_n^{(2)}(k_0 r)\} \end{bmatrix}. \tag{E.88}$$

and

$$\bar{\bar{B}}_n = \begin{bmatrix} j_n(k_1 r_1) & j_n(k_2 r_1) & -y_n(k_2 r_1) & 0 \\ d'_{r=r_1}\{r j_n(k_1 r)\} & -\frac{\mu_1}{\mu_2} d'_{r=r_1}\{r j_n(k_2 r)\} & -\frac{\mu_1}{\mu_2} d'_{r=r_1}\{r y_n(k_2 r)\} & 0 \\ 0 & j_n(k_2 r_2) & y_n(k_2 r_2) & -h_n^{(2)}(k_0 r_2) \\ 0 & d'_{r=r_1}\{r j_n(k_2 r)\} & d'_{r=r_2}\{r y_n(k_2 r)\} & -\frac{\mu_2}{\mu_0} d'_{r=r_3}\{r h_n^{(2)}(k_0 r)\} \end{bmatrix}, \tag{E.89}$$

while $\bar{\bar{0}}$ is a 4-by-4 matrix whose elements are all zero. In the above expressions

$$d'_{r=r_k}\{r_k w_n^{(c)}(k_i r_k)\} = w_n^{(c)}(k_i r_k) + k_i r_k w_n^{(c)\prime}(k_i r_k), \tag{E.90}$$

where $w_n^{(c)\prime}(x) = dw_n^{(c)}/dx$. The relation (E.86) can be solved for the unknown expansion coefficients as

$$\vec{D}_{nm} = \left[\bar{\bar{S}}_n\right]^{-1} \vec{\Omega}_{nm}, \quad n = 1, 2, \dots, \quad \text{and} \quad m = -n, \dots n \tag{E.91}$$

This form of the solution allows one to account for the various EHD locations in a very simple manner and, therefore, is very convenient from an understanding and implementation point of view. The only thing that changes in the matrix equation (E.91) as the EHD changes its location is the excitation vector $\vec{\Omega}_{nm}$.

In closing this section it is interesting to note that the first four elements of the excitation vector, $\vec{\Omega}_{nm}$, i.e., $\Omega_{i,nm}$, $i = 1, \dots 4$, are used only in the determination of the TM coefficients, i.e., $A_{i,nm}$, $i = 1, \dots 4$, while the last four elements of $\vec{\Omega}_{nm}$, i.e., $\Omega_{i,nm}$, $i = 5, \dots 8$, are used only in the the determination of the TE coefficients. Mathematically, this is due to the presence of the $\bar{0}$ matrices in the expression for $\bar{\bar{S}}_n$ in (E.87). Physically this is caused by the fact that the TM and TE modes are linearly independent and, hence, their coefficients $A_{i,nm}$ and $B_{i,nm}$ are in fact uncoupled. Alternatively, the system of equations used to determine the TM coefficients $A_{i,nm}$ do not depend on TE coefficients $B_{i,nm}$, and vice versa.

E.2.3 Final remarks

At the end of Section E.1.5 it was noted that for the purpose of plotting the EHD field, as is e.g. done in Chapter 5, the SVWF-based expressions for the electric and magnetic fields in (E.58), with the infinite summations truncated to some finite N_{max}, are replaced by the simple expressions in (E.65a) and (E.65b), which are exact. This replacement has an important theoretical implication when a given structure is introduced next to the EHD, where it becomes relevant to e.g., depict the total fields, rather than the EHD field alone, as was likewise performed in Chapter 5. However, as noted below, the theoretical implication is of little practical importance for the resonant electrically small MTM-based structures of interest to this work.

In the practical implementation of the unknown fields derived in Section E.2.2, the employed summations must likewise be truncated to some N_{max}. For the purpose of this section let a given unknown field (UF) from Section E.2.2 be denoted generically as

$$\text{UF} = a \sum_{n=1}^{N_{max}} \sum_{m=-n}^{n} \text{UF-EC}_{nm}\ \text{SVWF}_{nm}, \tag{E.92}$$

where a is some constant, UF-EC$_{nm}$ is the expansion coefficient of the UF, and SVFW$_{nm}$ is a relevant SVWF. The field in (E.92) is not exact, but is, at most, a very good approximation to the UF, since $N_{max} \neq \infty$. The UF can also be expressed as

$$\text{UF} = \text{exact UF} + \delta\text{UF} \,, \tag{E.93}$$

where δUF is the deviation of the UF in (E.92) from the exact UF (the exact UF equals the UF in (E.92) provided that $N_{max} = \infty$).

On the other hand, when the SVWF-based EHD field is, for plotting purposes, replaced by the simple approach field expressions, it means that exact field of the EHD, is plotted. Plotting such an exact EHD field together with approximations to the UFs obviously leads to a discontinuity across the relevant physical interfaces of the structure in question. To exemplify, let us assume that the EHD is in region 1 of the scattering problem considered in the present appendix. With reference to previous sections, the total electric field in this region is the sum of the scattered electric field, i.e., the UF $\vec{E}_{1s}$, for this region and the electric field of the EHD, $\vec{E}_{\text{EHD}}$. In the determination of the unknown field coefficients, this total electric field must be matched across the interface at $r = r_1$ with the total electric field, i.e., the UF $\vec{E}_{2s}$, for region 2 of the structure. Thus,

$$\hat{t} \cdot \vec{E}_{\text{EHD}}(r = r_1) + \hat{t} \cdot [\vec{E}_{1s}(r = r_1) + \delta\vec{E}_{1s}(r = r_1)] = \hat{t} \cdot [\vec{E}_{2s}(r = r_1) + \delta\vec{E}_{2s}(r = r_1)] \,, \tag{E.94}$$

where $\hat{t}$ equals either $\hat{\theta}$ or $\hat{\phi}$. From (E.94) it is clear that $\delta\vec{E}_{1s}(r = r_1)$ and $\delta\vec{E}_{2s}(r = r_1)$, which are the deviations of the approximate UFs from the exact UFs $\vec{E}_{1s}$ and $\vec{E}_{2s}$, respectively, lead to a discontinuity at $r = r_1$ since they do not have a corresponding counterpart in the exact $\vec{E}_{\text{EHD}}$ which is used in the plotting process[E.6]. However, for resonant electrically small MTM-based structures treated in Chapter 5, in which a given mode, e.g., the dipolar or the quadrupolar one, is the dominant one, this discontinuity, which essentially is contained in the higher-order modes, is negligible. This is due to the resonant nature of the MTM-based structures of interest to this work, for which very little information in the UFs is contained in the modes $n \in [N_{max}, \infty]$, i.e., the terms such as e.g., $\delta\vec{E}_{1s}(r = r_1)$ and $\delta\vec{E}_{2s}(r = r_1)$ are very small. In other words, the approximate UF, which make use of truncated summations, are very close to the exact UF, in which these summations are infinite. Indeed, as observed in Chapter 5, the total fields appear to be continuous across the relevant interfaces of the resonant electrically small MTM-based structures, although this is not the case in strict analytical sense. This is illustrated further by the results shown in Figure E.4, where the θ component of the total electric field of the quadrupolar DPS-DNG structure treated in Chapter 5 is shown as a function of r in regions 1, 2, and 3, for $\theta = 90^o$ and $\phi = 0^o$ (Figure E.4(a)), and for $\theta = 90^o$ and $\phi = 180^o$ (Figure E.4(b)). More specifically, it is the quantity $20 \log_{10} |E_\theta|$ which is shown for the specified θ and ϕ values. The EHD is taken to be z-directed, and to have the dipole moment $p_s = 0.01$ Am, and to be located at ($r_s = 5$ mm, $\theta_s = 90^o, \phi_s = 0^o$).
The fields in Figures E.4(a) and (b) are identical except from the fact that a peak in the field is found for $r = 5$ mm in Figure E.4(a). This is expected, since the EHD is located at this particular observation point. Although the total fields in the three regions seem to be continuous at the interface $r = r_1$ (they are, of course, continuous at $r = r_2$) there is an extremely small difference in the total field values at $r = r_1$ in Figure E.4(a). While the total field in region 1 (red curve) in Figure E.4(a), has the value of 220.1266 dB at $r = r_1$, the total field in region 2 (blue curve) evaluated at $r = r_1$ has the value of 220.1265 dB. Since these two values are extremely close to each other, the said discontinuity at $r = r_1$ is indeed negligible for this particular EHD location. Moreover, it is noted that no discontinuity at all is observed in Figure E.4(b), because this part of the interface is much farther away from the EHD then the part for which $\phi = 0^o$.

Although not included here, similar behaviour of the fields was observed for EHD locations very close to the interface of the quadrupolar DPS-DNG structure. In these cases, the discontinuity across the

[E.6]This discontinuity can also be explained in the following, equivalent way. The exact EHD field, which is used for plotting is equivalent to the SVWF-based EHD field expressions in which the infinite summations are employed. As noted before, the infinite summations in the UFs must be truncated to some finite N_{max}. The electromagnetic boundary conditions, which are used to determine the unknown expansion coefficients give these coefficients for each n and the associated m, i.e., the relevant equations are solved mode for mode. It is therefore clear that the mode-to-mode matching of the various total fields across the interfaces of the structure occurs up to N_{max}. After N_{max}, the modes $n \in [N_{max}, \infty]$ of the exact EHD field do not have the corresponding modes in the UFs with which they can be matched, i.e., a discontinuity is expected at a relevant interface in such graphical representations of the total fields.

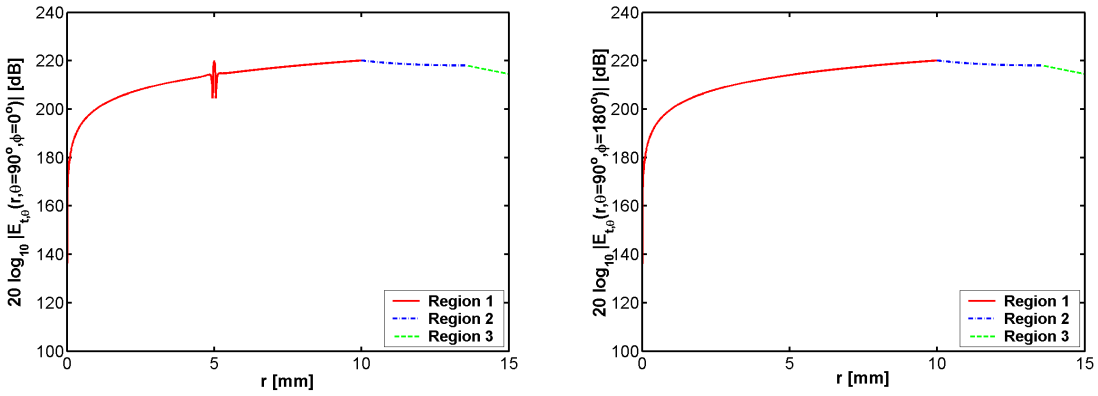

(a) (b)

Figure E.4: *The electric field of the quadrupolar DPS-DNG structure treated in Chapter 5 as a function of r in regions 1, 2, and 3, for $\theta = 90^o$ and $\phi = 0^o$ (a), and for $\theta = 90^o$ and $\phi = 180^o$ (b). See the main text for further details.*

physical interface at $r = r_1$ was somewhat increased relative to the above case, but in all cases it was very small, and therefore it can be neglected for all practical purposes.

As a consequence, the replacement of the SVWF-based EHD fields by the exact simpler expressions for the purposes of plotting the total fields of a given structure is justified for resonant electrically small structures.

E.3 Derived quantities

The figures of merit employed in the numerical investigations found in Chapter 5 are

- the total average radiated power, P_t, henceforth termed the total power.
- the directivity, D.

E.3.1 Introduction

In order to derive the total power and the directivity, the total far field in region 3 are needed. In the case where the EHD is in region 3, the total electric and magnetic fields, denoted by $\vec{E}_{3t}$ and $\vec{H}_{3t}$, respectively, equal the sum of the EHD field (E.8) defined for $r > r_s$ and the scattered field in (E.66c) defined for region 3, i.e., $\vec{E}_{3t} = \vec{E}^{r>r_s}_{\text{EHD}} + \vec{E}_{3s}$ and $\vec{H}_{3t} = \vec{H}^{r>r_s}_{\text{EHD}} + \vec{H}_{3s}$, while $\vec{E}_{3t} = \vec{E}_{3s}$ and $\vec{H}_{3t} = \vec{H}_{3s}$ when the EHD is in either region 1 or 2. The relevant expression for these total fields are easily obtained for $r \to \infty$ by using the large argument approximation of the spherical Hankel function contained in the fields for region 3. In particular, the following results make use of [119, Ch. 11]

$$h_n^{(2)}(kr) \sim j^{n+1} \, \frac{e^{-jkr}}{kr}, \quad r \to \infty \,, \tag{E.95}$$

$$\frac{1}{r} \, \partial_r [r h_n^{(2)}(kr)] \sim j^n \, \frac{e^{-jkr}}{r}, \quad r \to \infty \,. \tag{E.96}$$

Using (E.95) and (E.96), the far-field versions of the SVWFs used in the EHD field expansion given in (E.8) for $r > r_s$ can be expressed as

$$\lim_{r\to\infty} \vec{M}^{(\Gamma),(4)}_{nm} \quad = \quad \hat{\theta} \, \gamma_0 \, j^{n+1} \, \frac{e^{-jk_0 r}}{k_0 r} \, \frac{jm}{\sin\theta} \, P_n^{|m|}(\cos\theta) \, e^{jm\phi}$$

$$- \hat{\phi}\, \gamma_0\, j^{n+1}\ \frac{e^{-jk_0r}}{k_0r}\ \frac{d}{d\theta}\ P_n^{|m|}(\cos\theta)\, e^{jm\phi}, \quad \text{(E.97)}$$

$$\begin{aligned}\lim_{r\to\infty} \vec{N}_{nm}^{(\Gamma),(4)} \;&=\; \hat{\theta}\, \gamma_0\, j^n\, \frac{e^{-jk_0r}}{k_0r}\ \frac{d}{d\theta}\ P_n^{|m|}(\cos\theta)\, e^{jm\phi} \\ &\quad + \hat{\phi}\, \gamma\, j^n\, \frac{e^{-jk_0r}}{k_0r}\ \frac{jm}{\sin\theta}\ P_n^{|m|}(\cos\theta)\, e^{jm\phi}\,, \quad \text{(E.98)}\end{aligned}$$

with $\gamma_0 = \varepsilon_0$ for $\Gamma = \text{TE}$, and $\gamma_0 = \mu_0$ for $\Gamma = \text{TM}$. The corresponding far-field versions of the SVWFs used to represent $\vec{E}_{3s}$ are obtained straightforwardly in the same manner. As a consequence, the total electric far field $\vec{E}_t^f$ reads

$$\begin{aligned}\vec{E}_t^f \;&=\; \vec{E}_{\text{EHD}}^{r>r_s,f} + \vec{E}_{3s}^f = \\ &= \sum_{n=1}^{\infty}\sum_{m=-n}^{m=+n}\Big[\ \frac{1}{j\omega\varepsilon_0\mu_0}\,\alpha_{nm}\ \lim_{r\to\infty}\vec{N}_{nm}^{(\text{TM}),(4)} - \frac{1}{\varepsilon_0}\,\beta_{nm}\ \lim_{r\to\infty}\vec{M}_{nm}^{(\text{TE}),(4)}\ \Big] \\ &= \hat{\theta}\sum_{n=1}^{\infty}\sum_{m=-n}^{m=+n}\Big[\ \frac{1}{\omega\varepsilon_0}\ \alpha_{nm}\ \frac{d}{d\theta}P_n^{|m|}(\cos\theta) + \ \beta_{nm}\ \frac{1}{k_0}\ \frac{jm}{\sin\theta}\ P_n^{|m|}(\cos\theta)\ \Big]\, j^{n-1}\, e^{jm\phi}\ \frac{e^{-jk_0r}}{r} \\ &+ \hat{\phi}\sum_{n=1}^{\infty}\sum_{m=-n}^{m=+n}\Big[\ \frac{1}{\omega\varepsilon_0}\,\alpha_{nm}\ \frac{jm}{\sin\theta}\ P_n^{|m|}(\cos\theta)\ -\ \beta_{nm}\ \frac{1}{k_0}\ \frac{d}{d\theta}P_n^{|m|}(\cos\theta)\ \Big]\, j^{n-1}\, e^{jm\phi}\ \frac{e^{-jk_0r}}{r} \\ &= \hat{\theta}\, E_{t,\theta}^f + \hat{\phi}\, E_{t,\phi}^f\,, \quad \text{(E.99)}\end{aligned}$$

where $E_{t,\theta}^f$ and $E_{t,\phi}^f$ are its θ- and ϕ- components. Similarly, the total magnetic far field $\vec{H}_t^f$ is expressed as

$$\begin{aligned}\vec{H}_t^f \;&=\; \vec{H}_{\text{EHD}}^{r>r_s,f} + \vec{H}_{3s}^f = \\ &= \sum_{n=1}^{\infty}\sum_{m=-n}^{m=+n}\Big[\ \frac{1}{j\omega\varepsilon_0\mu_0}\,\beta_{nm}\ \lim_{r\to\infty}\vec{N}_{nm}^{(\text{TE}),(4)} + \frac{1}{\mu_0}\,\alpha_{nm}\ \lim_{r\to\infty}\vec{M}_{nm}^{(\text{TM}),(4)}\ \Big] \\ &= \hat{\theta}\sum_{n=1}^{\infty}\sum_{m=-n}^{m=+n}\Big[\ \frac{1}{\omega\mu_0}\ \beta_{nm}\ \frac{d}{d\theta}P_n^{|m|}(\cos\theta)\ -\ \alpha_{nm}\ \frac{1}{k_0}\ \frac{jm}{\sin\theta}\ P_n^{|m|}(\cos\theta)\ \Big]\, j^{n-1}\, e^{jm\phi}\ \frac{e^{-jk_0r}}{r} \\ &+ \hat{\phi}\sum_{n=1}^{\infty}\sum_{m=-n}^{m=+n}\Big[\ \frac{1}{\omega\mu_0}\,\beta_{nm}\ \frac{jm}{\sin\theta}\ P_n^{|m|}(\cos\theta)\ +\ \alpha_{nm}\ \frac{1}{k_0}\ \frac{d}{d\theta}P_n^{|m|}(\cos\theta)\ \Big]\, j^{n-1}\, e^{jm\phi}\ \frac{e^{-jk_0r}}{r} \\ &= \hat{\theta}\, H_{t,\theta}^f + \hat{\phi}\, H_{t,\phi}^f\,, \quad \text{(E.100)}\end{aligned}$$

with $H_{t,\theta}^f$ and $H_{t,\phi}^f$ being its θ- and ϕ-components. In (E.99) and (E.100), the terms

$$\alpha_{nm} = \begin{cases} A_{4,nm} & \text{when the EHD is in region 1 or 2,} \\ a_{nm}^{(4)} + A_{4,nm} & \text{when the EHD is in region 3 ,}\end{cases} \quad \text{(E.101)}$$

and

$$\beta_{nm} = \begin{cases} B_{4,nm} & \text{when the EHD is in region 1 or 2,} \\ b_{nm}^{(4)} + B_{4,nm} & \text{when the EHD is in region 3 .}\end{cases} \quad \text{(E.102)}$$

E.3.2 Total power

The total power P_t is given by the general expression

$$P_t = \frac{1}{2}\int_{\theta=0}^{\pi}\int_{\phi=0}^{2\pi} \mathcal{R}e\{\vec{E}_t^f \times \vec{H}_t^{f*}\}\cdot d\vec{s}, \tag{E.103}$$

where $\vec{E}_t^f$ and $\vec{H}_t^f$ are the total electric and magnetic far fields, respectively, in region 3. The character $*$ denotes the complex conjugate, and $d\vec{s} = \hat{r}\, r^2\, \sin\theta\, d\phi\, d\theta$ is the outward pointing vector differential element on the surface of integration. To evaluate the relation (E.103) one must consider the component of the Poynting vector along the radial direction[E.7]

$$(\vec{E}_t^f \times \vec{H}_t^{f*})\cdot\hat{r} = \Big[\big(\hat{\theta}E_{t,\theta}^f + \hat{\phi}E_{t,\phi}^f\big)\times\big(\hat{\theta}H_{t,\theta}^{f*} + \hat{t,\phi}H_{\phi}^{f*}\big)\Big]\cdot\hat{r} = E_{t,\theta}^f H_{t,\phi}^{f*} - E_{t,\phi}H_{t,\theta}^{f*}. \tag{E.104}$$

Consequently, the total power in (E.103) is now given by the expression

$$\begin{aligned}
P_t \;=\; & \frac{1}{2}\int_{\phi=0}^{2\pi}\int_{\theta=0}^{\pi} r^2\,\sin\theta\, d\theta\, d\phi \\
& \mathcal{R}e\Big\{\Big[\sum_{n=1}^{\infty}\sum_{m=-n}^{m=+n}\Big(\frac{1}{\omega\varepsilon_0}\,\alpha_{nm}\,\frac{d}{d\theta}P_n^{|m|}(\cos\theta) + \beta_{nm}\,\frac{1}{k_0}\,\frac{jm}{\sin\theta}\,P_n^{|m|}(\cos\theta)\Big) \\
& \times \sum_{n'=1}^{\infty}\sum_{m'=-n'}^{m'=+n'}\Big(\frac{1}{\omega\mu_0}\,\beta_{nm}^*\,\frac{-jm'}{\sin\theta}\,P_{n'}^{|m'|}(\cos\theta) + \alpha_{nm}^*\,\frac{1}{k_0}\,\frac{d}{d\theta}P_{n'}^{|m'|}(\cos\theta)\Big) \\
& \times j^{n-1}\,\frac{e^{-jk_0r}}{r}\,e^{jm\phi}\,(-j)^{n'-1}\,\frac{e^{jk_0r}}{r}\,e^{-jm'\phi}\Big] \\
& -\Big[\sum_{n=1}^{\infty}\sum_{m=-n}^{m=+n}\Big(\frac{1}{\omega\varepsilon_0}\,\alpha_{nm}\,\frac{jm}{\sin\theta}\,P_n^{|m|}(\cos\theta) - \beta_{nm}\,\frac{1}{k_0}\,\frac{d}{d\theta}P_n^{|m|}(\cos\theta)\Big) \\
& \times \sum_{n'=1}^{\infty}\sum_{m'=-n'}^{m'=+n'}\Big(\frac{1}{\omega\mu_0}\,\beta_{nm}^*\,\frac{d}{d\theta}P_{n'}^{|m'|}(\cos\theta) - \alpha_{nm}^*\,\frac{1}{k_0}\,\frac{-jm'}{\sin\theta}\,P_{n'}^{|m'|}(\cos\theta)\Big) \\
& \times j^{n-1}\,\frac{e^{-jk_0r}}{r}\,e^{jm\phi}\,(-j)^{n'-1}\,\frac{e^{jk_0r}}{r}\,e^{-jm'\phi}\Big]\Big\}.
\end{aligned} \tag{E.105}$$

The last expression can be rearranged into the form[E.8]

$$\begin{aligned}
P_t \;=\; & \frac{1}{2}\,\frac{1}{\omega k_0}\,\mathcal{R}e\Big\{\sum_{n=1}^{\infty}\sum_{m=-n}^{m=+n}\sum_{n'=1}^{\infty}\sum_{m'=-n'}^{m'=+n'} j^{n-1}\,(-j)^{n'-1} \\
& \times\Big[\frac{\alpha_{nm}\alpha_{n'm'}^*}{\varepsilon_0} + \frac{\beta_{nm}\beta_{n'm'}^*}{\mu_0}\Big] \\
& \times \int_{\theta=0}^{\pi}\Big\{\frac{d}{d\theta}P_n^{|m|}(\cos\theta)\frac{d}{d\theta}P_{n'}^{|m'|}(\cos\theta) + \frac{m^2}{\sin\theta}\,P_n^{|m|}(\cos\theta)P_{n'}^{|m'|}(\cos\theta)\Big\}\,\sin\theta\,d\theta \\
& \times \int_{\phi=0}^{2\pi} e^{j(m-m')\phi}d\phi\Big\}.
\end{aligned} \tag{E.106}$$

[E.7] The electric and magnetic fields in (E.103) can also be the near fields. However, to evaluate the expression most efficiently, the far-fields will be used. In this case, there is no radial component of either the electric or magnetic fields.

[E.8] Note that the terms in (E.105), where the TM coefficients are multiplied by the TE coefficients and vice versa, are disregarded since they always yield a product which is not real.

Using the orthogonality relation

$$\int_{\phi=0}^{2\pi} e^{j(m-m')\phi} d\phi = 2\pi\ \delta_{mm'}\ , \tag{E.107}$$

where it is recalled that the Kronecker delta function $\delta_{mm'}$ equals 1 if $m = m'$, and zero otherwise, it follows that (E.106) becomes

$$\begin{aligned} P_t = \frac{\pi}{\omega k_0}\, \mathcal{R}e\Big\{ \sum_{n=1}^{\infty} \sum_{m=-n}^{m=+n} \sum_{n'=0}^{\infty}\ j^{n-1}\ (-j)^{n'-1} \Big[\ \frac{\alpha_{nm}\alpha^*_{n'm'}}{\varepsilon_0} + \frac{\beta_{nm}\beta^*_{n'm'}}{\mu_0}\ \Big] \\ \times \int_{\theta=0}^{\pi} \Big\{ \frac{d}{d\theta} P_n^{|m|}(\cos\theta) \frac{d}{d\theta} P_{n'}^{|m'|}(\cos\theta) \\ + \frac{m^2}{\sin\theta}\ P_n^{|m|}(\cos\theta) P_{n'}^{|m'|}(\cos\theta) \Big\}\ \sin\theta\ d\theta\ \Big\}\ . \end{aligned} \tag{E.108}$$

Furthermore, using the orthogonality condition for the associated Legendre functions [118, p. 489]

$$\begin{aligned} \int_{\theta=0}^{\pi} \Big\{ \frac{d}{d\theta} P_n^{|m|}(\cos\theta) \frac{d}{d\theta} P_{n'}^{|m|}(\cos\theta) + \frac{m^2}{\sin\theta}\ P_n^{|m|}(\cos\theta) P_{n'}^{|m|}(\cos\theta) \Big\}\ \sin\theta\ d\theta \\ = \frac{2}{2n+1}\ \frac{(n+|m|)!}{(n-|m|!)}\ n(n+1)\ \delta_{nn'}\ , \end{aligned} \tag{E.109}$$

it follows that (E.108) reduces to

$$P_t = \frac{\pi}{\omega k_0} \sum_{n=1}^{\infty} \sum_{m=-n}^{m=+n} \frac{2}{2n+1}\ \frac{(n+|m|)!}{(n-|m|!)}\ n(n+1)\ \left[\ \frac{|\alpha_{nm}|^2}{\varepsilon_0} + \frac{|\beta_{nm}|^2}{\mu_0}\ \right]\ . \tag{E.110}$$

which is the final expression for the total power.

In Chapter 5 considerable attention has been devoted to the power ratio (PR), which is the ratio of the total power in (E.110) to the power radiated by the EHD in free space. The latter quantity, denoted by P_i, is actually given by (E.110) with $\alpha_{nm} = a^{(4)}_{nm}$ and $\beta^{(4)}_{nm} = b^{(4)}_{nm}$. However, the quantity P_i has a considerably simpler, well-known form if it is not expressed in terms of SVWFs. In particular, it is given by [120, p. 137]

$$P_i = \frac{\eta_0 \pi}{3} \left| \frac{p_s k_0}{2\pi} \right|^2\ . \tag{E.111}$$

Thus, the PR reads

$$\text{PR} = \frac{P_t}{P_i}, \tag{E.112}$$

where P_t and P_i are given, respectively, by (E.110) and (E.111).

Although it is analytically difficult to see how the power radiated by the EHD in free space given in terms of the SVWFs, i.e., (E.110) with $\alpha_{nm} = a^{(4)}_{nm}$ and $\beta^{(4)}_{nm} = b^{(4)}_{nm}$, is actually equal to the simple expression in (E.111). To confirm that they are identical, the two approaches have been applied to calculate P_i for a z-directed EHD having $p_s = 0.01$ Am and being located along the positive x-axis at a distance $r_s = 5$ mm. The respective powers are depicted in Figure E.5, which clearly demonstrates their equality.

E.3.3 Directivity

In order to determine the directivity $D(\theta, \phi)$, the radiation intensity $U(\theta, \phi)$ must first be calculated. The radiation intensity is the total power per unit solid angle, and is given by

$$U_f(\theta, \phi) = \frac{1}{2}\ r^2\ \mathcal{R}e\{\vec{E}^f_t\,(r, \theta, \phi) \times \vec{H}^{f*}_t(r, \theta, \phi)\} \cdot \hat{r}. \tag{E.113}$$

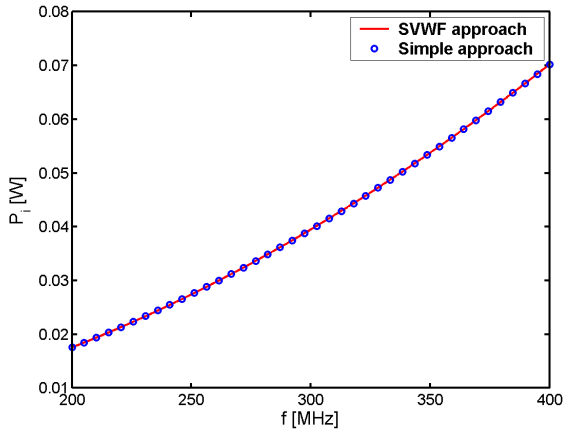

Figure E.5: *The power radiated by the EHD in free space as a function of frequency f. The power is calculated by the SVWFs approach as well as by the simple approach which does not rely on the SVWFs. Although the values of P_i are independent of the EHD location r_s, it has been selected to be $r_s = 5$ mm. See the main text for further explanations.*

Since the total solid angle subtended by a sphere is 4π radians, the total average power per unit solid angle is $P_t/4\pi$, with P_t given by (E.110). Thus, the directivity, which is the ratio of the radiation intensity $U(\theta,\phi)$ to the radiation intensity averaged over all directions, $P_t/4\pi$, reads

$$D(\theta,\phi) = \frac{U_f(\theta,\phi)}{P_t/4\pi} \,. \tag{E.114}$$

The radiation intensity, $U(\theta,\phi)$, in (E.113) can be explicitly written as

$$\begin{aligned} U_f(\theta,\phi) &= \frac{1}{2}\, r^2\, \mathcal{R}e\Big\{ \vec{E}_t^{\,f}(r,\theta,\phi) \times \vec{H}_t^{\,f*}(r,\theta,\phi) \Big\} \cdot \hat{r} \\ &= \frac{1}{2}\, r^2\, \mathcal{R}e\Big\{ E_{t,\theta}^{f}(r,\theta,\phi) H_{t,\phi}^{f*}(r,\theta,\phi) - E_{t,\phi}^{f}(r,\theta,\phi) H_{t,\theta}^{f*}(r,\theta,\phi) \Big\} \,. \end{aligned} \tag{E.115}$$

The field components in (E.115) are obtained from (E.99) and (E.100). To this end, one recalls from (E.99) and (E.100) that the far fields are

$$\vec{E}_t^{\,f}(r,\theta,\phi) = E_{t,\theta}^{f}(\theta,\phi)\,\hat{\theta} + E_{t,\phi}^{f}(\theta,\phi)\,\hat{\phi} = \Big[F_{t,\theta}(\theta,\phi)\,\hat{\theta} + F_{t,\phi}(\theta,\phi)\,\hat{\phi} \Big]\, \frac{e^{-jk_0 r}}{r} \,, \tag{E.116}$$

$$\begin{aligned} \vec{H}_t^{\,f}(r,\theta,\phi) &= H_{t,\theta}^{f}(\theta,\phi)\,\hat{\theta} + H_{t,\phi}^{f}(\theta,\phi)\,\hat{\phi} \\ &= \frac{\hat{r} \times \vec{E}_t^{\,f}(r,\theta,\phi)}{\eta_0} \\ &= \frac{\Big[F_{t,\theta}(\theta,\phi)\,\hat{\phi} - F_{t,\phi}(\theta,\phi)\,\hat{\theta} \Big]}{\eta_0}\, \frac{\exp(-jk_0 r)}{r} \,. \end{aligned} \tag{E.117}$$

In (E.116) and (E.117) the quantities $F_{t,\theta}(\theta,\phi)$ and $F_{t,\phi}(\theta,\phi)$ are the $\hat{\theta}$ - and $\hat{\phi}$ - components of the total radiation vector $\vec{F}_t(\theta,\phi) = F_{t,\theta}(\theta,\phi)\,\hat{\theta} + F_{t,\phi}(\theta,\phi)\,\hat{\phi}$, which is related to the total electric far field in (E.99) as $\vec{E}_t^{\,f}(r,\theta,\phi) = \vec{F}_t(\theta,\phi)\,\exp(-jk_0 r)/r$. In addition, $\eta_0 = \sqrt{\mu_0/\epsilon_0}$ is the intrinsic impedance of free space. Inserting these expressions into (E.115), one obtains

$$U_f(\theta,\phi) = \frac{1}{2\eta_0}\, \Big\{\, |F_{t,\theta}(\theta,\phi)|^2 + |F_{t,\phi}(\theta,\phi)|^2 \,\Big\} \,, \tag{E.118}$$

and the directivity thus becomes

$$D(\theta,\phi) = \frac{2\pi}{\eta_0}\,\frac{1}{P_t}\left\{\,|F_{t,\theta}(\theta,\phi)|^2 + |F_{t,\phi}(\theta,\phi)|^2\,\right\}, \tag{E.119}$$

with P_t being defined by (E.110).

E.4 Resonance condition for electrically small designs

In Appendix D, it was shown that that the expansion coefficient of the field exterior to a single cylinder which is illuminated by an ELS become resonant when the magnitude of the relevant determinant used in the determination of the coefficient is minimum. Moreover, this was also found to be the case with the concentric cylinder configurations, see Chapter D. For cylinders made of lossless DPS and DNG materials, this minimum was attained when the imaginary part of the determinant was set to zero. In the limit of electrically small designs, it was moreover noted that the same resonance condition applies for cylinders made of lossless DPS and DNG cylinders, as for those made of SNG materials.

By means of the same procedure as for the cylindrical counterparts, it can be shown that for lossless DPS- and DNG-based concentric spheres, the relevant expansion coefficients, i.e., $A_{4,nm}$ and $B_{4,nm}$, attain a maximum, i.e., a resonance occurs, when the imaginary part of the determinants of the matrices used to determine these coefficients is zero[E.9]. With reference to Section E.2, the matrix, which is to be inverted to determine the expansion coefficients $A_{i,nm}$ and $B_{i,nm}$, has the form

$$\bar{\bar{\Gamma}}_n = \begin{bmatrix} j_n(k_1r_1) & j_n(k_2r_1) & -y_n(k_2r_1) & 0 \\ d'_{r=r_1}\{rj_n(k_1r)\} & -\frac{\gamma_1}{\gamma_2}d'_{r=r_1}\{rj_n(k_2r)\} & -\frac{\gamma_1}{\gamma_2}d'_{r=r_1}\{ry_n(k_2r)\} & 0 \\ 0 & j_n(k_2r_2) & y_n(k_2r_2) & -h_n^{(2)}(k_0r_2) \\ 0 & d'_{r=r_1}\{rj_n(k_2r)\} & d'_{r=r_2}\{ry_n(k_2r)\} & -\frac{\gamma_2}{\gamma_3}d'_{r=r_3}\{rh_n^{(2)}(k_0r)\} \end{bmatrix}$$

$$= \begin{bmatrix} a & b & c & d \\ e & f & g & h \\ i & \jmath & k & l \\ m & n & o & p \end{bmatrix}, \tag{E.120}$$

where $\bar{\bar{\Gamma}}_n(\gamma_i = \varepsilon_i,\ i = 1,2\ ;\ \gamma_3 = \varepsilon_0) = \bar{\bar{A}}_n$ when the $A_{i,nm}$ are to be determined, and $\bar{\bar{\Gamma}}_n(\gamma_i = \mu_i,\ i = 1,2\ ;\ \gamma_3 = \mu_0) = \bar{\bar{B}}_n$ when the $B_{i,nm}$ are to be determined.

The determinant of $\bar{\bar{\Gamma}}_n$ in (E.120) reads

$$\det\bar{\bar{\Gamma}}_n = a\ [f(kp-lo) - g(\jmath p - ln)] - e\,[b(kp-lo) - c(\jmath p - ln)]$$

$$= (af-eb)(kp-lo) + (ec-ag)(\jmath p - ln)\,. \tag{E.121}$$

For lossless DPS or DNG materials, only the terms l and p are complex. One thus obtains

$$\mathcal{I}m\{\det\bar{\bar{\Gamma}}_n\} = \underbrace{(af-eb)(k\mathcal{I}m\{p\} - \mathcal{I}m\{l\}o)}_{\text{Term 1}} + \underbrace{(ec-ag)(\jmath\,\mathcal{I}m\{p\} - \mathcal{I}m\{l\}n)}_{\text{Term 2}} = 0\,, \tag{E.122}$$

which is the resonance condition. In the limit of electrically small designs, the expression in (E.122) must be evaluated for $|k_1|\rho_1 << 1$, $|k_2|\rho_1 << 1$, $|k_2|\rho_2$, and $k_0\rho_2 << 1$. To this end, the small argument expansions [119, Ch. 11]

$$j_n(x) = \frac{x^n}{(2n+1)!!}, \tag{E.123a}$$

$$y_n(x) = -\frac{(2n-1)!!}{x^{n+1}}\,, \tag{E.123b}$$

[E.9] The case of plane wave incidence on DPS spheres and the derivation of the conditions that maximize the relevant scattering coefficients has been treated in [121].

as $x \to 0$ are used. Moreover, the derivatives of these functions are evaluated by first noting that [119, Ch. 11]

$$w_n^{(c)\prime}(x) = \frac{n}{x} w_n^{(c)}(x) - w_{n+1}^{(c)}(x) \,, \tag{E.124}$$

where the prime denotes the derivative with respect to the entire argument[E.10]. As a consequence,

$$j_n'(x) = \frac{n}{x} \, \frac{x^n}{(2n+1)!!} - \frac{x^{n+1}}{(2n+3)!!} \,, \tag{E.125a}$$

$$y_n'(x) = -\frac{n}{x} \, \frac{(2n-1)!!}{x^{n+1}} + \frac{(2n+1)!!}{x^{n+2}} \,, \tag{E.125b}$$

as $x \to 0$.

Attention is first devoted to term 1 in (E.122), while term 2 in this relation is treated subsequently. One has

$$\begin{aligned}
\text{Term1} &= (af - eb)(k\mathcal{I}m\{p\} - \mathcal{I}m\{l\}o) \\
&= \Big\{ -\frac{\gamma_1}{\gamma_2} \frac{(k_1 r_1)^n}{(2n+1)!!} \left[\frac{(k_2 r_1)^n}{(2n+1)!!} + k_2 r_1 \left(\frac{n}{k_2 r_1} \frac{(k_2 r_1)^n}{(2n+1)!!} - \frac{(k_2 r_1)^{n+1}}{(2n+3)!!} \right) \right] \\
&\qquad + \frac{(k_2 r_1)^n}{(2n+1)!!} \left[\frac{(k_1 r_1)^n}{(2n+1)!!} + k_1 r_1 \left(\frac{n}{k_1 r_1} \frac{(k_1 r_1)^n}{(2n+1)!!} - \frac{(k_1 r_1)^{n+1}}{(2n+3)!!} \right) \right] \Big\} \\
&\times \Big\{ \frac{\gamma_2}{\gamma_3} \frac{(2n-1)!!}{(k_2 r_2)^{n+1}} \left[\frac{(2n-1)!!}{(k_0 r_2)^{n+1}} + k_0 r_2 \left(\frac{n}{k_0 r_2} \frac{(2n-1)!!}{(k_0 r_2)^{n+1}} - \frac{(2n+1)!!}{(k_0 r_2)^{n+2}} \right) \right] \\
&\qquad + \frac{(2n-1)!!}{(k_0 r_2)^{n+1}} \left[-\frac{(2n-1)!!}{(k_2 r_2)^{n+1}} + k_2 r_2 \left(-\frac{n}{k_2 r_2} \frac{(2n-1)!!}{(k_2 r_2)^{n+1}} + \frac{(2n+1)!!}{(k_2 r_2)^{n+2}} \right) \right] \Big\} \\
&= \frac{(2n-1)!!}{(2n+1)!!} \Big\{ (k_2 r_1)^n \left[\frac{(k_1 r_1)^n}{(2n+1)!!} + \frac{n}{(2n+1)!!} (k_1 r_1)^n - \frac{(k_1 r_1)^n (k_1 r_1)^2}{(2n+3)!!} \right] \\
&\qquad - \frac{\gamma_1}{\gamma_3} (k_1 r_1)^n \left[\frac{(k_2 r_1)^n}{(2n+1)!!} + \frac{n}{(2n+1)!!} (k_2 r_1)^n - \frac{(k_2 r_1)^n (k_2 r_1)^n}{(2n+3)!!} \right] \Big\} \\
&\times \Big\{ \frac{\gamma_2}{\gamma_3} \frac{1}{(k_2 r_2)^{n+1}} \left[\frac{(2n-1)!!}{(k_0 r_2)^{n+1}} + \frac{n(2n-1)!!}{(k_0 r_2)^{n+1}} - \frac{(2n+1)!!}{(k_0 r_2)^{n+1}} \right] \\
&\qquad - \frac{1}{(k_0 r_2)^{n+1}} \left[\frac{(2n-1)!!}{(k_2 r_2)^{n+1}} + \frac{n(2n-1)!!}{(k_2 r_2)^{n+1}} - \frac{(2n+1)!!}{(k_2 r_2)^{n+1}} \right] \Big\} \,.
\end{aligned} \tag{E.126}$$

Since

$$\frac{(2n-1)!!}{(2n+1)!!} = \frac{1}{2n+1} \,, \tag{E.127}$$

$$(2n+3)!! = (2n+1)!!(2n+3) \,, \tag{E.128}$$

the expression in (E.126) then reduces to

Term 1 =

[E.10] The relation (E.124) is used in the evaluation of terms such as $d'_{r=r_k}\{r_k w_n^{(c)}(k_i r_k)\} = w_n^{(c)}(k_i r_k) + k_i r_k w_n^{(c)\prime}(k_i r_k)$, which likewise are found in (E.122).

$$\frac{1}{2n+1}\frac{(2n-1)!!}{(2n+1)!!}\Big\{(k_2r_1)^n(k_1r_1)^n\left(1+n-\frac{(k_1r_1)^2}{2n+3}\right)-(k_1r_1)^n(k_2r_1)^n\,\frac{\gamma_1}{\gamma_2}\,\left(1+n-\frac{(k_2r_1)^2}{2n+3}\right)\Big\}$$
$$\times\Big\{\frac{1}{(k_2r_2)^{n+1}}\frac{1}{(k_0r_2)^{n+1}}\,\frac{\gamma_2}{\gamma_3}\,(1+n-(2n+1))$$
$$-\frac{1}{(k_0r_2)^{n+1}}\frac{1}{(k_2r_2)^{n+1}}\,(1+n-(2n+1))\Big\}$$

$$=\frac{1}{(2n+1)^2}\,\frac{r_1^{2n}}{r_2^{2n+2}}\,\frac{k_1^n}{k_0^n}\,\frac{1}{k_2k_0}\left\{(1+n)\frac{\gamma_2-\gamma_1}{\gamma_2}-\frac{(k_1r_1)^2}{2n+3}+\frac{\gamma_1}{\gamma_2}\frac{(k_2r_1)^2}{2n+3}\right\}n\,\frac{\gamma_3-\gamma_2}{\gamma_3}\,. \tag{E.129}$$

In similitude to the derivation of term 1, it is straightforward to demonstrate that term 2 in (E.122) reads

$$\begin{aligned}\text{Term 2}&=(ec-ag)(\jmath\,\mathcal{I}m\{p\}-\mathcal{I}m\{l\}n)\\&=\frac{1}{(2n+1)^2}\,\frac{k_1^n}{k_0^n}\,\frac{1}{k_2k_0}\,\frac{1}{r_1}\frac{1}{r_2}\,\left[(1+n)-\frac{\gamma_1}{\gamma_2}(1+n)+\frac{\gamma_1}{\gamma_2}(2n+1)-\frac{(k_1r_1)^2}{2n+3}\right]\\&\qquad\times\left[(1+n)-\frac{\gamma_2}{\gamma_3}(1+n)+\frac{\gamma_2}{\gamma_3}(2n+1)-\frac{(k_2r_2)^2}{2n+3}\right]\,.\end{aligned} \tag{E.130}$$

Since

$$\begin{aligned}&(1+n)-\frac{\gamma_1}{\gamma_2}(1+n)+\frac{\gamma_1}{\gamma_2}(2n+1)\\&=(n+1)-\frac{\gamma_1}{\gamma_2}(1+n)+\frac{\gamma_2}{\gamma_3}(1+n)+n\frac{\gamma_2}{\gamma_3}=\frac{(n+1)\gamma_2+n\gamma_1}{\gamma_2}\,,\end{aligned} \tag{E.131}$$

and similarly

$$(1+n)-\frac{\gamma_2}{\gamma_3}(1+n)+\frac{\gamma_2}{\gamma_3}(2n+1)=\frac{(n+1)\gamma_3+n\gamma_2}{\gamma_3}\,, \tag{E.132}$$

it follows that (E.130) takes on the form

$$\begin{aligned}\text{Term 2}=\frac{1}{(2n+1)^2}\,\frac{k_1^n}{k_0^n}\,\frac{1}{k_2k_0}\,\frac{1}{r_1}\frac{1}{r_2}\,&\left[(n+1)\gamma_3+n\gamma_2-\frac{(k_2r_2)^2}{2n+3}\gamma_3\right]\\&\times\left[(n+1)\gamma_2+n\gamma_1-\frac{(k_1r_1)^2}{2n+3}\gamma_2\right]\,\frac{1}{\gamma_2\gamma_3}\end{aligned} \tag{E.133}$$

According to (E.122), the resonance condition is now given by

$$-\text{Term 1}=\text{Term 2}, \tag{E.134}$$

which, when using the derived expressions for the two terms gives

$$-\frac{1}{(2n+1)^2}\,\frac{r_1^{2n}}{r_2^{2n+2}}\,\frac{k_1^n}{k_0^n}\,\frac{1}{k_2k_0}\,n(\gamma_3-\gamma_2)\,\left[(1+n)(\gamma_2-\gamma_1)-\gamma_2\frac{(k_1r_1)^2}{2n+3}+\gamma_1\frac{(k_2r_1)^2}{2n+3}\right]\,\frac{1}{\gamma_2\gamma_3}$$

$$\begin{aligned}=\frac{1}{(2n+1)^2}\,\frac{k_1^n}{k_0^n}\,\frac{1}{k_2k_0}\,\frac{1}{r_1}\frac{1}{r_2}\,&\left[(n+1)\gamma_3+n\gamma_2-\frac{(k_2r_2)^2}{2n+3}\gamma_3\right]\\&\times\left[(n+1)\gamma_2+n\gamma_1-\frac{(k_1r_1)^2}{2n+3}\gamma_2\right]\,\frac{1}{\gamma_2\gamma_3}\,.\end{aligned} \tag{E.135}$$

Since

$$\frac{r_1^{2n}}{r_2^{2n+2}}r_1r_2=\frac{r_1^{2n+1}}{r_2^{2n+1}}\,, \tag{E.136}$$

and since the terms in (E.135) that are proportional to $k_1 r_1$, $k_2 r_1$, $k_2 r_2$ are negligible compared to the other terms, it follows that

$$\frac{r_1}{r_2} \simeq \sqrt[2n+1]{\frac{[(n+1)\gamma_3 + n\gamma_2]\ [(n+1)\gamma_2 + n\gamma_1]}{n(n+1)(\gamma_2 - \gamma_3)(\gamma_2 - \gamma_1)}}\ , \tag{E.137}$$

which is the resonance condition for electrically small lossless DPS- and DNG-based concentric spheres. It is recalled that $\gamma_i = \varepsilon_i,\ i = 1, 2\ ;\ \gamma_3 = \varepsilon_0$ in (E.137) gives the condition for which the $A_{4,nm}$ are maximized, while $\gamma_i = \mu_i,\ i = 1, 2\ ;\ \gamma_3 = \mu_0$ gives the condition for which the $B_{4,nm}$ are maximized.

The resonance condition given by (E.137) has been used in Chapter 5 to determine, e.g., the approximate value of the outer radius r_2 of the electrically small structures which will excite the dominant mode of order n for various material parameters and values of the inner radius r_1.

Numerous numerical investigations of electrically small single-negative (SNG)-based concentric spheres, not included here, revealed that (E.137) is also applicable to SNG materials.

APPENDIX **F**

DRUDE AND LORENTZ DISPERSION MODELS

This appendix explains how the Drude and Lorentz dispersion models are used in this work to investigate the effects of frequency dispersion in metamaterials (MTMs). After a brief review of dispersion phenomena as it occurs in ordinary materials, the Drude and Lorentz material models are discussed. These dispersion models are examined numerically, and their ability to achieve the negative material parameters used in Chapter 4 at a desired frequency of operation is illustrated.

F.1 Introduction

As noted in Chapter 2, all materials exhibit what is known as frequency dispersion, henceforth referred to as simply dispersion. This means that their material parameters are frequency dependent.

In order to describe the frequency response of a given material several dispersion models have been developed in the literature. The Drude and Lorentz models, which are used extensively in the present work, are two important examples. Before presenting a derivation of these models, a few comments on the basics of the interaction of electromagnetic waves with materials are first given. The present exposition is based mainly on the study of [64], [77] and [115] where an excellent treatment of the relevant matters is given. In particular, [77] contains a very good introduction to the dispersion models and the theory of field interactions with materials. Accordingly, since much of that discussion is included herein, specific referencing of the individual equations used in the below derivation is omitted, but, nonetheless, they are understood to be coming from that reference.

When a given material is exposed to an electromagnetic field, its frequency response may be dominated by either the electric or the magnetic field. In a very large class of materials, known as dielectric materials, it is the response to the electric field which is dominant, and this leads to the concept of the electric susceptibility and permittivity of the material, as introduced below. Let the attention first be focused to dielectric materials, and thus their interactions with electric fields.

It is well-known that inside dielectric materials, there is no net charge and the material is charge neutral. However, once the field is applied, the positive and negative charges become displaced, and electric dipoles, with their associated electric dipole moments (EDMs), $\vec{p}_i$, are created. It is said that the dielectric material becomes polarized and the process of the creation of the electric dipoles is referred to as their polarization. Macroscopically, this polarization phenomena is accounted for by the polarization vector, $\vec{P}$, henceforth referred to as simply the polarization, which is given by

$$\vec{P} = \lim_{dv \to 0} \frac{\sum_{i=1}^{N dv} \vec{p}_i}{dv} = \lim_{dv \to 0} \frac{\vec{p}_t}{dv} \,, \tag{F.1}$$

where dv is a very small volume of the dielectric material, N is the total number of dipoles per unit volume and $\vec{p}_i$ is the EDM of the i'th dipole. Thus, the number of dipoles inside the volume dv is Ndv and the total EDM, $\vec{p}_t$, inside the volume dv is $\sum_{i=1}^{Ndv} \vec{p}_i$. In other words, the polarization (F.1) is the volume density of the EDMs. Assuming that all of the electric dipoles are identical and thus have the same EDM, $\vec{p}$, it follows that (F.1) can be expressed as

$$\vec{P} = N\vec{p} \,. \tag{F.2}$$

If the positive charge inside the dielectric material is denoted by q, the EDM $\vec{p}$ is given by

$$\vec{p} = q\vec{r} \,, \tag{F.3}$$

where $\vec{r}$ is the displacement vector of the positive and negative charges. The connection between this displacement and the polarization is then given as

$$\vec{P} = Nq\vec{r}\,. \tag{F.4}$$

As a consequence, once the displacement of the positive and negative charges inside a dielectric material is known for a given electric field, the polarization of the material is then given by (F.4). If the electric field which acts on the charges is denoted by $\vec{E}_i$, the polarization can also be expressed as

$$\vec{P} = \varepsilon_0 \chi_e \vec{E}_i\,, \tag{F.5}$$

where χ_e is the electric susceptibility of the material; a parameter that gives the response of the material to the field $\vec{E}_i$. The behaviour of a dielectric material is commonly expressed in terms of the relative permittivity, ε_r, which is related to the electric susceptibility by the relation

$$\varepsilon_r = 1 + \chi_e\,. \tag{F.6}$$

It is thus found that once the displacement $\vec{r}$ of the positive and negative charges in the material is known for a given applied field, the polarization is known as well. This in turn implies that the material response, in terms of either the electric susceptibility or the permittivity, also is known according to (F.5) and (F.6), respectively. Therefore, in order to find the response to a given electric field, one must first find the displacement, or equivalently the polarization $\vec{P}$ for a given applied field. This is done in the following for a specific time-varying electromagnetic field.

F.2 Analytical results

With the above basics in mind it is next of interest to derive some common material models for time-varying fields. As noted, e.g., in [1, Ch. 1] and [77, Ch. 19], the derivation of the Lorentz model assumes that the electrons can be treated as driven and damped harmonic oscillators, i.e., as a mass (of some charge q) connected to some elastic object of negligible mass (the spring) that is fixed at the other end (nucleus). With reference, e.g., to these two works, the governing equation of motion that describes the positions of the electrons in this case takes the form of

$$\frac{d^2\vec{r}}{dt^2} + \Gamma\frac{d\vec{r}}{dt} + \omega_0^2\vec{r} = \frac{1}{m}\vec{F}\,. \tag{F.7}$$

With reference to [77], the first term on the left-hand side (LHS) of (F.7) is responsible for the charge acceleration, the second term on the LHS is responsible for the damping mechanisms, Γ being termed the damping coefficient or the collision frequency, and the third term on the LHS is the term representing the restoring force and has the natural angular frequency ω_0. Moreover, m is the mass of the charge q, which could be a single charge or an aggregate of charges with total charge q, and $\vec{F}$ is the force driving the resulting harmonic oscillator. In the present case, the driving force is the Lorentz force given

$$\vec{F} = q(\vec{E}_i + \vec{v} \times \vec{B}_i)\,, \tag{F.8}$$

where $\vec{v}$ is the velocity of the electrons and $\vec{B}_i$ is the magnetic flux density associated with the electric field $\vec{E}_i$. Since $\vec{v} \times \vec{B}_i$ is much smaller than $\vec{E}_i$, then

$$\vec{F} = \vec{F}_e = q\vec{E}_i\,, \tag{F.9}$$

and the resulting differential equation for the displacement $\vec{r}$ thus becomes

$$\frac{d^2\vec{r}}{dt^2} + \Gamma\frac{d\vec{r}}{dt} + \omega_0^2\vec{r} = \frac{q}{m}\vec{E}_i\,. \tag{F.10}$$

Using (F.4), the differential equation in (F.10) can be expressed as

$$\frac{d^2\vec{P}}{dt^2} + \Gamma\frac{d\vec{P}}{dt} + \omega_0^2\vec{P} = \varepsilon_0\omega_p^2\vec{E}_i\,, \tag{F.11}$$

where $\omega_p^2 = Nq^2/(\varepsilon_0 m)$ is the square of the angular plasma frequency ω_p.

For a time harmonic excitation, where the time factor $\exp(j\omega t)$ is used, one can write

$$\vec{E}_i(\vec{r},t) = \mathcal{R}e\{\vec{E}_i^p e^{j\omega t}\}\ , \tag{F.12}$$

$$\vec{P}(\vec{r},t) = \mathcal{R}e\{\vec{P}^p e^{j\omega t}\}\ , \tag{F.13}$$

where $\vec{E}_i^p$ and $\vec{P}^p$ denote the electric field and polarization phasors, respectively, the differential equation in (F.11) is now transformed into the algebraic equation

$$-\omega\vec{P}^p + j\omega\Gamma\vec{P}^p + \omega_0^2\vec{P}^p = \varepsilon_0\omega_p^2\vec{E}^p\ , \tag{F.14}$$

where the time factor $\exp(j\omega t)$ has been suppressed. This relation is solved with the result

$$\vec{P}^p = \varepsilon_0\frac{\omega_p^2}{-\omega^2 + j\Gamma\omega + \omega_0^2}\vec{E}_i^p = \varepsilon_0\chi_{e,\mathrm{L}}(\omega)\vec{E}_i^p\ , \tag{F.15}$$

where $\chi_{e,L}(\omega)$ is the frequency dependent electric susceptibility. The second equality sign was obtained by recalling the result in (F.5). Using (F.6) it is found that the frequency dependent relative permittivity, $\varepsilon_{r,\mathrm{L}}(\omega)$ is

$$\varepsilon_{r,\mathrm{L}}(\omega) = 1 + \chi_{e,\mathrm{L}}(\omega) = 1 - \frac{\omega_p^2}{\omega^2 - j\Gamma\omega - \omega_0^2}\ . \tag{F.16}$$

This expression represents the frequency response of the material to the field in (F.12). It is found that the harmonic oscillator model, which is the simplest realistic model that can be constructed for the present purposes, implies a lossy (complex $\varepsilon_{r,\mathrm{L}}$) and dispersive (frequency dependent $\varepsilon_{r,\mathrm{L}}$) material. The model in (F.16) is known as the Lorentz dispersion model, and some of its interesting features are considered in Section F.3.

As noted in [77], there are several special cases of the Lorentz model (F.16). The one which is also used extensively in the present work is the Drude model. It follows from (F.7) by setting the term which represents the restoring force equal to zero. The frequency dependent permittivity, $\varepsilon_{r,\mathrm{D}}$ then takes on the following form

$$\varepsilon_{r,\mathrm{D}}(\omega) = 1 - \frac{\omega_p^2}{\omega(\omega - j\Gamma)}\ . \tag{F.17}$$

The details of this model are likewise considered in Section F.3.

The above discussion pertains to dielectric materials in which the response to the electric field is dominant. However, in certain materials it is the response to the magnetic field which is dominant, and thus these materials exhibit large magnetic responses in terms of a frequency dependent magnetic susceptibility and permeability. For example, this is the case for various magnetic materials such as ferrites. The response of magnetic materials exposed to a magnetic field is treated in similitude to the above case of dielectric materials. To this end, one may recall that although the origins of the magnetic dipoles and their moments, which give rise to the magnetic polarization, are circulating currents, they can be treated mathematically as displaced magnetic charges, see e.g., [1] and [77]. Consequently, the situation resembles the one described above for the derivation of the frequency dependent permittivity and then naturally leads to the concept of a frequency dependent magnetic susceptibility and permeability. The Lorentz and Drude models of the permeability thus will resemble those of the permittivity. Their explicit forms are presented in the following section in which a discussion of some of the interesting features of these models, as applied in the present work, is given.

F.3 Numerical results

The Drude models of the relative permittivity and permeability, respectively, read

$$\epsilon_{r,\mathrm{D}}(\omega) = \epsilon'_{r,\mathrm{D}}(\omega) - j\epsilon''_{r,\mathrm{D}}(\omega) = 1 - \frac{\omega_{pe}^2}{\omega(\omega - j\Gamma_e)}$$

$$= 1 - \frac{\omega_{pe}^2}{\omega^2 + \Gamma_e^2} - j\frac{\omega_{pe}^2}{\omega(\omega^2 + \Gamma_e^2)} \,, \tag{F.18a}$$

$$\mu_{r,\mathrm{D}}(\omega) = \mu'_{r,\mathrm{D}}(\omega) - j\mu''_{r,\mathrm{D}}(\omega) = 1 - \frac{\omega_{pm}^2}{\omega(\omega - j\Gamma_m)}$$
$$= 1 - \frac{\omega_{pm}^2}{\omega^2 + \Gamma_m^2} - j\frac{\omega_{pm}^2}{\omega(\omega^2 + \Gamma_m^2)} \,, \tag{F.18b}$$

while the corresponding Lorentz models read

$$\epsilon_{r,\mathrm{L}}(\omega) = \epsilon'_{r,\mathrm{L}}(\omega) - j\epsilon''_{r,\mathrm{L}}(\omega) = 1 - \frac{\omega_{pe}^2}{\omega^2 - j\Gamma_e\omega - \omega_{er}^2}$$
$$= 1 - \frac{\omega_{pe}^2(\omega^2 - \omega_{er}^2)}{(\omega^2 - \omega_{er}^2)^2 + (\Gamma_e\omega)^2} - j\frac{\omega\Gamma_e\omega_{pe}^2}{(\omega^2 - \omega_{er}^2)^2 + (\Gamma_e\omega)^2} \,, \tag{F.19a}$$

$$\mu_{r,\mathrm{L}}(\omega) = \mu'_{r,\mathrm{L}}(\omega) - j\mu''_{r,\mathrm{L}}(\omega) = 1 - \frac{\omega_{pm}^2}{\omega^2 - j\Gamma_m\omega - \omega_{mr}^2}$$
$$= 1 - \frac{\omega_{pm}^2(\omega^2 - \omega_{mr}^2)}{(\omega^2 - \omega_{mr}^2)^2 + (\Gamma_m\omega)^2} - j\frac{\omega\Gamma_m\omega_{pm}^2}{(\omega^2 - \omega_{mr}^2)^2 + (\Gamma_m\omega)^2} \,. \tag{F.19b}$$

In the above relations ω_{pe} and ω_{pm} are the electric and magnetic plasma frequencies, while Γ_e and Γ_m are the electric and magnetic collision frequencies (also termed damping factors, see Chapter 2). In the Lorentz models, ω_{er} and ω_{mr} are the resonance frequencies of the permittivity and permeability, respectively. For the Drude model, the collision frequencies control the imaginary parts of the material parameters and, hence, their losses. The plasma frequencies mainly control the zero crossings of the real parts of these models and, hence, the real parts of the relative permittivity and permeability. For the Lorentz models, which are resonant, the collision frequencies control the width of the resonances and the plasma frequencies control the amplitudes of the peaks of these resonant responses.

Henceforth, the relative permittivity and permeability are referred to as simply the permittivity and permeability, respectively. It is explained how these models are used in the simulations performed in this work.

In order to account for dispersion in a material, the above models can be designed to yield the desired material parameters at a specified frequency of operation. From Chapters 4 and 5 it is recalled that the two models were designed in a manner which ensures that the real parts of the so-obtained material parameters resemble, at the frequency of operation $f_0 = 300$ MHz, the lossless material parameters used in the initial numerical studies in these chapters.

Thus, as the first step, one must select, e.g., the values of the real part of the material parameters that the respective models must produce at the specified frequency of operation. Below, these models are designed such that $\epsilon'_{r,\mathrm{D}}(\omega_0) = \epsilon'_{r,\mathrm{L}}(\omega_0) \equiv \epsilon'_r(\omega_0) = -1$ and $\mu'_{r,\mathrm{D}}(\omega_0) = \mu'_{r,\mathrm{L}}(\omega_0) \equiv \mu'_r(\omega_0) = -4$, where $\omega_0 = 2\pi f_0$ is the angular frequency of operation. From Chapter 4 it is recalled that these are the material parameters of the lossless dipolar DPS-DNG structures. As the second step, the collision frequencies must be assumed. Corresponding to the assumption of lossy material parameters, they are set to zero. If lossy models are desired, the collision frequencies are set to positive non-zero values. For both the Drude and Lorentz models, the assumption

$$\Gamma_e \;=\; \Gamma_m \;=\; \xi_e\omega_t \;=\xi_m\omega_t \;=\; \xi\omega_0 \;=\; 10^{-5}\omega_0. \tag{F.20}$$

is made. This means that the electric and magnetic losses are equal and, furthermore, that they are small but not negligible. As the third step, the values of ω_{pe}^2 and ω_{pm}^2 must be determined. For the Drude

model, these are determined from the real parts of (F.18a) and (F.18b), respectively, evaluated at ω_0 to recover the specified real parts of the material parameters. With the relation (F.20), it is found that

$$\begin{bmatrix} \omega_{pe}^2 \\ \omega_{pm}^2 \end{bmatrix} = \left[1 - \begin{pmatrix} \epsilon_r'(\omega_0) \\ \mu_r'(\omega_0) \end{pmatrix}\right] \left(1+\xi^2\right) \omega_0^2 \,. \tag{F.21}$$

For the Lorentz model ω_{pe}^2 and ω_{pm}^2 in (F.19a) and (F.19b), respectively, are determined from the real part of (F.19a) and (F.19b), respectively, likewise evaluated at ω_0 to recover specified real parts of the material parameters. Thus,

$$\begin{bmatrix} \omega_{pe}^2 \\ \omega_{pm}^2 \end{bmatrix} = \frac{1}{(\omega_t^2 - \omega_{er(mr)}^2)} \left[1 - \begin{pmatrix} \epsilon_r'(\omega_0) \\ \mu_r'(\omega_0) \end{pmatrix}\right] \left[(\omega_0^2 - \omega_{er(mr)}^2)^2 + \xi^2 \omega_{er(mr)}^2 \omega_0^2\right]. \tag{F.22}$$

When the design objective is to determine the values of ω_{pe}^2 (ω_{pm}^2) in the Lorentz models, it is the resonant frequency $\omega_{er} = 2\pi f_{er}$ ($\omega_{mr} = 2\pi f_{mr}$) which must be selected first and then the plasma frequencies are calculated. In both the electric and magnetic cases, the resonance frequency is chosen to be $f_{er} = f_{mr} = 290$ MHz. With the assumption of small losses, this means that the frequency of operation must lie far above the resonance frequency of the material parameters in order to obtain the required negative material parameters.

Next, it is of interest to examine numerically the frequency behaviour of the permittivity and permeability. First, the results obtained by the Drude model are shown, and second, those obtained by the Lorentz model are shown.

Figure F.1 shows $\epsilon_{r,\mathrm{D}}'(\omega)$, $\mu_{r,\mathrm{D}}'(\omega)$ as well as $\epsilon_{r,\mathrm{D}}''(\omega)$ and $\mu_{r,\mathrm{D}}''(\omega)$. As can be observed in this figure, these models indeed recover the desired values of $\epsilon_{r,\mathrm{D}}'(\omega_0) = -1$ and $\mu_{r\mathrm{D}}'(\omega_0) = -4$ at $f_0 = 300$ MHz. As to the imaginary parts of the material parameters, it also is observed that the losses are very small, this being in compliance with the low value of the collision frequencies selected in (F.20).

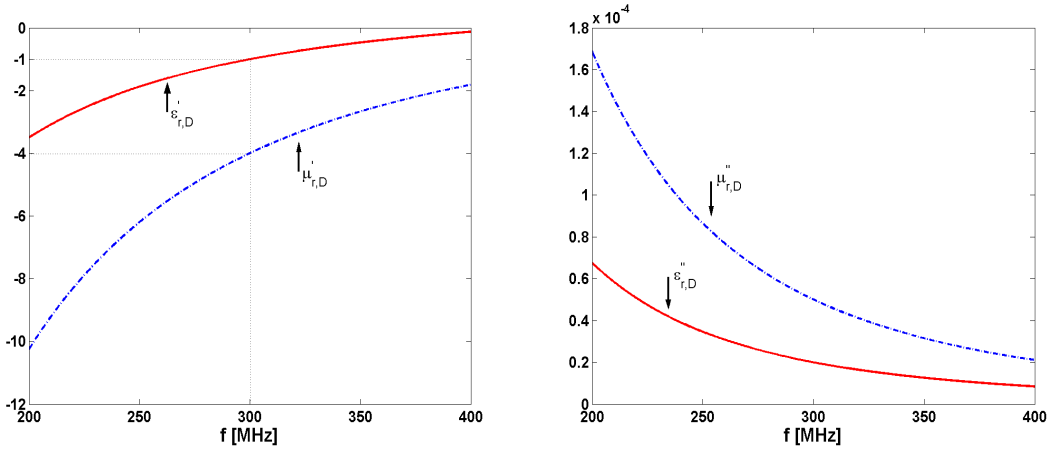

(a) (b)

Figure F.1: *The Drude dispersion model. (a) the real parts $\epsilon_{r,D}'(\omega)$ and $\mu_{r,D}'(\omega)$, and (b) the imaginary parts $\epsilon_{r,D}''(\omega)$ and $\mu_{r,D}''(\omega)$. Note that $\omega = 2\pi f$.*

Figure F.2 shows the results obtained for the Lorentz model. As can be observed in this figure, the Lorentz model is highly resonant. A narrower frequency range is required to illuminate the details because of the sharpness of the resonance when the losses are small. It is found that $\epsilon_{r,\mathrm{L}}''(\omega)$ and $\mu_{r,\mathrm{L}}''(\omega)$ both have their peak amplitudes at the resonance frequency 290 MHz, i.e., the losses are the largest at the resonance frequency of the material parameters. In the frequency region slightly below and above the resonance frequency, abnormal dispersion occurs, i.e., in this region $\epsilon_{r,\mathrm{L}}'(\omega)$ and $\mu_{r,\mathrm{L}}'(\omega)$ have negative slopes with respect to the frequency. For frequencies further away from the resonance frequency, regions of normal

dispersion occur, i.e., those for which $\epsilon_r'(\omega)$ and $\mu_r'(\omega)$ have positive slopes. Although it is difficult to observe from the figure, it has been verified that the desired values of $\epsilon_{r,\mathrm{L}}'(\omega_0) = -1$ and $\mu_{r,\mathrm{L}}'(\omega_0) = -4$ are indeed obtained at $f_0 = 300$ MHz, in a region of normal dispersion, slightly to the right of the resonance frequency of the material parameters.

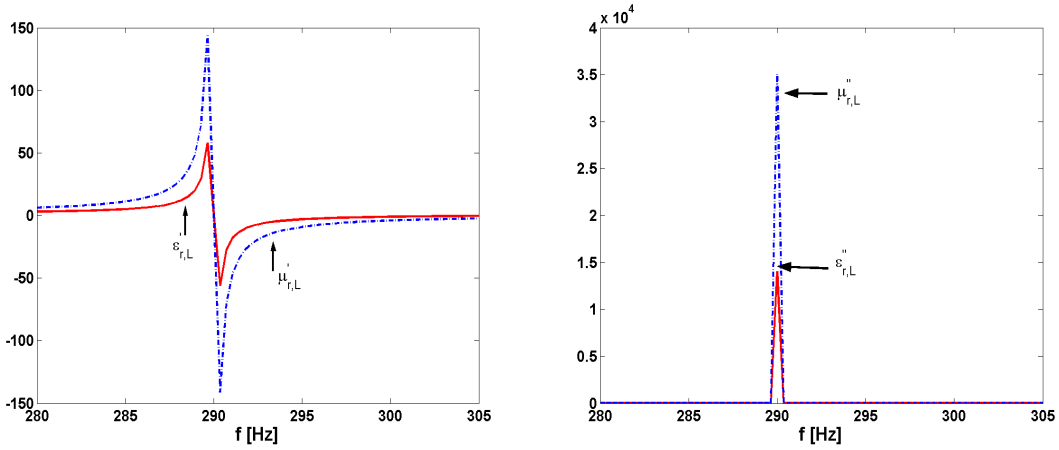

(a) (b)

Figure F.2: *The Lorentz dispersion model. (a) the real parts $\epsilon_{r,L}'(\omega)$ and $\mu_{r,L}'(\omega)$, and (b) imaginary parts $\epsilon_{r,L}''(\omega)$ and $\mu_{r,L}''(\omega)$. Note that $\omega = 2\pi f$.*

Bibliography

[1] N. Engheta and R.W. Ziolkowski, Eds., *Metamaterials: physics and engineering explorations*, John Wiley & Sons, 2006.

[2] C. Caloz and T. Itoh, *Electromagnetic metamaterials: transmission line theory and microwave applications - the engineering approach*, John Wiley & Sons, 2006.

[3] G. Eleftheriades and K. G. Balmain, *Negative-refraction metamaterials - fundamental principles and applications*, John Wiley & Sons, 2005.

[4] V. G. Veselago, "The electrodynamics of substances with simultaneously negative values of ε and μ," *Sov. Phys. Usp.*, vol. 10, no. 4, pp. 509-514, 1968.

[5] J. B. Pendry, A. J. Holden, W. J. Stewart, and I. Youngs, "Extremely low frequency plasmons in metallic meso structures," *Phys. Rev. Lett.*, vol. 76, no. 25, pp. 4773-4776, June 1996.

[6] J. B. Pendry, A. J. Holden, D. J. Robbins, and W. J. Stewart, "Low frequency plasmons in thin wire structures," *J. Phys. Condens. Matter*, vol. 10, pp. 4785-4809, 1998.

[7] J. B. Pendry, A. J. Holden, D. J. Robbins, and W. J. Stewart, "Magnetism from conductors and enhanced nonlinear phenomena," *IEEE Trans. Microwave Theory Techniques*, vol. 47, no. 11, pp. 2075-2084, Nov. 1999.

[8] D. R. Smith, W. J. Padilla, D. C. Vier, S. C. Nemat-Nasser, and S. Schultz, "Composite medium with simultaneously negative permeability and permittivity," *Phys. Rev. Lett.*, vol. 84, no. 18, pp. 4184-4187, May 2000.

[9] D. R. Smith, D. C. Vier, N. Kroll, S. Schultz, "Direct calculation of permeability and permittivity for a left-handed metamaterial," *Appl. Phys. Lett.*, vol. 77, no. 14, pp. 2246-2248, Oct. 2000.

[10] R. A. Shelby, D. R. Smith, S. C. Nemat-Nasser, and S. Schultz, "Microwave transmission through a two-dimensional, isotropic, left-handed metamaterial," *Appl. Phys. Lett.*, vol. 78, no. 4, pp. 489-491, Jan. 2001.

[11] J.B. Pendry, "Negative refraction makes a perfect lens," *Phys. Rev. Let.*, vol. 85, no. 18, pp. 3966-3969, 2000.

[12] R. W. Ziolkowski and E. Heyman, "Wave propagation in media having negative permittivity and permeability," *Phys. Rev. E*, vol. 64, 056 625, 2001.

[13] C. Caloz, C.-C. Chang, and T. Itoh, "Full-wave verification of the fundamental properties of left-handed materials in waveguide configurations," *J. Appl. Phys.*, vol. 90, pp. 5483-5486, Dec. 2001.

[14] D. R. Smith and N. Kroll, "Negative refractive index in left-handed materials," *Phys. Rev. Lett.*, vol. 85, no. 14, pp. 2933-2936, Oct. 2000.

[15] R. A. Shelby, D. R. Smith, and S. Schultz, "Experimental verification of a negative index of refraction," *Science*, vol. 292, no. 5514, pp. 77-79, Apr. 2001.

[16] C. G. Parazzoli, R. B. Greegor, K. Li, B. E. C. Koltenbah, and M. Tanielian, "Experimental verification and simulation of negative index of refraction using Snell's law," *Phys. Rev. Lett.*, vol. 90, 107 401, 2003.

[17] G. V. Eleftheriades, A. K. Iyer, and P. C. Kremer, "Planar negative refractive index media using periodically L-C loaded transmission lines," *IEEE Trans. Microw. Theory Tech.*, vol. 50, no. 12, pp. 2702-2712, Dec. 2002.

[18] S. A. Ramakrishna, and O. J. F. Martin, "Resolving the wave vector in negative refractive index media," *Optics Lett.*, vol. 30, no. 19, pp. 2626-2628, Oct. 2005.

[19] N. Garcia, and M. Nieto-Vesperinas, "Left-handed materials do not make a perfect lens," *Phys. Rev. Let.*, vol. 88, no. 20, pp. 4031-4034, May 2002.

[20] V. G. Veselago, "Left-handed materials and phenomena of negative refraction," *27th ESA Antenna Workshop on Innovative Periodic Antennas*, pp. 13-20, Santiago de Compostela, Spain, March 9-11, 2004.

[21] S. Arslanagic and O. Breinbjerg, "A note on the sign of some important parameters in double-negative materials," *Internal Report*, IR 781, ElectroScience, Ørsted•DTU, Technical University of Denmark, March, 2007.

[22] I. V. Lindell, S. A. Tretyakov, K. I. Nikoskinen, and S. Iivonen, "BW media - media with negative parameters, capable of supporting backward waves," *Microwave Opt. Technol. Lett.*, vol. 31, no. 2, pp. 129-133, Oct. 2001.

[23] A. L. Pokrovsky and A. L. Efros, "Sign of refractive index and group velocity in left-handed media ," *Solid State Commun.*, vol. 124, pp. 283-287, 2002.

[24] J. Pendry, "Perfect cylindrical lenses," *Optics Express*, vol. 11, no.7, pp. 755-760, Apr. 2003.

[25] S. A. Ramakrishna and J. Pendry, "Spherical perfect lens: solutions of Maxwell's equations for spherical geometry," *Phys. Rev. B*, vol. 68, 115 115, 2004.

[26] N. Fang and X. Zhang, "Imaging properties of a metamaterial superlens," *Appl. Phys. Lett.*, vol. 82, no.2, 161-163, Jan. 2003.

[27] L. Shen and S. He, "Studies of imaging characteristics for a slab of a lossy left-handed material," *Phys. Lett. A*, vol. 309, pp. 298-305, 2003.

[28] P. F. Loshialpo, D. L. Smith, D. W. Forester, and F. J. Rachford, "Electromagnetic waves focused by a negative-index planar lens," *Phys. Rev. E*, vol. 67, 025 602, 2003.

[29] R. Marqués and J. Baena, "Effects of losses and dispersion on the focusing properties of left-handed media," *Microwave Opt. Technol. Lett.*, vol. 41, no. 4, pp. 290-294, May 2004.

[30] A. N. Lagarkov and V. N. Kissel, "Near-perfect imaging in a focusing system based on a left-handed-material plate," *Phys. Rev. Lett.*, vol. 92, no.7, 077 401, Feb. 2004.

[31] J. D. Wilson, Z. D. Schwartz, "Multifocal flat lens with left-handed metamaterial," *Appl. Phys. Lett.*, vol. 86, 021 113, 2005.

[32] A. Grbic and G. Eleftheriades, "Overcoming the diffraction limit with a planar left-handed transmission-line lens," *Phys. Rev. Lett.*, vol. 92, no. 11, 117 403, March, 2004.

[33] N. Engheta, "An idea for thin subwavelength cavity resonators using metamaterials with negative permittivity and permeability," *IEEE Antennas Wireless Propag. Lett.*, vol. 1, no. 1, pp. 10-13, 2002.

[34] S. Hrabar, J. Bartolic, and Z. Sipus, "Experimental investigation of subwavelength resonator based on backward-wave meta-material," *in Proc. IEEE AP-S*, Monterey, 2004, pp. 2568-2571.

[35] Y. Li, L. Ran, H. Chen, J. Huangfu, X. Zhang, K. Chen, T. M. Grzegorczyk, and J. A. Kong, "Experimental realization of a one-dimensional LHM-RHM resonator," *IEEE Trans. Microwave Theory Tech.*, vol. 53, no. 4, pp. 1522-1526, Apr. 2004.

[36] A. Alú and N. Engheta, "Sub-wavelength resonant structures containing double-negative (DNG) or single-negative (SNG) media: planar, cylindrical, and spherical cavities, waveguides, and open scatterers," *Progress In Electromagnetic Research*, Waikiki, HI, Oct. 13-16, 2003, p. 12.

[37] A. Alú and N. Engheta, "Resonances in sub-wavelength cylindrical structures made of pairs of double-negative (DNG), and double-positive (DPS) or ε-negative (ENG) and μ-negative (MNG) coaxial shells," *in Proc. Intl. Conference on Electromagnetics in Advanced Applications*, Turin, Italy, Sept. 8-12, 2003, p. 210.

[38] A. Alú and N. Engheta, "Guided modes in a waveguide filled with a pair of single-negative (SNG), double-negative (DNG) and/or double-positive (DPS) layers," *IEEE Trans. Microwave Theory Tech.*, vol. 52, no. 1, pp. 199-210, Jan. 2004.

[39] R. Marqués, J. Martel, F. Mesa, and F. Medina, "Left-handed simulation and transmission of EM waves in subwavelength split-ring resonator-loaded metallic waveguides," *Phys. Rev. Lett.*, vol. 89, no. 18, 183 901, Oct. 2002.

[40] P. A. Belov and C. R. Simovski, "Subwavelength metallic waveguides loaded by uniaxial resonant scatterers," *Phys. Rev. E*, vol 72, 036 618, 2005

[41] S. Hrabar, J. Bartolic, and Z. Sipus, "Waveguide miniaturization using uniaxial negative permeability material," *IEEE Trans. Antennas Propag.*, vol. 53, no. 1, pp. 110-119, Jan. 2005.

[42] A. Alú and N. Engheta, "Achieving transparency with plasmonic coatings," *Phys. Rev. E*, vol. 72, 016 623, July 2005.

[43] V. Kuzmiak, and A. A. Maradudin, "Scattering properties of a cylinder fabricated from a left-handed material," *Phys. Rev. B.*, vol. 66, pp. 1161-1167, July 2002.

[44] R. Ruppin, "Intensity distribution inside scatterers with negative-real permittivity and permeability," *Microwave Opt. Technol. Lett.*, vol. 36, pp. 150-154, Feb. 2003.

[45] R. Ruppin, "Surface polaritons and extinction properties of a left-handed cylinder," *J. Phys.: Condens. Matter.*, vol. 16, pp. 5991-5998, Aug. 2004.

[46] M. M. Khodier, "Radiation characteristics of an infinite line source surrounded by concentric shells of metamaterials," *in Proc. IEEE AP-S* , Monterey, CA, June 20-26, 2004.

[47] S. R. Nelatury, "Comparing double-negative and double-positive covers around a radiating line current," *Microwave Opt. Technol. Lett.*, vol. 48, pp. 250-252, Feb. 2006.

[48] A. Alú and N. Engheta, "Polarizabilities and effective parameters for collections of spherical nano-particles of concentric double-negative (DNG), single-negative (SNG) and/or double-positive (DPS) metamaterial layers," *J. Appl. Phys.*, vol. 97, 094 310, May 2005.

[49] A. Shooshtari and A. R. Sebak, "Electromagnetic scattering by parallel metamaterial cylinders," *Progress In Electromagnetic Research*, PIER 57, pp. 165-177, 2006.

[50] C. Li and Z. Shen, "Electromagnetic scattering by a conducting cylinder coated with metamaterials," *in Proc. Progress in Electromagnetic Research Society*, Honolulu, Hawaii, pp. 91-105, 2003.

[51] Z. Liu, Z. Lin, and S. T. Chui, "Electromagnetic scattering by spherical negative-refractive index particles: low-frequency resonance and localization parameters," *Phys. Rev. E*, vol. 69, 016 619, 2004.

[52] R. Ruppin, "Extinction properties of a sphere with negative permittivity and permeability," *Solid State Commun.*, vol. 116, pp. 411-415, 2000.

[53] J. Sun, W. Sun, T. Jiang, and Y. Feng, "Directive electromagnetic radiation of a line source scattered by a conducting cylinder coated with left-handed material," *Microwave Opt. Technol. Lett.*, vol. 47, pp. 274-279, Nov. 2005.

[54] A.-K. Hamid, "Study of lossy effects on the characteristics of axially slotted circular or elliptical cylindrical antennas coated with metamaterials," *IEE Proc.-Microw: Antennas Propag.*, vol. 152, no. 6, pp. 485-490, Dec. 2005.

[55] B.-I. Wu, W. Wang, J. Pacheco, X. Chen, J. Lu, T. M. Grzegorczyk, J. A. Kong, P. Kao, P. A. Theophelakes, and M. J. Hogan, "Anisotropic metamaterials as antenna substrate to enhance directivity," *Microwave and Opt. Technol. Lett.*, vol. 48, no. 4, pp. 680-683, Apr. 2006.

[56] R. W. Ziolkowski and A. Kipple, "Application of double negative metamaterials to increase the power radiated by electrically small antennas," *IEEE Trans. Antennas Propag.*, vol. 51, no. 10, pp. 2626-2640, Oct. 2003.

[57] R. W. Ziolkowski and A. Kipple, "Reciprocity between the effects of resonant scattering and enhanced radiated power by electrically small antennas in the presence of nested metamaterial shells," *Phys. Rev. E*, vol. 72, 036602, Sept. 2005.

[58] R. W. Ziolkowski and A. Erentok, "Metamaterial-based efficient electrically small antennas," *IEEE Trans. Antennas Propag.*, vol. 54, no. 7, pp. 2113-2130, July 2006.

[59] R. W. Ziolkowski and A. Erentok, "At and beyond the Chu limit: passive and active broad bandwidth metamaterial-based efficient electrically small antennas," submitted to *IEE Proceedings*, Dec. 2005.

[60] S. A. Tretyakov, S. I. Maslovski, A. A. Sochava, and C. R. Simovski, "The influence of complex material coverings on the quality factor of simple radiating systems," *IEEE Trans. Antennas Propag.*, vol. 53, no. 3, pp. 965-970, Mar. 2005.

[61] H. R. Stuart and A. Pidwerbetsky,"Electrically small antenna elements using negative permittivity resonators," *IEEE Trans. Antennas Propag.*, vol. 54, no. 6, pp. 1644-1653, June 2006.

[62] S. F. Mahmoud, "A new miniaturized annular ring patch resonator partially loaded by a metamaterial ring with negative permeability and permittivity," *IEEE Antennas Wireless Propag. Lett*, vol. 3, pp. 19-22, Nov. 2004.

[63] A. Alú, F. Bilotti, N. Engheta, and L. Vegni,"Subwavelength, compact, resonant patch antennas loaded with metamaterials," *IEEE Trans. Antennas Propag.*, vol. 55, no. 1, pp. 13-25, Jan. 2007.

[64] J. A. Kong, *Electromagnetic wave theory*, EMW Publishing, 2000.

[65] R.E. Collin, *Field theory of guided waves*, John Wiley & Sons, 1991.

[66] J.D. Joannopoulos, R.D. Meade and J.N.Winn, *Photonic crystals*, Princeton University Press, 1995.

[67] E. Yablonovitch, "Photonic band-gap structures," *J. Opt. Soc. Am. B*, vol. 10, no. 2. pp. 283-295, 1993.

[68] D. Sievenpiper, L. Zhang, R. F. J. Broas, N.G. Alexopoulus, and E. Yablonovitch, "High-impedance electromagnetic surfaces with a forbidden frequency band," *IEEE Trans. Microwave Theory Techniques*, vol. 47, no. 11, pp. 2059-2074, 1999.

[69] J. McVay, N. Engheta, and A. Hoorfar, "High-impedance metamaterial surfaces using Hilbert-curve inclusions," *IEEE Microwave Wireless Components Lett.*, vol. 14, no. 3, pp. 130-132, 2004.

[70] J. McVay, N. Engheta, and A. Hoorfar, "Peano high-impedance surfaces," *Radio Sci.*, vol. 40, RS6S03, 2005.

[71] S. A. Tretyakov, "Research on negative refraction and backward.wave media: a historical perspective," *in Proc. Latsis Symposium*, Lausanne, Switzerland, pp. 30-35, March, 2005.

[72] P. Belov, "Analyical modelling of metamaterials and a new principle of sub-wavelength imaging," *PhD. Thesis, Report S 284*, Helsinki University of Technology, Sept. 2006.

[73] A. Lakhtakia, M. W. McCall, and W. S. Weiglhofer, "Brief overview of recent developments on negative phase-velocity mediums (alias left-handed materials)," *Int. J. Electron. Commun.*, vol. 56, no. 6, pp. 407-410, 2002.

[74] J. Brown, "Artificial dielectrics having refractive indices less than unity," *Proc. IEEE*, vol. 100, no. 62R, pp. 51-62, 1953.

[75] W. Rotman, "Plasma simulations by artificial dielectrics and parallel-plate media," *IRE Trans. Ant. Propag.*, vol. 10, pp. 82-85, 1962.

[76] S. A. Schelkunoff and H. T. Friis, *Antennas: theory and practice*, John Wiley & Sons, 1952.

[77] J. R. Reitz, F. J. Milford, and R. W. Christy, *Foundations of electromagnetic theory*, *Addison-Wesley*, 4th ed., 1993.

[78] A. Kipple, "Fundamental investigations of double-negative (DNG) metamaterials including applications for antenna systems," *PhD. Thesis*, The University of Arizona, 2004.

[79] S. O'Brien and J. Pendry, "Magnetic activity at infrared frequencies in structured metallic photonic crystals," *J. Phys. Condens. Matter*, vol. 14, pp. 6383-6394, 2002.

[80] S. O'Brien, D. McPeake, S. A. Ramakrishna, and J. Pendry, "Near-infrared photonic band gaps and nonlinear effects in negative magnetic metamaterials," *Phys. Rev. B*, vol. 69, 241 101, 2004.

[81] C. R. Simovski and S. He, "Frequency range and explicit expressions for negative permittivity and permeability for an isotropic medium formed by a lattice of perfectly conducting omega particles based on the quasi-static Lorentz theory," *Phys. Lett. A*, vol. 311, pp. 254-263, 2003.

[82] J. Huangfu, L. Ran, H. Chen, X. Zhang, K. Chen, T. Grzegorczyk, and J. Kong, "Experimental confirmation of negative refractive index of a metamaterial composed of Ω-like metallic patters," *Appl. Phys. Lett*, vol. 84, pp. 1537-1539, Mar. 2004.

[83] L. Ran, J. Huangfu, H. Chen, X. Zhang, K. Chen, T. Grzegorczyk, and J. Kong, "Experimental study of several left-handed metamaterials," *Progress in Electromagnetic research, PIER*, vol. 51, pp. 249-279, 2005.

[84] H. Chen, L. Ran, J. Huangfu, X. Zhang, K. Chen, T. Grzegorczyk, and J. Kong, "Left-handed metamaterials composed of only S-shaped resonators," *Phys. Rev. E*, vol. 70, 057 605, 2004.

[85] R. W. Ziolkowski, "Design, fabrication, and testing of double negative materials," *IEEE Trans. Antennas Propag.*, vol. 51, no. 7, pp. 1516-1529, July 2003.

[86] R. Margués, F. Medina, and R. Rafii-El-Idrissi, "Role of bianisotropy in negative permeability and left-handed materials," *Phys. Rev. B*, vol. 65, 144 440 , 2002.

[87] R. Margués, J. Martel, F. Mesa, and F. Medina, "A new 2D isotropic left-handed metamaterial design: theory and experiment," *Microwave Opt. Technol. Lett.*, vol. 36, pp. 405-408, 2002.

[88] P. G.-Balmaz and O. J. F. Martin, "Efficient isotropic magnetic resonators," *Appl. Phys. Lett.*, vol. 81, pp. 939-941, July, 2002.

[89] C. L. Holloway, E. F. Kuester, J. Baker-Levis, and P. Kabos, "A double negative (DNG) composite medium composed of magnetodielectric spherical particles embedded in a matrix," *IEEE Trans. Antennas Propagat.*, vol. 51, no. 10, pp. 2596-2603, Oct. 2003.

[90] O. G. Vendik and M. S. Gashinova, "Artificial double negative (DNG) media composed by two different dielectric sphere lattices embedded in a dielectric matrix," *in Proc. European Microwave Conf.*, Amsterdam, The Netherlands, pp. 1209-1212. Oct. 2004.

[91] T. Koschny, L. Zhang, and C. Soukoulis, "Isotropic three-dimensional left-handed metamaterials," *Phys. Rev. B*, vol. 71, 121 103, 2005.

[92] A. A. Oliner, "A periodic-structure negative-refractive-index medium without resonant elements ," *in URSI Digest, IEEE AP-S USNC/URSI National Radio Science Meeting*, San Antonio, TX, USA, p. 41, June 2002.

[93] C. Caloz and T. Itoh, "Application of the transmission line theory of left-handed (LH) materials to the realization of a microstrip LH transmission line," *in Proc. IEEE AP-S USNC/URSI National Radio Science Meeting*, vol. 2, San Antonio, TX, USA, pp. 412-415, June 2002.

[94] A. K. Iyer and G. Eleftheriades, "Negative refractive index metamaterials supporting 2-D waves," *in Proc. IEEE MTT Int. Symp.*, vol. 2, Seattle, WA, USA, pp. 412-415, June 2002.

[95] A. Sanada, C. Caloz, and T. Itoh, "Characteristics of the composite right/left handed transmission lines," *IEEE Microwave Wireless Compon. Lett.*, vol. 14, no. 2, pp. 68-70, Feb. 2004.

[96] P. Russer and Michael Zedler, "Three-dimensional metamaterials," *in Proc. IVth. Int. Workshop on Electromagnetic Wave Scattering*, Gebze, Turkey, pp. 8.3-8.8, Sept. 2006.

[97] V. A. Podolskiy, A. K. Sarychev, and V. M. Shalaev, "Plasmon modes in metal nanowires and left-handed materials," *J. Nonlin. Opt. Phys.*, vol. 11, no. 3, pp. 65-74, 2002.

[98] N. Engheta, "Ideas for double-negative metamaterials, negative-index nano-layers, nano-circuit elements and transmission lines at optical frequencies," *in Proc. Latsis Symp.*, Lausanne, Switzerland, pp. 54-56, March 2005.

[99] T. J. Yen, W. Padilla, N. Fang, D. Vier, D. Smith, J. Bendry, D. Basov, and X. Zhang, "Terahertz magnetic response from artificial materials," *Science*, vol. 303, pp. 1494-1496, March 2004.

[100] S. Linden, C. Enkrich, M. Wegener, J. Zhou, T. Koschny, and C. Soukoulis, "Magnetic response of metamaterials at 100 THz," *Science*, vol. 306, pp. 1351-1353, 2004.

[101] N. Wongkasem, A. Akyurtlu, J. Li, A. Tibolt, K. Zhang, and W.D. Goodhue, "Novel braodband terahertz negative refractive index metamaterials," *Progress In Electromagnetic Research*, PIER 64, pp. 205-218, 2006.

[102] M. Duncan (Ed.), "Focus issue: negative refraction and metamaterials," *Optic Express*, vol. 11, no.7, Apr. 2003.

[103] R. W. Ziolkowski and N. Engheta (Eds.), "Special issue on metamaterials," *IEEE Trans. Antennas Propag.*, vol. 51, no.10, Oct. 2003.

[104] T. Itoh and A. A. Oliner (Eds.), "Special issue on metamaterial structures, phenomena and applications " *IEEE Trans. Microw. Theory Tech.*, Vol. 53, No. 4, Apr. 2005.

[105] F. Martín and A. Toscano, (Eds.), "Special issue on metamaterials and special materials for electromagnetic applications and TLC," *Microwave Opt. Technol. Lett.*, vol. 48, no. 12, Dec. 2006.

[106] D. R. Smith, J. B. Pendry, and M. C. K. Wiltshire, "Metamaterials and negative refractive index," *Science*, vol. 305, pp. 788-792, Aug. 2004.

[107] N. Engheta and R. W. Ziolkowski, "A positive future for double negative metamaterials," *IEEE Trans. Antennas Propag.*, vol. 53, no. 4, pp. 1535-1556, April 2005.

[108] T. M. Grzegorczyk and J. A. Kong, "Review of left-handed metamaterials: evolution from theoretical and numerical studies to potential applications," *J. of Electromagn. Waves and Appl.*, vol. 20, no. 14, pp. 2053-2064, 2006.

[109] H. Chen, B.-I. Wu, and J. A. Kong, "Review of electromagnetic theory in left-handed materials," *J. of Electromagn. Waves and Appl.*, vol. 20, no. 15, pp. 2137-2151, 2006.

[110] A. von Hippel, *Dielectrics and waves*, Artech House, New ed., 1994.

[111] J. A. Stratton, *Electromagnetic theory*, McGraw-Hill, 1941.

[112] M. Born and E. Wolf, *Principles of optics*, Cambridge University Press, 6th ed., 1980.

[113] R. F. Harrington, *Time-harmonic electromagnetic fields*, McGraw-Hill, 1961.

[114] S. Ramo, J. R. Whinnery, and T. Van Duzer, *Fields and waves in communication electronics*, John Wiley & Sons, 3rd ed., 1994.

[115] D. K. Cheng, *Field and wave electromagnetics*, Addison-Wesley, 2nd ed., 1989.

[116] M. Kerker and C. G. Blatchford, "Elastic scattering, absorption, and surface-enhanced Raman scattering by concentric spheres comprised of a metallic and a dielectric region," *Phys. Rev. B*, vol. 26, no. 8, pp. 4052-4063, Oct. 1982.

[117] C. A. Balanis, *Advanced engineering electromagnetics*, John Wiley & Sons, 1989.

[118] D.S. Jones, *The theory of electromagnetism*, Pergamon Press, 1964.

[119] M. Abramowitz and I. A. Stegun, *Handbook of mathematical functions*, Dover Publications, 1965.

[120] C. A. Balanis, *Antenna theory: analysis and design*, John Wiley & Sons, 2nd. Ed., 1997.

[121] R. Englman and R.Ruppin, "Optical lattice vibrations in finite ionic crystals: II," *J. Phys. C*, vol. 1, pp. 630-643, 1968.

[122] R. Englman and R.Ruppin, "Optical lattice vibrations in finite ionic crystals: III," *J. Phys. C*, vol. 1, pp. 1515-1531, 1968.

[123] F. B. Hildebrand, *Methods of applied mathematics*, Prentice Hall, 2nd. Ed., 1965.

[124] R. W. Ziolkowski, private communication, 2005.

[125] P. M. Johansen and O. Breinbjerg, "An exact line integral representation of the physical optics scattered field: the case of a perfectly conducting polyhedral structure illuminated by electric Hertzian dipoles," *IEEE Trans. on Antennas and Propagation*, vol. 43, no. 7, pp. 689-698, July 1995.

[126] J. E. Hansen, Ed., *Spherical near-field antenna measurements*, Peter Peregrinus Ltd., 1988.